Università Cattolica del Sacro Cuore
University of Notre Dame

Doctoral Thesis

Cooperative effects in quantum systems: superradiance and long-range interactions

Author:
Francesco Mattiotti

Matricola:
4613853

Supervisors:
Prof. G. Luca Celardo
Prof. Fausto Borgonovi
Prof. Boldizsár Jankó

A thesis submitted in fulfillment of the requirements
for the degree of Doctor of Philosophy

in the

International Doctoral Programme in Science

S.S.D.: FIS/02, FIS/03

Ciclo XXXII

Academic year 2019/2020

Abstract

This Ph.D. thesis studies the interplay of cooperativity and noise in realistic systems, largely focusing on superradiance. Cooperative effects emerge from the collective interaction of an ensemble of elements to an external field. Notable examples are superconductivity, where the electron Cooper pairs interact with the lattice vibrations, plasmon excitations, arising from the collective interaction of electrons in a metal with the Coulomb field, and superradiance, that is a cooperative spontaneous emission process stemming from an aggregate of identical emitters. Cooperative effects are typically robust to disorder and noise, making them interesting for applications to quantum devices operating at room temperature. In this work, we first present a general master equation formalism that describes the collective coupling of an aggregate of emitters/absorbers to the electromagnetic field, valid both when the size of the aggregate is larger or smaller than the emitted/absorbed wavelength. Also, the formalism is valid both for weak and strong coupling of the emitters to the electromagnetic field and, most importantly, it allows to correctly describe superradiance in different regimes.

Within such formalism, the interplay of superradiance and thermal noise is studied both for molecular nanotubes (of size smaller than the transition wavelength) that are present in the antenna complexes of photosynthetic Green Sulfur Bacteria, and also for novel solid state quantum dot superlattices, having size larger than the emitted wavelength. In both cases it is shown that coherence can persist in presence of thermal noise at the temperatures where these systems have been experimentally analyzed (room temperature for molecular nanotubes, and 6 K for quantum dot superlattices). Specifically, in natural molecular nanotubes we show that the macroscopic coherent delocalization of the excitation at room temperature, covering hundreds of molecules, can be considered an emergent effect originating from the combined effect of the specific geometric disposition of the molecules and the presence of cooperatively enhanced couplings between cylinder subunits. These results open the path to new ways of engineering quantum wires robust to noise thanks to cooperativity. Moreover, our analysis of solid state systems based on perovskite ($CsPbBr_3$) quantum dot superlattices provides a theoretical framework able to explain recent observations of superradiant emission. Based on our theory, we suggest that further experiments, using smaller quantum dots, could significantly increase the robustness of the system to thermal noise, paving the way towards room-temperature superradiance in solid-state systems. We also considered the antenna complexes of Purple Bacteria, where cooperative effects are

well known to boost the transfer and storage of photo-absorbed excitations. We show how these properties can be exploited to create a bio-inspired molecular aggregate laser medium, where natural sunlight, although weak, would be used as a pumping source. The efficient energy transfer within this system would effectively focus the absorbed excitation on a suitably chosen molecular dimer, composed by a pair of interacting molecules. The orientation of the molecule transition dipole moment in each dimer is such to concentrate all the dipole strength in the highest energy level, leaving the lower excitonic state dark. A molecular dimer in such configuration, which is ideal to achieve population inversion, is called H-dimer. Such an H-dimer in our proposed architecture for a bio-inspired laser medium, is placed at the center of the bio-inspired molecular aggregates. The H-dimers, pumped by the surrounding molecular aggregates, reach population inversion and, therefore, can lase when such aggregates are placed in an optical cavity. Turning the incoherent energy supply provided by the Sun into a coherent laser beam would overcome several of the practical limitations inherent in using sunlight as a source of clean energy. For example, laser beams are highly effective at driving chemical reactions which convert sunlight into chemical energy. Further, since bacterial photosynthetic complexes tend to operate in the near-infrared spectral region, our proposal naturally lends itself for realising short-wavelength infrared lasers which would allow their beams to travel nearly losslessly over large distances, thus efficiently distributing the collected sunlight energy.

In search of a common mechanism to cooperativity and its robustness, we have compared the Cooper pair model of superconductivity and single-excitation superradiance, showing many similarities between the two: in particular, superradiant systems present an imaginary gap in the complex plane (that is, a segregation between the lifetimes of the system eigenstates) that, similarly to the superconducting gap, makes these systems robust to static disorder. More in general, we show that any long-range interaction between the constituents of a system generates collective behaviours, manifested by gaps in the excitonic spectrum. Therefore, our further analysis considers the effect of long-range interactions on excitation transport along disordered chains. We show that the presence of a gapped, collective state affects the whole spectrum of the system, generating quite counter-intuitive disorder-enhanced and disorder-independent transport regimes, that extend over many orders of magnitude of the disorder strength. We also prove that a chain strongly coupled to a cavity mode is equivalent to a long-range interacting chain, thus being very promising for future experiments and applications. Specifically, we show that realistic molecular chains, state-of-the-art trapped ions and Rydberg atoms are all able to reach the needed long-range interaction strength that would show disorder-enhanced or disorder-independent transport, aiming to the realization of dissipationless transport of energy in disordered quantum wires.

Publication list

The results presented in this thesis have been published, or are available as preprints, in the following papers:

- Marco Gullì, Alessia Valzelli, Francesco Mattiotti, Mattia Angeli, Fausto Borgonovi, and G. Luca Celardo, "Macroscopic coherence as an emergent property in molecular nanotubes", *New J. Phys.* **21**, 013019 (2019);
- Nahum C. Chávez, Francesco Mattiotti, J. A. Méndez-Bermúdez, Fausto Borgonovi, and G. Luca Celardo, "Real and imaginary energy gaps: a comparison between single excitation superradiance and superconductivity and robustness to disorder", *Eur. Phys. J. B* **92**, 144 (2019);
- Francesco Mattiotti, William M. Brown, Nicola Piovella, Stefano Olivares, Erik M. Gauger, and G. Luca Celardo, "Bio-inspired sunlight-pumped lasers", *arXiv:2007.04314* (2020);
- Francesco Mattiotti, Masaru Kuno, Fausto Borgonovi, Boldizsár Jankó, and G. Luca Celardo, "Thermal decoherence of superradiance in lead halide perovskite nanocrystal superlattices", *Nano Lett.* **20**, 7382–7388 (2020);
- Nahum C. Chávez, Francesco Mattiotti, J. A. Méndez-Bermúdez, Fausto Borgonovi, and G. Luca Celardo, "Disorder-enhanced and disorder-independent transport with long-range hopping: application to molecular chains in optical cavities", accepted for publication on *Phys. Rev. Lett.* (2021) as Editors' Suggestion, *arXiv:2010.08060* (2020).

Acknowledgements

The work presented in this thesis is the result of my past four years of research in the International Doctoral Program in Science, and it has been conducted in many places around the world, in a very *international* spirit. I would have never been able to conclude this experience by myself, and various acknowledgements are more than needed.

I would like to thank my supervisor, Luca Celardo, for having guided me throughout this journey. Thank you for the many opportunities that you have offered me, for all the energy that you have always put in our work and for being always available to answer my doubts. I also want to thank my co-supervisors, Fausto Borgonovi and Boldizsár Jankó for their expert guidance. Thank you both for showing me and teaching me a methodical approach to research, how to face unexpected results and how to focus the work consistently to a target. I also thank Ken Kuno for his crucial intuitions that initiated my research in Notre Dame, and for his constant and efficient tutoring during my time at Notre Dame. Without any doubt, I have grown significantly as a scientist thanks to our interactions. Moreover, I thank the other members of my Research Committee at Notre Dame, Mark Caprio and Morten Eskildsen. Our discussions have been of great help in focusing my research. I am also grateful to Luca Gavioli, Prashant Kamat and all the people who ideated and directed the International Program in Science: it is a unique opportunity, that has allowed me to meet a lot of experts from various backgrounds, increasing my experience significantly.

Now, I would like to thank some people that I met in the various places where I have conducted my research. First, many thanks to the Quantum Biology group at Università Cattolica in Brescia, including past and present members: Giulio, Mattia, Chahan, Marco, Alessia, Pietro, Federica, thank you for all the time spent together and for the stimulating discussions. At the Department of Mathemathics and Physics in Brescia, I also thank Claudio Giannetti and Francesco Banfi, for very interesting exchanges that we had while I have been in Brescia. Then, I cannot forget my colleagues Ph.D. students: Marco, Giulio, Gina, Andrea, Antonio, Sonia, Paolo and the others. Thank you all for the great time that we shared in our tiny, very welcoming department.

I must also thank some people that I have met at the Insitituto de Fisica of Benemerita Universitad Autonoma de Puebla, in Mexico. First, I am very grateful to Felix Izrailev, J. Antonio Mendez-Bermudez, Francisco Rivas and J. Mauricio Torres for everything that I learnt from discussing with you guys. I also thank my fellow Ph.D. students in Puebla, Samy, Diana, but mostly Nahum: man, I thank you for all the time that we shared, for everything that we learnt from each other, and for your true friendship. About my time in Mexico, I am also deeply grateful to Thomas Seligman and Thomas Stegmann for the amazing gatherings that they organized at the Centro Internacional de Ciencias of the Universidad Nacional Autonoma de Mexico in Cuernavaca: I always loved the atmosphere of those meetings and I always felt enriched after participating.

Then, moving to the United States, I must thank some other people that I have not mentioned above. First, I thank all the Condensed Matter Physics Group at Notre Dame: Shubin, Tony, Xiaoyu, Whenzhao, Sushrut and Lihao, you have all been very kind and welcoming, and I also learnt a lot from our discussions. I also thank all the members of Ken Kuno's group at the Department of Chemistry of Notre Dame: Ilia, Kyle, Mike, Maksym, Zhuoming, Kirill, Tianle, Irina, thank you all for the great time that we had, for the very interesting group meetings and for your friendship. I also thank Chris and Barbara, for being very warm and accomodating landlords and roommates, making me feel really at home since the very first moment that I arrived to South Bend and throughout all my stay.

Moreover, I must thank a handful of international collaborators that do not fall in the above categories. Many thanks go to Erik Gauger and Will Brown from Heriot-Watt University in Edinburgh, as well as to Nicola Piovella and Stefano Olivares from Università degli Studi di Milano: thank you for your expert guidance and collaboration and for the amazing results that we obtained together. I am also very grateful to Mohan Sarovar from Sandia Laboratories for all that I learnt about photon sensors and for making me fall in love with San Francisco. Then, I thank Lev Kaplan, Armin Kargol, Aaron Kelly, Ron, Cole and Katherine for the very stimulating discussions about Green Sulfur Bacteria.

Finally, I must thank my family and my friends. Although I have been away from Italy most of the time in the past years, I always felt you guys closer than ever, and this feeling helped me go through the hardest moments.

Infine, un grande grazie è dovuto alla mia famiglia e ai miei amici. Anche se in questi anni sono stato lontano dall'Italia buona parte del tempo, vi ho sempre sentiti tutti vicinissimi a me, e questa sensazione mi ha aiutato ad attraversare i momenti più difficili.

My final words of these pages go to Brenda: my ray of sunshine, my brightest star. Thank you for making my heart beat every time that I see you, or hear you, or think about you. Thank you for giving me strength, for being incredibly patient with me, and for dreaming, with me, our future together.

November 2020
Francesco

Contents

Abstract iii

Publication list v

Acknowledgements vii

1 Introduction 1
- 1.1 Collective phenomena: a common mechanism . . . 2
- 1.2 Extension of Fano's approach: long-range interactions and energy gaps . 4
- 1.3 Superradiance, i.e. cooperative light-matter coupling . . . 6
  - 1.3.1 Superradiance in the time domain: superlinear scaling, single-excitation superradiance and subradiance . . . 7
  - 1.3.2 Superradiance in the frequency domain . . . 10
  - 1.3.3 Superradiance in the photon statistics: photon bunching . . . 12
- 1.4 Supertransfer of excitations . . . 12
- 1.5 Coupling strength to the electromagnetic field . . . 16
- 1.6 Cooperativity, long-range interactions and robustness to disorder and noise . . . 19
  - 1.6.1 Unit-rank interactions: robustness to static disorder . . . 19
  - 1.6.2 Unit-rank interactions: robustness to dephasing . . . 20
  - 1.6.3 Unit-rank interactions: robustness to thermal noise . . . 20
  - 1.6.4 Finite-range interactions: robustness to static disorder, dephasing and thermal noise . . . 21
- 1.7 Thesis outline . . . 22

2 Cooperative effects in light-matter interaction 25
- 2.1 Hamiltonian and Master Equation for the whole system . . . 25
- 2.2 Born and Markov approximations . . . 27
- 2.3 Secular approximation . . . 27
- 2.4 Explicit calculation of the rates . . . 28
  - 2.4.1 Real Part . . . 30
  - 2.4.2 Imaginary Part (Lamb Shift) . . . 33
  - 2.4.3 Final expression . . . 36

2.5 Stationary solution for a single site 36
2.6 Superradiance for two coupled sites 37
2.6.1 Many-excitation superradiance, single-excitation superradiance and subradiance 40
2.7 Single excitation approximation and effective non-Hermitian Hamiltonian 41
2.7.1 Radiative non-Hermitian Hamiltonian at zero temperature 42
2.7.2 Regime of validity for two sites 43
2.8 Including an extra coupling between the sites 43
2.8.1 Long-wavelength approximation 46
2.9 Comparison with the stochastic model of sunlight 47

3 Interplay of superradiance and noise in photosynthetic molecular nanotubes 49
3.1 Introduction 50
3.2 The models 52
3.3 The Hamiltonian and the dipole approximation 54
3.4 Single Cylindrical structures: Results 57
3.4.1 Collective Dipole Strength 57
3.4.2 Delocalized excitonic states at room temperature 59
3.4.3 Thermal Coherence Length 60
3.5 Relationship between structure and macroscopic coherence 62
3.5.1 Structure of ring eigenstates coupling 63
3.5.2 Super and Sub-Transfer 68
3.5.3 Super-Transfer and density of states 70
3.6 Natural concentric structures 72
3.7 Conclusions and Perspectives 74
3.8 Appendix 77
3.8.1 Geometry of the models 77
3.8.2 Comparison between dipole strengths and radiative decay widths 82
3.8.3 Comparison between radiative and dipole approximations 82
3.8.4 Participation ratio of the eigenstates 82
3.8.5 Super-Transfer in the WT model 84
3.8.6 Robustness to Static Disorder 85
3.8.7 Concentric cylinders 87

4 Applications of superradiance in photosynthetic molecular aggregates to sunlight-pumped lasers 89
4.1 Introduction 90
4.2 Lasing equations for molecular aggregates 92
4.3 Lasing with dimers 96
4.4 Bio-inspired lasers 98
4.5 Conclusions and perspectives 101
4.6 Appendix 103
4.6.1 A possible geometry for an H-dimer 103
4.6.2 The Bloch-Redfield master equation 104

4.6.3 From Bloch-Redfield to Lindblad master equation 106
4.6.4 Lasing equations for molecular aggregates 109
4.6.5 Population inversion for a dimer 112
4.6.6 Coupling dimer to a cavity: modification of the Hamiltonian . . . 112
4.6.7 Including dephasing and the coupling to the cavity in the Bloch-Redfield master equation 115
4.6.8 Full 4-level Bloch-Redfield: coherent laser equations 116
4.6.9 Results with 4-level Bloch-Redfield static field model 118
4.6.10 Electric field with strong dephasing: incoherent rates 119
4.6.11 Electric field with strong dephasing: incoherent laser equation . . 123
4.6.12 Comparing coherent and incoherent laser equations 124
4.6.13 Bio-inspired aggregate: Purple Bacteria 127
4.6.14 Threshold density at 3000 K for purple bacteria bio-inspired aggregates 132
4.6.15 Bio-inspired aggregate: Green Sulfur Bacteria 134

5 Superradiance in quantum dot superlattices 139
5.1 Introduction 139
5.2 Model, results and discussion 140
5.3 Conclusions 147
5.4 Appendix 149
5.4.1 Non-Hermitian Hamiltonian for NC superlattices 149
5.4.2 Point dipole validity 154
5.4.3 Time-resolved fluorescence at T = 0 K without disorder 156
5.4.4 Geometry dependence of the SR states position 157
5.4.5 Time-resolved fluorescence with non-zero temperature 160
5.4.6 Fitting parameters for the saturation function 161
5.4.7 The saturation assumption 161
5.4.8 Time-resolved fluorescence at T = 0 K with static disorder 164
5.4.9 Emission redshift 167
5.4.10 Static disorder and inhomogeneous linewidth 169
5.4.11 A remark on the role of the imaginary coupling in the robustness to disorder 173

6 Real and imaginary energy gaps: a comparison between single excitation Superradiance and Superconductivity 175
6.1 Introduction 176
6.2 Analytical Results for N levels 179
6.2.1 Hermitian case 180
6.2.2 Non-Hermitian case 183
6.3 Numerical Results 186
6.4 Imaginary Energy gap and robustness to perturbations 187
6.4.1 Non-Hermitian perturbative approach 188
6.4.2 Robustness of superradiance to static diagonal disorder 189

6.5 Relation between the gapped regime and the interaction range 191
6.6 Conclusions and Perspectives 193
6.7 Appendix 194
  6.7.1 Non-Hermitian coupling: widths of the subradiant states 194
  6.7.2 Long and short-range interaction 196

7 Interplay of long-range interactions and disorder in energy transport 199
7.1 Introduction 200
7.2 The Model 201
7.3 Results for long-range systems 204
7.4 Applications to molecular chains in optical cavities 206
7.5 Conclusions 207
7.6 Appendix 208
  7.6.1 Realistic Parameters for different systems 208
  7.6.2 Energy Gap and Long Range Interaction 208
  7.6.3 Transmission 209
  7.6.4 Shape of Eigenfunctions 214
  7.6.5 Master Equation *vs.* Schrödinger equation approach to compute the current 222
  7.6.6 Current and typical current 227
  7.6.7 Scaling of the transport regimes with the long-range coupling strength 228
  7.6.8 Mapping between a molecular chain in an optical cavity and a system with long-range hopping 229
  7.6.9 Dynamics: wave packet spreading and stationary state 232

8 Conclusions and perspectives 237

Bibliography 243

Chapter 1

Introduction

Cooperativity is the ability of many elements in a system to act in coordination, so that some physical property of the system results different from that of a single element. Cooperative quantum effects emerge from the interaction between the constituents of a system and they are often connected to important functional aspects. Cooperative effects show also robustness to disorder and noise, so that their understanding can be essential to develop quantum devices able to work at room temperature.

In this thesis we have explored different cooperative effects showing how they can help to shed new light into the functionality of biological systems, molecular and solid-state aggregates, and in general for interacting emitters where light-matter interaction is a relevant factor. Cooperative effects have always been at the center different research fields for their functional properties [1–7]. In particular the discovery of the role of cooperative effects in biological systems, for instance superradiance and super-transfer in photosynthetic systems, have inspired different proposals of bio-mimetic devices. Following this line of research on bio-mimetic quantum devices, we have proposed a design for a bio-inspired sunlight-pumped laser. Specifically, a new architecture, inspired to photosynthetic systems, for a sunlight-pumped laser has been shown to lower the lasing threshold by different orders of magnitude, making a laser pumped by natural sunlight possible. Such a laser, if realized, could greatly help the solution of the energy problem, transforming the incoherent sunlight into coherent laser beams, that can be used to drive chemical reactions and, therefore, being good candidates for absorbing sunlight energy and storing it efficiently [8–11].

At the same time, we have followed a more fundamental line of research in this thesis, focusing on the common mechanism to cooperativity and its robustness to disorder and noise. There are many examples of cooperative effects in condensed matter physics such as superconductivity, superradiance, plasmon excitations and giant resonances in nuclei. As was pointed out by U. Fano [12], a common mechanism underlies all the above mentioned collective phenomena. Following Fano's point of view, we unveil a deep connection between cooperative effects, long-range interactions and robustness to noise.

In this chapter we introduce and discuss these points, by first recalling Fano's idea on a common mechanism behind cooperative effects, then connecting it to long-range interactions, and presenting the effects of superradiance and supertransfer that these interactions can induce. Finally, we show different coupling strength regimes where cooperative effects can emerge and, in these regimes, we discuss in which sense cooperativity can emerge and how it can make the systems robust to disorder and noise.

1.1 Collective phenomena: a common mechanism

When studying the interaction of aggregates of similar physical objects (*e.g.* electrons, atoms, molecules…) with propagating fields, such as photons or phonons, cooperative effects arise, due to the mutual interaction between the different components of the system, mediated by their common coupling to the field. Such interaction induces a wide range of collective phenomena: superconductivity, plasmon excitations, superradiance.

Different theoretical treatments for these phenomena have been developed in the late 1950s [13–15]. Though originating from quite different physics, they share the same mathematical mechanism, as pointed out by U. Fano [12]. Common to these phenomena is the presence of a dense spectrum of independent levels, ϵ_n, satisfying the Schrödinger equation

$$H_0 \left| n \right\rangle = \epsilon_n \left| n \right\rangle \ . \tag{1.1}$$

The common coupling to the field modifies the Hamiltonian, that becomes $H = H_0 + V$. An eigenstate $\left|\psi\right\rangle$ of the full Hamiltonian H satisfies

$$H \left|\psi\right\rangle = E \left|\psi\right\rangle \tag{1.2}$$

and it can be decomposed on the basis of H_0 as $\left|\psi\right\rangle = \sum_n c_n \left|n\right\rangle$. Calculating the expectation value $\langle m|H|\psi\rangle = \langle m|(H_0 + V)|\psi\rangle$ and solving for c_m gives the identity

$$c_m = \frac{\sum_n c_n V_{mn}}{E - \epsilon_m} \tag{1.3}$$

where $V_{mn} = \langle m|V|n\rangle$ is the coupling between the levels induced by the field.

Fano observes [12] that cooperative phenomena emerge when the field-induced coupling between the levels can be factorized as

$$V_{mn} = v_m^* v_n \ . \tag{1.4}$$

This condition applies for example to the BCS theory of superconductivity [13, 16], where the electron-phonon coupling between the electron levels close to the Fermi surface is well approximated by a constant, $V_{\mathbf{k},\mathbf{k}'} = -V_0$ for $\epsilon_{\mathbf{k}} - \epsilon_{\mathbf{k}'} < \hbar\omega_D$ (ω_D being the Debye frequency). This is also true for plasmon excitations, where the dipole-dipole interaction between oscillating charges in a lattice, when written in terms of the normal modes $\left|n\right\rangle$ having wavelengths much longer than the lattice step, are factorized as $V_{mn} \propto f_m^{1/2} f_n^{1/2}$, where f_n is the oscillator strength of the n-th normal mode [12]. Finally, as we describe more in detail in Chapter 6, in the case of superradiance, for

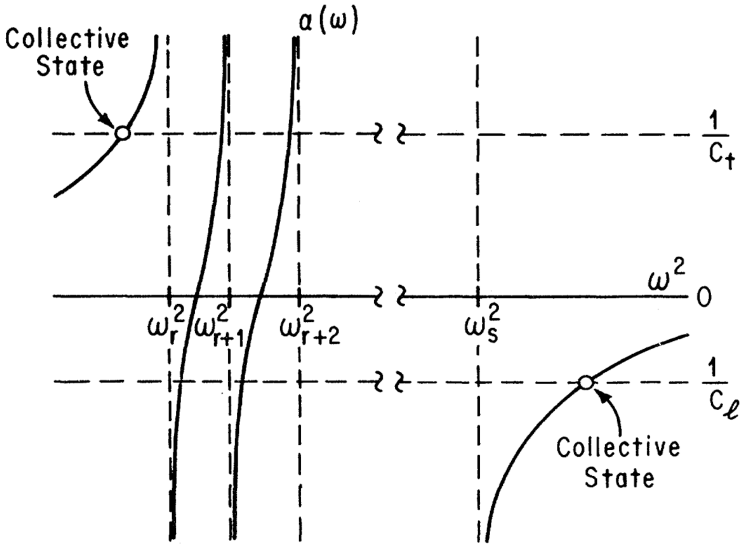

Figure 1.1: Graphic solutions of the gap equation (1.5) in the case of plasmon excitations. Following Ref. [12], the right-hand side of Eq. (1.5) is interpreted as the product $C\alpha(\omega)$ between the polarizability function $\alpha(\omega)$ (continuous curve in the figure) and a polarization factor C, which can be positive ($C_l = \frac{2}{3}$ for longitudinal polarization) or negative ($C_t = -\frac{1}{3}$ for transverse polarization), see horizontal dashed lines. The electron oscillations are treated as coupled classical harmonic oscillators, as done in Ref. [12], and one still obtains Eq. (1.5), where the energies in the denominator are replaced by the squared frequencies ($E \to \omega^2$ and $\epsilon_n \to \omega_n^2$). Figure reproduced from Ref. [12].

aggregates smaller than their emitted wavelength, the field induces an effective non-Hermitian coupling between the emitter single-excitation states $|j\rangle$, and such coupling has the factorized expression $V_{ij} \approx -i\frac{\gamma}{2}$ in the simple case where the emitters are all parallel.

Having established this requirement, Eq. (1.4) can be substituted into Eq. (1.3). Then, multiplying both sides of Eq. (1.3) by v_m, summing both sides over m and dividing by $\sum_m c_m v_m$ gives the relation

$$1 = \sum_n \frac{|v_n|^2}{E - \epsilon_n} , \tag{1.5}$$

that we call *gap equation* as a reference to the corresponding BCS equation [13, 16]. The gap equation can be parametrized in terms of some physical quantities relevant to the problem, and the solution of Eq. (1.5) for the case of plasmon excitations is shown in Fig. 1.1. The specific case of plasmon excitations already shows a more general feature of collective phenomena: the effect of the dipole-dipole interaction, although weak, is all concentrated in one collective state. As proved in Ref. [12], such collective state retains most of the oscillator strength of the whole system and it is gapped on the low-energy or high-energy side of the spectrum, depending on the polarization, as shown in Fig. 1.1.

Such gap is a mathematical consequence of having a unit-rank interaction. Indeed, see Eq. (1.4), the factorized interaction matrix V is a unit-rank matrix with only one eigenvalue different from zero and equal to $\sum_n |v_n|^2$.

The gap has the same expression both for the case of plasmon excitations and for the Cooper problem of superconductivity and, with a proper generalization, also for the case of superradiance. Indeed Fano mentions the case of molecular aggregates and how some collective, extended states can retain all the oscillator strength, basically extending his approach to superradiance (more details in Chapter 6).

When the interaction V is strong, one eigenstate of the whole system hamiltonian H becomes identical to the eigenstate of the interaction matrix V that has a non-zero eigenvalue, thus producing a gapped state which concentrates all the interaction strength. The presence of a gapped state allows the manifestation cooperative effects despite the presence of noise and disorder. Thus the emergence of cooperative effects in general occurs only above a critical strength of the interaction V (this has been discussed in Chapter 6). Nevertheless, in presence of symmetries in the system, such that $[H_0, V] = 0$, already for weak coupling V the system can show cooperative effects. This is the case of several molecular aggregates discussed in this thesis, see Chapters 3 and 4. Finally, we would like to stress that even if one eigenstate of the system concentrates all the coupling strength of V, either due to symmetry or to a large enough V, in order for cooperativity to emerge, the coherent collective behaviour connected with the cooperative eigenstates must be robust to the disorder or noise present in the system, as we discuss in section 1.6.

1.2 Extension of Fano's approach: long-range interactions and energy gaps

In the previous section, following Fano's approach [12], we have shown a mathematical condition that determines collective behaviours: the interaction operator induced by the external field among the system levels must be unit-rank, so that it can be factorized as in Eq. (1.4). A simple example of unit-rank interaction is where the system hamiltonian H_0 in Eq. (1.1) represents unperturbed eigenstates $|n\rangle$, with an additional all-to-all coupling $V_{mn} = V_0 \; \forall m, n$, that represents an infinite-range interaction between the eigenstates of H_0. This all-to-all interaction is present both in the Cooper pair model of superconductivity and the the superradiance model in the small-volume limit, where the wavelength is larger than the system size, as shown in Chapter 6. This is clearly an example of long-range interaction, and it is characterized by having one non-vanishing eigenvalue, NV_0, where all the interaction strength is collectively concentrated, and $(N-1)$ vanishing eigenvalues, that are gapped by an amount NV_0 from the first one. The eigenstate corresponding to the gapped eigenvalue is the fully extended state $|\psi\rangle = \frac{1}{\sqrt{N}} \sum_n |n\rangle$.

Indeed, all the examples of factorized interactions introduced in section 1.1 involve long-range interactions: long-range Coulomb forces are present in the case of plasmon excitations; long-range interactions, mediated by the presence of a coupling to a common external environment, are present both in superconductivity and superradiance. In the case of superconductivity, phonons mediate an attractive interaction between the electrons (which is long-range in momentum space), while in the case of superradiance, the interaction mediated by the electromagnetic field (EMF) is long-range in real space.

Up to now we have only considered unit-rank interactions. In the following, we propose some extensions of Fano's approach to cases where the interaction is not unit-rank. The first extension that we are going to propose is where V is a long-range interaction. The second extension of Fano's theory that we will discuss is to the case of non-hermitian interactions V. The third extension is related to intrinsic cooperative effects that are not due to the range of interaction but to intrinsic geometric properties of the system.

When the interaction range is not infinite, the rank of the interaction is not unit but, as we show in Chapter 6, we propose to extend the mechanism proposed by Fano to more generic long-range interactions of the form $V_{mn} \propto |m-n|^{-\alpha}$ (where $\alpha < d$, and d is the dimensionality of the system) are *effectively low-rank*, meaning that the interaction matrix is characterized by few very large engenvalues with the rest of the eigenvalues being very small. This implies that their spectra show similar features to the infinite-range interaction discussed above: one (or few) of their eigenvalues are gapped from the rest of the (nearly) vanishing eigenvalues. The presence of a gapped, collective state also affects the robustness of the system to noise and disorder, as we discuss in section 1.6.

Motivated by this analogy, in this work we analyze different long-range interacting systems, that can be reconducted to this scheme, and we analyze their interplay with disorder and noise. Indeed, all the physical systems considered in this thesis are characterized by long-range interactions. In the case of superradiance, the coupling of emitters to a common EMF induces a non-Hermitian interaction, meaning that the V interaction matrix is non-hermitian, $V = V_R + iV_I$. Non-Hermiticity arises from the fact that an excitation can be lost by emission, making the physics of this system non-unitary. Both the real and the imaginary part are characterized by long-range interactions which decay as $1/r^3$ at short distances and $1/r$ at large distances, where r is the distance between the emitters. Different regimes exist, depending on the size and dimensionality of the system, where V_R or V_I (or both of them, or even neither) can have an effective low rank. For instance, in the small-volume limit ($r \ll \lambda$, where λ is the emitter transition wavelength), V_R represents a dipole interaction, which is not low-rank due to the fact that the dipole coupling $V_R \sim 1/r^3$ is not long-range. On the other side, in the small-volume limit, V_I represents an all-to-all interaction, which has unity rank. If the imaginary part of the interaction is particularly strong, an imaginary gap can arise in correspondence of superradiant states, characterized by large imaginary energy (corresponding to their decay width or inverse lifetime). Interestingly even an imaginary gap can donate robustness to the system as we discuss in Chapter 6. Such a scheme of a complex V applies to all our studies of molecular aggregates (Green Sulfur Bacteria nanotubes in Chapter 3, Purple Bacteria in Chapter 4) and solid-state systems (perovskites quantum dots superlattices in Chapter 5). We also focused on systems with intrinsic long-range interactions, showing the different transport regimes which arise due to the emergence of cooperativity and energy gaps in such systems (see Chapter 7). This analysis has implications in many realistic systems as trapped ions, Rydberg atoms, polar molecules and emitters in cavities. Specifically, in Chapter 7 we demonstrate that the coupling to a cavity mode induces a long-range interaction between the emitters.

Finally, note that long-range interactions are not the only possible extension of Fano's approach that we discuss in this thesis. Indeed, in Chapter 3 we show that even an effective short-range interaction ($V_R \sim 1/r^3$ is a short-range interaction in quasi-one-dimensional nanotubes) can lead to strong cooperative effects, due to the specific geometry of the system, and these effects are robust to thermal noise and disorder. This shows that the low rank of the interaction might not be a necessary requirement for important cooperative effects to emerge, and this opens another path for extending Fano's approach on cooperativity.

1.3 Superradiance, i.e. cooperative light-matter coupling

One of the most interesting cooperative effects is superradiance. As introduced by Dicke in 1954 [15], superradiance is the collective emission of light from an ensemble of identical emitters, due to the formation of coherent, extended excitations among the emitters. Superradiance manifests itself both in the time domain and in the frequency domain, and it has been observed in a variety of systems [17], with some of the most recent examples being cold atomic clouds [18], photosynthetic antenna complexes [19], molecular aggregates [20, 21], quantum dots [22, 23] and nitrogen vacancies in nanodiamonds [24]. This effect is relevant in enhancing absorption and energy transfer, which has been proposed to improve the efficiency of light-harvesting systems [1–5]. Superradiance also leads to spectrally ultranarrow laser beams [6].

Being a collective effect, superradiance is quenched by inhomogeneities such as static disorder and noise [25, 26]. As regards the spatial arrangement, superradiance may or may not require a regular disposition on the emitters, depending on the aggregate size and its density. Specifically, for a very dense aggregate of emitters occupying a volume smaller than the emission wavelength (such as the case of molecular aggregates), a regular arrangement is required to produce a collective coupling to the light field. On the other hand, for dilute aggregates of emitters extended over a volume much larger than their emission wavelength (like the case of cold atomic clouds), superradiance does not require an ordered arrangement, and collective coupling to the light field is present also for completely random dispositions of the elements.

In the following we give some examples of the main experimental signatures of superradiance for different physical systems.

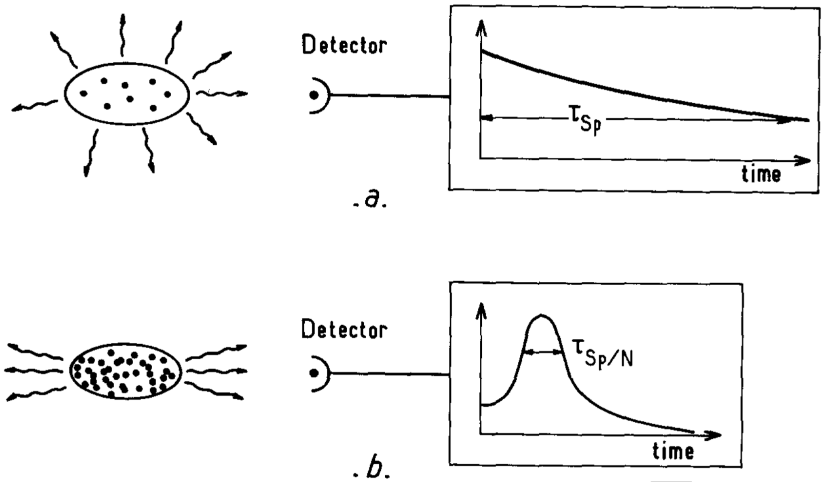

Figure 1.2: Comparison between the general characteristics of ordinary fluorescence and superradiance experiments. (a) Ordinary spontaneous emission is essentially isotropic with an exponentially decaying intensity (time constant τ_{sp}). (b) Superradiance is anisotropic with an emission occurring in a short burst of duration $\sim \tau_{sp}/N$. Figure reproduced from Ref. [27].

1.3.1 Superradiance in the time domain: superlinear scaling, single-excitation superradiance and subradiance

The main signature of superradiance can be observed when an aggregate of N emitters is prepared in a state where all the emitters are excited. In such situation, where N excitations are initially present in the system, the emitters will spontaneously decay by emitting a light intensity, that ultimately decays with time. As clearly described by Gross and Haroche [27], see Fig. 1.2, the emitted light intensity from an ensemble of independent emitters would be isotropic and it would decay in time exponentially with the single-emitter radiative lifetime τ_{sp} (see Fig. 1.2a), independent of the number N of emitters. On the other hand, if the emitters are densely packed, so that they interact cooperatively with the light field, they emit along a well-defined direction that depends upon the sample geometry and the emitted intensity increases initially with time, producing a light burst that lasts $\approx \tau_{sp}/N$ and whose intensity scales superlinearly as N^2 (see Fig. 1.2b). These signatures reflects the fact that the collective interaction with the EMF induces a build-up of a collective polarization, that is responsible of the cooperative light emission.

Interestingly, cooperative emission shows clear signatures also when the system is not initially fully excited, but a single excitation is photo-induced in the system. In this situation, superradiance is related to a coherent delocalization of the excitation among the emitters, and it results in a fast decay of the emitted light, with a collective lifetime faster than the individual emitters. Moreover, the emission is along the same direction of the incoming light that excited the system, as opposed to the isotropic spontaneous

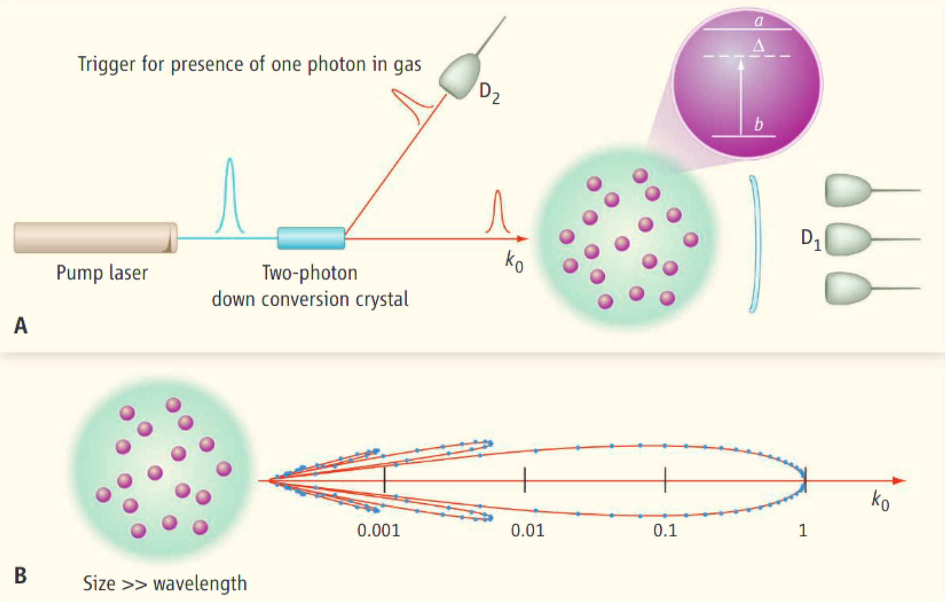

Figure 1.3: Scheme of an experiment to observe single-excitation superradiance and subradiance from cold atomic clouds. Figure reproduced from Ref. [28].

emission that one would have from independent emitters. Such effect is a clear manifestation of the coherent delocalization of the initial excitation, and it has therefore been referred to by Marlan Scully as “The super of superradiance” [28], or *single-excitation superradiance*. Moreover, when the initial state is not exactly a collective eigenstate of the light-matter coupling, at long times the excitation decays much slower than the single-emitter case. Such phenomenon, called *subradiance*, is due to the presence of collective states where a destructive interference slows down the spontaneous emission process.

Single-excitation superradiance and subradiance have been observed in a variety of systems. Many interesting results have been obtained in cold atomic clouds, where the single-excitation state is initially created by exciting the system with an off-resonant laser, as sketched in Fig. 1.3a. As a result, the light is emitted mostly along the same direction of the excitation laser, see Fig. 1.3b. Once the excitation laser turns off, the emitted radiation decays in time faster than the single-atom spontaneous decay time, as is shown in Fig. 1.4(a,b). The decay is faster when the optical thickness b_0 (a parameter that quantifies cooperativity in this system) is increased. At long times, on the other hand, the intensity emitted by such cold atomic clouds decays much slower than the single-atom case, as is shown in Fig. 1.4(c). Such subradiant decay has a cooperative origin, as is proven by the fact that the decay gets slower when the cooperativity parameter b_0 is increased.

A striking variation of the radiative recombination time due to cooperative emission has also been observed in pseudoisocyanine (PIC) bromide molecular aggregates [20]. These aggregates are classified as J-aggregates, as most of the coupling of the aggre-

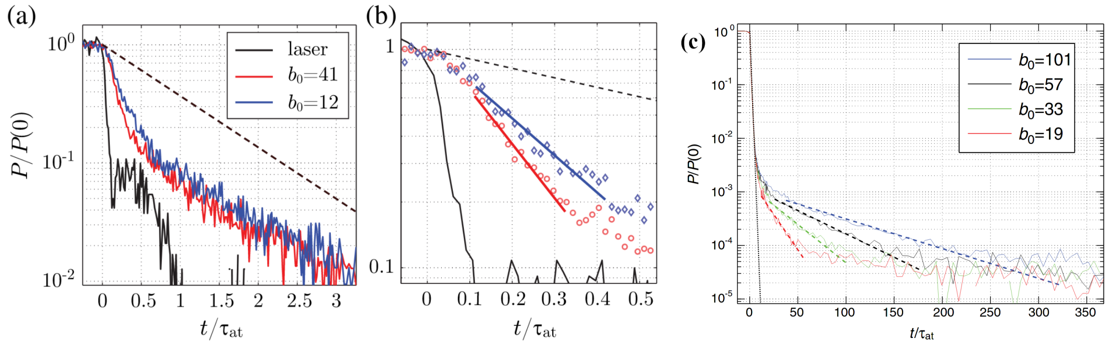

Figure 1.4: Decay of the measured fluorescence power after switching off the excitation laser (black line) in time from a cloud of ^{87}Rb atoms at temperature $T \approx 50\ \mu$K. Here $b_0 = 3N/(kR)^2$ is the optical thickness of the cloud, where $N \approx 10^9$ is the number of atoms, $k = 2\pi/\lambda$ is the wavenumber related to the atomic transition ($\lambda = 780$ nm) and $R \approx 1$ mm is the radius of the sample. Here the laser is detuned by $\Delta = -6\gamma$ from the atomic transition, with $\gamma/(2\pi) = 6$ MHz being the single-atom radiative decay rate. Panel (b) shows the same data as panel (a), but on a shorter time scale and including an exponential fit of the decays. Panel (c) shows a different experiment under the same conditions, reaching longer times. In all panels, the dashed lines represent the single-atom exponential decay. Panels (a,b) reproduced from Ref. [18], panel (c) reproduced from Ref. [29].

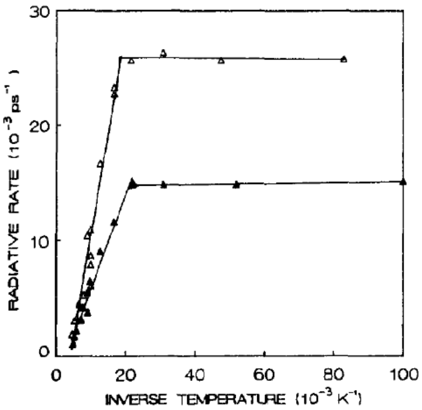

Figure 1.5: Radiative recombination rate from pseudoisocyanine (PIC) bromide molecular aggregates. The rates are obtained from the fluorescence lifetime, as a function of the inverse temperature. Open and filled symbols refer to the emission at different wavelengths, while the lines serve as a guide for the eye. The radiative rate at high temperature is equal to the monomer rate. As temperature is lowered, the rate becomes dominated by the lowest-energy eigenstate, that is superradiant. Figure reproduced from Ref. [20].

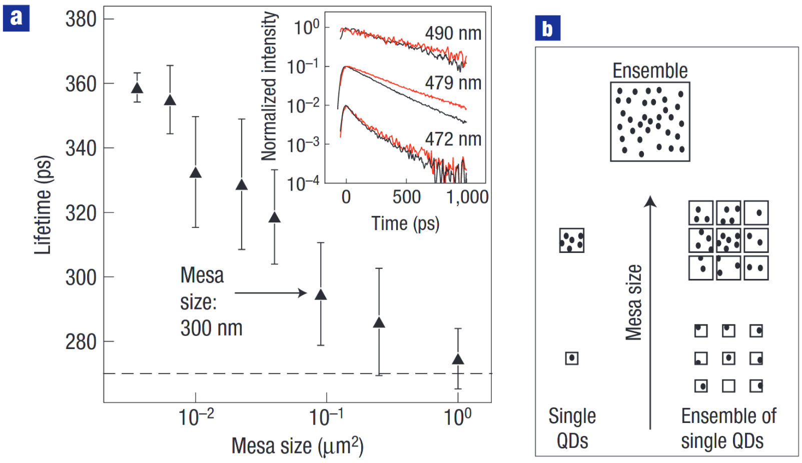

Figure 1.6: (a) Radiative lifetime of a layer of self-assembled CdSe/ZnSe quantum dots *vs.* the aggregate size ("mesa size"). The radiative lifetime is measured from an exponential fit of the photoluminescence decay (see inset). As the size of the ensemble grows, the lifetimes decreases up to the whole ensemble lifetime (dashed line), indicating cooperative enhancement of the radiative rate. In panel (b) the meaning of the mesa size is pictorially represented: the quantum dot layer is separated into independent subsystems, each of area equal to the "mesa size". Figure reproduced from Ref. [22].

gate to the light is concentrated in a collective, red-shifted state extended along the whole aggregate. At zero temperature, all the fluorescence emission comes from this extended state, while at very high temperatures, the aggregate emits in the same way as independent molecules would do. As is shown in Fig. 1.5, the radiative recombination rate obtained from fluorescence experiments in PIC aggregates increases by a large factor as the temperature is decreased towards zero, thus showing the emergence of superradiance.

Finally, superradiant emission has also been observed in quantum dot aggregates [22]. In the experiment shown in Fig. 1.6, the radiative decay time of a dense ensemble of quantum dots is measured by artificially varying the size of the aggregate ("mesa size" in Fig. 1.6). As the aggregate gets larger, the emission lifetime gets shorter, suggesting the presence of cooperative radiation from the ensemble.

1.3.2 Superradiance in the frequency domain

Single-excitation superradiance originates from the existence of extended, coherent states across an ensemble of emitters, where most of the coupling to the EMF is concentrated. The presence of these extended states can also produce observable features in the absorption and fluorescence spectra of the aggregates. In fact, such extended states manifest themselves as a very bright and sharp peak in the absorption spectrum and, for the case of the so-called J-aggregates, also in the fluorescence spectrum. This

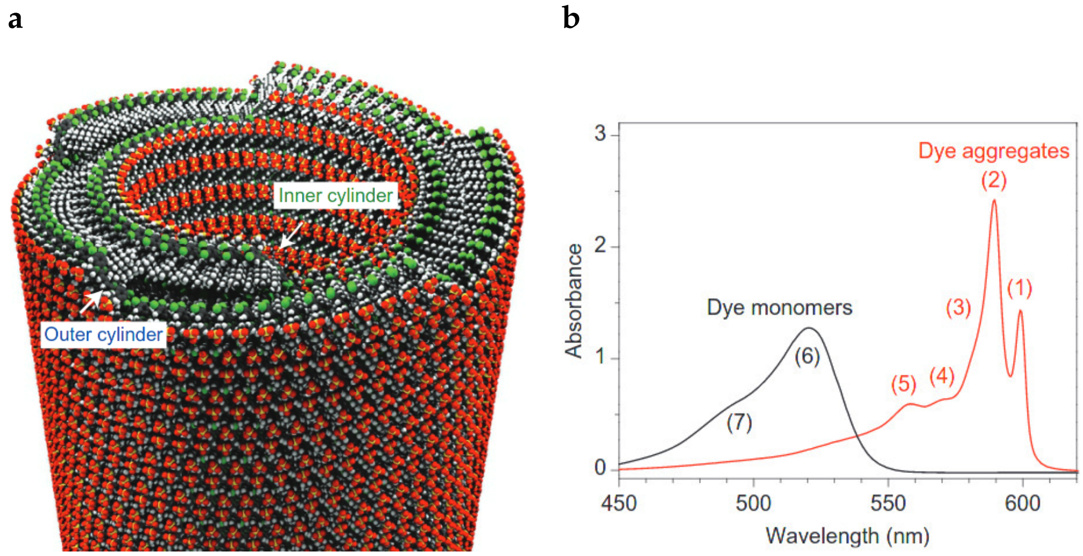

Figure 1.7: (a) Representation of a C8S3 nanotube, with a distinction between the inner wall and the outer wall of the tube. (b) Absorption spectrum of C8S3 nanotubes (red line) compared to the monomer absorption spectrum (black line). The peak (1) is associated to the inner wall, while the peak (2) to the outer wall. Figure reproduced from Ref. [30].

peak originates from the segregation of the whole oscillator strength (quantifying the coupling to the EMF) of the aggregate to one (or few) extended state(s). Since these eigenstates are extended, they are less affected by inhomogeneous broadening, due to self-averaging of the fluctuations throughout the emitters, and therefore they appear narrower than their single-emitter counterparts.

The energy of the extended superradiant states is typically shifted with respect of that of a single emitter, by an amount proportional to the coupling between the emitters. This is particularly evident in molecular aggregates, where the couplings are typically strong, as compared to $k_B T$ (with $T = 300$ K). Molecular aggregates that show a blue-shift of their main absorption peak are called *H-aggregates*, while the ones having a red-shifted peak are defined *J-aggregates*. An example of this is shown in Fig. 1.7, where the absorption spectrum of self-assembled molecular dye nanotubes is compared with the spectrum of the corresponding monomers. As one can see, the aggregate spectrum shows two distinct, bright and narrow absorption lines, that are associated to delocalized eigenstates along the inner and outer walls of the nanotube.

A redshifted peak is also observed from natural nanotubular structures. Specifically, Fig. 1.8(a,b,c) shows the fluorescence spectrum of the antenna complexes of Chlorobium tepidum, a kind of Green Sulfur Bacteria, from Ref. [31]. Such antenna complexes are formed by tubular structures of bacterio-chlorophyll molecules, forming J-aggregates that lie on the bacterial membrane. As it can be seen from Fig. 1.8(a,b,c), their emission spectrum peaks between 750 nm and 800 nm, which is significantly red-

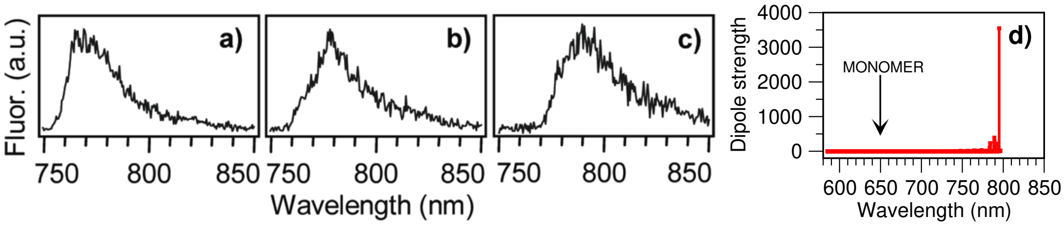

Figure 1.8: Fluorescence peak for wild type Chlorobium tepidum chlorosomes. Panels (a,b,c) are reproduced from Ref. [31], and each panel show a single-chlorosome fluorescence spectrum. Panel (d) shows the dipole strength from single-walled WT tube simulations (results presented also in Chapter 3). The monomer transition frequency at 650 nm is marked in panel (d).

shifted from the BChl fluorescence peak (650 nm). We analyze these models more in detail in Chapter 3, where we introduce a model able to reproduce the emission peak between 750 nm and 800 nm, reported also here in Fig. 1.8(d).

Finally, circular dichroism is a further specific feature of the light emitted by symmetrically arranged molecular aggregates, and it has been associated to cooperative emission [31].

1.3.3 Superradiance in the photon statistics: photon bunching

Superradiant emission can also be identified from the photon statistics of the emitted light. Specifically, the photons emitted from a superradiant medium show *bunching*, that is a correlation effect where the photons tend to be emitted in groups. Photon correlation can be measured by splitting the emitted light and introducing a delay $\Delta\tau$ between the two beams, as schematically shown in the inset of Fig. 1.9a. For example, in Ref. [32] some molecular aggregates have been switched between a J-aggregate configuration (see Fig. 1.9b) and different configurations, having mixed (J/H)-aggregate features (Fig. 1.9a) or no specific aggregation at all (Fig. 1.9c). As we mentioned in the previous section, J-aggregates are characterized by superradiant emission. As it can be seen from Fig. 1.9, the superradiant J-aggregate configuration shows photon bunching, characterized by a photon cross-correlation parameter $g^{(2)}(\Delta\tau) = \langle I(t)I(t+\Delta\tau)\rangle \;/\; \langle I(t)\rangle^2$ that is higher than unity for small $\Delta\tau$ and decreases exponentially to one for large $\Delta\tau$. Moreover, photon bunching in Fig. 1.9 is seen only for the superradiant J-aggregate configuration. This example reflects the general relationship that exists between superradiance and photon bunching.

1.4 Supertransfer of excitations

Another important cooperative effect, that is connected to single-excitation superradiance, is *supertransfer* of excitation between aggregates [7]. If two aggregates have su-

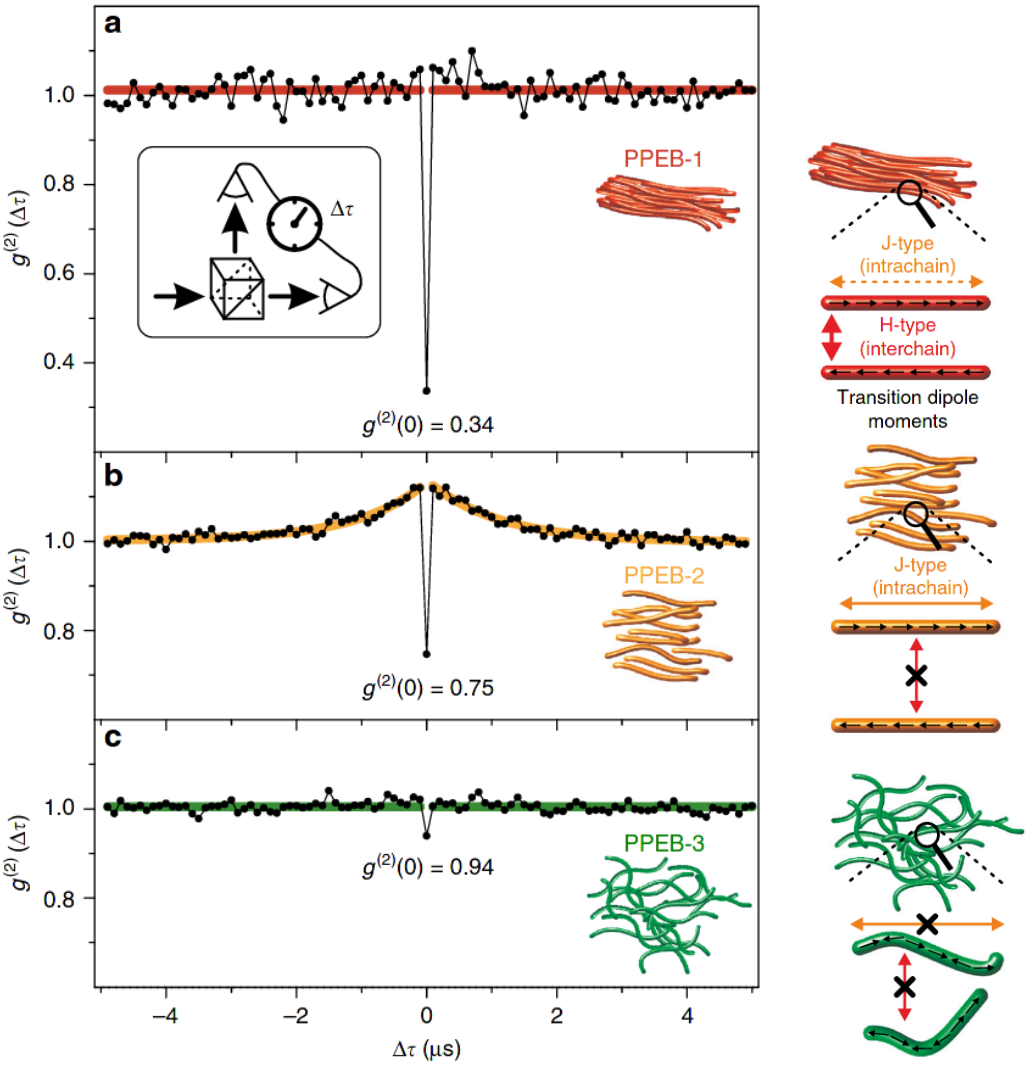

Figure 1.9: Second-order cross-correlation function $g^{(2)}(\Delta\tau) = \langle I(t)I(t+\Delta\tau)\rangle \,/\, \langle I(t)\rangle^2$ of the emitted fluorescence intensity $I(t)$ in time from PPEB aggregates. Different panels show different configurations, where PPEB-2 is a J-aggregate, PPEB-1 has mixed features of J- and H- aggregates, while PPEB-3 is neither a J- nor an H- aggregate. In panel (b), the orange exponential fit highlights photon bunching for $|\Delta\tau| > 0$. Figure reproduced from Ref. [32].

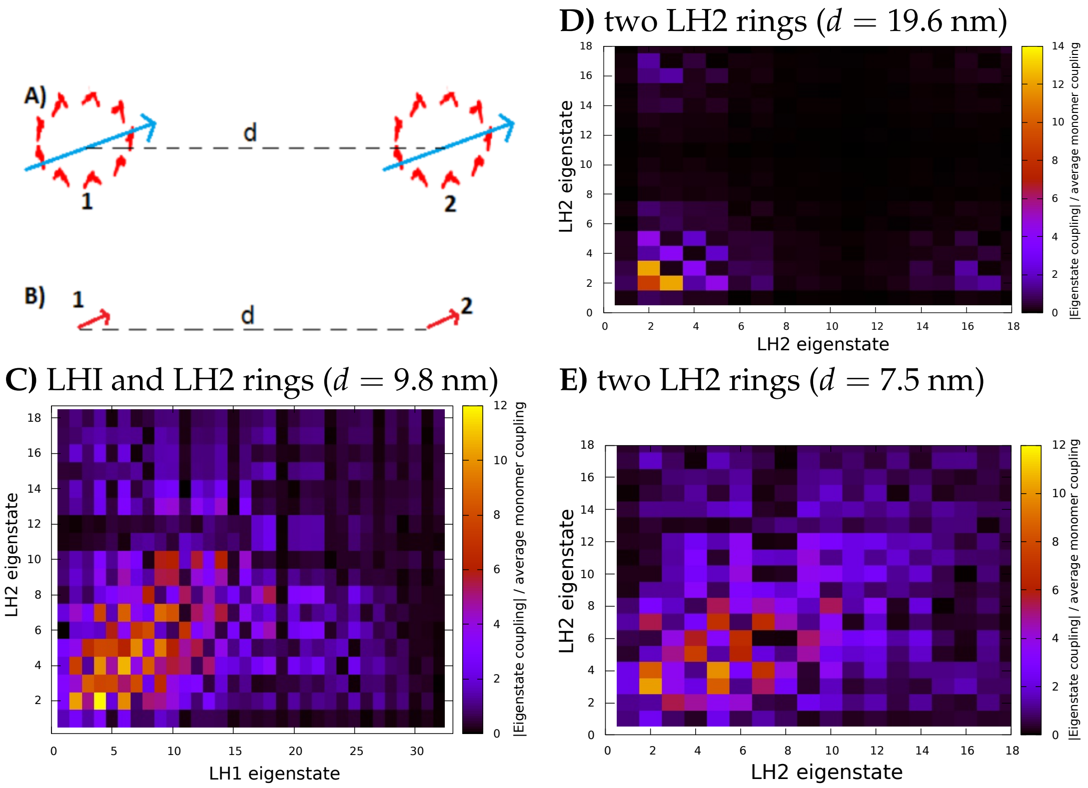

Figure 1.10: (a,b) Pictorial example of the supertransfer effect. In panel (b), two emitters at a distance d have a dipole-dipole coupling $\approx \mu^2/d^3$, where μ is the single-emitter transition dipole moment. In panel (a), two Purple Bacteria LH2 aggregates are at the same distance d. Each LH2 aggregate has a superradiant state with dipole strength $\approx \sqrt{N}\mu$, where $N = 18$ is the number of emitters in each aggregate. As a result, the coupling between the aggregates is $N\mu^2/d^3$, enhanced by a factor N. (c,d,e) Supetransfer coupling between the eigenstates of LHI and LH2 Purple Bacteria antenna complex (see Chapter 4). On the axes, the index indicate the eigenstates ordered by energy. Both LHI and LH2 have two superradiant states (states nr. 2 and 3 in the figure) and $N-1$ subradiant states. On the color bar, the absolute value of the coupling between eigenstates is shown, divided by the average coupling between molecules of the two aggregates considered in each panel. Both LHI and LH2 are rings with radii, respectively, $R_{LHI} = 4.7$ nm and $R_{LH2} = 2.6$ nm, and containing $N_{LHI} = 32$ and $N_{LH2} = 18$ molecules, respectively.

perradiant eigenstates characterized by a large transition dipole, at large distances each aggregate can be characterized by the dipole moment of its superradiant state and the transfer between aggregates can be boosted by a factor proportional to the number of emitters in the aggregates.

To better illustrate, let us consider the example shown in Fig. 1.10(a,b): we have two small, regular ring-like aggregates, at a distance d much larger than each aggregate diameter. The regular arrangement of the emitters in each aggregate results in the presence of a superradiant state, whose transition dipole moment is $\approx \sqrt{N}\mu$, much larger than the single-emitter transition dipole moment μ. Now, if the two aggregates are at a distance much larger than the aggregate size (as illustrated in Fig. 1.10a), then each aggregate is well approximated by a giant point dipole with magnitude $\approx \sqrt{N}\mu$, so that the dipole coupling between the aggregates is $\approx N\mu^2/d^3$. As a comparison, the dipole coupling between two independent emitters at the same distance (see Fig. 1.10b) is $\approx \mu^2/d^3$. The coupling is thus enhanced by a factor N, the number of emitters in each aggregate, due to cooperative effects. The coupling determines the speed at which the excitation is transferred, so an enhanced coupling implies a faster, super-transfer of excitation.

Super-transfer can also occur between aggregates at small distances d with $d \ll L$, where L is the aggregate size. For aggregates at small distances, it is the specific geometry which determines which eigenstates have an enhanced coupling with respect to the single molecules. The possible relevance of short-distance super-transfer in natural light-harvesting complexes is an important question that has been discussed in literature [3, 33–35]. An example of supertransfer taken from natural photosynthetic systems is shown in Fig. 1.10(c,d,e), where we consider the coupling between the eigenstates of LHI and LH2 aggregates of Purple Bacteria antenna complexes (see Chapter 4). Both LHI and LH2 are ring-like aggregates, and they both possess two superradiant states each, corresponding to the first and second excited states. In Fig. 1.10d the coupling between the eigenstates of two far apart LH2 rings (the center-to-center distance d is 3.7 times the ring radius) shows that the two superradiant states of each ring are strongly coupled between one another, with a coupling up to 14 times larger than the average coupling between molecules of the two aggregates. Such enhancement factor is close to $N = 18$ and denotes supertransfer. On the other hand, all the other subradiant eigenstates have nearly vanishing couplings: this effect is called *subtransfer* and it emerges between the subradiant states of aggregates very far apart. Then, in Fig. 1.10e we show the couplings between eigenstates of two LH2 rings at the nearest distance that they have in nature: here d is just 1.5 times the ring diameter. In this case, due to the short distance, there are large couplings also between subradiant eigenstates. Interestingly, because of the symmetry in the LH2 rings, supertransfer couplings are present between some pairs of eigenstates, with enhancement factors of up to 12. Similarly, supertransfer couplings are present between the LH2 and the LHI rings at their natural distance (d is comparable to the diameters), see Fig. 1.10c, with enhancement factors of up to 12. Notably, the enhanced couplings are accumulated in the lower part of the spectrum, where most of the excitation is present at thermal equilibrium. Therefore, these cooperative effects could be relevant also at finite temperature.

In conclusion, cooperativity with respect to energy transfer is determined by the coupling matrix V between the aggregates. The coupling matrix ultimately depends on the specific geometry and, for small distances, V selects different cooperative states than the ones selected by the coupling with the EMF (superradiant states). Surprisingly, in natural system, the geometry of the aggregates is such to make it possible to have both a super-absorption of light and a super-transfer between aggregates at room temperature, as discussed in Chapters 3, 4 and references therein. Nevertheless, the functional role of symmetries in natural antenna complexes is still under debate [33–35].

1.5 Coupling strength to the electromagnetic field

The aim of this thesis is to analyze the interplay of cooperative effects (with a larger focus on superradiance) with disorder and noise in aggregates of point-like emitters. The specific examples of point-like emitters under our consideration are molecular aggregates and quantum-dot super-lattices, but we also show the applicability of part of our results to generic two-level systems, such as trapped ions and Rydberg atoms. Specifically, we are interested in how such interplay affects the optical properties of the aggregate and its efficiency in transport and storage of energy.

Our analysis considers systems where the strength of the collective EMF-mediated coupling varies significantly. We propose to quantify the cooperative coupling strength by the “gap” induced in the spectrum: in the case of unit-rank imaginary coupling, the energy gap is imaginary and equal to the maximal energy width $\hbar\Gamma_{SR}$ of the superradiant state, while in the case of unit-rank real coupling, the energy gap is real and equal to the energy difference between the extended ground state and the first excited state. Here, we propose to use the imaginary gap $\hbar\Gamma_{SR}$ to quantify the strength of cooperativity in all the systems under our study that exhibit superradiance, namely Green Sulfur Bacteria nanotubes (Chapter 3), Purple Bacteria antenna complexes (Chapter 4) and quantum dot superlattices (Chapter 5). In the case of molecular chains in cavities (Chapter 7), we instead quantify the cooperative coupling by means of the real energy gap induced by the coupling to the cavity mode.

Under such definition, following a common characterization used in cavity physics [36–40], the *weak coupling* is defined as where the gap is much smaller than the mean level spacing. Then, the *strong coupling* regime is where the gap is much larger than the mean level spacing. Finally, the *ultra-strong coupling* regime is characterized by gaps even larger than the spectral width of the excitonic spectrum, that we define as the $\max\{4\Omega, W, k_B T\}$, where 4Ω roughly quantifies the spectral width in absence of disorder at $T = 0$ K, Ω is the nearest-neigbour coupling, W is the amount of static disorder (inhomogeneous broadening) and $k_B T$ is the thermal energy (homogeneous broadening). In this regime, the gapped collective states are well separated from the rest of the spectrum, they can achieve very large populations and an entirely different physics can emerge. In Fig. 1.11 we show how the realistic systems described in the following

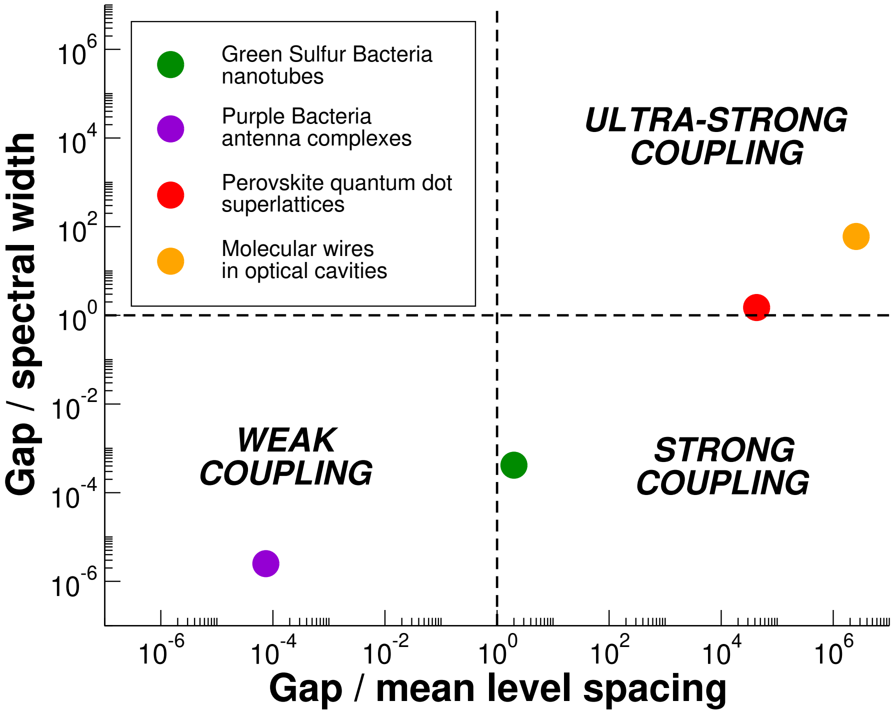

Figure 1.11: A diagram of the coupling regimes as described in the text. The realistic systems described in the thesis are placed at their corresponding parameters, see Table 1.1. The mean level spacing is computed in absence of disorder. The spectral width here is defined as $\max\{4\Omega, W, k_B T\}$, where 4Ω quantifies the spectral width in absence of disorder, Ω is the nearest-neighbour coupling, W is the static disorder and $k_B T$ is the thermal energy. Note that the spectral width cannot be smaller than the mean level spacing, so that the gap cannot at the same time be larger than the spectral width and smaller than the mean level spacing: for this reason, the upper-left part of the diagram is always empty and undefined.

System	Green Sulfur Bacteria nanotubes	Purple Bacteria antenna complexes	Perovskite quantum dot superlattices	Molecular chains in cavities
Chapter	3	4	5	7
Gap	$1.2 \cdot 10^{-4}$ eV	$7 \cdot 10^{-7}$ eV	$3 \cdot 10^{-3}$ eV	3 eV
Γ_{SR}/γ	5000	16	2000	—
MLS	$6 \cdot 10^{-5}$ eV	10^{-2} eV	$7 \cdot 10^{-8}$ eV	$4 \cdot 10^{-6}$ eV
Ω	$7 \cdot 10^{-2}$ eV	$7 \cdot 10^{-2}$ eV	$1.4 \cdot 10^{-4}$ eV	$1.2 \cdot 10^{-2}$ eV
W	$2.5 \cdot 10^{-2}$ eV	$2.5 \cdot 10^{-2}$ eV	$2 \cdot 10^{-3}$ eV	$2.5 \cdot 10^{-2}$ eV
$k_B T$	$2.5 \cdot 10^{-2}$ eV	$2.5 \cdot 10^{-2}$ eV	$5 \cdot 10^{-4}$ eV	$2.5 \cdot 10^{-2}$ eV
$\hbar\omega_0$	1.9 eV	1.6 eV	2.4 eV	2 eV

Table 1.1: Summary of the relevant parameters for the systems considered in this thesis, and reference to the corresponding chapters. Here, the gap is either the imaginary gap $\hbar\Gamma_{SR}$ (where Γ_{SR} is the most superradiant decay rate), or the polaritonic gap (only in the case of molecular chains in cavities), while Γ_{SR}/γ is the ratio of the maximal superradiant rate over the single emitter radiative rate (the quantity is undefined for molecular chains in cavities), MLS is the mean level spacing in absence of disorder, Ω is the nearest-neighbour coupling, W is the strength of static disorder, $k_B T$ is the experimental temperature at which these systems are studied, and $\hbar\omega_0$ is the single-emitter excitation energy. The parameters in this table are used to plot the points in Fig. 1.11. The parameters for Green Sulfur Bacteria are referred to the largest set of 4 concentric cylindrical structures ($N = 19680$, see Figs. 3.10, 3.21), while for Purple Bacteria are referred to a single LHI ring ($N = 32$, see section 4.6.13), for the superlattice we consider the largest simulated structure ($N = 30^3$, see Fig. 5.1a) and for the molecular chains in a cavity we refer to the longest simulated chain ($N = 10^4$, see Fig. 7.3).

chapters are located in these regimes. The corresponding values of the parameters are reported in Table 1.1.

It is important to note that our definition of the cooperative coupling strength has clear meaning for unit-rank interactions that are purely hermitian ($V = V_R$) or purely anti-hermitian ($V = iV_I$), but it has some limitations for more general long-range interactions. Finite-range interactions of the form $V_{mn} \propto |m-n|^{-\alpha}$ ($\alpha > 0$), for example, may not create a unique gap in the spectrum, but many gaps, or more in general they can affect the density of states of a certain part of the spectrum. Moreover, as we show in Chapter 3, some cooperative effects can emerge even in presence of short-range interactions, depending on the system geometric features. Therefore, focusing on the gap of a single state may not always be the best choice to quantify cooperativity. Moreover, in the case of complex interactions ($V = V_R + iV_I$), the imaginary gap would mostly account for the cooperative interaction contained in V_I, neglecting the collective effects present in V_R. Collective effects in V_R can be very important, because they can lower the density of states and make the system robust to thermal noise, as our results in

Chapter 3 show.

Therefore, our proposed quantification of cooperative coupling is a starting point that is certainly valid for purely real or purely imaginary unit-rank interactions. In the future we plan to generalize our classification of the coupling strength regimes by extending it to general non unit-rank interactions, also including both the effect of the hermitian and anti-hermitian parts, V_R and V_I, in the measure of cooperativity. Moreover, inspired by our results in Chapter 3, we should also try to quantify cooperativity that emerges from short-range interactions for reasons different from the interaction range, such as some geometric properties.

1.6 Cooperativity, long-range interactions and robustness to disorder and noise

Cooperativity, stemming from long-range interactions, can make a system robust to static disorder, dephasing and thermal noise by different mechanisms. Different effects arise depending on the rank of the long-range interaction, that is unity (for infinite-range interactions) or low-rank (for more general finite-range interactions, see discussion in section 1.2). An important role is also played by the form of the long-range interaction, V (see section 1.1), that can be hermitian (represented by a real matrix V_R), anti-hermitian (represented by a purely imaginary symmetric matrix iV_I), or generically non-hermitian (represented by a symmetric matrix of the form $V_R + iV_I$). The effect of cooperativity depends also on the strength of the coupling, whether it is weak, strong or ultra-strong (see section 1.5).

1.6.1 Unit-rank interactions: robustness to static disorder

The case of unit-rank long-range interactions is better understood. As regards static disorder, for unit-rank anti-hermitian ($V = iV_I$) long-range interactions, it is known that the robustness to such disorder [25, 41] depends on the coupling strength: (a) in the weak-coupling regime, the robustness of the system is unaffected by the long-range interaction, while (b) in the strong coupling regime the long-range interaction makes the system more robust to disorder and (c) in the ultra-strong coupling regime, the robustness to static disorder is even stronger, and it is determined by the imaginary gap induced by the long-range interaction. These conclusions are drawn in Chapter 6, and in Ref. [42].

Also in the unit-rank hermitian case, for weak coupling the robustness to disorder is unaffected by the long-range interaction, while in the ultra-strong coupling regime the emergence of a real-energy gap gives the system cooperative robustness to disorder, affecting its transport properties [42, 43] (see Chapter 7).

1.6.2 Unit-rank interactions: robustness to dephasing

Dephasing is the decay of quantum coherences in a system, and it is typically caused by random dynamical fluctuations of the site energies. In excitonic systems, the role of dephasing is often studied within the Haken-Strobl approach [26, 44, 45], that assumes uncorrelated white-noise fluctuations of the site energies within a given range $\hbar\gamma_\phi$, representing the dephasing strength.

The interplay of dephasing with unit-rank anti-hermitian long-range interactions has been studied in Refs. [26, 46], showing that: (a) the interplay of two different environments, one inducing dephasing and another inducing imaginary cooperative decay, can be described in terms of a master equation which includes dephasing and the anti-hermitian long-range term $V = iV_I$ in an additive way [46], as long as the dephasing strength is smaller than the bandwidth of the environment that induces decay; (b) the imaginary gap induces cooperative robustness to dephasing, in the sense that the dephasing strength needed to destroy cooperativiy increases proportionally to the system size N [26].

For hermitian unit-rank interactions, in the ultra-strong coupling regime, the presence of a gap is also expected to make the system robust to dephasing, similarly to what happens with static disorder.

1.6.3 Unit-rank interactions: robustness to thermal noise

Finally, as regards the interplay of unit-rank interactions with finite temperature noise, a clear picture can be drawn for hermitian long-range interactions ($V = V_R$): (a) in the weak coupling regime the spectrum is basically unaffected by the long-range term, and therefore the interplay with thermal noise is the same as the case without long-range interactions; (b) in the ultra-strong coupling regime, a gap emerges between the lowest excitonic eigenstate and the rest of the spectrum, and at thermal equilibrium the cooperative ground state will be populated with near-unity probability, as long as the thermal energy $k_B T$ is much smaller than the gap, thus allowing the cooperative properties of the ground state to emerge even at finite temperature.

On the other hand, the interplay of finite temperature noise with anti-hermitian unit-rank interactions is more complicated: (a) for weak coupling, the imaginary long-range interaction can be considered as a small perturbation to the hermitian spectrum, and one can assume thermal equilibrium on the real energies determined by the hermitian part; in this regime, cooperative effects can survive to thermal noise, as long as $k_B T$ is smaller than the spectral range (we followed this approach in Chapter 5); (b) for strong and ultra-strong coupling regimes, the interplay of different environments (inducing thermal relaxation and cooperative decay) is less trivial. To better understand what is the problem in studying the interplay of thermal relaxation and cooperativity in the strong or ultra-strong coupling regimes (with respect to the imaginary coupling V_I) one can note the following: standard master equation approaches are based on well-defined system eigenstates and energy. In the case of strong and ultra-strong coupling, the energies of the system eigenstates are not well-defined due to the coupling to another environment which induces a finite lifetime (energy width) to the states. In this case what are the energies according to which the system can thermalize is not clear, and a microscopic master equation approach should be developed to address this problem consistently. We plan to address this problem in the future.

1.6.4 Finite-range interactions: robustness to static disorder, dephasing and thermal noise

In the general case, the coupling to an external field does not induce neither a unit-rank Hermitian nor a purely anti-hermitian interaction matrix, but instead a non-hermitian matrix $V = V_R + iV_I$ characterized by long-range interactions. The rank of V can be small but different from unity. Specifically, V_R and V_I can have different ranks and different coupling strength. This is the case of the radiative hamiltonian presented in Chapter 2 and applied to Green Sulfur Bacteria nanotubes (Chapter 3), Purple Bacteria antenna complexes (Chapter 4) and perovskite quantum-dot superlattices (Chapter 5). In these general cases, the classification of the cooperativity strength presented in section 1.5, based on the presence of an energy gap (either imaginary or real), may not be the best choice to properly represent the effect of cooperativity. Indeed, different routes to robustness can arise in this case. For instance, even if the imaginary part of the interaction is in the weak coupling regime, the contribution of the real part together with the specific geometry of the system can donate robustness to the cooperative effects.

In the case of Purple Bacteria antenna complexes (Chapter 4), the ring arrangement of the molecules allows the emergence of a superradiant state close to the ground state. Indeed in this case V_I commutes the Hermitian part of the Hamiltonian due to the geometry of the system, allowing the coupling to the EMF to be concentrated in few specific states, despite the weakness of such coupling. Moreover, even if the effect of long-range interactions is very weak, the system is intrinsically robust to disorder and thermal noise, because the couplings between the molecules are very strong with respect to $k_B T$ and the system is small, producing large level spacings.

The case of Green Sulfur Bacteria (Chapter 3) is similar in the sense that the imaginary part V_I is unit-rank and almost commutes with the Hermitian part of the Hamiltonian, allowing the emergence of a superradiant state close to the ground state. Nevertheless, it is also different from the case of Purple Bacteria since in such antenna complexes a large number of molecules (10^5) is involved. This might suggest a high density of states and thus a high sensitivity of the system to noise and disorder. Nevertheless, as we show in Chapter 3, the Hermitian part of the interaction with the EMF produces a strong suppression of the density of states close to the ground state, making cooperative effects robust to thermal noise and disorder. Therefore V_R, even if it is a short-range interaction ($1/r^3$ in quasi-1D systems), produces effects on the system that are very similar to the presence of a gap, by suppressing the density of states near the ground state (the presence of a gap can be considered a special case of a suppressed density of states). This occurs due to the specific arrangement of the molecules in natural photosynthetic nanotubes. This further suggests that long-range interactions might not be required to have strong cooperativity, and specific geometric features may also induce collective behaviours.

Finally, in the case of perovskite superlattices (Chapter 5) neither V_R nor V_I is unit rank, but the role of long range interaction is important and V_I has a low rank and it lies close to the ultra-strong coupling regime in absence of disorder, as can be seen in Fig. 1.11. In this regime we observe gaps in the complex spectrum of the ordered system that are larger than the mean level spacing on the real axis (see Fig. 5.1a). The presence of such gaps effectively suppresses the density of states in the complex eigenvalue plane. The low-rank imaginary coupling V_I plays therefore a major role and the overall effect of $V_R + iV_I$ makes the system robust to static disorder, as it can be seen from Fig. 5.12. Note that, if one includes the effect of natural disorder, the imaginary gap $\hbar\Gamma_{SR}$ becomes smaller, moving the system towards the weak-coupling regime. Because of this, in Chapter 5 we were able to study the effect of thermal noise assuming a weak coupling regime, meaning that thermal equilibrium is determined just by the real parts of the complex energies, and we also discussed how to improve the robustness of the system to thermal noise.

In conclusion, long-range interactions are certainly important and they constitute a natural generalization of the common mechanism to robust cooperative effects proposed by U. Fano, as explored in this thesis in Chapter 6. Nevertheless, in realistic systems the presence of long-range interactions cannot by itself explain the robustness of cooperative effects, and the symmetries present in the system, with respect to the interaction matrix with the field, play an essential role. We plan to further investigate the different mechanisms to robust cooperative effects based on long range interactions and symmetries in the future.

1.7 Thesis outline

In the following, we give a brief outline of the thesis, pointing also to which coupling regime is considered in each chapter, following the classification proposed in section 1.5. Chapters 2-5 focus more specifically on superradiance, its interplay with disorder and noise and possible applications. Chapters 6-7 focus instead on more general long-range interactions within aggregates, their consequences on the aggregate spectra and their effect on transport.

Specifically, in Chapter 2 the interaction of an aggregate of emitters with the EMF is calculated, starting from a first-principle Hamiltonian for the whole system, including the emitters and the modes of the quantized EMF. A quantum master equation is derived, which describes the collective coupling to the EMF, it is equivalent to a non-Hermitian Hamiltonian in the single-excitation regime and it is then employed throughout the following chapters.

In Chapter 3 the interplay of collective radiation and thermal noise is studied in the case of natural molecular nanotubes present on the membranes of Green Sulfur Bacteria. These systems lie on the boundary between the weak- and strong-coupling regimes, as it can be seen in Fig. 1.11, but they fall more in the weak-coupling description. In

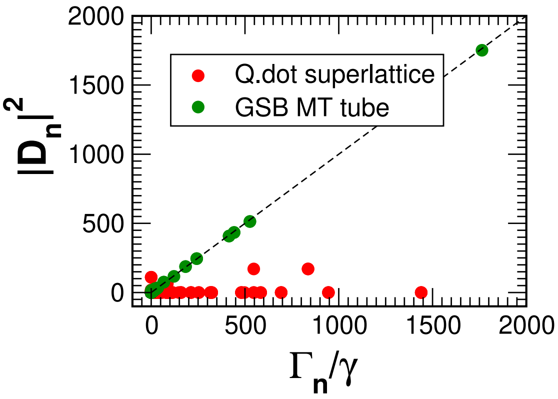

Figure 1.12: Coupling of all the eigenstates of a system to the elecromagnetic field, computed in a perturbative way (the dipole strength, $|D_n|^2$, see Chapter 3) and in a non-perturbative way (the relative radiative width Γ_n/γ, see Chapter 3). The dashed line is the identity (where $|D_n|^2 = \Gamma_n/\gamma$). "Q.dot superlattice" is a cubic $CsPbBr_3$ quantum-dot superlattice made of $N = 20^3$ quantum dots (see Chapter 5), that is in the strong-coupling regime (Gap/mean level spacing $\approx 10^4$). "GSB MT tube" refers to a single-wall Green Sulfur Bacteria nanotube mutant type made of $N = 6000$ molecules (see Chapter 3), that is in the weak-coupling regime (Gap/mean level spacing ≈ 0.1).

this regime, as it can be seen in Fig. 1.12, the correct coupling of all the eigenstates to the EMF, Γ_n/γ, is well captured by the perturbative method of the dipole strengths, $|D_n|^2$. In particular, the effect of the EMF-mediated hopping is studied, by estimating the coherence present in the nanotubes at room temperature. Our results show that the natural configuration of Green Sulfur Bacteria photosynthetic nanotubular antenna complexes ensures a high, macroscopic coherence at thermal equilibrium, as compared to alternative tubular configurations, thanks to the effect of EMF-mediated long-range hopping of excitation.

In Chapter 4 the well-known efficiency of photosynthetic Purple Bacteria in absorbing sunlight and storing the excitation thanks of cooperative effects is used as a basis for proposed applications. Purple Bacteria lie clearly in the weak-coupling regime, as it is seen from Fig. 1.11. Specifically, the excitation funneling mechanism is proposed to overcome the known limitations of sunlight-pumped lasers, stemming from the extremely dilute nature of sunlight.

In Chapter 5 a theory of collective radiation is presented for a novel material: superlattices made of $CsPbBr_3$ quantum dots. These systems lie between the strong and the ultra-strong coupling regimes because of the large static disorder (see Fig. 1.11 and Table 1.1), and in this regime the perturbative dipole strength approach fails to correctly reproduce the correct coupling to the EMF (see Fig. 1.12). Recent experiments on such systems [47] have shown the hallmarks of superradiance, at the cryogenic temperature $T = 6$ K. We provide a theory that explains the experiments, specifically we show that the surprisingly low degree of collective emission observed in this material is a result of the interplay of long-range radiative interactions, thermal noise and static disorder. Moreover, our proposed theory is used to make quantitative predictions, indicating the way to obtain superradiance at higher temperatures in such system.

Inspired by the many interesting properties of superradiance, and motivated by the similarity between different collective phenomena introduced here in Section 1.1, in Chapter 6 we analyze the more general problem of the effect of long-range interactions between levels with a constant density of states. A comparison is made between the purely imaginary long-range coupling associated to superradiant emission, and the real long-range coupling, typical of single-excitation superconductivity. While the real long-range coupling ultimately reproduces the well-known superconducting gap, a novel parallel is drawn between such real gap and the purely imaginary gap arising in the superradiant case. Both gaps, although different in the physical meaning, are shown to provide robustness to static disorder.

In Chapter 7 we study how energy transport is affected by the interplay of long-range interactions and disorder. Studying a paradigmatic model, that is shown to be realized by placing a nano-chain inside a resonant cavity, we find that such interplay produces quite nontrivial disorder-enhanced and disorder-independent transport regimes. The molecular chains analyzed here lie in the ultra-strong coupling regime, as is shown in Fig. 1.11.

Finally, in Chapter 8 we summarize the main conclusions from the previous chapters and we indicate some perspectives.

Chapter 2

Cooperative effects in light-matter interaction

In this chapter the problem of an ensemble of emitters coupled to the models of the electromagnetic field is considered. The field is considered as coming from a black body at a finite temperature, which is a rough model for sunlight. A master equation is derived that is valid both for aggregates smaller than the transition wavelength and larger than that, reproducing previous results [27, 48]. When the black-body temperature is vanishing, the master equation models cooperative radiative decay. A simple case of two coupled emitters is shown to exhibit superradiance, and the master equation is compared to the well-known non-Hermitian Hamiltonian approach.

2.1 Hamiltonian and Master Equation for the whole system

Let us consider an aggregate of N two-level systems all having the same excitation energy ω_0. Below we refer to the two-level systems as "sites". In these calculations we use natural units so that $\hbar = 1$. The aggregate is assumed to interact with the radiation emitted by a black body at temperature T_S. The full Hamiltonian is written as

$$\hat{H} = \hat{H}_S + \hat{H}_B + \hat{H}_I \,. \tag{2.1}$$

Here the site Hamiltonian is

$$\hat{H}_S = \frac{\omega_0}{2} \sum_{j=1}^{N} \hat{\sigma}_j^z \tag{2.2}$$

with $\hat{\sigma}_j^z$ being the z Pauli matrix for the j-th site. The black body Hamiltonian is

$$\hat{H}_B = \sum_{\vec{k},\lambda} \omega_k \hat{b}^\dagger_{\vec{k},\lambda} \hat{b}_{\vec{k},\lambda} \tag{2.3}$$

where the summation runs over the modes $\vec{k}$ and the polarizations $\lambda = 1, 2$ of the field, the dispersion relation is $\omega_k = ck$ and the creation/annihilations operators follow the commutation rules $[\hat{b}_{\vec{k},\lambda},\hat{b}^{\dagger}_{\vec{k}',\lambda'}]=\delta_{\vec{k},\vec{k}'}\delta_{\lambda,\lambda'}$. Finally, the interaction Hamiltonian is

$$\hat{H}_I=-\sum_{j=1}^{N}\hat{\vec{D}}_j\cdot\hat{\vec{E}}(\vec{r}_j) \tag{2.4}$$

where

$$\hat{\vec{D}}_j=\vec{d}_j(\hat{\sigma}_j^{+}+\hat{\sigma}_j^{-}) \tag{2.5}$$

is the dipole operator on the j-th site, $\vec{d}_j$ is the transition dipole moment of the same site, $\hat{\sigma}_j^{\pm}=(\hat{\sigma}_j^{x}\pm i\hat{\sigma}_j^{y})/2$ and

$$\hat{\vec{E}}(\vec{r}_j)=i\sum_{\vec{k},\lambda}\sqrt{\frac{2\pi\omega_k}{V}}\vec{e}_{\vec{k},\lambda}\left[e^{i\vec{k}\cdot\vec{r}_j}\hat{b}_{\vec{k},\lambda}-e^{-i\vec{k}\cdot\vec{r}_j}\hat{b}^{\dagger}_{\vec{k},\lambda}\right] \tag{2.6}$$

is the electric field in the position $\vec{r}_j$, with $\vec{e}_{\vec{k},\lambda}$ being a unit vector which specifies the polarization.

The dynamics of the full system is described by the Liouville master equation which, in the interaction picture, reads [49]

$$\frac{d\hat{\rho}(t)}{dt}=-i\left[\hat{H}_I(t),\hat{\rho}(t)\right] \tag{2.7}$$

where $\hat{\rho}(t)$ is the density matrix in the interaction picture and it is related to the density matrix in the Schrödinger picture $\hat{\rho}$ by

$$\hat{\rho}(t)=e^{i(\hat{H}_S+\hat{H}_B)t}\,\hat{\rho}\,e^{-i(\hat{H}_S+\hat{H}_B)t}\,. \tag{2.8}$$

Note that also the density matrix $\hat{\rho}$ in the Schrödinger picture is time-dependent. Here we choose to write explcitly the dependence on time just for the operators representend in the interaction picture, to distinguish them to their respective Schrödinger representation.

The interaction Hamiltonian in the interaction picture can be factorized as

$$\hat{H}_I(t)=\sum_{\omega=\pm\omega_0}\sum_{j=1}^{N}e^{-i\omega t}\hat{A}_j(\omega)\otimes\hat{B}_j(t)=\sum_{\omega=\pm\omega_0}\sum_{j=1}^{N}e^{+i\omega t}\hat{A}_j^{\dagger}(\omega)\otimes\hat{B}_j(t) \tag{2.9a}$$

where $\hat{A}_j(\omega)$ are operators acting on the system,

$$\hat{A}_j(\omega_0)=\hat{\sigma}_j^{-}\,,\qquad \hat{A}_j(-\omega_0)=\hat{A}_j^{\dagger}(\omega_0)=\hat{\sigma}_j^{+} \tag{2.10}$$

and $\hat{B}_j(t)$ are hermitian operators acting only on the black body, given by

$$\hat{B}_j(t)=i\sum_{\vec{k},\lambda}\sqrt{\frac{2\pi\omega_k}{V}}\left(\vec{d}_j\cdot\vec{e}_{\vec{k},\lambda}\right)\left[e^{i(\vec{k}\cdot\vec{r}_j-\omega_k t)}\hat{b}_{\vec{k},\lambda}-e^{-i(\vec{k}\cdot\vec{r}_j-\omega_k t)}\hat{b}^{\dagger}_{\vec{k},\lambda}\right]\,. \tag{2.11}$$

2.2 Born and Markov approximations

Eq. (2.7) can be integrated from 0 to t to obtain

$$\hat{\rho}(t) = \hat{\rho}(0) - i \int_0^t dt' \left[\hat{H}_I(t'), \hat{\rho}(t')\right] \tag{2.12}$$

which, substituted back into (2.7), gives the integro-differential equation

$$\frac{d\hat{\rho}(t)}{dt} = -i \left[\hat{H}_I(t), \hat{\rho}(0)\right] - \int_0^t dt' \left[\hat{H}_I(t), \left[\hat{H}_I(t'), \hat{\rho}(t')\right]\right] . \tag{2.13}$$

Here, we perform the *Born approximation*: the interaction between the system and the black body is assumed to be weak, so that it does not affect the black body, not even generating correlations between the system and the black body. Formally, the Born approximation translates in approximating the density matrix of the full system as [49]

$$\hat{\rho}(t) \approx \hat{\rho}_S(t) \otimes \hat{\rho}_B, \tag{2.14}$$

where the black-body part $\hat{\rho}_B$ is also assumed independent of time, so that $[\hat{H}_B, \hat{\rho}_B] = 0$. Making the change of variable $\tau = t - t'$ into the integral, taking the trace $\mathrm{tr}_B\{\dots\}$ over the degrees of freedom of the black body and assuming that the average value of the electric field vanishes, *i.e.*

$$\mathrm{tr}_B \left\{ \left[\hat{H}_I(t), \hat{\rho}(0)\right] \right\} = 0 \,, \tag{2.15}$$

we have

$$\frac{d\hat{\rho}_S(t)}{dt} = - \int_0^t d\tau \, \mathrm{tr}_B \left\{ \left[\hat{H}_I(t), \left[\hat{H}_I(t-\tau), \hat{\rho}_S(t-\tau) \otimes \hat{\rho}_B\right]\right] \right\} . \tag{2.16}$$

Now we perform the *Markov approximation* [49]: the memory effects between the system and the black body are neglected, i.e., formally we approximate the density matrix as

$$\hat{\rho}_S(t-\tau) \approx \hat{\rho}_S(t) \tag{2.17}$$

(first Markov approximation) and we extend the integration to ∞ (second Markov approximation). This gives the Redfield Equation

$$\frac{d\hat{\rho}_S(t)}{dt} = - \int_0^\infty d\tau \, \mathrm{tr}_B \left\{ \left[\hat{H}_I(t), \left[\hat{H}_I(t-\tau), \hat{\rho}_S(t) \otimes \hat{\rho}_B\right]\right] \right\} . \tag{2.18}$$

2.3 Secular approximation

Let us now rewrite Eq. (2.18) more explicitly. We use the notation

$$\left\langle \hat{C} \right\rangle_B = \mathrm{tr}_B \left\{ \hat{C} \hat{\rho}_B \right\} \tag{2.19}$$

to indicate the average value of some operator $\hat{C}$ on the black body and "h.c." for the Hermitian conjugate. Thus, Eq. (2.18) becomes

$$\frac{d\hat{\rho}_S(t)}{dt} = \int_0^\infty d\tau \, \left[\left\langle \hat{H}_I(t-\tau) \hat{\rho}_S(t) \hat{H}_I(t) \right\rangle_B - \left\langle \hat{H}_I(t) \hat{H}_I(t-\tau) \hat{\rho}_S(t) \right\rangle_B \right] + \text{h.c.} \tag{2.20}$$

Now we use Eq. (2.9) to write the interaction Hamiltonian explicitly as

$$\hat{H}_I(t) = \sum_{\omega'=\pm\omega_0} \sum_{i=1}^{N} e^{i\omega' t} \hat{A}_i^\dagger(\omega') \otimes \hat{B}_i(t) \tag{2.21}$$

$$\hat{H}_I(t-\tau) = \sum_{\omega=\pm\omega_0} \sum_{j=1}^{N} e^{-i\omega(t-\tau)} \hat{A}_j(\omega) \otimes \hat{B}_j(t-\tau) \tag{2.22}$$

and, substituting into (2.20), we have

$$\frac{d\hat{\rho}_S(t)}{dt} = \sum_{\omega,\omega'} e^{i(\omega'-\omega)t} \sum_{i,j} \Gamma_{ij}(\omega,t) \left[\hat{A}_j(\omega)\hat{\rho}_S(t)\hat{A}_i^\dagger(\omega') - \hat{A}_i^\dagger(\omega')\hat{A}_j(\omega)\hat{\rho}_S(t)\right] + \text{h.c.} \tag{2.23}$$

where we have defined the rates $\Gamma_{ij}(\omega,t)$ as the half-sided Fourier transformed correlators of the black body

$$\Gamma_{ij}(\omega,t) = \int_0^\infty d\tau\, e^{i\omega\tau} \left\langle \hat{B}_i(t)\hat{B}_j(t-\tau)\right\rangle_B . \tag{2.24}$$

Since we assumed $\hat{\rho}_B$ stationary, the rates $\Gamma_{ij}(\omega)$ are independent of time, namely

$$\Gamma_{ij}(\omega) = \int_0^\infty d\tau\, e^{i\omega\tau} \left\langle \hat{B}_i(\tau)\hat{B}_j(0)\right\rangle_B . \tag{2.25}$$

At this point we perform the *secular approximation*: we neglect the terms proportional to $e^{\pm 2i\omega_0 t}$, which oscillate faster than the relaxation time and, in a coarse-grained time scale, they average to 0 [49]. So, keeping just the terms with $\omega = \omega'$, we get a master equation in the Lindblad form [49]:

$$\frac{d\hat{\rho}_S(t)}{dt} = \sum_{\omega=\pm\omega_0} \sum_{i,j} \Gamma_{ij}(\omega) \left[\hat{A}_j(\omega)\hat{\rho}_S(t)\hat{A}_i^\dagger(\omega) - \hat{A}_i^\dagger(\omega)\hat{A}_j(\omega)\hat{\rho}_S(t)\right] + \text{h.c.} \tag{2.26}$$

It is important to stress that the positivity of populations is guaranteed only by the secular approximation. The Redfield Eq. (2.18) can have unphysical solutions with negative populations.

2.4 Explicit calculation of the rates

Now we proceed to write explicitly the rates $\Gamma_{ij}(\omega)$. By substituting the expressions (2.11) into (2.25) we have

$$\begin{aligned}\Gamma_{ij}(\omega) = \int_0^\infty d\tau\, e^{i\omega\tau} \sum_{\vec{k},\lambda,\vec{k}',\lambda'} \frac{2\pi\sqrt{\omega_k\omega_{k'}}}{V} \left(\vec{d}_i \cdot \vec{e}_{\vec{k},\lambda}\right)\left(\vec{d}_j \cdot \vec{e}_{\vec{k}',\lambda'}\right) \Big[& e^{i(\vec{k}\cdot\vec{r}_i - \vec{k}'\cdot\vec{r}_j - \omega_k\tau)} \left\langle \hat{b}_{\vec{k},\lambda}\hat{b}^\dagger_{\vec{k}',\lambda'}\right\rangle_B \\ & - e^{i(\vec{k}\cdot\vec{r}_i + \vec{k}'\cdot\vec{r}_j - \omega_k\tau)} \left\langle \hat{b}_{\vec{k},\lambda}\hat{b}_{\vec{k}',\lambda'}\right\rangle_B + e^{-i(\vec{k}\cdot\vec{r}_i - \vec{k}'\cdot\vec{r}_j - \omega_k\tau)} \left\langle \hat{b}^\dagger_{\vec{k},\lambda}\hat{b}_{\vec{k}',\lambda'}\right\rangle_B \\ & - e^{-i(\vec{k}\cdot\vec{r}_i + \vec{k}'\cdot\vec{r}_j - \omega_k\tau)} \left\langle \hat{b}^\dagger_{\vec{k},\lambda}\hat{b}^\dagger_{\vec{k}',\lambda'}\right\rangle_B \Big] .\end{aligned} \tag{2.27}$$

Now we assume that the black body is at thermal equilibrium, i.e.

$$\hat{\rho}_B = \frac{e^{-\beta \hat{H}_B}}{\mathrm{tr}_B \left\{ e^{-\beta \hat{H}_B} \right\}} \tag{2.28}$$

where $\beta = 1/(k_B T)$ is the inverse temperature. In this case one can show that the correlators in (2.27) are

$$\left\langle \hat{b}_{\vec{k},\lambda} \hat{b}_{\vec{k}',\lambda'} \right\rangle_B = 0 \tag{2.29a}$$

$$\left\langle \hat{b}^\dagger_{\vec{k},\lambda} \hat{b}^\dagger_{\vec{k}',\lambda'} \right\rangle_B = 0 \tag{2.29b}$$

$$\left\langle \hat{b}_{\vec{k},\lambda} \hat{b}^\dagger_{\vec{k}',\lambda'} \right\rangle_B = \delta_{\vec{k},\vec{k}'} \delta_{\lambda,\lambda'} \left(1 + N(\omega_k)\right) \tag{2.29c}$$

$$\left\langle \hat{b}^\dagger_{\vec{k},\lambda} \hat{b}_{\vec{k}',\lambda'} \right\rangle_B = \delta_{\vec{k},\vec{k}'} \delta_{\lambda,\lambda'} N(\omega_k) \tag{2.29d}$$

where we have defined the Bose-Einstein function

$$N(\omega_k) = \frac{1}{e^{\beta \omega_k} - 1} \, . \tag{2.30}$$

Thus, defining $\vec{r}_{ij} = \vec{r}_i - \vec{r}_j$, Eq. (2.27) can be written as

$$\begin{aligned} \Gamma_{ij}(\omega) = \int_0^\infty d\tau \, e^{i\omega\tau} \sum_{\vec{k},\lambda} \frac{2\pi\omega_k}{V} \left(\vec{d}_i \cdot \vec{e}_{\vec{k},\lambda}\right) \left(\vec{d}_j \cdot \vec{e}_{\vec{k},\lambda}\right) \\ \left[e^{i(\vec{k}\cdot\vec{r}_{ij} - \omega_k \tau)} \left(1 + N(\omega_k)\right) + e^{-i(\vec{k}\cdot\vec{r}_{ij} - \omega_k \tau)} N(\omega_k) \right] . \end{aligned} \tag{2.31}$$

As regards the sum over $\vec{k}$, we take the continuum limit

$$\frac{1}{V} \sum_{\vec{k}} \rightarrow \frac{1}{(2\pi)^3} \int d\vec{k} = \frac{1}{(2\pi c)^3} \int d\Omega \int_0^\infty d\omega_k \, \omega_k^2 \, . \tag{2.32}$$

Now, if we assume that the dipoles have all the same magnitude μ but different orientation, namely $\vec{d}_j = \mu \, \hat{p}_j$, and defining the function

$$F_{ij}(x) = \frac{1}{4\pi} \sum_\lambda \int_0^{2\pi} d\phi \int_{-1}^{1} d(\cos\theta) \left(\hat{p}_i \cdot \vec{e}_{\vec{k},\lambda}\right) \left(\hat{p}_j \cdot \vec{e}_{\vec{k},\lambda}\right) e^{ix\cos\theta} \tag{2.33}$$

choosing a frame where the z axis has the same direction as $\vec{r}_{ij}$, we have

$$\Gamma_{ij}(\omega) = \int_0^\infty d\tau \, e^{i\omega\tau} \int_0^\infty d\omega_k \frac{\mu^2 \omega_k^3}{\pi c^3} \left[e^{-i\omega_k \tau} F_{ij}(kr_{ij}) \left(1 + N(\omega_k)\right) + e^{i\omega_k \tau} F_{ij}(-kr_{ij}) N(\omega_k) \right] . \tag{2.34}$$

Now we perform the integral over τ using the relation

$$\int_0^\infty d\tau\, e^{i\omega\tau} = \pi\delta(\omega) + i\mathrm{P}\frac{1}{\omega} \tag{2.35}$$

where $\delta(x)$ is the Dirac delta and P is the Cauchy principal value. So, we can split the rates into their real and an imaginary parts,

$$\Gamma_{ij}(\omega) = \frac{1}{2}\gamma_{ij}(\omega) + iS_{ij}(\omega) \tag{2.36}$$

which are, respectively,

$$\gamma_{ij}(\omega) = \int_0^\infty d\omega_k \frac{2\mu^2\omega_k^3}{c^3}\left[\delta(\omega-\omega_k)F_{ij}(kr_{ij})\left(1+N(\omega_k)\right) + \delta(\omega+\omega_k)F_{ij}(-kr_{ij})N(\omega_k)\right] \tag{2.37}$$

$$S_{ij}(\omega) = \mathrm{P}\int_0^\infty d\omega_k \frac{\mu^2\omega_k^3}{\pi c^3}\left[\frac{F_{ij}(kr_{ij})\left(1+N(\omega_k)\right)}{\omega-\omega_k} + \frac{F_{ij}(-kr_{ij})N(\omega_k)}{\omega+\omega_k}\right] \tag{2.38}$$

2.4.1 Real Part

Let us start from the real part (2.37). The two integrals are easily performed, taking into account that the only possible values of ω are $\pm\omega_0$. By defining $k_0 = \omega_0/c$ we get

$$\gamma_{ij}(\omega) = \frac{2\mu^2\omega_0^3}{c^3}\left[\delta_{\omega,\omega_0}F_{ij}(k_0r_{ij})\left(1+N(\omega_0)\right) + \delta_{\omega,-\omega_0}F_{ij}(-k_0r_{ij})N(\omega_0)\right]. \tag{2.39}$$

To have the explicit dependence of $\gamma_{ij}(\omega)$ on the parameters, let us evaluate $F_{ij}(x)$. First of all, let us compute the sum over λ in (2.33), writing the three cartesian component of each vector $\alpha, \beta = 1, 2, 3$:

$$\sum_\lambda \left(\hat{p}_i \cdot \vec{e}_{\vec{k},\lambda}\right)\left(\hat{p}_j \cdot \vec{e}_{\vec{k},\lambda}\right) = \sum_\lambda \sum_{\alpha,\beta=1}^{3} p_i^\alpha p_j^\beta e_\lambda^\alpha e_\lambda^\beta . \tag{2.40}$$

Here, since the two polarizations $\lambda = 1, 2$ and the propagation unit vector $\hat{k}$ form an orthonormal basis, $\left\{\vec{e}_1, \vec{e}_2, \hat{k}\right\}$, we have

$$\sum_{\lambda=1,2} e_\lambda^\alpha e_\lambda^\beta = \delta^{\alpha\beta} - \frac{k^\alpha k^\beta}{k^2} \tag{2.41}$$

so that we obtain

$$\sum_\lambda \left(\hat{p}_i \cdot \vec{e}_{\vec{k},\lambda}\right)\left(\hat{p}_j \cdot \vec{e}_{\vec{k},\lambda}\right) = \hat{p}_i \cdot \hat{p}_j - \left(\hat{p}_i \cdot \hat{k}\right)\left(\hat{p}_j \cdot \hat{k}\right). \tag{2.42}$$

Then, we split $F_{ij}(x)$ into two integrals:

$$\begin{aligned}F_{ij}(x) =& \frac{1}{4\pi}\left(\hat{p}_i \cdot \hat{p}_i\right)\int_0^{2\pi} d\phi \int_{-1}^{1} d(\cos\theta) e^{ix\cos\theta} \\ &- \frac{1}{4\pi}\int_0^{2\pi} d\phi \int_{-1}^{1} d(\cos\theta)\left(\hat{p}_i \cdot \hat{k}\right)\left(\hat{p}_j \cdot \hat{k}\right) e^{ix\cos\theta} .\end{aligned} \tag{2.43}$$

The first integral can be easily performed and it has the value

$$\int_0^{2\pi} d\phi \int_{-1}^{1} d(\cos\theta) e^{ix\cos\theta} = 4\pi\frac{\sin x}{x} . \tag{2.44}$$

As regards the second integral, we have to expand the scalar products. Since we are working in spherical coordinates, we can expand the unit vector $\hat{k}$ over the cartesian components $\hat{k} = \cos\phi\sin\theta\,\hat{x} + \sin\phi\sin\theta\,\hat{y} + \cos\theta\,\hat{z}$, and this helps us write the scalar products

$$\begin{aligned}&\left(\hat{p}_i \cdot \hat{k}\right)\left(\hat{p}_j \cdot \hat{k}\right) = p_i^x p_j^x \cos^2\phi \sin^2\theta + p_i^y p_j^y \sin^2\phi\sin^2\theta + p_i^z p_j^z \cos^2\theta \\ &+ \left(p_i^x p_j^y + p_i^y p_j^x\right)\cos\phi\sin\phi\sin^2\theta + \left(p_i^x p_j^z + p_i^z p_j^x\right)\cos\phi\sin\theta\cos\theta \\ &+ \left(p_i^y p_j^z + p_i^z p_j^y\right)\sin\phi\sin\theta\cos\theta\end{aligned} \tag{2.45}$$

so that, if we can compute the integral over ϕ, we have only 2 nonvanishing terms,

$$\begin{aligned}\int_0^{2\pi} d\phi \left(\hat{p}_i \cdot \hat{k}\right)\left(\hat{p}_j \cdot \hat{k}\right) =& \pi\left(p_i^x p_j^x + p_i^y p_j^y\right)\sin^2\theta + 2\pi p_i^z p_j^z \cos^2\theta \\ =& \pi\left(\hat{p}_i \cdot \hat{p}_j\right)\left(1-\cos^2\theta\right) + \pi\left(\hat{p}_i \cdot \hat{r}_{ij}\right)\left(\hat{p}_j \cdot \hat{r}_{ij}\right)\left(3\cos^2\theta - 1\right)\end{aligned} \tag{2.46}$$

where we used the fact that the unit vector $\hat{r}_{ij}$ is along the z axis. So, we have only 2 integrals over θ to perform:

$$\int_{-1}^{1} d\left(\cos\theta\right) e^{ix\cos\theta} = 2\frac{\sin x}{x} \tag{2.47a}$$

$$\begin{aligned}\int_{-1}^{1} d(\cos\theta)\cos^2\theta\, e^{ix\cos\theta} &= -\frac{\partial^2}{\partial x^2}\int_{-1}^{1} d\left(\cos\theta\right) e^{ix\cos\theta} = -2\frac{\partial^2}{\partial x^2}\left(\frac{\sin x}{x}\right) \\ &= 2\frac{\sin x}{x} + 4\frac{\cos x}{x^2} - 4\frac{\sin x}{x^3}\end{aligned} \tag{2.47b}$$

from which

$$\pi\int_{-1}^{1} d(\cos\theta)\,\left(1-\cos^2\theta\right) e^{ix\cos\theta} = 4\pi\left(-\frac{\cos x}{x^2} + \frac{\sin x}{x^3}\right) \tag{2.48}$$

$$\pi\int_{-1}^{1} d(\cos\theta)\,\left(3\cos^2\theta - 1\right) e^{ix\cos\theta} = 4\pi\left(\frac{\sin x}{x} + 3\frac{\cos x}{x^2} - 3\frac{\sin x}{x^3}\right) . \tag{2.49}$$

Summing up all the similar terms, we finally have

$$\begin{aligned} F_{ij}(x) = & \left[\frac{\sin x}{x} + \frac{\cos x}{x^2} - \frac{\sin x}{x^3}\right] (\hat{p}_i \cdot \hat{p}_j) \\ & + \left[-\frac{\sin x}{x} - 3\frac{\cos x}{x^2} + 3\frac{\sin x}{x^3}\right] (\hat{p}_i \cdot \hat{r}_{ij}) (\hat{p}_j \cdot \hat{r}_{ij}) \, . \end{aligned} \tag{2.50}$$

Note that $F_{ij}(x)$ is an even function of x which, in our case, gives the useful equality $F_{ij}(-k_0 r_{ij}) = F_{ij}(k_0 r_{ij})$. Moreover, one can see that $F_{ji}(x) = F_{ij}(x)$, which implies that both the matrices $\gamma_{ij}(\omega)$ and $S_{ij}(\omega)$ are symmetric. As regards the diagonal terms ($i = j$) we can analytically extend the function to $x = 0$ thanks to the limit

$$\lim_{x \to 0} F_{ii}(x) = \frac{2}{3} \, . \tag{2.51}$$

Let us write the real parts of the rates as

$$\gamma_{ij}(\omega) = \frac{3\gamma}{2} F_{ij}(k_0 r_{ij}) \left[\delta_{\omega,\omega_0} \left(1 + N(\omega_0)\right) + \delta_{\omega,-\omega_0} N(\omega_0)\right]$$

where we have defined the diagonal decay rates

$$\gamma = \frac{4}{3} \mu^2 \frac{\omega_0^3}{c^3} \, . \tag{2.52}$$

Now let us compute the contribution of the real parts computed above to the master equation. Since $\gamma_{ji}(\omega) = \gamma_{ij}(\omega)$ we have

$$\begin{aligned} \left[\frac{d\hat{\rho}_S(t)}{dt}\right]_{real} &= \sum_{\omega=\pm\omega_0} \sum_{i,j} \frac{1}{2} \gamma_{ij}(\omega) \left[\hat{A}_j(\omega) \hat{\rho}_S(t) \hat{A}_i^\dagger(\omega) - \hat{A}_i^\dagger(\omega) \hat{A}_j(\omega) \hat{\rho}_S(t)\right] + \text{h.c.} \\ &= \sum_{\omega=\pm\omega_0} \sum_{i,j} \gamma_{ij}(\omega) \left[\hat{A}_j(\omega) \hat{\rho}_S(t) \hat{A}_i^\dagger(\omega) - \frac{1}{2} \left\{\hat{A}_i^\dagger(\omega) \hat{A}_j(\omega), \hat{\rho}_S(t)\right\}\right] \end{aligned} \tag{2.53}$$

where $\{\cdot,\cdot\}$ denotes the anti-commutator and, taking $A_j(\omega)$ from (2.10), we have

$$\begin{aligned} \left[\frac{d\hat{\rho}_S(t)}{dt}\right]_{real} = & \sum_{i,j} \gamma_{ij} \left(1 + N(\omega_0)\right) \left[\hat{\sigma}_j^- \hat{\rho}_S(t) \hat{\sigma}_i^+ - \frac{1}{2} \left\{\hat{\sigma}_i^+ \hat{\sigma}_j^-, \hat{\rho}_S(t)\right\}\right] \\ & + \sum_{i,j} \gamma_{ij} N(\omega_0) \left[\hat{\sigma}_j^+ \hat{\rho}_S(t) \hat{\sigma}_i^- - \frac{1}{2} \left\{\hat{\sigma}_i^- \hat{\sigma}_j^+, \hat{\rho}_S(t)\right\}\right] \end{aligned} \tag{2.54}$$

which is clearly written in the Lindblad form [49] and where we have defined the coefficients

$$\gamma_{ij} = \frac{\gamma_{ij}(\omega_0)}{1 + N(\omega_0)} = \frac{\gamma_{ij}(-\omega_0)}{N(\omega_0)} = \frac{3}{2} \gamma F_{ij}(k_0 r_{ij}) \, . \tag{2.55}$$

2.4.2 Imaginary Part (Lamb Shift)

Let us now focus on the imaginary part contribution to the master equation. Thanks to the symmetry $S_{ji}(\omega) = S_{ij}(\omega)$ we have

$$\begin{aligned}\left[\frac{d\hat{\rho}_S(t)}{dt}\right]_{imag} =& i \sum_{\omega=\pm\omega_0} \sum_{i,j} S_{ij}(\omega) \left[\hat{A}_j(\omega)\hat{\rho}_S(t)\hat{A}_i^\dagger(\omega) - \hat{A}_i^\dagger(\omega)\hat{A}_j(\omega)\hat{\rho}_S(t)\right] + \text{h.c.} \\ =& -i \sum_{\omega=\pm\omega_0} \sum_{i,j} S_{ij}(\omega) \left[\hat{A}_i^\dagger(\omega)\hat{A}_j(\omega), \hat{\rho}_S(t)\right] = -i\left[\hat{H}_{LS}, \hat{\rho}_S(t)\right] , \end{aligned} \tag{2.56}$$

where we have defined the Lamb shift Hamiltonian using (2.10)

$$\hat{H}_{LS} = \sum_{\omega=\pm\omega_0} \sum_{i,j} S_{ij}(\omega)\hat{A}_i^\dagger(\omega)\hat{A}_j(\omega) = \sum_{i,j}\left[S_{ij}(\omega_0)\hat{\sigma}_i^+\hat{\sigma}_j^- + S_{ij}(-\omega_0)\hat{\sigma}_j^-\hat{\sigma}_i^+\right] . \tag{2.57}$$

Let us start by separating the diagonal terms of $\hat{H}_{LS}$ from the off-diagonal ones. Thanks to the Pauli matrices commutation rules $\left[\hat{\sigma}_i^+, \hat{\sigma}_j^-\right] = \delta_{ij}\hat{\sigma}_z$ we have

$$\hat{H}_{LS} = \sum_i \left[S_{ii}(\omega_0)\hat{\sigma}_i^+\hat{\sigma}_i^- + S_{ii}(-\omega_0)\hat{\sigma}_i^-\hat{\sigma}_i^+\right] + \sum_{\substack{i,j\\ i\neq j}} \Delta_{ij}\hat{\sigma}_i^+\hat{\sigma}_j^- \tag{2.58}$$

where we have defined the coupling terms

$$\Delta_{ij} = S_{ij}(\omega_0) + S_{ij}(-\omega_0) . \tag{2.59}$$

To make the evaluation of the coupling terms easier, let us first rewrite $S_{ij}(\omega_0)$ by separating the terms depending on the black body temperature ($N(\omega_k)$) from the ones which are independent of it. That means

$$S_{ij}(\omega_0) = \frac{\mu^2}{\pi c^3}\mathrm{P}\int_0^\infty d\omega_k \frac{\omega_k^3}{\omega_0 - \omega_k} F_{ij}(kr_{ij}) + \frac{\mu^2}{\pi c^3}\mathrm{P}\int_0^\infty d\omega_k \frac{2\omega_0\omega_k^3 N(\omega_k)}{\omega_0^2 - \omega_k^2} F_{ij}(kr_{ij}) . \tag{2.60}$$

To compute Δ_{ij} we need $S_{ij}(-\omega_0)$. Now, if we replace ω_0 with $-\omega_0$ in the previous expression, by performing the change of variable $\omega_k \to (-\omega_k)$ in the first integral, we have

$$S_{ij}(-\omega_0) = \frac{\mu^2}{\pi c^3}\mathrm{P}\int_{-\infty}^0 d\omega_k \frac{\omega_k^3}{\omega_0 - \omega_k} F_{ij}(kr_{ij}) - \frac{\mu^2}{\pi c^3}\mathrm{P}\int_0^\infty d\omega_k \frac{2\omega_0\omega_k^3 N(\omega_k)}{\omega_0^2 - \omega_k^2} F_{ij}(kr_{ij}) . \tag{2.61}$$

Therefore, if we sum $S_{ij}(\omega_0) + S_{ij}(-\omega_0)$, the terms depending on the black body temperature cancel and the first integral is extended through the whole real axis, i.e.

$$\Delta_{ij} = \frac{\mu^2}{\pi c^3}\mathrm{P}\int_{-\infty}^\infty d\omega_k \frac{\omega_k^3}{\omega_0 - \omega_k} F_{ij}(kr_{ij}) . \tag{2.62}$$

Before evaluating the above integral, let us change the integration variable to $x = \omega_k r_{ij}/c$ and define the parameter $x_0 = \omega_0 r_{ij}/c$, so that we have

$$\Delta_{ij} = \frac{\mu^2}{\pi r_{ij}^3} \mathrm{P} \int_{-\infty}^{\infty} dx \frac{x^3}{x_0 - x} F_{ij}(x) \,. \tag{2.63}$$

By expanding $F_{ij}(x)$ using (2.50) we have

$$\begin{aligned} \Delta_{ij} =& \frac{\mu^2}{\pi r_{ij}^3} \left[-\left(\hat{p}_i \cdot \hat{p}_j\right) + 3\left(\hat{p}_i \cdot \hat{r}_{ij}\right)\left(\hat{p}_j \cdot \hat{r}_{ij}\right) \right] I_0 + \\ &+ \frac{\mu^2}{\pi r_{ij}^3} \left[\left(\hat{p}_i \cdot \hat{p}_j\right) - 3\left(\hat{p}_i \cdot \hat{r}_{ij}\right)\left(\hat{p}_j \cdot \hat{r}_{ij}\right) \right] I_1 + \\ &+ \frac{\mu^2}{\pi r_{ij}^3} \left[\left(\hat{p}_i \cdot \hat{p}_j\right) - \left(\hat{p}_i \cdot \hat{r}_{ij}\right)\left(\hat{p}_j \cdot \hat{r}_{ij}\right) \right] I_2 \end{aligned} \tag{2.64}$$

where the three real integrals I_0,I_1 and I_2 can be all related to one complex integral

$$I_0 = \mathrm{Im}\left(\mathcal{I}_0\right) \,, \quad I_1 = \mathrm{Re}\left(\mathcal{I}_1\right) \,, \quad I_2 = \mathrm{Im}\left(\mathcal{I}_2\right) \tag{2.65}$$

which is

$$\mathcal{I}_n = \mathrm{P} \int_{-\infty}^{\infty} dx \frac{x^n \, e^{ix}}{x_0 - x} \,. \tag{2.66}$$

To compute $\mathcal{I}_n$ let us consider the contour integral

$$\mathcal{Y}_n = \oint_C dz \frac{z^n \, e^{iz}}{x_0 - z} \tag{2.67}$$

where C here is the closed curve shown as a solid line in Fig. 2.1.

As one can see from Fig. 2.1, the path C has been chosen so that we can split $\mathcal{Y}_n$ into four terms,

$$\mathcal{Y}_n = \mathcal{I}_n^- + c_n^\epsilon + \mathcal{I}_n^+ + C_n^R \,. \tag{2.68}$$

If we take the limit $R \to \infty$, then $C_n^R \to 0$ thanks to Jordan's Lemma. Moreover, $\mathcal{Y}_n$ can be computed by means of the residue theorem and has the value

$$\mathcal{Y}_n = 2\pi i \mathrm{Res}\left[\frac{z^n \, e^{iz}}{x_0 - z}\right]_{z = x_0} = -2\pi i x_0^n e^{i x_0} \,. \tag{2.69}$$

So, if we take the limit $\epsilon \to 0$ we have

$$\begin{aligned} \mathcal{I}_n^- + \mathcal{I}_n^+ &= \lim_{\epsilon \to 0} \left[\int_{-\infty}^{x_0 - \epsilon} dx \frac{x^n \, e^{ix}}{x_0 - x} + \int_{x_0 + \epsilon}^{\infty} dx \frac{x^n \, e^{ix}}{x_0 - x} \right] = \mathrm{P} \int_{-\infty}^{\infty} dx \frac{x^n \, e^{ix}}{x_0 - x} = \mathcal{I}_n \\ &= \mathcal{Y}_n - \lim_{\epsilon \to 0} c_n^\epsilon \,. \end{aligned} \tag{2.70}$$

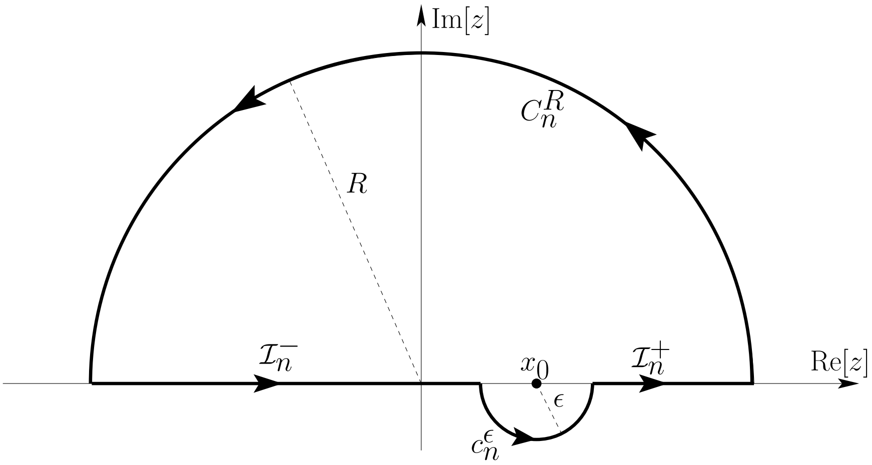

Figure 2.1: Path of the contour integral $\mathcal{Y}_n$ (2.67) in the complex plane.

We can compute c_n^ϵ explicitly by choosing the parametrization $z = x_0 + \epsilon e^{i\theta}$ for $\theta \in [-\pi, 0]$, thus having

$$c_n^\epsilon = \int_{-\pi}^{0} \left(i\epsilon e^{i\theta}\right) d\theta \frac{x_0^n e^{ix_0}}{-\epsilon e^{i\theta}} + o(\epsilon) = -i\pi x_0^n e^{ix_0} + o(\epsilon)\,. \tag{2.71}$$

Substituting (2.69) and (2.71) into (2.70) we finally have

$$\mathcal{I}_n = -i\pi x_0^n e^{ix_0}\,. \tag{2.72}$$

Now we can put $\mathcal{I}_n$ into (2.65) to compute the explicit expression of Δ_{ij}, which is

$$\begin{aligned}\Delta_{ij} =& -\frac{\mu^2}{r_{ij}^3}\left[-\left(\hat{p}_i\cdot\hat{p}_j\right) + 3\left(\hat{p}_i\cdot\hat{r}_{ij}\right)\left(\hat{p}_j\cdot\hat{r}_{ij}\right)\right]\cos x_0 \\ &+ \frac{\mu^2}{\pi r_{ij}^3}\left[\left(\hat{p}_i\cdot\hat{p}_j\right) - 3\left(\hat{p}_i\cdot\hat{r}_{ij}\right)\left(\hat{p}_j\cdot\hat{r}_{ij}\right)\right] x_0\sin x_0 \\ &- \frac{\mu^2}{\pi r_{ij}^3}\left[\left(\hat{p}_i\cdot\hat{p}_j\right) - \left(\hat{p}_i\cdot\hat{r}_{ij}\right)\left(\hat{p}_j\cdot\hat{r}_{ij}\right)\right] x_0^2\cos x_0\end{aligned} \tag{2.73}$$

where we can define $x_{ij} = x_0 = k_0 r_{ij}$ and rearrange it to

$$\begin{aligned}\Delta_{ij} =& \frac{3\gamma}{4}\left[-\frac{\cos x_{ij}}{k_0 r_{ij}} + \frac{\sin x_{ij}}{x_{ij}^2} + \frac{\cos x_{ij}}{x_{ij}^3}\right]\left(\hat{p}_i\cdot\hat{p}_j\right) \\ &+ \frac{3\gamma}{4}\left[\frac{\cos x_{ij}}{k_0 r_{ij}} - 3\frac{\sin x_{ij}}{x_{ij}^2} - 3\frac{\cos x_{ij}}{x_{ij}^3}\right]\left(\hat{p}_i\cdot\hat{r}_{ij}\right)\left(\hat{p}_j\cdot\hat{r}_{ij}\right)\,.\end{aligned} \tag{2.74}$$

As regards the diagonal terms ($i = j$) of $\hat{H}_{LS}$, they produce a correction to the site energy (changing it to a “dressed” energy) which is independent of the site itself, but it diverges. The renormalization of the dressed energy is not treated here, though.

2.4.3 Final expression

Let us now re-write the master equation that we derived. In the Schrödinger picture we have

$$\begin{aligned}\frac{d\hat{\rho}_S}{dt} =& -i\left[\hat{H}_S+\hat{H}_{LS},\hat{\rho}_S\right]+\sum_{i,j}\gamma_{ij}\left(1+N(\omega_0)\right)\left[\hat{\sigma}_j^-\hat{\rho}_S\hat{\sigma}_i^+-\frac{1}{2}\left\{\hat{\sigma}_i^+\hat{\sigma}_j^-,\hat{\rho}_S\right\}\right]\\ &+\sum_{i,j}\gamma_{ij}N(\omega_0)\left[\hat{\sigma}_j^+\hat{\rho}_S\hat{\sigma}_i^--\frac{1}{2}\left\{\hat{\sigma}_i^-\hat{\sigma}_j^+,\hat{\rho}_S\right\}\right]\end{aligned} \tag{2.75}$$

were $N(\omega_0)$ is the Bose-Einstein function and, defining the parameters $x_{ij} = \omega_0 r_{ij}/c$ and $\gamma = \frac{4}{3}\mu^2\frac{\omega_0^3}{c^3}$ we have

$$\begin{aligned}\gamma_{ij} =&\frac{3\gamma}{2}\left[\frac{\sin x_{ij}}{x_{ij}}+\frac{\cos x_{ij}}{x_{ij}^2}-\frac{\sin x_{ij}}{x_{ij}^3}\right]\left(\hat{p}_i\cdot\hat{p}_j\right)+\\ &+\frac{3\gamma}{2}\left[-\frac{\sin x_{ij}}{x_{ij}}-3\frac{\cos x_{ij}}{x_{ij}^2}+3\frac{\sin x_{ij}}{x_{ij}^3}\right]\left(\hat{p}_i\cdot\hat{r}_{ij}\right)\left(\hat{p}_j\cdot\hat{r}_{ij}\right)\,.\end{aligned} \tag{2.76}$$

As regards the Hamiltonian term, subtracting the terms proportional to the identity, we have

$$\hat{H}_S+\hat{H}_{LS} = \frac{\overline{\omega_0}}{2}\sum_i\hat{\sigma}_i^z+\sum_{\substack{i,j\\ i\neq j}}\Delta_{ij}\hat{\sigma}_i^+\hat{\sigma}_j^- \tag{2.77}$$

where the dressed site energy is obtained from (2.58)

$$\overline{\omega_0} = \omega_0+\frac{4\mu^2\omega_0}{\pi c^3}\mathrm{P}\int_0^\infty d\omega_k\frac{\omega_k^3\mathrm{ctanh}\frac{\beta\omega_k}{2}}{\omega_0^2-\omega_k^2} \tag{2.78}$$

and the coupling terms Δ_{ij} are given by (2.74). The dressed energy is divergent, but equal for all levels and therefore it can be neglected.

2.5 Stationary solution for a single site

As a first simple example, here we present the solution of the master equation (2.75) at the steady state for a single site. In this trivial case, we have

$$\begin{aligned}\frac{d\hat{\rho}_S}{dt} =& -i\frac{\overline{\omega_0}}{2}\left[\hat{\sigma}^z,\hat{\rho}_S\right]+\gamma\left(1+N(\omega_0)\right)\left[\hat{\sigma}^-\hat{\rho}_S\hat{\sigma}^+-\frac{1}{2}\left\{\hat{\sigma}^+\hat{\sigma}^-,\hat{\rho}_S\right\}\right]\\ &+\gamma N(\omega_0)\left[\hat{\sigma}^+\hat{\rho}_S\hat{\sigma}^--\frac{1}{2}\left\{\hat{\sigma}^-\hat{\sigma}^+,\hat{\rho}_S\right\}\right]\end{aligned} \tag{2.79}$$

and, projecting onto the ground state $|g\rangle$ and the excited state $|e\rangle$ we have

$$\frac{d\rho_{00}}{dt} = \gamma N(\omega_0)\left(\rho_{ee} - \rho_{00}\right) + \gamma\rho_{ee} \tag{2.80a}$$

$$\frac{d\rho_{ee}}{dt} = \gamma N(\omega_0)\left(\rho_{00} - \rho_{ee}\right) - \gamma\rho_{ee}\,. \tag{2.80b}$$

The solution at the steady state then is

$$\rho_{00}(\infty) = \frac{1}{1+e^{-\beta\omega_0}} \tag{2.81a}$$

$$\rho_{ee}(\infty) = \frac{e^{-\beta\omega_0}}{1+e^{-\beta\omega_0}}\,, \tag{2.81b}$$

showing that the two-level system reaches thermal equilibrium with the black body.

2.6 Superradiance for two coupled sites

Now, let us consider the next nontrivial case of $N = 2$ sites. It is useful to define the operators

$$\hat{S} = \frac{1}{2}\left(\hat{\sigma}_1^z + \hat{\sigma}_2^z\right) \qquad \hat{\sigma}_\pm^+ = \frac{\hat{\sigma}_1^+ \pm \hat{\sigma}_2^+}{\sqrt{2}} \qquad \hat{\sigma}_\pm^- = \frac{\hat{\sigma}_1^- \pm \hat{\sigma}_2^-}{\sqrt{2}} \tag{2.82}$$

in order to write the master equation (2.75) in a diagonal form,

$$\begin{aligned}\frac{d\hat{\rho}_S}{dt} = &-i\left[\hat{H}_S + \hat{H}_{LS}, \hat{\rho}_S\right] + \sum_{k=\pm}\gamma_k\left(1+N(\omega_0)\right)\left[\hat{\sigma}_k^-\hat{\rho}_S\hat{\sigma}_k^+ - \frac{1}{2}\left\{\hat{\sigma}_k^+\hat{\sigma}_k^-, \hat{\rho}_S\right\}\right]\\ &+ \sum_{k=\pm}\gamma_k N(\omega_0)\left[\hat{\sigma}_k^+\hat{\rho}_S\hat{\sigma}_k^- - \frac{1}{2}\left\{\hat{\sigma}_k^-\hat{\sigma}_k^+, \hat{\rho}_S\right\}\right]\end{aligned} \tag{2.83}$$

where we defined $\gamma_\pm = \gamma \pm \gamma_{12}$ and the Hamiltonian is

$$\hat{H}_S + \hat{H}_{LS} = \overline{\omega_0}\,\hat{S} + \Delta_{12}\left(\hat{\sigma}_+^+\hat{\sigma}_+^- - \hat{\sigma}_-^+\hat{\sigma}_-^-\right)\,. \tag{2.84}$$

Each site is a two-level system made of a ground state $|g\rangle$ and an excited state $|e\rangle$. The eigenbasis of the many-body Hamiltonian is given by the four states

$$|0\rangle = |g\rangle\,|g\rangle \tag{2.85a}$$

$$|\pm\rangle = \frac{|e\rangle\,|g\rangle \pm |g\rangle\,|e\rangle}{\sqrt{2}} \tag{2.85b}$$

$$|\bar{e}\rangle = |e\rangle\,|e\rangle \tag{2.85c}$$

whose dressed energies are

$$\left(\hat{H}_S + \hat{H}_{LS}\right)|0\rangle = -\overline{\omega_0}\,|0\rangle \tag{2.86a}$$

$$\left(\hat{H}_S + \hat{H}_{LS}\right)|\pm\rangle = \pm\Delta_{12}\,|\pm\rangle \tag{2.86b}$$

$$\left(\hat{H}_S + \hat{H}_{LS}\right)|\bar{e}\rangle = \overline{\omega_0}\,|\bar{e}\rangle\,. \tag{2.86c}$$

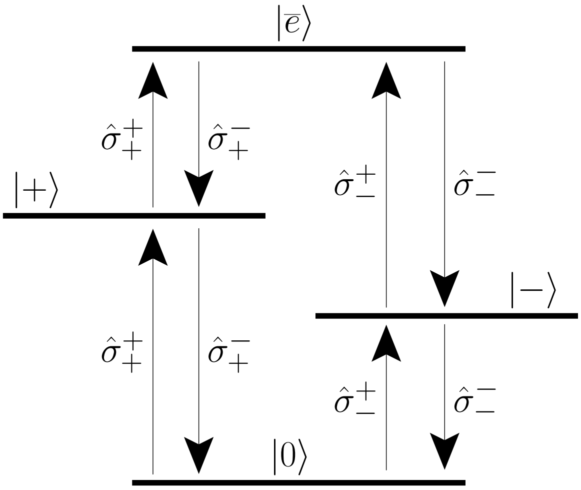

Figure 2.2: Pictorial representation of the energy levels (2.85) and how the operators $\hat{\sigma}_k^\pm$ (with $k = \pm$, see (2.82)) connect those states.

To write the master equation on this basis we need to know how the $\hat{\sigma}_k^\pm$ operators (with $k = \pm$) act on the states. A pictorial representation of the basis and of the action of the operators is shown in Fig. 2.2.

Fig. 2.2 should be read this way: whenever I apply an operator to the state at the origin of the arrow, I get the state at the end of the arrow. So, for example,

$$\hat{\sigma}_+^+ |0\rangle = |+\rangle \ , \quad \hat{\sigma}_-^+ |0\rangle = |-\rangle \ , \quad \hat{\sigma}_+^+ |+\rangle = |\bar{e}\rangle \ , \tag{2.87}$$

but, if there is no connection between two states mediated by a specific operator, then if I apply that operator to the origin state I get 0. For example,

$$\hat{\sigma}_+^+ |\bar{e}\rangle = 0 \, , \quad \hat{\sigma}_+^- |0\rangle = 0 \, , \quad \hat{\sigma}_+^+ |-\rangle = 0 \, , \quad \hat{\sigma}_-^+ |+\rangle = 0 \ldots \tag{2.88}$$

Thanks to the above relations we can project the master equation (2.83) on the basis states to get the dynamics of the populations of those states. Since the equation is in a diagonal form, the dynamics of the populations is decoupled from that of the coherences and we have

$$\frac{d\rho_{00}}{dt} = N(\omega_0)\gamma_+ \left(\rho_{++} - \rho_{00}\right) + N(\omega_0)\gamma_- \left(\rho_{--} - \rho_{00}\right) + \gamma_+\rho_{++} + \gamma_-\rho_{--} \tag{2.89a}$$

$$\frac{d\rho_{\pm\pm}}{dt} = N(\omega_0)\gamma_\pm \left(\rho_{00} - \rho_{\pm\pm}\right) + N(\omega_0)\gamma_\pm \left(\rho_{\overline{ee}} - \rho_{\pm\pm}\right) + \gamma_\pm \left(\rho_{\overline{ee}} - \rho_{\pm\pm}\right) \tag{2.89b}$$

$$\frac{d\rho_{\overline{ee}}}{dt} = N(\omega_0)\gamma_+ \left(\rho_{++} - \rho_{\overline{ee}}\right) + N(\omega_0)\gamma_- \left(\rho_{--} - \rho_{\overline{ee}}\right) - \left(\gamma_+ + \gamma_-\right)\rho_{\overline{ee}} \, . \tag{2.89c}$$

Now, let us consider the simple case of two sites having parallel transition dipole moments and being close to each other, so that their distance is much smaller than the wavelength associated to the optical transition of each site ($k_0 r_{12} \ll 1$). In this case we have

$$\Delta_{12} \approx \frac{\mu^2}{r_{12}^3}\,, \quad \gamma_{12} \approx \gamma\,, \quad \gamma_+ \approx 2\gamma\,, \quad \gamma_- \approx 0 \tag{2.90}$$

and we can simplify (2.89) to

$$\frac{d\rho_{00}}{dt} \approx 2\gamma N(\omega_0)\left(\rho_{++} - \rho_{00}\right) + 2\gamma\rho_{++} \tag{2.91a}$$
$$\frac{d\rho_{++}}{dt} \approx 2\gamma N(\omega_0)\left(\rho_{00} - \rho_{++}\right) + 2\gamma N(\omega_0)\left(\rho_{\overline{ee}} - \rho_{++}\right) + 2\gamma\left(\rho_{\overline{ee}} - \rho_{++}\right) \tag{2.91b}$$
$$\frac{d\rho_{--}}{dt} \approx 0 \tag{2.91c}$$
$$\frac{d\rho_{\overline{ee}}}{dt} \approx 2\gamma N(\omega_0)\left(\rho_{++} - \rho_{\overline{ee}}\right) - 2\gamma\rho_{\overline{ee}}\,. \tag{2.91d}$$

Finally, let us consider the zero temperature case, $N(\omega_0) = 0$, where only spontaneous emission is present. In such case we have

$$\frac{d\rho_{00}}{dt} \approx 2\gamma\rho_{++} \tag{2.92a}$$
$$\frac{d\rho_{++}}{dt} \approx 2\gamma\left(\rho_{\overline{ee}} - \rho_{++}\right) \tag{2.92b}$$
$$\frac{d\rho_{--}}{dt} \approx 0 \tag{2.92c}$$
$$\frac{d\rho_{\overline{ee}}}{dt} \approx -2\gamma\rho_{\overline{ee}}\,, \tag{2.92d}$$

whose solution is

$$\rho_{00}(t) = 1 - \rho_{--}(0) - \left[\rho_{++}(0) + (1 + 2\gamma t)\rho_{\overline{ee}}(0)\right]\, e^{-2\gamma t} \tag{2.93a}$$
$$\rho_{++}(t) = \left[\rho_{++}(0) + 2\gamma t\rho_{\overline{ee}}(0)\right]\, e^{-2\gamma t} \tag{2.93b}$$
$$\rho_{--}(t) = \rho_{--}(0) \tag{2.93c}$$
$$\rho_{\overline{ee}}(t) = \rho_{\overline{ee}}(0)\, e^{-2\gamma t}\,. \tag{2.93d}$$

This solution allows to computed the emitted light power, which is related to the probability per unit time to lose excitation from the system. The total excitation in the system at time t is $\rho_{++}(t) + \rho_{--}(t) + 2\rho_{\overline{ee}}(t)$, so that the emitted power by the two sites is

$$\begin{aligned} W_2(t) &= -\omega_0 \frac{d}{dt}\left[\rho_{++}(t) + \rho_{--}(t) + 2\rho_{\overline{ee}}(t)\right] \\ &= 2\gamma\omega_0\left[\rho_{++}(0) + (1 + 2\gamma t)\rho_{\overline{ee}}(0)\right]\, e^{-2\gamma t}\,. \end{aligned} \tag{2.94}$$

As a comparison, the emitted power by an isolated site is

$$W_1(t) = \gamma\omega_0 e^{-\gamma t}\,. \tag{2.95}$$

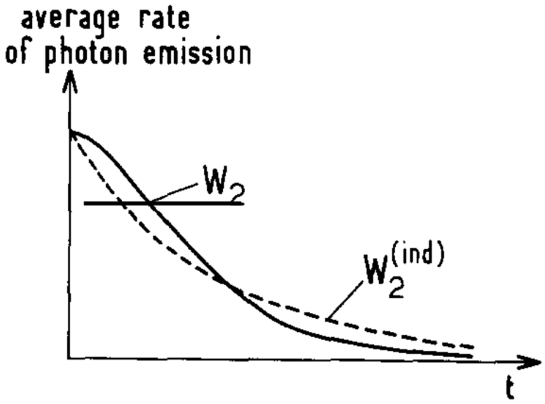

Figure 2.3: Time evolution of the power radiated from two emitters initially excited and cooperatively coupled to the radiation field, see Eq. (2.94). Here, the power emitted by two independent sites is twice the single-site power, that is $W_2^{(ind)} = 2W_1(t)$, where $W_1(t)$ is given by Eq. (2.95). Figure reproduced from Ref. [27].

2.6.1 Many-excitation superradiance, single-excitation superradiance and subradiance

Now, let us consider some specific initial conditions. If both sites are initially excited, meaning that the initial condition is $\hat{\rho}(0) = |\bar{e}\rangle \langle\bar{e}|$, the emitted power is $W_2(t) = 2\gamma\omega_0(1 + 2\gamma t)\, e^{-2\gamma t}$. This solution is compared to the single-site case in Fig. 2.3, reproduced from Ref. [27]. As one can see, the two-site evolution at short times, $W_2(t) \sim 1 - 2\gamma^2 t^2$, has a quadratic decay, that is slower than the single-site case $W_1(t) \sim 1 - 2\gamma t$. On the other hand, at long times the two-sites power ultimately decays as $\sim e^{-2\gamma t}$, with an exponential rate 2γ that is twice faster than the isolated site ($\sim e^{-\gamma t}$). These two features characterize the *many-excitation superradiance* [27]: the radiated power initially decays slower than the single-site case, but a macroscopic coupling to the field is built up with time and ultimately the emission decays N times faster than the case of N isolated emitters.

If instead one excitation is initially prepared on the symmetric $|+\rangle$ state, the emitted radiation decays exponentially as $W_2(t) = 2\gamma\omega_0\, e^{-2\gamma t}$, that is twice as fast as a single site. This phenomenon is called *single-excitation superradiance*, and it has been called “the super of superradiance” by Marlan Scully [28] since it is a distinguishing feature of an initial coherently prepared state.

Finally, if the excitation is initially prepared on the antisymmetric state $|-\rangle$, the excitation stays there forever and there is no emitted power. Such phenomenon, called *subradiance*, stems from a coherent coupling to the light field, where a destructive interference effect quenches the spontaneous emission.

As we introduced in Chapter 1, all these manifestations of superradiance have been observed experimentally, on different systems and appropriate experimental set-ups.

2.7 Single excitation approximation and effective non-Hermitian Hamiltonian

Let us now go back to a general aggregate of N emitters and consider only a subset of the full many-body basis: the state $|0\rangle$, where all the sites are in the ground state, and the single-excitation states $|j\rangle = \hat{\sigma}_j^+ |0\rangle$. Here we proceed to write the master equation neglecting the contribution of the states having more than one excitation, and this is equivalent to replacing $\hat{\sigma}_j^+$ with $|j\rangle \langle 0|$ and $\hat{\sigma}_j^-$ with $|0\rangle \langle j|$ into (2.75). If now we call $\hat{\rho} = \hat{\rho}_S$ the density matrix of the aggregate, we have

$$
\begin{aligned}
\frac{d\hat{\rho}}{dt} \simeq & -i\left[\hat{H}_S + \hat{H}_{LS}, \hat{\rho}\right] + \sum_{i,j} \gamma_{ij}\left(1 + N(\omega_0)\right)\left[\rho_{ji}\,|0\rangle\langle 0| - \frac{1}{2}\left\{|i\rangle\langle j|, \hat{\rho}\right\}\right] \\
& + \sum_{i,j} \gamma_{ij} N(\omega_0)\left[\rho_{00}\,|j\rangle\langle i| - \frac{1}{2}\delta_{ij}\left\{|0\rangle\langle 0|, \hat{\rho}\right\}\right] \qquad (2.96)
\end{aligned}
$$

with the Hamiltonian

$$
\hat{H}_S + \hat{H}_{LS} \simeq \overline{\omega_0} \sum_i |i\rangle\langle i| + \sum_{\substack{i,j \\ i \neq j}} \Delta_{ij}\,|i\rangle\langle j| \,. \qquad (2.97)
$$

Now, let us consider the particular case where there exist a common eigenbasis $|\alpha\rangle$ for both $\left(\hat{H}_S + \hat{H}_{LS}\right)$ and $\sum_{i,j} \gamma_{ij}\,|i\rangle\langle j|$ such that

$$
\langle\alpha|\,\hat{H}_S + \hat{H}_{LS}\,|\beta\rangle = E_\alpha \delta_{\alpha\beta} \qquad (2.98)
$$

$$
\langle\alpha|\left(\sum_{i,j} \gamma_{ij}\,|i\rangle\langle j|\right)|\beta\rangle = \gamma_\alpha \delta_{\alpha\beta} \,. \qquad (2.99)
$$

We can then write (2.96) on such basis and have

$$
\begin{aligned}
\frac{d\hat{\rho}}{dt} \simeq & -i \sum_\alpha E_\alpha \left[|\alpha\rangle\langle\alpha|, \hat{\rho}\right] + \sum_\alpha \gamma_\alpha \left(1 + N(\omega_0)\right)\left[\rho_{\alpha\alpha}\,|0\rangle\langle 0| - \frac{1}{2}\left\{|\alpha\rangle\langle\alpha|, \hat{\rho}\right\}\right] \\
& + \sum_\alpha \gamma_\alpha N(\omega_0)\left[\rho_{00}\,|\alpha\rangle\langle\alpha| - \frac{1}{2}\left\{|0\rangle\langle 0|, \hat{\rho}\right\}\right] . \qquad (2.100)
\end{aligned}
$$

If we consider the diagonal elements, which describe the dynamics of the populations of $|0\rangle$ and of the eigenstates $|\alpha\rangle$, that part of the master equation can be mapped into a Pauli master equation, which reads

$$
\frac{d\rho_{00}}{dt} = \sum_\alpha T_\alpha \left(\rho_{\alpha\alpha} - \rho_{00}\right) + \sum_\alpha \gamma_\alpha \rho_{\alpha\alpha} \qquad (2.101)
$$

$$
\frac{d\rho_{\alpha\alpha}}{dt} = T_\alpha \left(\rho_{00} - \rho_{\alpha\alpha}\right) - \gamma_\alpha \rho_{\alpha\alpha} \,. \qquad (2.102)
$$

Therefore, in this regime we can define the absorption and stimulated emission rates $T_\alpha = N(\omega_0)\gamma_\alpha$ for each eigenstate.

2.7.1 Radiative non-Hermitian Hamiltonian at zero temperature

At zero temperature, the occupation number of photons is $N(\omega_0) = 0$, so that the single-excitation master equation (2.96) simplifies to

$$\frac{d\hat{\rho}}{dt} \simeq -i\left[\hat{H}_S + \hat{H}_{LS}, \hat{\rho}\right] + \sum_{i,j} \gamma_{ij} \left[\rho_{ji} \left|0\right\rangle \left\langle 0\right| - \frac{1}{2}\left\{\left|i\right\rangle \left\langle j\right|, \hat{\rho}\right\}\right] \tag{2.103}$$

that can be also written as

$$\frac{d\hat{\rho}}{dt} \simeq -i\left(\hat{\mathcal{H}}\hat{\rho} - \hat{\rho}\hat{\mathcal{H}}^{\dagger}\right) + \sum_{i,j} \gamma_{ij}\rho_{ji} \left|0\right\rangle \left\langle 0\right| \tag{2.104}$$

where we have defined the effective non-Hermitian Hamiltonian

$$\begin{aligned} \hat{\mathcal{H}} &= \hat{H}_S + \hat{H}_{LS} - \frac{i}{2}\sum_{i,j} \gamma_{ij} \left|i\right\rangle \left\langle j\right| \\ &= \sum_{j} \left(\omega_0 - \frac{i\gamma}{2}\right) \left|j\right\rangle \left\langle j\right| + \sum_{\substack{i,j \\ i\neq j}} \left(\Delta_{ij} - \frac{i}{2}\gamma_{ij}\right) \left|i\right\rangle \left\langle j\right| , \end{aligned} \tag{2.105}$$

with the hermitian elements Δ_{ij} given by Eq. (2.74) and the non-hermitian ones, γ_{ij}, by Eq. (2.76). Such Hamiltonian is called *radiative Hamiltonian* since it models the coupling and the losses induced in the system due to the interaction with the collective emitted field.

As one can see, the evolution of an initial excitation in Eq. (2.104) is uniquely determined by $\hat{\mathcal{H}}$, since the last term in Eq. (2.104) (sometimes called "quantum jump term") simply accounts for the refilling of $\left|0\right\rangle$ due to the loss of excitation. Therefore, an analysis of the complex spectrum of $\hat{\mathcal{H}}$ allows to completely characterize the features of the system coupled to the decay channels of the vacuum electromagnetic field. Following this approach, in Chapters 3 and 5 we start our analysis precisely from the radiative hamiltonian, $\hat{\mathcal{H}}$.

For non-vanishing black-body temperatures, we can see from Eq. (2.96) that all the imaginary terms γ_{ij} are multiplied by a common factor $(1 + N(\omega_0))$, while the real terms Δ_{ij} are unaffected by temperature. In a sense, the presence of a finite-temperature black-body induces stimulated emission processes, which is simply added up to the zero-temperature spontaneous emission process. Therefore, one could define a "finite-temperature non-Hermitian Hamiltonian" as $\Delta_{ij} - \frac{i}{2}\gamma_{ij}(1 + N(\omega_0))$. Nevertheless, even with such definition, the full master equation (2.96) at finite temperature includes the last term, modeling absorption of photons, and therefore a simple form like Eq. (2.104) cannot be derived for finite black-body temperature. Therefore, even though a finite-temperature Hamiltonian can be proposed, it would not completely describe the coupling of the system to the field, because it would only describe stimulated emission not including absorption.

2.7.2 Regime of validity for two sites

Here we want to find the regime of validity of the single-excitation approximation for $N = 2$ sites. If we solve (2.91) at the steady state we have

$$\rho_{00}(\infty) \approx \frac{1}{1+x+x^2} \tag{2.106a}$$

$$\rho_{++}(\infty) \approx \frac{x}{1+x+x^2} \tag{2.106b}$$

$$\rho_{\overline{e}\overline{e}}(\infty) \approx \frac{x^2}{1+x+x^2} \tag{2.106c}$$

where $x = e^{-\beta\omega_0}$. In the case of BChl molecules ($\omega_0/(2\pi c) = 12911$ cm^{-1}) coupled to a black body at the Sun temperature ($T = 1/(k_B\beta) = 6000$ K) we have $x \simeq 0.05$ and thus

$$\rho_{00}(\infty) \approx 0.95\,, \quad \rho_{++}(\infty) \approx 0.048\,, \quad \rho_{\overline{e}\overline{e}}(\infty) \approx 0.002\,. \tag{2.107}$$

With these numbers the state $|\overline{e}\rangle$ with two excitations can be neglected, in a typical case of two coupled molecules. On the contrary, when the temperature of the black body is much higher than ω_0/k_B, then we have $x \approx 1$ and

$$\rho_{00}(\infty) \approx \rho_{++}(\infty) \approx \rho_{\overline{e}\overline{e}}(\infty) \approx \frac{1}{3}\,. \tag{2.108}$$

In such case, clearly, we cannot neglect the double-excited state $|\overline{e}\rangle$.

2.8 Including an extra coupling between the sites

In the previous sections we have always started from non-interacting resonant sites. A dipole-dipole interaction emerged as an effect of the EM field. Here instead we start from a case where the sites are already coupled, and we discuss how this affects our master equation derivation. The master equation resulting from this section has been used in Chapter 4.

The sites hamiltonian (2.2) is conveniently written on its eigenbasis,

$$\hat{H}_S = \sum_{\alpha=1}^{N} \frac{\omega_\alpha}{2} \hat{\sigma}^z_\alpha \tag{2.109}$$

where where ω_α are the eigenvalues of the single-excitation part of $\hat{H}_S$. In many molecular and solid-state systems, the range of energy spanned by the eigenvalues covers the range $|\max_\alpha(\omega_\alpha) - \min_\alpha(\omega_\alpha)| \approx 0.1$ eV and it is smaller than the average value $\omega_0 = \langle\omega_\alpha\rangle_\alpha \approx 1$ eV.

For calculation purposes, we decompose the site-field interaction hamiltonian (2.4) on $\hat{H}_S$'s eigenbasis. Specifically, the raising/lowering operators contained in (2.5) are decomposed as

$$\hat{\sigma}_j^+ = \sum_{\alpha=1}^{N} (c_j^\alpha)^* \hat{\sigma}_\alpha^+ \tag{2.110a}$$

$$\hat{\sigma}_j^- = \sum_{\alpha=1}^{N} c_j^\alpha \hat{\sigma}_\alpha^- \tag{2.110b}$$

where $c_j^\alpha = \langle 0| \hat{\sigma}_j^- \hat{\sigma}_\alpha^+ |0\rangle$ is the amplitude of the α-th eigenstate on the j-th site, and $|0\rangle$ is the ground state of the system, where all the sites are in their ground state. The interaction hamiltonian is decomposed on eigenoperators of $\hat{H}_S$ as

$$\hat{H}_I = \sum_{\omega \in \{\pm\omega_\alpha\}} \sum_j \hat{A}_j(\omega) \otimes \hat{B}_j \tag{2.111a}$$

$$= \sum_{\omega \in \{\pm\omega_\alpha\}} \sum_j \hat{A}_j^\dagger(\omega) \otimes \hat{B}_j \tag{2.111b}$$

where the first sum runs over all the eigenvalues ω_α and their opposite values $-\omega_\alpha$, the interaction operators acting on the sites are

$$\hat{A}_j(\omega_\alpha) = c_j^\alpha \hat{\sigma}_\alpha^- \ , \tag{2.112a}$$

$$\hat{A}_j(-\omega_\alpha) = \hat{A}_j^\dagger(\omega_\alpha) = (c_j^\alpha)^* \hat{\sigma}_j^+ \tag{2.112b}$$

and the operators acting on the bath are

$$\hat{B}_j = i \sum_{\vec{k},\lambda} \sqrt{\frac{2\pi\omega_k}{V}} \left(\vec{d}_j \cdot \vec{e}_{\vec{k},\lambda} \right) \left[e^{i\vec{k}\cdot\vec{r}_j} \hat{b}_{\vec{k},\lambda} - e^{-i\vec{k}\cdot\vec{r}_j} \hat{b}_{\vec{k},\lambda}^\dagger \right] . \tag{2.113}$$

Moving to the interaction picture we have

$$\hat{H}_I(t) = \sum_{\omega \in \{\pm\omega_\alpha\}} \sum_j e^{-i\omega t} \hat{A}_j(\omega) \otimes \hat{B}_j(t) = \sum_{\omega \in \{\pm\omega_\alpha\}} \sum_j e^{i\omega t} \hat{A}_j^\dagger(\omega) \otimes \hat{B}_j(t) \tag{2.114}$$

with $\hat{B}_j(t)$ given by (2.11).

As one can see, we mapped the interaction hamiltonian into a form similar to (2.9). The only difference is that here the sum over ω runs over all the eigenvalues $\pm\omega_\alpha$ ($2N$ values), while in the previous treatment (identical non-interacting sites) the sum ran over $\pm\omega_0$ (2 values).

Thanks to the above mapping, we can recall some of the previous results. Under the Born-Markov approximations we obtain the Redfield Equation (2.23)

$$\frac{d\hat{\rho}_S(t)}{dt} = \sum_{\omega,\omega'} e^{i(\omega'-\omega)t} \sum_{i,j} \Gamma_{ij}(\omega) \left[\hat{A}_j(\omega)\hat{\rho}_S(t)\hat{A}_i^\dagger(\omega') - \hat{A}_i^\dagger(\omega')\hat{A}_j(\omega)\hat{\rho}_S(t) \right] + \text{h.c.} \tag{2.115}$$

where we have defined the rates $\Gamma_{ij}(\omega)$ as the half-sided Fourier transformed correlators of the black body

$$\Gamma_{ij}(\omega) = \int_0^\infty d\tau \, e^{i\omega\tau} \left\langle \hat{B}_i(\tau)\hat{B}_j(0) \right\rangle_B \, . \tag{2.116}$$

The Redfield Equation in the Schrödinger picture reads

$$\frac{d\hat{\rho}_S}{dt} = -\, i \left[\hat{H}_S \, , \, \hat{\rho}_S \right] + \sum_{\omega,\omega'} \sum_{i,j} \Gamma_{ij}(\omega) \left[\hat{A}_j(\omega)\hat{\rho}_S\hat{A}_i^\dagger(\omega') - \hat{A}_i^\dagger(\omega')\hat{A}_j(\omega)\hat{\rho}_S \right] + \text{h.c.} \tag{2.117}$$

where the sums over ω and ω' both run over the $\pm\omega_\alpha$ eigenvalues. One can already appreciate how the rates $\Gamma_{ij}(\omega)$ depend on the eigenvalues ω_α and not on the site energy ω_0.

Now let us perform the *secular approximation*: we neglect the terms having $\omega' \neq \omega$ in (2.115), which oscillate faster than the relaxation time and, in a coarse-grained time scale, they average to 0. This approximation is allowed only where the level spacing $|\omega_\alpha - \omega_\beta|_{\alpha\neq\beta}$ is always larger than the inverse relaxation time $1/\tau_R$. Typical values for molecular aggregates are $|\omega_\alpha - \omega_\beta|_{\alpha\neq\beta} \approx 100 \text{ cm}^{-1}$ and $1/\tau_R \approx 5 \text{ cm}^{-1}$, so the secular approximation is justified. Note that in a disordered system, it is possible that some levels have a small spacing $|\omega_\alpha - \omega_\beta|_{\alpha\neq\beta} < 1/\tau_R$, and in such cases the secular approximation could not be applied.

Nevertheless, under the secular approximation we can keep just the terms with $\omega = \omega'$, so that we get a master equation in the Lindblad form in the Schrödinger picture

$$\frac{d\hat{\rho}_S}{dt} = -\, i \left[\hat{H}_S \, , \, \hat{\rho}_S \right] + \sum_{\omega\in\{\pm\omega_\alpha\}} \sum_{i,j} \Gamma_{ij}(\omega) \left[\hat{A}_j(\omega)\hat{\rho}_S\hat{A}_i^\dagger(\omega) - \hat{A}_i^\dagger(\omega)\hat{A}_j(\omega)\hat{\rho}_S \right] + \text{h.c.} \tag{2.118}$$

Also for the $\Gamma_{ij}(\omega)$ rates, we can recall the previous results. The rates have both a real and an imaginary part,

$$\Gamma_{ij}(\omega) = \frac{1}{2}\gamma_{ij}(\omega) + iS_{ij}(\omega) \, . \tag{2.119}$$

The imaginary parts effectively modify the hamiltonian $\hat{H}_S$ and its spectrum. Therefore, here we assume that their effect is already absorbed into the system hamiltonian $\hat{H}_S$ and we focus only on the real parts. Our previous calculations yield

$$\gamma_{ij}(\omega) = \begin{cases} \frac{3\gamma_0}{2} \left(\frac{\omega_\alpha}{\omega_0}\right)^3 F_{ij}\left(\frac{\omega_\alpha r_{ij}}{c}\right) (1 + N(\omega_\alpha)) & \text{for } \omega = \omega_\alpha \\ \frac{3\gamma_0}{2} \left(\frac{\omega_\alpha}{\omega_0}\right)^3 F_{ij}\left(\frac{\omega_\alpha r_{ij}}{c}\right) N(\omega_\alpha) & \text{for } \omega = -\omega_\alpha \end{cases} \tag{2.120}$$

where $\gamma_0 = 4\mu^2\omega_0^3/(3c^3)$ is the single-site radiative rate, ω_0 is the single-site transition frequency, $F_{ij}(x)$ is given by (2.50) and $N(\omega_\alpha) = [e^{\omega_\alpha/(k_B T)} - 1]^{-1}$ is the Bose-Einstein occupation of photons at temperature T and frequency ω_α.

Neglecting the imaginary part of the rates, the Lindblad master equation reads

$$\frac{d\hat{\rho}_S}{dt} = -i\left[\hat{H}_S\,,\,\hat{\rho}_S\right] + \mathcal{D}_{BB}[\hat{\rho}] \tag{2.121}$$

where the black-body dissipator is

$$\begin{aligned}\mathcal{D}_{BB}[\hat{\rho}] = &\sum_{\omega_\alpha,i,j} \gamma_{ij}(\omega_\alpha)(c_i^\alpha)^* c_j^\alpha \left[\hat{\sigma}_\alpha^- \hat{\rho}_S \hat{\sigma}_\alpha^+ - \frac{1}{2}\left\{\hat{\sigma}_\alpha^+\hat{\sigma}_\alpha^-, \hat{\rho}_S\right\}\right] \\ &+ \sum_{\omega_\alpha,i,j} \gamma_{ij}(-\omega_\alpha)(c_i^\alpha)^* c_j^\alpha \left[\hat{\sigma}_\alpha^+ \hat{\rho}_S \hat{\sigma}_\alpha^- - \frac{1}{2}\left\{\hat{\sigma}_\alpha^-\hat{\sigma}_\alpha^+, \hat{\rho}_S\right\}\right].\end{aligned} \tag{2.122}$$

2.8.1 Long-wavelength approximation

If the inter-site distances r_{ij} are shorter than the average wavelength $\lambda_0 = 2\pi c/\omega_0$, we can approximate

$$F_{ij}\left(\frac{\omega_\alpha r_{ij}}{c}\right) \approx \frac{2}{3}\hat{p}_i \cdot \hat{p}_j\,. \tag{2.123}$$

This allows us to approximate the sum over i, j in the black-body dissipator as

$$\sum_{i,j} \gamma_{ij}(\omega)(c_i^\alpha)^* c_j^\alpha \approx \begin{cases} \gamma_0 |\vec{p}_\alpha|^2 \left(\frac{\omega_\alpha}{\omega_0}\right)^3 (1 + N(\omega_\alpha)) & \text{for } \omega = \omega_\alpha \\ \gamma_0 |\vec{p}_\alpha|^2 \left(\frac{\omega_\alpha}{\omega_0}\right)^3 N(\omega_\alpha) & \text{for } \omega = -\omega_\alpha \end{cases} \tag{2.124}$$

where we use the eigenstate dipole strength

$$\vec{p}_\alpha = \sum_j c_j^\alpha \hat{p}_j\,. \tag{2.125}$$

Therefore, the master equation has a diagonal expression and we can recall the previous results obtained in the single-excitation approximation (see section 2.7): each eigenstate emits with a rate $\gamma_0 |\vec{p}_\alpha|^2 \left(\frac{\omega_\alpha}{\omega_0}\right)^3 (1 + N(\omega_\alpha))$ and has an absorption rate equal to $\gamma_0 |\vec{p}_\alpha|^2 \left(\frac{\omega_\alpha}{\omega_0}\right)^3 N(\omega_\alpha)$. In the typical case where the eigenvalues ω_α cover a small range of energy, compared to the average excitation energy ω_0, we can safely approximate $\omega_\alpha = \omega_0$ and recover the results of section 2.7. On the other hand, for strongly coupled systems, the derivation presented in this section more accurately describes the dependence of the absorption and emission rates on the eigenstate energy.

2.9 Comparison with the stochastic model of sunlight

Here we compare the master equation model of thermal light introduced in this chapter with the stochastic model of sunlight introduced in previous works [50, 51].

Let us consider a dimer pumped by sunlight, as in Ref. [50]. Since sunlight is dilute, we consider just the lowest-energy states of the dimer, that is the ground state $|0\rangle$ (both molecules in their ground state) and the two single-excitation states $|1\rangle = \hat{\sigma}_1^+ |0\rangle$ (first molecule excited, second molecule in its ground state) and $|2\rangle = \hat{\sigma}_2^+ |0\rangle$ (second molecule excited, first molecule in its ground state). Each molecule can absorb excitation from sunlight and the excitation can be lost from each molecule with a rate k. We describe the dynamics with the following Lindblad master equation, in units $\hbar = c = 1$:

$$\frac{d\hat{\rho}_S}{dt} = -i[\hat{H}_S, \hat{\rho}_S] + \mathcal{D}_s[\hat{\rho}_S] + \mathcal{D}_k[\hat{\rho}_S] \tag{2.126}$$

where the hamiltonian of the dimer is

$$\hat{H}_S = \omega_1 \left|_1\right\rangle \langle 1| + \omega_2 |2\rangle \langle 2| + \Delta_{12}(|1\rangle \langle 2| + H.c.)\ . \tag{2.127}$$

For the sunlight pumping super-operator we use the last term of Eq. (2.96) in the long-wavelength approximation ($k_0 r_{12} \ll 1$), namely

$$\mathcal{D}_s[\hat{\rho}_S] = \sum_{i=1}^{2} \sum_{j=1}^{2} N(\omega_0)\gamma \hat{p}_i \cdot \hat{p}_j \left(\rho_{00} |i\rangle \langle j| - \frac{1}{2} |0\rangle \langle 0| \hat{\rho}_S - \frac{1}{2} \hat{\rho}_S |0\rangle \langle 0| \right) \tag{2.128}$$

where $N(\omega_0) = [e^{\beta_s \omega_0} - 1]^{-1}$ is the Bose occupation of photons at the average site energy $\omega_0 = (\omega_1 + \omega_2)/2$, $\beta_s = 1/(k_B T_s)$ is the Sun inverse temperature ($T_s \approx 6000$ K), $\gamma = \frac{4}{3}\mu^2\omega_0^3$ is the single-molecule spontaneous decay rate, $\hat{p}_j$ is the direction of the transition dipole moment of the jth molecule and $\rho_{00} = \langle 0| \hat{\rho}_S |0\rangle$ is the population of the ground state. The decay super-operator is

$$\mathcal{D}_k[\hat{\rho}_S] = \sum_{i=j}^{2} k \left(\rho_{jj} |0\rangle \langle 0| - \frac{1}{2} |j\rangle \langle j| \hat{\rho}_S - \frac{1}{2} \hat{\rho}_S |j\rangle \langle j| \right). \tag{2.129}$$

The hamiltonian $\hat{H}_S$ is diagonalized in the excitonic basis $\{|+\rangle, |-\rangle, |0\rangle\}$ and it reads $\hat{H}_S = \omega_+ |+\rangle \langle +| + \omega_- |-\rangle \langle -|$. The transition dipole moments associated to each eigenstate are

$$\hat{p}_\pm = \hat{p}_1 \langle 1|\pm\rangle + \hat{p}_2 \langle 2|\pm\rangle\ . \tag{2.130}$$

The master equation in such basis reads

$$\frac{d\rho_{++}}{dt} = N(\omega_0)\gamma |\hat{p}_+|^2 \rho_{00} - k\rho_{++} \tag{2.131a}$$

$$\frac{d\rho_{--}}{dt} = N(\omega_0)\gamma |\hat{p}_-|^2 \rho_{00} - k\rho_{--} \tag{2.131b}$$

$$\frac{d\rho_{+-}}{dt} = -i\left(\omega_+ - \omega_-\right)\rho_{+-} + N(\omega_0)\gamma \hat{p}_+^* \cdot \hat{p}_- \rho_{00} - k\rho_{+-}\ . \tag{2.131c}$$

We consider the initial condition $\hat{\rho}_S(t = 0) = |0\rangle\langle 0|$ and the weak field condition $\rho_{00} \approx 1$. We also define the energy difference $\omega = \omega_+ - \omega_-$. In such condition, the solution of the master equation is

$$\rho_{++}(t) = \frac{N(\omega_0)\gamma|\hat{p}_+|^2}{k}\left(1 - e^{-kt}\right) \tag{2.132a}$$

$$\rho_{--}(t) = \frac{N(\omega_0)\gamma|\hat{p}_-|^2}{k}\left(1 - e^{-kt}\right) \tag{2.132b}$$

$$\rho_{+-}(t) = \frac{N(\omega_0)\gamma\hat{p}_+^* \cdot \hat{p}_-}{(i\omega + k)}\left(1 - e^{-(i\omega+k)t}\right) , \tag{2.132c}$$

which is identical to the white-noise solution reported in Ref. [50] [see Eqs. (8a-c) therein].

Both the white-noise and the Lindblad approach predict dynamical and static coherence in the case where $\omega \neq 0$ and $\hat{p}_+^* \cdot \hat{p}_- \neq 0$. That is, sunlight can generate coherences between the eigenstates of the system in the case where it is pumping a state that is not an eigenstate of $\hat{H}_S$. Note that we obtained this result by applying a sunlight super-operator that has been derived assuming resonant energy sites, and later we applied such operator to the hamiltonian $\hat{H}_S$ where the site energies are non-resonant. If we had derived the sunlight super-operator starting from $\hat{H}_S$ and applying the Born-Markov and secular approximations, we would have obtained a super-operator in the form of Eqs. (2.121), (2.122) and (2.124). In such case, instead, we would have obtained a very different result with no coherence between the eigenstates, because the secular approximation would have removed this effect. So, our Lindblad approach to sunlight is able to reproduce some non-secular peculiarities of the white-noise approach (namely, the coherences between the eigenstates), only if we derive the Lindblad super-operator assuming degenerate sites with an energy equal to the average site energy, as done in this section, and applying such Libdblad super-operator *a posteriori* to the non-degenerate Hamiltonian. While it is certainly interesting that our phenomenological approach is able recover some non-secular features into a Lindblad master equation, we leave a systematic justification of this correspondence for a further investigation.

Chapter 3

Interplay of superradiance and noise in photosynthetic molecular nanotubes

In this chapter we analyze the interplay of superradiance and thermal noise in the nanotubular aggregates present in Green Sulfur Bacteria photosynthetic antenna complexes. Results from this chapter have been published as: Marco Gullì, Alessia Valzelli, Francesco Mattiotti, Mattia Angeli, Fausto Borgonovi, and G. Luca Celardo, "Macroscopic coherence as an emergent property in molecular nanotubes", New J. Phys. **21***, 013019 (2019). I contributed in understanding the origin of the depressed density of states from the long-range coupling, analyzing the eigenstates of the nanotubes and the gap between the two lowest eigenstates, as well as training and tutoring two Bachelor/Master students, Marco Gullì and Alessia Valzelli, who performed the rest of the numerical simulations.*

Nanotubular molecular self-aggregates are characterized by a high degree of symmetry and they are fundamental systems for light-harvesting and energy transport. While coherent effects are thought to be at the basis of their high efficiency, the relationship between structure, coherence and functionality is still an open problem. We analyze natural nanotubes present in Green Sulfur Bacteria. We show that they have the ability to support macroscopic coherent states, i.e. delocalized excitonic states coherently spread over many molecules, even at room temperature. Specifically, assuming a canonical thermal state we find, in natural structures, a large thermal coherence length, of the order of 1000 molecules. By comparing natural structures with other mathematical models, we show that this macroscopic coherence cannot be explained either by the magnitude of the nearest-neighbour coupling between the molecules, which would induce a thermal coherence length of the order of 10 molecules, or by the presence of long-range interactions between the molecules. Indeed we prove that the existence of macroscopic coherent states is an emergent property of such structures due to the interplay between geometry and cooperativity (superradiance

and super-transfer). In order to prove that, we give evidence that the lowest part of the spectrum of natural systems is determined by a cooperatively enhanced coupling (super-transfer) between the eigenstates of modular sub-units of the whole structure. Due to this enhanced coupling strength, the density of states is lowered close to the ground state, thus boosting the thermal coherence length. As a striking consequence of the lower density of states, an energy gap between the excitonic ground state and the first excited state emerges. Such energy gap increases with the length of the nanotube (instead of decreasing as one would expect), up to a critical system size which is close to the length of the natural complexes considered.

3.1 Introduction

Coherent effects, as fragile as they may seem, might be able to survive in complex systems even in presence of strong noise induced by the coupling to an external environment. They are often related to functions in complex chemical and biophysical systems [52–54]. Understanding under which conditions robust coherent effects can be sustained even at room temperature is a central issue for designing efficient quantum devices.

Molecular nanotubes are among the most interesting and most investigated structures. They are present in several natural photosynthetic complexes, for instance in the Green Sulphur Bacteria [55–62] or in Phycobilisome Antennas [63–66]. They are also present in other biomolecular systems, for instance in Microtubules, which are fundamental biological structures, showing interesting similarities with photosynthetic Antenna complexes [67, 68]. Also artificial molecular nanotubes are at the centre of research interest [69–72]. Nanotubular molecular aggregates are extremely efficient for light-harvesting and energy transport and they present a very ordered structure with a high degree of symmetry [57–59, 73–76]. The high degree of symmetry concerns both the molecule positions and the orientation of their transition dipoles. Despite all that, a clear understanding of how structural features in molecular aggregates can sustain coherent effects and explain their high efficiency is still missing.

Some of the primary coherent effects which are thought to be responsible for the high efficiency of molecular nanotubes are induced by the delocalization of the excitation over many molecules. Since the sunlight is very dilute, usually only one excitation is present in such complexes, so that single-excitation delocalized states are usually investigated. Delocalized excitonic states can lead to cooperative effects, such as superradiance [19, 60, 61, 73, 77–79] and super-transfer [3, 7], and they can be useful in both natural or artificial light-harvesting complexes [1, 19, 25, 26, 41, 45, 70, 80–86]. Specifically, coherently delocalized excitonic states can have a large dipole strength which strongly couples them to the electromagnetic field. Thus, these states are able to superabsorb light at a rate much larger than the single-molecule absorbing rate, since the absorption rate of delocalized excitonic states can increase with the number of molecules over which the excitation is delocalized [60, 61]. States with a large dipole strength can also couple between themselves efficiently, inducing a super-transfer coupling between distant molecular aggregates [7] or different parts of the same aggregate as we show here. Delocalized single excitonic states over a large number of molecules are called macroscopic coherent states and they are studied both for applications and basic science [30, 37, 39, 87–90].

Molecular nanotubes are composed by a network of self-assembled photo-active molecules. Each molecule can be treated as a two level system, characterized by both an excitation energy and a transition dipole moment which determines its coupling with the electromagnetic field and with the other molecules. The interaction between the molecules is often assumed to be dipole-dipole [73–76] which decays with the distance as $1/r^3$ or, in some approximate scheme, as nearest-neighbour [72] only. While the results thus obtained are certainly very interesting, care is needed to use such simplifications in large molecular structures. Indeed, dipole-dipole interaction is valid when the distance between the molecules is sufficiently large and the overall system size L is considerably smaller than the wavelength λ_0 connected with the excitation energy of the molecules (small volume limit). Since nanotubular aggregates can be large, here we consider a more accurate Hamiltonian interaction [91] which takes into account the interaction between oscillating charges in each molecule. Such description reduces to the usual dipole-dipole interaction in the small volume limit.

Using such radiative Hamiltonian, we have analyzed the existence of macroscopic coherent states at room temperature in different, natural and artificial, molecular nanotubes. Since the molecules in such structures are tightly packed, their interaction energy can be strong, of the order of several times $k_B T \approx 200\,\mathrm{cm}^{-1}$ with $T = 300K$. Such strong interaction is thought to be able to support excitonic delocalization even at room temperature. Nevertheless here we show that the symmetric arrangement of the molecules is able to induce excitonic delocalization at room temperature well beyond what one could expect from the magnitude of the nearest-neighbour coupling between the molecules. Moreover, by comparing natural structures with few mathematical models of self-aggregated molecular nanotubes we show that the degree of macroscopic coherence cannot be explained even by the long-range nature of the coupling between the molecules. We connect such enhanced delocalization to the super-transfer coupling present inside such structures, which induces the emergence of a gapped superradiant state in the low energy region of the spectrum. Thus our main result is that macroscopic coherence in natural molecular nanotubes is an emergent property produced by specific cooperative effects which cannot be reduced either to the range of the interaction or to the magnitude of the coupling between the molecules. The presence of a large coherence length at room temperature in molecular nanotubes suggests the possibility that such structures can exploit superabsorption of light and supertransfer of excitation for efficient light-harvesting and energy transport. Superabsorption, induced by giant dipoles, can enhance the absorption rate of sun-light [3, 33] while supertransfer can enhance the diffusion coefficient for energy transfer [7]. Both such effects induced by excitonic delocalization are thought to play an important role in natural photosynthetic complexes [3, 7, 33, 55].

Specifically, in this chapter we investigate the *Chlorobium Tepidum* Antenna complexes of Green Sulfur bacteria. Green Sulfur bacteria are photosynthetic organisms which live in deep water where the sunlight flux is very low [56] and they are among the most efficient photosynthetic systems [57–59]. Similarly to other antenna complexes present in nature [63–66], they present a high degree of symmetry being arranged in nontrivial cylindrical structures with an ordered orientation of the molecule dipoles. We analyze both the wild type (WT) and the triple mutant type (MT), which have been recently investigated in [92, 93].

Understanding the connection between functionality and structure in such complexes will enhance our comprehension of natural photosynthesis and it could also inspire efficient bio-mimetic devices for energy transport and light-harvesting.

In Section 3.2 and 3.3 we present the cylindrical models studied. In Section 3.4.1 the existence of a delocalized superradiant state close to the ground state for the natural models is shown. In Sections 3.4.2 and 3.4.3 the thermal coherence length is introduced and analyzed. Natural complexes are shown to be able to support the largest thermal coherence length with respect to the other models considered. The evidence produced in these Sections allows to conclude that the large thermal coherence length of natural aggregates cannot be explained by the magnitude of the coupling or by the range of the interaction between the molecules. In Section 3.5 we explain that the origin of such macroscopic coherent states found in natural complexes lies in their specific geometry which induces a supertransfer coupling inside the complexes. Such supertransfer coupling strongly affects the lowest part of the spectrum thus enhancing the thermal coherence length. In Section 3.6, we analyze structures which are more complex than single cylindrical surfaces. Specifically, we consider tubular structures made of four concentric cylindrical surfaces, as they appear in natural antenna complexes of Green Sulfur bacteria [92–95]. We show that these structures display an enhanced delocalization of the excitation with respect to single cylindrical surfaces. Finally in Section 3.7 we give our conclusions and perspectives.

3.2 The models

The natural Antenna complexes present in Green Sulphur bacteria have lengths of 1000 - 2000 Å, widths of 100 - 600 Å and they can contain a number of molecules between $50,000$ and $250,000$, typically arranged into concentric cylindrical surfaces [56, 96]. It is important to remark that, depending on the environment and on the growing conditions [97], some samples could show an alternation between tubular aggregates and non-tubular curved lamellae [98, 99]. Nevertheless, in spite of the heterogeneity of the structures experimentally observed, we will consider here cylindrical surfaces only with a radius of 6 nm and length up to $L = 250$ nm composed of about $15,000$ molecules.

Specifically, we analyze five different cylindrical models with fixed radius ($R = 60$ Å) and total number of chromophores N. These models differ for the geometrical arrangement of the chromophores along the cylindrical surface. In details they are:

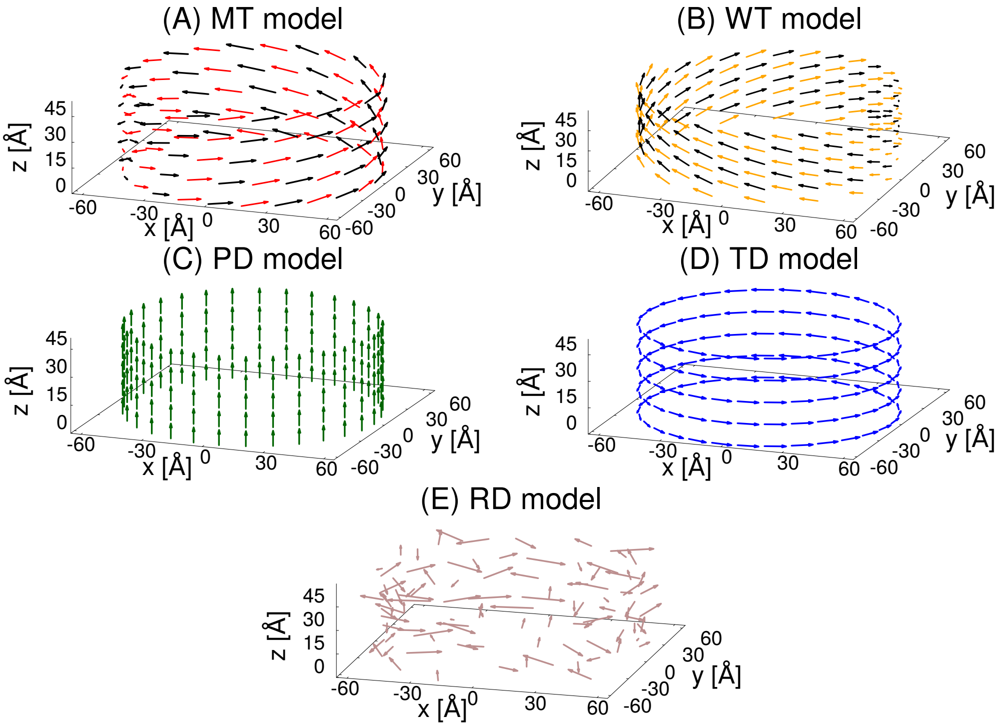

Figure 3.1: Sections of the different models. In all panels we show cylinders with the same radius $R = 60$ Å. For the sake of clarity we show only 30 dipoles per ring instead of 60 as we considered in this chapter. Moreover the distances along the $z-$axis are enhanced by a factor of 5 with respect to the distances on the $x - y$ axes. The same factor and also a reduction of the number of dipoles have been used for WT model. In all models but the WT, where the dipoles are arranged in a helical structure, the dipoles are arranged into $N_1 = 5$ rings.

- *Chlorobium Tepidum* bchQRU triple mutant (MT),
- *Chlorobium Tepidum* wild type (WT),
- parallel dipoles cylinder (PD),
- tangent dipoles cylinder (TD),
- random dipoles cylinder (RD).

While the first two are representative of natural systems, the others are mathematical models with a suitable symmetric arrangements of chromophores (TD and PD) while the last one (RD) is characterized by a random orientation of the dipole moments. The molecule positions and dipole orientations for the natural models have been taken from literature [92, 93, 95] and they correspond to the values capable to reproduce experimental results.

A schematic view of the arrangement of the dipoles on the cylindrical surfaces for all models is shown in Figure 3.1, while all other technical details can be found in 3.8.1. Notice that all the models but the WT share the same basic structure: the cylinder is made by a collection of N_1 rings composed of $N_2 = 60$ molecules equally spaced on each ring. The difference between them lies in the dipole orientation only:

- PD model: all dipoles are oriented parallel to the z axis
- TD model: all dipole are perpendicular to the z direction and tangential to the cylindrical surface
- MT model: here the dipoles have a fixed z component, but also a component perpendicular to the z direction, see 3.8.1 for details. Note that the component perpendicular to the z direction points inward and outward alternatively with respect to the plane tangent to the cylindrical surface with a small angle α (see black and red arrows in Figure 3.1(A)).
- RD model: the position of the dipoles is the same of the other three models but the orientation of the dipoles is fully random on the unit sphere.

On the other hand the WT model, see Figure 3.1(B), is not composed of separated rings but instead is arranged in a complicated helical structure, see 3.8.1 for details.

3.3 The Hamiltonian and the dipole approximation

Each molecule is represented as a two-level system with an excitation energy e_0 and a transition dipole moment $\vec{\mu}$. The parameters of the aggregates considered here have been taken from literature [100, 101] to be the ones characterizing the Antenna Complexes in Green Sulfur bacteria. Specifically we set for the excitation energy of all the molecules $e_0 = 15390\ \text{cm}^{-1}$ [101], corresponding to $\lambda_0 \approx 650$ nm, so that

$$k_0 = 2\pi e_0 \times 10^{-8} = 9.670 \times 10^{-4}\ \text{Å}^{-1}.$$

$\mu = \sqrt{30}$ D [100] so that $|\mu|^2 = 151024\ \text{Å}^3\ \text{cm}^{-1}$ (for the conversion, see [1]).

---

[1] Let us recall that, in Gaussian units, the unit dipole-dipole interaction energy is $[E] = [\mu]^2[d]^{-3}$, where $[\mu]$ is the unit dipole and $[d]$ the unit distance. We express the dipoles in D (Debye), the distance in Å and the energy in cm^{-1} units (applying the standard conversion $[E]/(hc)$, with h being the Planck constant and c the speed of light), so that $[\mu]^2/(hc) = \text{cm}^{-1}\text{Å}^3$. Now, from the definition $1\ \text{D} = 10^{-18}\ \text{cm}^{5/2}\ \text{g}^{1/2}\ \text{s}^{-1}$ we have $1\ \text{D}^2 = 10^{-12}\ \text{cm}^2\ \text{g}\ \text{s}^{-2}\ \text{Å}^3$. Recalling the Planck constant $h = 6.626 \cdot 10^{-27}\ \text{cm}^2\ \text{g}\ \text{s}^{-1}$ and the speed of light $c = 2.998 \cdot 10^{10}\ \text{cm}\ \text{s}^{-1}$, we have $1\ \text{D}^2/(hc) = 5034\ \text{cm}^{-1}\ \text{Å}^3$. So, a transition dipole $\mu = \sqrt{30}$ D results in $|\mu|^2 = 30 \times 5034\ \text{cm}^{-1}\ \text{Å}^3 = 151020\ \text{cm}^{-1}\ \text{Å}^3$. Note that in these calculations we write explicitly where the energy is divided by hc for clarity, while in the text we always assume implicitly that any energy is divided by hc.

$\gamma = 4|\mu|^2 k_0^3/3 = 1.821 \times 10^{-4}$ cm^{-1}, corresponding to the radiative lifetime $\tau_\gamma =$ 29.15 ns (for the conversion, see [2]).

Choosing the basis states in the single excitation manifold, where the state $|i\rangle$ refers to a state in which the i^{th} molecule is excited while all the others are in the ground state, the nanotubes can be described through a Non-Hermitian Hamiltonian which takes into account the interaction between the molecules mediated by the electromagnetic field (EMF). The effective Non-Hermitian Hamiltonian (also called radiative Hamiltonian), is commonly used to model the interaction with the EMF in different systems, such as natural light-harvesting complexes [44, 91] and cold atomic clouds [102]. The radiative Hamiltonian has been derived by many authors, see for instance Ref.s [27, 44], and it is accurate when the intensity of the electromagnetic field is weak so that the single excitation approximation is valid. Such approximation is extremely good for sun-light absorption since sunlight is very diluted. The radiative Hamiltonian reads:

$$H = \sum_{i=1}^{N} e_0 |i\rangle\langle i| + \sum_{i\neq j} \Delta_{ij} |i\rangle\langle j| - \frac{i}{2} \sum_{i,j=1}^{N} Q_{ij} |i\rangle\langle j| . \tag{3.1}$$

The terms Δ_{ij} and Q_{ij} derive from the interaction with the EMF. The real and imaginary diagonal parts of the intermolecular coupling are given respectively, by

$$\Delta_{nn} = 0\,, Q_{nn} = \frac{4}{3}\mu^2 k_0^3 = \gamma\,, \tag{3.2}$$

with $\mu = |\vec{\mu}|$ being the transition dipole, while the off-diagonal ($n \neq m$) by

$$\begin{aligned} \Delta_{nm} = \frac{3\gamma}{4} \Bigg[& \left(-\frac{\cos(k_0 r_{nm})}{(k_0 r_{nm})} + \frac{\sin(k_0 r_{nm})}{(k_0 r_{nm})^2} + \frac{\cos(k_0 r_{nm})}{(k_0 r_{nm})^3} \right) \hat{\mu}_n \cdot \hat{\mu}_m + \\ & - \left(-\frac{\cos(k_0 r_{nm})}{(k_0 r_{nm})} + 3\frac{\sin(k_0 r_{nm})}{(k_0 r_{nm})^2} + 3\frac{\cos(k_0 r_{nm})}{(k_0 r_{nm})^3} \right) (\hat{\mu}_n \cdot \hat{r}_{nm}) (\hat{\mu}_m \cdot \hat{r}_{nm}) \Bigg] , \end{aligned} \tag{3.3}$$

$$\begin{aligned} Q_{nm} = \frac{3\gamma}{2} \Bigg[& \left(\frac{\sin(k_0 r_{nm})}{(k_0 r_{nm})} + \frac{\cos(k_0 r_{nm})}{(k_0 r_{nm})^2} - \frac{\sin(k_0 r_{nm})}{(k_0 r_{nm})^3} \right) \hat{\mu}_n \cdot \hat{\mu}_m + \\ & - \left(\frac{\sin(k_0 r_{nm})}{(k_0 r_{nm})} + 3\frac{\cos(k_0 r_{nm})}{(k_0 r_{nm})^2} - 3\frac{\sin(k_0 r_{nm})}{(k_0 r_{nm})^3} \right) (\hat{\mu}_n \cdot \hat{r}_{nm}) (\hat{\mu}_m \cdot \hat{r}_{nm}) \Bigg] , \end{aligned} \tag{3.4}$$

where $\hat{\mu}_n := \vec{\mu}_n/\mu$ is the unit dipole moment of the n-th site and $\hat{r}_{nm} := \vec{r}_{nm}/r_{nm}$ is the unit vector joining the n-th and the m-th sites.

Diagonalizing the Hamiltonian (3.1) we obtain the complex eigenvalues $\varepsilon_n = \mathrm{E}_n - \mathrm{i}\frac{\Gamma_n}{2}$ where Γ_n is the radiative decay of the n^{th} eigenstate. In general it

---

[2] The lifetime related to an energy width γ is defined as $\tau_\gamma = \hbar/\gamma$. Note that we implicitly divide each energy by hc (with h being the Planck constant and c the speed of light), so that $[\gamma]/(hc) = [\mathrm{cm}]^{-1}$. Therefore, the unit time is $[\tau_\gamma] = \frac{h}{2\pi[\gamma]} = \left(2\pi c[\mathrm{cm}]^{-1}\right)^{-1}$, where $c = 2.998 \cdot 10^{-2}$ cm ps^{-1}. Thus, given a width in $[\mathrm{cm}]^{-1}$ units, its lifetime is obtained by multiplying the width by $2\pi c = 0.1884$ cm ps^{-1} and taking the reciprocal of the result.

differs from the radiative decay of the single molecule γ. In particular, when the ratio $\Gamma_n/\gamma \gg 1$ we will talk about a "superradiant state" (SRS), otherwise when $\Gamma_n/\gamma \ll 1$ the state is called "subradiant". In other words, a SRS can radiate much faster than a single molecule, while a subradiant one radiates at a rate much slower than the single molecule radiative decay.

Within the range of parameters considered here, the imaginary part Q_{ij} can be considered a small perturbation of the real part of the Hamiltonian (3.1), moreover the system size is small compared to wavelength associated with the optical transition of the molecules (maximum size considered here is $L/\lambda_0 \approx 0.4$). In such case, the optical absorption of an eigenstate of the aggregate can be estimated in terms of its dipole strength, computed only from the real part of the Hamiltonian (3.1). Denoting the n^{th} eigenstate of the real part of the Hamiltonian (3.1) with $|E_n\rangle$, we can expand it on the site basis, so that

$$|E_n\rangle = \sum_{i=1}^{N} C_{ni}\,|i\rangle. \tag{3.5}$$

Note that the site basis is referred to the molecules and is composed by the states $|i\rangle$, each of them carrying a dipole moment $\vec{\mu}_i$. If N is the total number of molecules, then we will express the transition dipole moment $\vec{D}_n$ associated with the n^{th} eigenstate as follows:

$$\vec{D}_n = \sum_{i=1}^{N} C_{ni}\,\hat{\mu}_i. \tag{3.6}$$

The dipole strength of the n^{th} eigenstate is defined by $|\vec{D}_n|^2$ (note that due to normalization $\sum_{n=1}^{N} |\vec{D}_n|^2 = N$). Under the approximation that the imaginary part of the Hamiltonian (3.1) can be treated as a perturbation and $L/\lambda_0 \ll 1$ we have $|\vec{D}_n|^2 \approx \Gamma_n/\gamma$, which is valid for states with a large radiative decay rate (see 3.8.2 for a comparison between dipole strengths and radiative decay widths for all models).

Thus, in the following we will consider only the real part of the Hamiltonian (3.1),

$$H_r = \sum_{i=1}^{N} e_0|i\rangle\langle i| + \sum_{i\neq j} \Delta_{ij}|i\rangle\langle j|, \tag{3.7}$$

where $\Delta_{i,j}$ is given in equation (3.3).

Finally we note that for small systems, when $k_0 r_{ij} \ll 1$, the Hamiltonian (3.1) becomes

$$\begin{aligned} Q_{ij} &\simeq \gamma\hat{\mu}_i\hat{\mu}_j, \\ \Delta_{ij} &\simeq \frac{\vec{\mu}_i\cdot\vec{\mu}_j - 3(\vec{\mu}_i\cdot\hat{r}_{ij})(\vec{\mu}_j\cdot\hat{r}_{ij})}{r_{ij}^3}. \end{aligned} \tag{3.8}$$

In this limit, the real term Δ_{ij} represents a dipole-dipole interaction energy with $\mu = |\vec{\mu}_j|$ and the radiative decay $\gamma = \frac{4}{3}|\mu|^2 k_0^3$. The dipole approximation is widely used in literature to model molecular aggregates which are small compared to the wavelength of the absorbed light. Nevertheless when the dimension of the aggregate becomes comparable with the wavelength λ_0 the dipole-dipole approximation fails. For the maximal sizes considered here ($L/\lambda_0 \approx 0.4$) the dipole approximation can be considered good, even if there are already non-negligible deviations in some quantities between the dipole-dipole interaction in equation (3.8) and the Hamiltionian in equation (3.7), see 3.8.3. For this reason in the following we will use the expression given in equation (3.7).

3.4 Single Cylindrical structures: Results

In this Section we analyze first the collective dipole strengths of the eigenstates of the different models, showing the emergence of a superradiant state close to the ground state in natural complexes, see section 3.4.1. The coherence length is defined in section 3.4.2 where also a new model with only nearest-neighbor couplings is introduced. Finally in section 3.4.3 the results of our analysis about the thermal coherence length for the different models is shown.

3.4.1 Collective Dipole Strength

As a first goal let us analyze the dipole strengths associated with the eigenstates of the Hamiltonian models described in the previous section. For the five models introduced previously we diagonalized the Hamiltonian in equation (3.7), and we analyzed in detail the dipole strengths $|D_n|^2$ of all eigenstates. In Figure 3.2(A-E) we plot $|D_n|^2$ as a function of the energy $E_n - e_0$ of the corresponding eigenstate. All models but the random one (E) are characterized by the presence of SRS in different positions of the energy spectrum. For instance for the MT model the state having the largest dipole strength is the ground state while for the WT model it is very close to it. Note that the position of the superradiant state is below the excitation energy of a single molecule. Since the dipole strength of the eigenstates determines the absorption spectrum [60, 61], a superradiant ground state implies a red-shifted absorption spectrum which is a typical behaviour for molecular J-aggregates [60, 61, 70, 73]. On the other hand for both the TD and PD models the SRSs are in the middle of the energy spectrum (C,D). Contrary to this general trend, the absence of ordering characterizing the random model (RD) does not guarantee the presence of SRS. Indeed it is well known that in the small volume limit $L/\lambda \ll 1$ symmetry is necessary to preserve super- and sub-radiance [27].

This is a clear indication that natural structures tend to push the SRS to the lowest energy region. Moreover, as the comparison with the other symmetric structure shows, this is not a trivial consequence of the symmetric arrangement. Other symmetric arrangements, such as the TD and PD, are still characterized by SRS but “living” in an energy region far from the ground state.

SRSs are typically characterized by a collective dipole strength which grows with the length of the cylindrical structure. This is clearly shown in Figure 3.2(F) where the maximal dipole strength $|D_{\max}|^2$ is shown as a function of the length L of the cylinder.

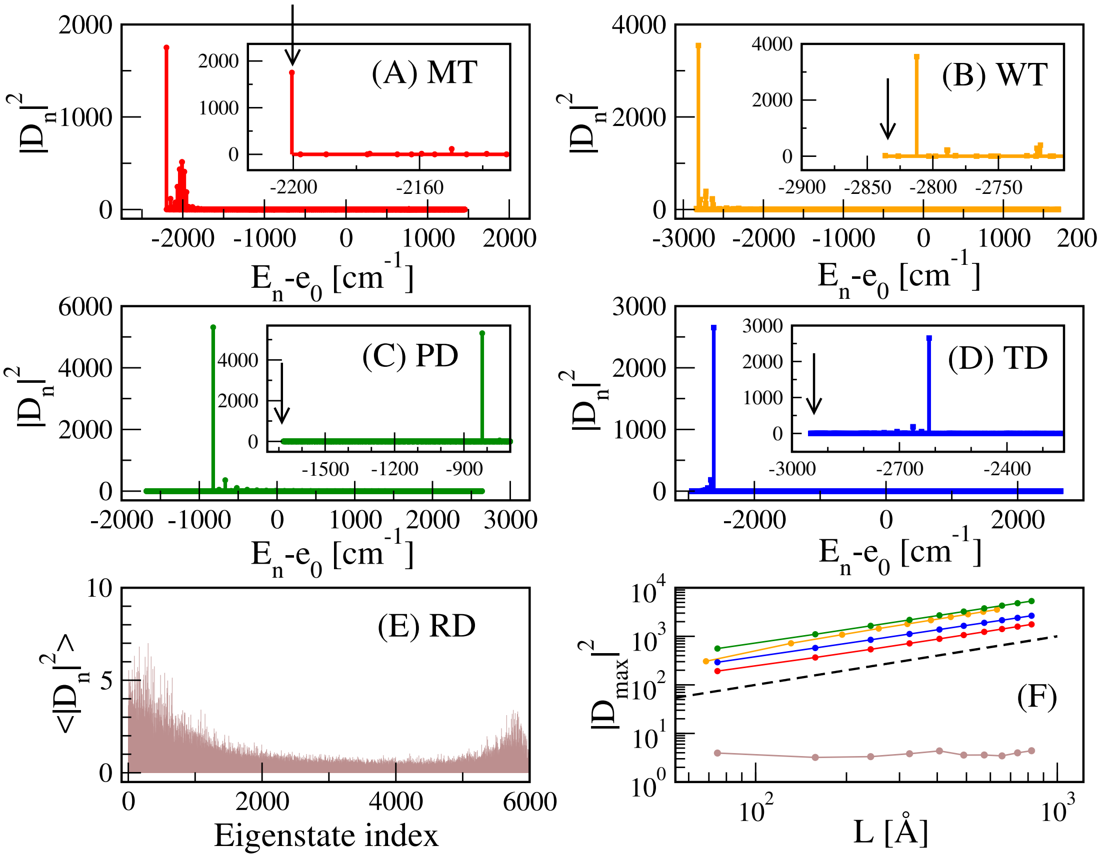

Figure 3.2: (A) - (D) Squared dipole strength $|D_n|^2$ as a function of the energy $E_n - e_0$. Superradiance arises in all cylindrical models since they are characterized by a high degree of geometrical symmetry. However, in the engineered structures made up of parallel and tangent dipoles (panels (C,D)) the SRS does not coincide definitely with the ground state, nor it is close to it. On the other hand, in the MT model (A) the ground state is superradiant while in the WT model (B) the SRS, even if it does not coincide with the ground state, it is indeed very close to it. In panels (A,B,C,D) insets are shown with a magnification of the energy spectrum close to the SRS. In the insets the arrows indicate the position of the ground state. (E) Average squared dipole strength $\langle |D_n|^2 \rangle$ as a function of the eigenstate index. The average has been computed over 10 disorder realizations. (F) $|D_{max}|^2$ as a function of the cylindrical length L. A linear dependence, as given by the dashed line $|D_{max}|^2 \propto L$, emerges clearly from all structures except the RD model (brown). Different colours stand for different models : MT (red), WT (orange), PD (green), TD (blue) and RD (brown). In panels (A-E) we considered cylindrical structures made of 6000 dipoles. In panel (F) we considered cylindrical structures with a number of dipoles varying from 60 to 6000.

As one can see the maximal dipole strength grows $\propto L$ for all models but the random one for which it is independent of L.

3.4.2 Delocalized excitonic states at room temperature

Given a quantum state specified by the density matrix $\hat{\rho}$ it is possible to define its coherence length in the single excitation manifold defined by the basis states $|i\rangle$ [103, 104]:

$$L_\rho = \frac{1}{N} \frac{\left(\sum_{ij} |\rho_{ij}|\right)^2}{\sum_{ij} |\rho_{ij}|^2}. \tag{3.9}$$

The expression of L_ρ in equation (3.9) measures how much a single excitation is spread coherently over the molecules composing the aggregate. To give an idea of its physical meaning let us consider three different simple cases:

- a pure localized state, $\hat{\rho} = |i\rangle\langle i|$; then it is easy to see that the coherence length defined in equation (3.9) is given by $L_\rho = 1/N$. This case represents the minimal value that L_ρ can get.
- A completely delocalized mixed state characterized by the density matrix $\hat{\rho} = (1/N)\sum_{i=1}^{N} |i\rangle\langle i|$. In this case we have $L_\rho = 1$. This state is maximally delocalized in the basis, but it is completely incoherent.
- Lastly we consider the fully delocalized coherent state: $\hat{\rho} = (1/N)\sum_{i,j=1}^{N} |i\rangle\langle j|$. In this case we have $L_\rho = N$. Note that any pure state with constant amplitude $1/\sqrt{N}$ over the sites and arbitrary phases would give the same result.

Generally speaking we can see that $1/N \le L_\rho \le N$. The closer L_ρ is to N, the higher a coherent delocalization can be assigned to our state. In the same way $L_\rho < 1$ indicates an incoherent localized state. States characterized by $L_\rho \sim 1$ have a little ambiguity (since both localization and coherence are measured on the same length scale).

In what follows we will consider the previous models of cylindrical structures and we will compare them with an additional model where the positions of the molecule are the same of the MT model, but their interaction is only nearest-neighbour. In this way we will be able to address the relevance of the range of the interaction to the thermal coherence length. For this purpose, let us consider a variant of the MT model, in which the Hamiltonian matrix elements are defined as follows:

$$H_{NN} = \begin{cases} \sum_{i=1}^{N} e_0 |i\rangle\langle i| + \sum_{i\neq j} \Delta_{ij} |i\rangle\langle j| & \text{if} \quad r_{ij} \le \bar{d}, \\ 0 & \text{if} \quad r_{ij} > \bar{d}, \end{cases} \tag{3.10}$$

where we have introduced the cut-off distance $\bar{d} = 9$ Å and $\Delta_{i,j}$ is defined in equation (3.7). In other words any lattice point interacts only with its four nearest neighbours.

For all the models above we have computed the thermal coherence length at room temperature ($T = 300K$), defined for a state at the canonical equilibrium and whose matrix elements are given by:

$$\rho_{ij} = \sum_n \frac{e^{-\beta E_n}}{\mathrm{Tr}(e^{-\beta \hat{H}})} \langle i|E_n\rangle\langle E_n|j\rangle, \tag{3.11}$$

where $\beta = 1/k_B T$. A very important question to be answered is how much the symmetrical arrangements that give rise to SRS are also able to produce a large thermal coherence length at room temperature. Note that even if we consider the coherence length at thermal equilibrium, this does not mean that out-of-equilibrium processes are not important in molecular nanotubes. Indeed in Ref. [105] strong evidence of ultra-fast transport in natural structures with transfer times less than 100 fs have been discussed. Nevertheless thermal equilibrium can be considered as a worst case scenario for coherences, see also discussion in the conclusions. For this reason assuming thermal equilibrium can be considered a good starting point to assess the structural robustness of quantum coherence to thermal noise.

In that regard we calculate the coherence length L_ρ according to equation (3.9), using a thermal density matrix as in equation (3.11), as a function of the cylindrical length L for each of the cylindrical models studied so far, including the NN model described by equation (3.10).

As a final remark for this Section, let us note that for zero temperature L_ρ depends only on how much the ground state is delocalized, while for infinite temperature we have a fully mixed state with $\hat{\rho} = (1/N)\sum_{i=1}^{N} |i\rangle\langle i|$, so that $L_\rho = 1$ as explained above even if all eigenstates are fully delocalized. On the other hand at finite temperature the thermal coherence length is determined by how much the energy eigenstates are delocalized on the site basis and also on how many eigenstates have an energy approximately within $k_B T$ above the ground state (i.e. from the density of states within an energy $k_B T$ from ground state). For this reason, it is important to study the delocalization properties of the eigenstates of the nanostructures considered here. This analysis is shown in 3.8.4, where we show that the eigenstates of all models but the RD one have fully delocalized eigenstates with a very similar degree of delocalization.

3.4.3 Thermal Coherence Length

It is usually thought that natural photosynthetic structures can support delocalized states even at room temperature because the nearest-neighbour (NN) coupling between the molecules is larger than the room temperature energy $k_B T \approx 200$ cm^{-1}. In Table 3.1 we show the nearest-neighbour coupling for the different models considered here. As one can see these couplings are larger than $k_B T$, and the maximal value between $\Omega_{1,2}$ are of the same order among the different models.

Let us now consider the thermal coherence length of the structures analyzed here at room temperature. Figure 3.3(A) shows the dependence of L_ρ on the cylinder length L

	Ω_1 [cm^{-1}]	Ω_2 [cm^{-1}]
MT	618	248
WT	115	629
PD	610	528
TD	1218	264

Table 3.1: Nearest-neighbour (NN) coupling for the different models. Ω_1: azimuthal coupling for NN sites in the same ring (or between two adjacent chains for the WT). Ω_2: vertical coupling for NN sites between rings (or in the same chain for the WT).

(with a corresponding number of dipoles N ranging from 120 to 9600).
In all models but the RD, the coherence length L_ρ increases quite markedly for small L until it reaches a plateau for larger L values. Apart from the RD structure, that exhibits a coherence length $L_\rho \approx 1$, the other structures are characterized by $1 \leq L_\rho \leq$ N. This means that the thermal state at room temperature of these structures has a high degree of excitonic delocalization. Moreover it emerges clearly that the natural complexes (MT and WT) show the highest values of thermal coherence length if compared with the other engineered structures. It is interesting to note that the MT complex supports a coherent delocalization of the excitation over hundreds of molecules even at room temperature, which is one order of magnitude larger than the delocalization supported by the NN model despite the fact that in the NN model the molecules have the same position and the same nearest-neighbour coupling of the MT model. This shows that the ability of such structures to support large delocalized excitation even at room temperature goes beyond the strength of the NN coupling between their molecules. From Figure 3.3(A) we can also deduce that the large coherence length of the natural systems cannot be explained by the presence of long range interactions. Indeed long-range interactions are present also in the PD and TD models, but their thermal coherence length is one order of magnitude smaller. By comparing the different cylindrical structures, one may also observe that the further the SRS is from the ground state, the lower is L_ρ. One could argue that natural structures concentrate the most radiative states (states with the largest dipole strength) close to the ground state in order to maximize their thermal coherence length. We will discuss the relationship between the presence of the SRS close to the ground state and a large coherence length in the next Section.

The presence of a large thermal coherence length can be related to the structural properties of the energy spectrum. To this end we consider the mean energy density $\delta(k_B T)$ defined as the number of states contained in a unit of thermal energy $k_B T$, i.e.

$$\delta(k_B T) = \frac{1}{k_B T} \int_{E_1}^{E_1 + k_B T} N(E)\, dE, \tag{3.12}$$

where E_1 is the ground state and $N(E)$ is the density of states (number of states per unit energy). In particular, we would like to study the dependence of the average density of states, equation (3.12), on the cylindrical length L. Results are shown in Figure 3.3(B) and they clearly indicate that not only, in general, the average density in-

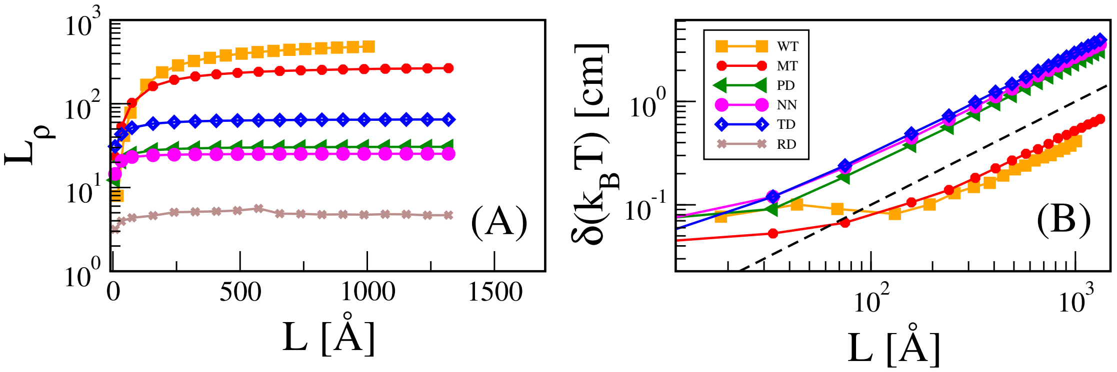

Figure 3.3: (A) Coherence length L_ρ as a function of the cylindrical length in the 6 cylindrical models at $T = 300$ K. The total number of chromophores N varies from 120 to 9600. (B) $\delta(k_B T)$, as given by equation (3.12), as a function of the cylindrical length L at a fixed temperature $T = 300$ K. All models have a total number of dipoles ranging from 120 to 9600. Note that since energy is measured in $[\mathrm{cm}]^{-1}$, the mean energy density in the thermal energy width $k_B T$ is measured in [cm], see equation (3.12).

creases proportionally to L, but, more importantly, natural structures are characterized by the smallest average densities (approximately one order of magnitude less than the other structures). Such a low density of states in the lower part of the spectrum induces, see Figure 3.3(B), an enhanced thermal coherence length. Indeed, if all the eigenstates have approximately the same degree of delocalization, as measured by their PR for instance, then for a smaller number of states within an energy $k_B T$ from the ground state, the thermal coherence length is larger, as explained above. In order to explain the origin of the low density of states, let us observe that: (*i*) it cannot be due to the intensity of the NN coupling. Indeed the NN model, which has the same NN coupling as the MT model, has a much higher density of states and a smaller thermal coherence length; (*ii*) it cannot be due to the range of interaction since also the TD and PD model are characterized by the same interaction range but they display a higher density of states and as a consequence a smaller thermal coherence length. Below we propose an explanation of the connection between the presence of a SRS close to the ground state and a low density of states, implying a large thermal coherence length.

3.5 Relationship between structure and macroscopic coherence

In this section we propose an explanation of why such a low density of states is connected to the presence of SRS close to the ground state of the system. As we will show below, the low energy part of the spectrum for both the MT and WT models arises from a super-transfer coupling between states with a large (giant) dipole belonging to some sub-unit of the whole cylinder. In the case of MT we will show that the super-transfer coupling arises between giant dipole eigenstates of single rings, while in the case of WT the super-transfer arises between eigenstates belonging to different sub-units of the whole cylinder. The presence of super-transfer induces a large coupling energy which decreases the density of states. As a clear signature of this, we show below that super-transfer is also able to induce the emergence of an energy gap between the ground state and the first excited state.

Specifically in section 3.5.1 we analyze cylinders made of a sequence of rings and we show that the symmetry present in the system implies that each eigenstate of a ring couples only to a correspondent eigenstate of the other rings. We also show that the dipole strength of the eigenstates of each ring is concentrated in few superradiant states. In section 3.5.2 we show that the coupling between superradiant states in each ring displays a super-transfer effect, while the coupling between the subradiant states is characterized by a sub-transfer effect. Finally in section 3.5.3 we show how in natural structures the super-transfer coupling produces a depressed density of states close to the ground state, thus enhancing the thermal coherence length.

3.5.1 Structure of ring eigenstates coupling

In order to analyze the super-transfer effect, let us consider the properties of the eigenstates of the single rings composing three different nanotubes: MT, TD and PD. All the above mentioned models are composed of a sequence of rings, each containing 60 molecules, as explained in Section 3.2. The case of the WT model will be discussed later since its structure is more complicated. In Figure 3.4 the dipole strength of few eigenstates (ordered from low to high energy) of a single ring, containing 60 dipoles, is shown for the different structures. Note that the sum of all the dipole strengths must be equal to the number of the dipoles in the ring $N_2 = 60$ as explained in the previous Sections. As one can see in the MT case the whole dipole strength is concentrated in the lowest three eigenstates, each having a dipole strength approximately equal to $N_2/3$. Each dipole strength is oriented in a different spatial position with the ground state having a dipole strength along z corresponding to the direction of the cylinder axis and the other two states perpendicular to it in the ring plane, see inset in Figure 3.4(A). In the TD model in Figure 3.4(B), the dipole strengths are concentrated in the first and second excited state (which are degenerate and having $|D_n|^2 = N_2/2$ each) and their direction lies in the plane perpendicular to the direction of the cylinder axis. Finally for the PD model in Figure 3.4(C), the whole dipole strength is concentrated in the most excited state and it is directed along the z axis (cylinder axis).

A common feature of these structures is their invariance under a $2\pi/N_2$ rotation around the cylinder axis. Strictly speaking, in the MT model such symmetry is slightly broken due to the presence of alternating α angles, see 3.8.1. Nevertheless since α is very small the change due to the symmetry breaking is negligible. As a consequence the Hamiltonian for each ring is a circulant matrix, i.e. each row can be obtained by a cyclic permutation of the previous one. Circulant matrices are diagonalized by the Fourier basis, so that the components of the eigenstates of each ring $|\varphi_q\rangle$ on the site

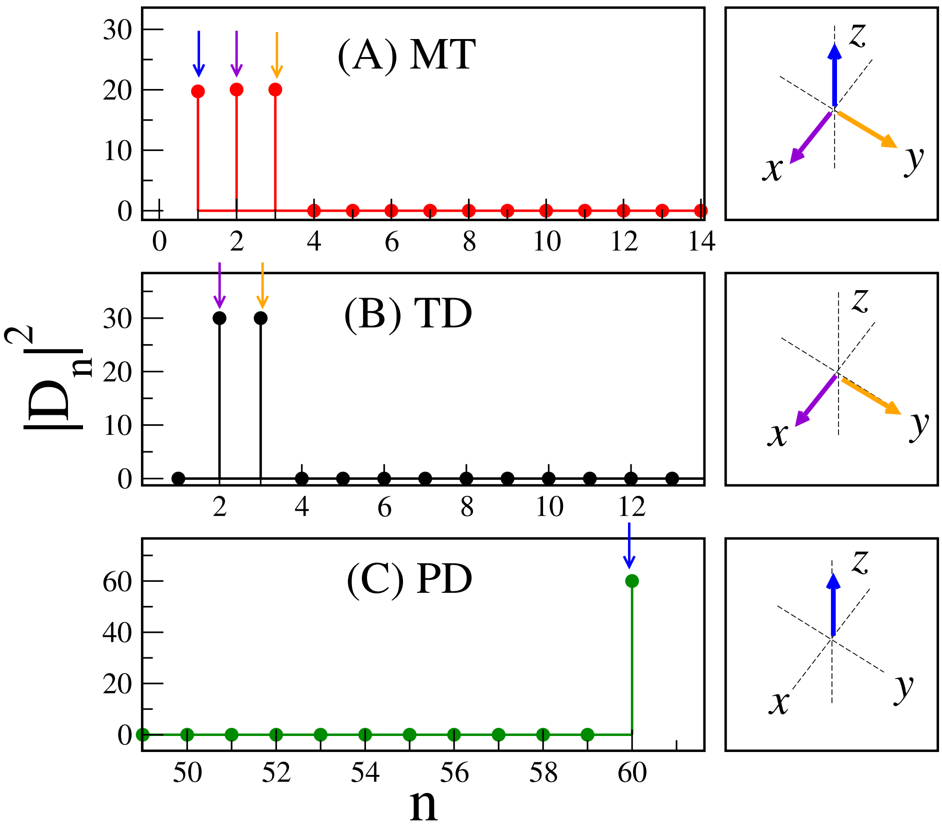

Figure 3.4: Dipole strength of few eigenstates (in the lowest or highest part of the energy spectrum) *vs.* the eigenstate index n, for a single ring composing three different nanotubular structures: MT, TD and PD. Lateral panels indicate the spatial direction of the giant dipoles of the SRS. Each ring of the three structures considered (A,B,C) is composed by $N_2 = 60$ dipoles.

basis $|j\rangle$ are given by

$$\langle j|\varphi_q\rangle = \frac{1}{\sqrt{N_2}} e^{i2\pi jq/N_2} \quad \text{for} \quad q = 1, ..., N_2. \tag{3.13}$$

Due to the rotational invariance the coupling matrix between two rings is also circulant.

To make this point explicit, let us work out a specific example of two rings. The Hamiltonian reads:

$$H_r = \begin{bmatrix} D & V \\ V & D \end{bmatrix} \tag{3.14}$$

where D refers to the Hamiltonian of a single ring (which is diagonal in the Fourier basis given in equation (3.13)) and V represents the interaction between two rings. The total Hamiltonian matrix H_r can be made block diagonal by the matrix

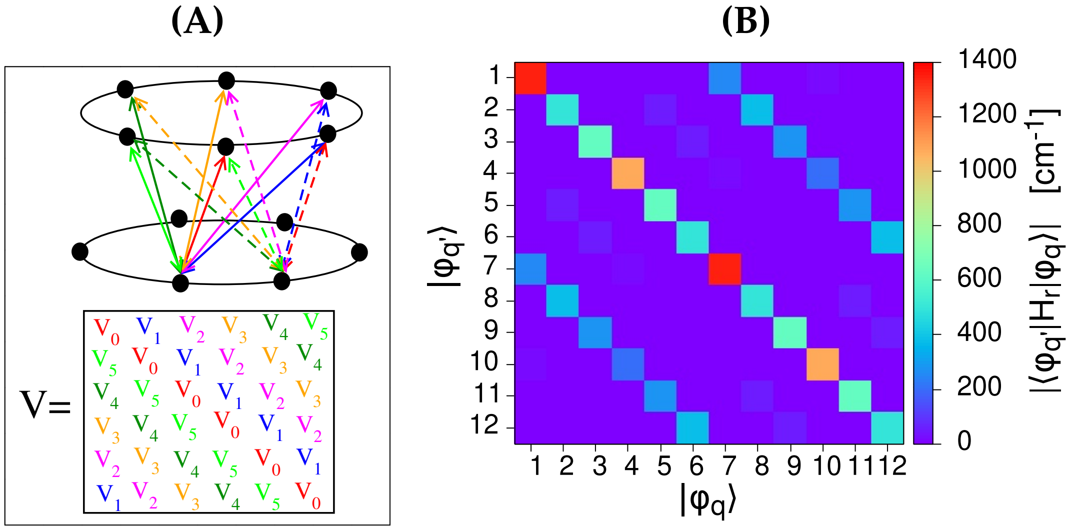

$$V=\begin{bmatrix} V_0 & V_1 & V_2 & V_3 & V_4 & V_5 \\ V_5 & V_0 & V_1 & V_2 & V_3 & V_4 \\ V_4 & V_5 & V_0 & V_1 & V_2 & V_3 \\ V_3 & V_4 & V_5 & V_0 & V_1 & V_2 \\ V_2 & V_3 & V_4 & V_5 & V_0 & V_1 \\ V_1 & V_2 & V_3 & V_4 & V_5 & V_0 \end{bmatrix}$$

Figure 3.5: (A) Graphical representation of the coupling between the sites of two rings, each formed by six molecules. Same colours indicate the same couplings. The circulant coupling matrix V, see equation (3.14), generated by the symmetric coupling is represented below. (B) Modulus of the Hamiltonian H_r (3.14) matrix elements for the MT model, for the case sketched in (A) in the Fourier basis. Each ring eigenstate is mainly coupled only to one corresponding eigenstate in all the other rings.

$$U_r = \begin{bmatrix} U & 0 \\ 0 & U \end{bmatrix}$$

where the elements of U are given by equation (3.13): $U_{j,q} = \langle j|\varphi_q\rangle$. In other words, each ring eigenstate is coupled only with one corresponding eigenstate of any other ring. This is clearly shown in Figure 3.5(B), where the matrix elements of the Hamiltonian of a small cylinder composed of two rings of 6 sites each, are represented in the basis given by the tensor product of the Fourier basis of each ring. As one can see, this results in a block structure where each block has only diagonal elements.

As a consequence of the symmetric structure of the nanotubes considered above, all the eigenstates of the whole cylinder can be "generated" by the coupling between the eigenstates of single rings, see also discussion in [106]. Specifically the SRS of the whole cylinder is generated by the coupling of the SRS of the single rings. In order to prove that, we show in Figure 3.6(A, B, C) the most SRS for the different models projected along the eigenstates of the single rings. In the figure we considered cylinders made of $N_1 = 160$ rings, with $N_2 = 60$ molecules per ring, for a total number of dipoles of $N = 9600$. Let us analyze the single models individually:

1. For the MT model, one can see that the most SRS (having a dipole along the cylinder axis) has components only on the ground states of the single rings (indicated

by arrows in the inset of Figure 3.6(A)) that are also SRS with a dipole strength along the $z-$axis, see Figure 3.4(A).

2. In the PD model, Figure 3.6(B), the most SRS, $|E_{2814}\rangle$, projects itself on the most excited state in the single ring spectrum, which corresponds to the only SRS of the PD ring, see Figure 3.4(C). Note that $|E_{2814}\rangle$ indicates the 2813^{rd} excited state.

3. In the TD model there are two most SRS which are degenerate with a different polarization: one along the x direction and one along the y direction. In Figure 3.6(B) we considered only the SRS with a polarization along the y direction, which corresponds to the state $|E_{1083}\rangle$. Such state has non zero projections only onto the second excited states of the single ring with the same dipole direction of the SRS of the whole cylinder, see Figure 3.4(B). Correspondingly the other SRS with a polarization along the x direction will have projection only on the SRS of the single ring with the same polarization.

These findings allow for a further approximate scheme for the eigenstates of the cylindrical structures considered above. Indeed, since each eigenstate of any single ring is coupled only to a corresponding eigenstate of the other rings, we can decompose the whole cylinder into independent chains where each site of the chain corresponds to a single ring eigenstate. For a chain having N_s sites and nearest-neighbour interactions the eigenstates are independent of the coupling and given by:

$$\langle k|\psi_r\rangle = \sqrt{\frac{2}{N_s+1}}\sin\left(\frac{\pi k r}{N_s+1}\right), \tag{3.15}$$

where k represents the site index and $r = 1, .., N_s$. Clearly, when the interaction range is not nearest-neighbour, the above expression for the eigenstates is no longer valid. Nevertheless for the natural structures considered in this chapter the interaction is short-range, decaying as $1/r^3$ for the realistic cylinder length considered here, so that in a first scheme we can consider the nearest-neighbour eigenstates as a good approximation. Note however that care should be taken to generalize such approximation since the interaction between the molecules is much more complicated than a simple dipole-dipole one. For instance the coupling is also affected by the dipole strength of the ring eigenstates involved as we will see below. Nevertheless we can assume that the chain of eigenstates is diagonalized by the same eigenstates of a chain with nearest-neighbour coupling for the parameters and the realistic system sizes considered here. Building the eigenstates as a tensor product between the Fourier basis for the ring (3.13) and the one for the chain (3.15)

$$\langle j,s\rangle\, \Psi_{q,r} = \frac{1}{\sqrt{N_2}} e^{i2\pi jq/N_2} \sqrt{\frac{2}{N_1+1}}\sin\left(\frac{\pi s r}{N_1+1}\right) \tag{3.16}$$

(with $j,q = 1,\dots,N_2$ and $s,r = 1,\dots,N_1$) we can diagonalize the Hamiltonian of the whole cylinder in order to obtain an approximation of the actual spectrum of the whole

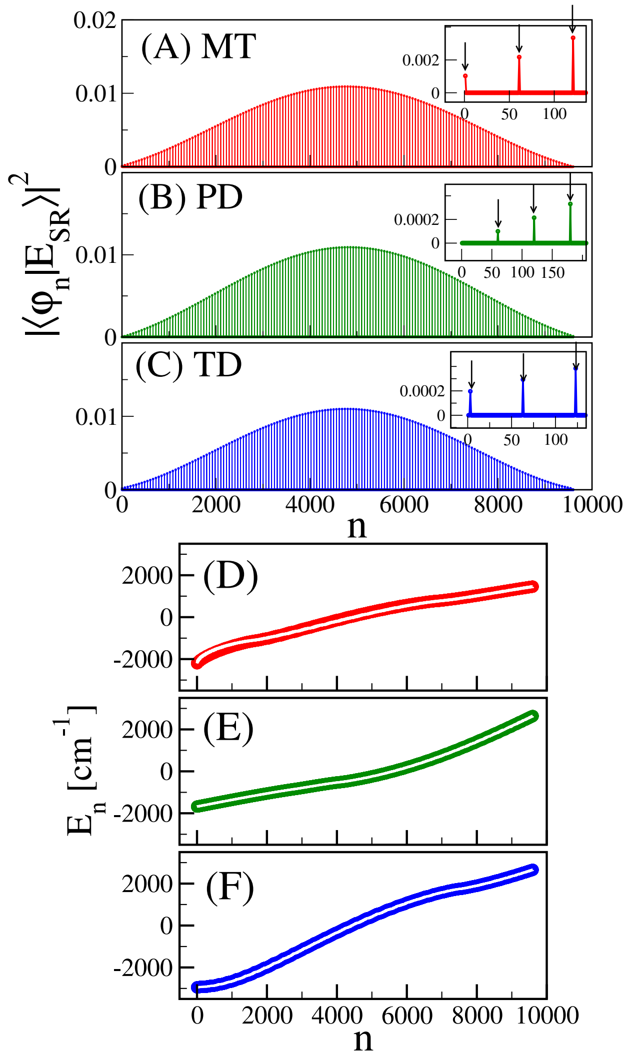

Figure 3.6: Left Panels: Projections of the most SRS of the whole cylinder $|E_{\mathrm{SR}}\rangle$ over the single ring eigenstates $|\varphi_n\rangle$ as a function of the eigenstate index n. In each case we selected a total number of dipoles $N = 9600$ (then n= 1, ..., 9600), which corresponds to $N_1 = 160$ rings and $N_2 = 60$ molecules in each ring. (A) MT model, (B) PD model, (C) TD model (in the insets the corresponding blow up of the low energy part of the energy spectrum). Arrows refer to the SRS of the single rings. Right Panels: energy spectrum of the three different cylindrical structures: (D) MT model, (E) PD model, (F) TD model. Coloured symbols represent the exact numerical spectrum, white lines stand for the spectrum obtained from the analytic approximate eigenstates, see equation (3.16).

structures. The results are shown in Figure 3.6(D, E, F) where the spectrum obtained from exact numerical diagonalization is compared with the spectrum obtained by diagonalizing the matrix with the eigenbase in equation (3.16). As one can see, the proposed analytic basis gives an excellent approximation of the spectrum obtained by exact numerical diagonalization.

3.5.2 Super and Sub-Transfer

In the previous section we have shown that each eigenstate of a single ring couples only with a corresponding eigenstate of the other rings (apart for a small symmetry breaking factor present in the MT model). Here we will show that the coupling between the eigenstates with a large dipole strength is enhanced with respect to the coupling between the single molecules within each ring by a factor proportional to the number of molecules placed on each ring. Such effect is known in literature as super-transfer [7]. At the same time we will show that the coupling between the eigenstates of the single rings with a small dipole strength is suppressed with respect to the coupling between the single molecules, giving rise to another collective sub-transfer effect, which has not been fully addressed in literature.

In order to prove the previous statements, let us compute the coupling strength between two eigenstates of two rings, say 1 and 2. Let us indicate the two corresponding q-th eigenstates of the two rings as

$$|\psi^{s,q}\rangle = \sum_k C_k^{s,q} |k\rangle,$$

where the states $|k\rangle$ represent the site basis of a ring and $s = 1, 2$. The coupling between two single ring eigenstates belonging to two different rings can be written as:

$$V_{12}^q = \langle \psi^{1,q} | V | \psi^{2,q} \rangle = \sum_{k,k'} (C_k^{1,q})^* C_{k'}^{2,q} V_{k,k'}. \tag{3.17}$$

Using equation (3.7) we have $V_{k,k'} = \Delta_{k,k'} = f(r_{k,k'}) \vec{\mu}_k \cdot \vec{\mu}_{k'} + g(r_{k,k'})(\vec{\mu}_k \cdot \hat{r}_{k,k'})(\vec{\mu}_{k'} \cdot \hat{r}_{k,k'})$. When the distance between the two rings is much larger than their diameter we can approximate $r_{k,k'} \approx R_{12}$ where R_{12} is the distance between the centres of the two rings. In this limit, equation (3.17) becomes

$$V_{12}^q = \sum_{k,k'} (C_k^{1,q})^* C_{k'}^{2,q} \left[f(R_{12}) \vec{\mu}_k \cdot \vec{\mu}_{k'} + g(R_{12}) (\vec{\mu}_k \cdot \hat{R}_{12})(\vec{\mu}_{k'} \cdot \hat{R}_{12}) \right] , \tag{3.18}$$

which can be expressed in terms of the dipole strengths using equation (3.6)

$$V_{12}^q = \left[f(R_{12}) |\vec{D}_q|^2 + g(R_{12}) (\vec{D}_q \cdot \hat{R}_{12})(\vec{D}_q^* \cdot \hat{R}_{12}) \right] . \tag{3.19}$$

As a result, we obtain $V_{12}^q \propto |D_q|^2 \propto N_2$. In other words the eigenstates with a large dipole strength will have a coupling enhanced by a factor proportional to the number of molecules N_2 in the ring.

The above expression represents the interaction between the giant dipoles of the eigenstates of each ring. Therefore states with a large dipole strength will have a super-transfer coupling (proportional to the dipole strength of the eigenstates), increasing

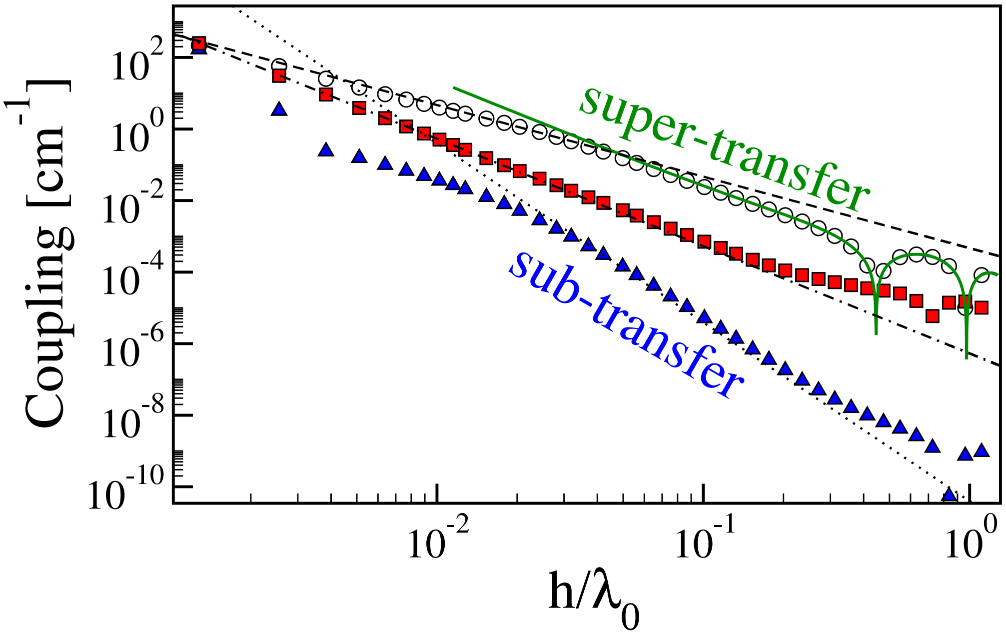

Figure 3.7: Coupling between ring eigenstates as a function of their distance h normalized to the wavelength $\lambda_0 = 650$ nm. Open circles represent the coupling V_{12}^{q} (see equation (3.17)) between the ground states of two rings for the MT model. Red squares stand for the maximal coupling between individual molecules in the two rings. Blue triangles represent the coupling between the most excited eigenstates of the two rings. Green curve represents the coupling between the giant dipoles of the ground states as given by equation (3.19). The three lines represent respectively the behaviours $1/r^2$ (dashed), $1/r^3$ (dot-dashed), $1/r^5$ (dotted).

linearly with the number of molecules N_2 in each ring. At the same time, the coupling between two eigenstates with zero dipole strengths will be suppressed, leaving only higher order multipole terms to contribute to the coupling. This will lead to a sub-transfer coupling. The super and sub-transfer effects for the MT model are shown in Figure 3.7 where we compare: (i) the coupling between the superradiant ground states (which have a large dipole strength) of two rings as a function of their rescaled distance (open circles); (ii) the maximal coupling between single molecules of each ring as a function of the distance between the two rings (red squares); (iii) the coupling between the most excited states (with a very small dipole strength) of each ring as a function of their distance (blue triangles).

Let us comment this figure in detail. First of all we note that the coupling between the states with a large dipole is clearly larger (by a factor $\sim N_2 = 60$) than the maximal coupling between the single molecules thus showing the super-transfer effect. Moreover, the coupling between the eigenstates with a small dipole strength is much smaller than the maximal coupling between single molecules: this shows the sub-transfer effect.

In the same figure, as a continuous green curve we show the coupling between the ground states as given by equation (3.19). As one can see, at sufficiently large distance, the couplings are well approximated by equation (3.19) thus confirming that the coupling is enhanced by a factor proportional to the number of molecules in each ring N_2.

Another important observation concerns the dependence of such couplings from the distance $r = h/\lambda_0$ and how it is modified by the super and sub-transfer effect. We can distinguish three different regimes: at small distances, at intermediate distances and at distances comparable with the wavelength of the optical transition. At large distances, when $h \sim \lambda_0$ an oscillatory behaviour arises due to the presence of oscillatory terms in the Hamiltonian of the system, see equation (3.7). At intermediate distances the super-transfer coupling decays with $1/r^3$ as the coupling between single molecules, consistently with the dipole-dipole nature of the interaction. On the other hand, the sub-transfer coupling decays as $1/r^5$ which is consistent with high order multipole expansion of the coupling since the dipole interaction is suppressed. At small distances the behaviour of the coupling with distance is less trivial: while the single molecule coupling still behaves as $1/r^3$, the sub-transfer coupling decays much faster and then it goes as $1/r^5$ as explained above. On the other hand the super-transfer coupling decays as $1/r^2$, which is much slower than the dipole coupling. Since all the couplings start from the same intensity at very small distances and the superradiant one has to go above the single molecule coupling, it makes sense that its decay is slower than $1/r^3$, but further analysis is needed to understand the origin of such slow decay of the interaction between giant dipoles.

3.5.3 Super-Transfer and density of states

From the discussion above we can conclude that all the SRS belonging to each ring will couple between themselves through a super-transfer coupling. For instance, in the case of the MT model, also the other two SRS of the single rings corresponding to the first and second excited states will couple between themselves by super-transfer, see Figure 3.4(A). While for the PD and the TD model the coupling between the SRS of the rings gives rise to the SRS of the whole cylinder which lies far away from the ground state, for the MT model the coupling between the SRS of the single rings determines completely the lowest part of the spectrum. In order to prove the last sentence we consider the $3N_1$ eigenvalues generated by the super-transfer coupling of the three SRS for each ring of the MT model. The spectrum generated by the three SRS is shown in Figure 3.8(A) together with the exact spectrum of the MT model. As one can see this simple approximation allows to compute with high accuracy the lowest energy part of the spectrum. The presence of super-transfer induces a large coupling energy in the lowest part of the spectrum, which in turn diminishes the density of states. This is also signaled in Figure 3.8(A) by the change of slope seen in the lower part of the spectrum. A further evidence of such decreased density of states induced by the super-

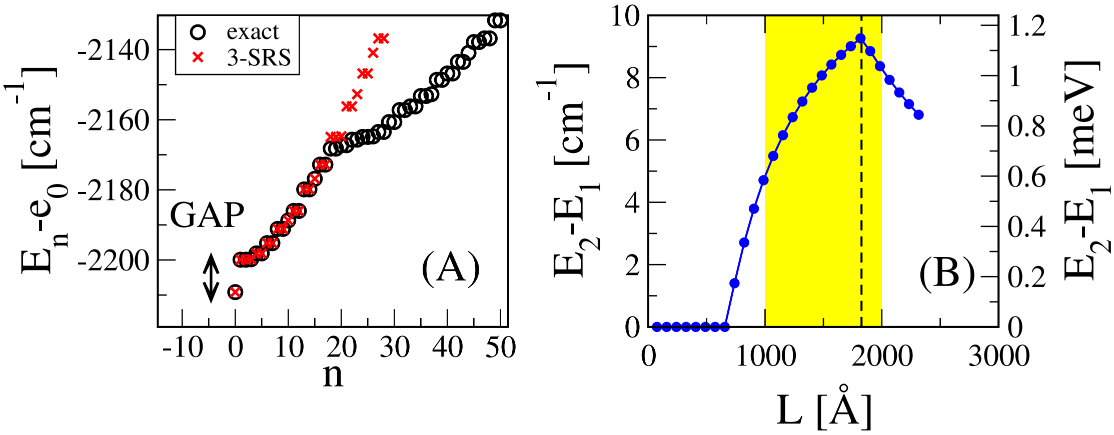

Figure 3.8: (A) The lowest part of the energy spectrum for a MT nanotube with 220 rings (open circles) compared with the spectrum generated by the super-transfer coupling between the the three most SRSs of each ring (crosses). Note the presence of a consistent energy gap between the ground state and the first excited state. (B) Energy gap (distance between the ground and the first excited state) for the MT model as a function of the nanotubular length. As one can see there is a region where the gap increases with the system size. Maximal gaps occurs at $L = 1826$ Å. The yellow vertical strip indicates the region where natural complexes operate.

transfer coupling of the SRS of each ring is shown in Figure 3.8(B). Here the energy gap between the ground state and the first excited state for the MT model is shown as a function of the length of the nanotube. Contrary to what can be expected for generic systems, the energy gap increases with the system size instead of decreasing, up to a critical system size, above which it decreases. The maximal energy gap occurs at a distance of $\sim$ 182.6 nm which is compatible with the typical length of such nanostructures found in nature, ranging between 100 and 200 nm. Note that it would be interesting to understand the critical system size at which the gap has a maximum. We intend to study this problem in a future work.

The results obtained so far can be generalized to more complicated structures, such as the WT model, as the preliminary results shown in 3.8.5 show. Indeed even for the WT model, where the disposition of dipoles is much more complicated than in the previous models, one can show that the superradiant state close to the ground state emerges from the supertransfer coupling between the superradiant states of cylindrical sub-units of the whole cylinder.

Summarizing, the analysis both for the MT and the WT models show how a precise ordering of the dipoles in these systems can favour the emergence of super-transfer between the eigenstates of sub-units of the whole structure, producing an enhancement of the thermal coherence length. This represents a clear example of the interplay between structure and functionality. Moreover, let us notice that even if the other models (TD, PD) have a super-transfer coupling between the ring eigenstates with the largest dipole strength, the resulting SRS lies in the middle of the spectrum and its effect on the thermal coherence length is less relevant (since the latter is sensitive to the density of states only in the lowest part of the energy spectrum). This argument strongly supports the relationship between the presence of a SRS close to the ground state and the thermal coherence length discussed above. As a last remark, we would like to mention that in order to assess the ability of such structures to sustain a large macroscopic coherence length, also the effect of other sources of noise should be considered. A preliminary study of the effect of static energetic disorder on the thermal coherence length of the different models considered here is shown in 3.8.6. The results of our analysis clearly show that natural structures are able to protect macroscopic coherence up to values of the static disorder strength much larger than the typical disorder present in natural systems.

3.6 Natural concentric structures

Natural antenna complexes in Green Sulphur Bacteria are not made by a single cylindrical surface. In order to take this into account, in this section we investigate a more complex configuration of dipoles on four concentric rolls as found in Green Sulfur bacteria *Chlorobium Tepidum*. Such structures have been extensively considered in literature (see for example [55, 93, 107, 108]). Inspired from these studies we considered here a model of *Chlorobium Tepidum* Triple mutant (bchQRU) formed by four concentric cylindrical surfaces, as shown in Figure 3.9(A). Our aim is to investigate whether concentric cylindrical aggregates can support delocalized excitonic states at room temperature more efficiently than single cylindrical structures.

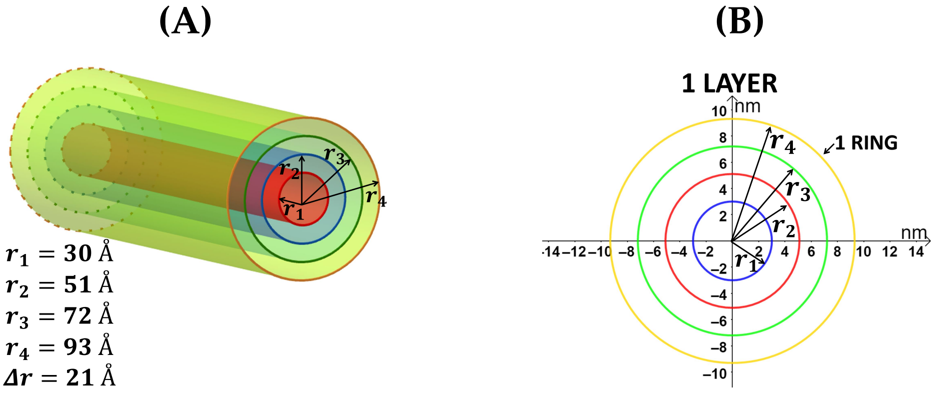

Figure 3.9: (A) Structure of an aggregate of Bchl molecules on four concentric rolls. The radius of the innermost roll is 30 Å, while the distance between consecutive layers is equal to 21 Å. (B) Single layer of the structure formed by four concentric rings. The whole aggregate has been obtained by overlying 100 layers [56].

The distribution of the dipoles on each cylindrical surface is the same as the MT model of the previous section. In Table 3.2 we report all parameters for this model.

Number of surfaces	4
Radius of the innermost roll	30Å
Distance between concentric rolls	21 Å
Radii of the cylinders	$30 - 51 - 72 - 93$ Å
Number of dipoles on each ring	$30 - 51 - 72 - 93$
Density (number of dipoles over radius of the ring Å)	1 constant value

Table 3.2: Main parameters used to engineer the structure with four concentric rolls.

The coupling between the EMF and the dipoles of the aggregate has been taken into account as in the Hamiltonian (3.7). As in the previous sections let us first analyze the dipole strengths associated with the eigenstates of the Hamiltonian (3.7).

Results are shown in Figure 3.10(A) for a complex made of 80 layers of 4 concentric rings. As one can see the maximal dipole strength is concentrated in an energy region close to the ground state (the 43^{rd} eigenstate has the maximal dipole strength, see inset in Figure 3.10(A)).

Such dipole strength is associated with eigenstates having a high degree of delocalization along the cylinders. A further evidence is given in Figure 3.10(B) where we show that the maximal dipole strength increases proportionally with the length L of the cylinders. We also note that the maximal dipole strength for concentric cylinders is between twice and 3 times larger than the maximal dipole strength of a single cylindrical surface with the same geometry, see Figure 3.10(B) where the same data of Figure 3.2(F) for the MT model have been reported for comparison. Note that the fact that concentric cylindrical surface can cooperate to create a larger SRS is not trivial since the interaction between molecules in different cylinders is very weak, of the order of 16 cm^{-1} which is one or two orders of magnitude smaller than the coupling between molecules inside each cylinder, see Table 3.1.

Finally, we have studied the effect of thermalization by putting the system in a thermal bath at room temperature $T = 300$ K. As before, we studied the thermal coherence length L_ρ, see equation (3.9).

Results are shown in Figure 3.11(A) and compared with the same results obtained for the MT model. A fitting with the function

$$L_\rho = L_\infty \left(1 - e^{-N/N_c}\right), \tag{3.20}$$

shown in figure as dashed lines, gives for the asymptotic coherence length (measured in number of layers) $L_\infty = 532.9$ for the 4 cylinders and $L_\infty = 249.8$ for the MT model. Keeping in mind that the radius of the cylinder for the MT model is an average of the four radii of the structure composed of 4 concentric cylinders, it is remarkable that the asymptotic coherence length is more than twice larger than the single cylindrical structure. This is highly non trivial, since for the concentric cylinders we have many

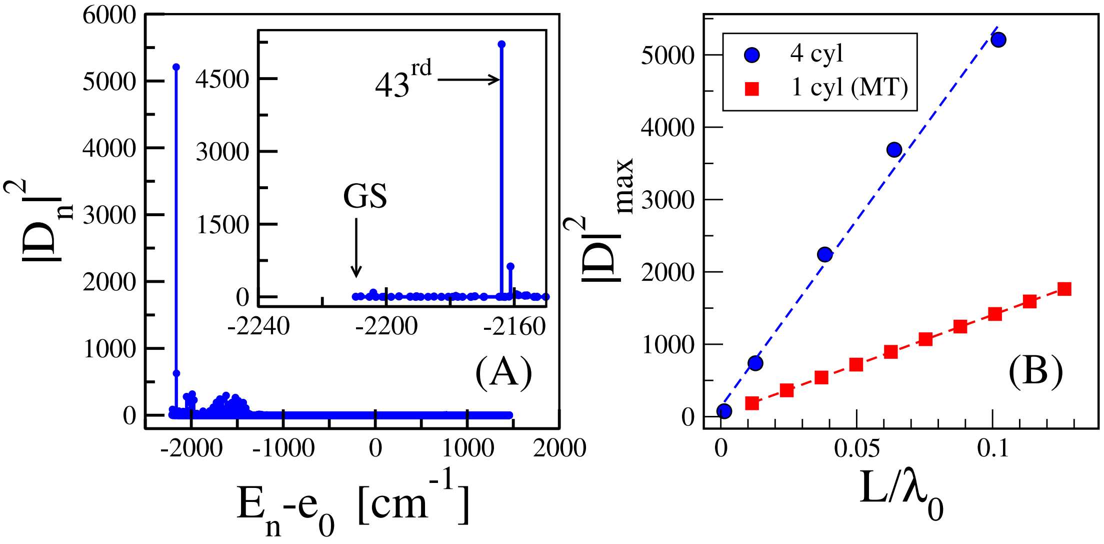

Figure 3.10: (A) Dipole strength associated with each eigenstates of the system composed of 80 layers of 4 concentric rings (a total of $N = 19680$ dipoles) for a total length of $L = 65.57$ nm, as a function of the eigenvalues. Inset : the low energy part of the spectrum. Arrows indicate the Ground State (GS) and the state with maximal dipole strength (the 43rd one). (B) Maximal dipole strength as a function of the rescaled length of the aggregate L/λ_0 where $\lambda_0 \approx 650$ nm. Dashed line represent the linear fits. Maximal length considered in this panel is $L = 65.57$ nm, corresponding to 80 layers of 4 concentric rings, for a total of $N = 19680$ dipoles.

more states and the density of states is larger than that for the single cylinder having the same length. For a discussion on this point see 3.8.7.

The results in this Section show that packing symmetrical structures in concentric cylinders as it is found in natural photosynthetic complexes produces, at room temperature, a larger thermal coherence length than a single cylinder. In the future it would be important to study the robustness of the thermal coherence length of such aggregate of concentric cylinder to other sources of noise, such as static disorder, as it has been done for the single cylinders in 3.8.6. Even if the coupling between molecules belonging to different cylinders is quite weak, supertransfer coupling between sub-structures of the different cylinders might help to protect the coherence length of the whole aggregate to disorder. More analysis is needed to assess this point.

3.7 Conclusions and Perspectives

We have analyzed realistic structures of self-aggregated molecular nanotubes of chlorophyll molecules as found in Antenna Complexes of Green Sulfur Bacteria. By taking into account position and dipole orientation of chlorophyll molecules which agree with experimental data we have shown that natural structures are able to support macro-

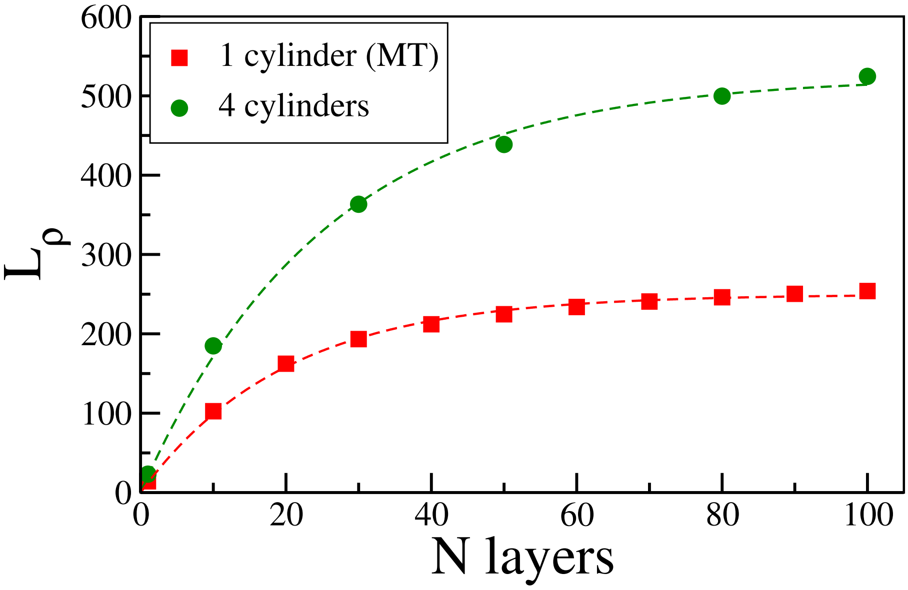

Figure 3.11: Thermal coherence length as a function of the number of layers in the cylinder for the system with four concentric cylinders (green circles) and the MT model with one cylinder only (red squares). Dashed lines are the fit with the expressions (3.20) whose parameters are $L_\infty = 249.8$ and $N_c = 19.9$ for the dashed green curve and $L_\infty = 523.9$ and $N_c = 25.2$ for the dashed red curve.

scopic coherent states even at room temperature. Indeed in natural complexes we have found delocalized thermal excitonic states with a coherence length extending over hundreds of molecules. We show that such thermal coherence length is much larger than that one could expect from the magnitude of the nearest-neighbour coupling and it cannot be explained even by the long-range nature of the interaction between the molecules. Instead, the ability of natural structures to support a large coherence length can be traced back to their specific geometric features.

In order to explain how this is possible, we first considered cylindrical structures made of a sequence of rings, each containing a fixed number of molecules equally spaced on the ring itself. Since the disposition of the dipoles is highly symmetric, in each ring we have few superradiant eigenstates (to which we associate a giant dipole) where most of the dipole strength of the system is concentrated, and many subradiant states with zero dipole strength. Moreover, due to the discrete rotational symmetry of the whole cylinder around its axis, each eigenstate of the ring sub-unit is coupled only with the correspondent eigenstate in the other rings. The coupling between the superradiant eigenstates in each ring gives rise to the super-transfer effect, i.e. a coupling which is enhanced by a factor proportional to the number of molecules in the ring. At the same time we have shown that the coupling between the subradiant states in each ring induces a sub-transfer effect, i.e. a suppressed coupling compared to the single molecule coupling. We have also demonstrated that in natural complexes the super-transfer coupling between the superradiant states in each ring generates the lower part of the energy spectrum of the whole cylinder. Since the spectral energy width of a system is proportional to the intensity of the coupling between its parts, the enhanced super-transfer coupling is able to increase the spectral width close to the ground state. This creates a depressed density of states in the lower part of the spectrum, allowing for a larger thermal coherence length. Indeed the latter increases as the number of states in an interval $k_B T$ above the ground state decreases. We also gave evidence that similar mechanisms are responsible for the large thermal coherence length that we have found in other natural structures (WT model) where the disposition of the dipoles is less simple than the one described above.

From our results we can predict that symmetry in cylindrical molecular nanotubes is essential to have robust structures, not only to thermal noise, as we have demonstrated here, but also to other sources of noise such as static disorder, as our preliminary results have shown. The structural requirement is to create a super-transfer coupling between the superradiant eigenstates of cylindrical sub-units able to generate the lower part of the spectrum of the whole structure.

Molecular nanotubes are fundamental structures in biological systems and they are among the most promising structures to be used in quantum devices. The most important message which can be extracted from our analysis is the fact that specific geometric features, connected to symmetries, allow to control the cooperative effects in molecular aggregates. Indeed it is due to the presence of such cooperatively enhanced coupling (super-transfer) inside the molecular aggregates that macroscopic coherent states are allowed to survive at room temperature. This is an emergent property of such structures which cannot be reduced either to the intensity of the coupling between the molecules, or to their interaction range.

The relevance of geometry in molecular aggregates and the emergent properties arising from it are fundamental to understand even more complicated structures. For instance, structures made of few concentric cylinders as they are found in Green Sulphur bacteria. Our preliminary study of such structures has shown that these aggregates have an enhanced thermal coherence length compared to the single cylindric surfaces. We would like to mention that recently, excitonic states have been analysed also in Microtubules [68], which are molecular nanotubes thought to be involved in many cellular functions. The analysis have confirmed the role of symmetry and geometry in such structures too. In the future it would be important to understand the general structural requirements necessary to induce macroscopic coherent states in generic molecular networks.

Finally, few clarifications are in order. Experimentally the presence of macroscopic coherence in molecular nanotubes can be verified by studying the absorption spectrum at room temperature. Also the role of Super and Sub-transfer can be detected experimentally analyzing the dynamics of exciton transfer. Super and subtransfer could be detected either controlling the initial state or by studying the long-time dynamics of the excitation transfer. In particular this study should reveal the presence of two different time scales (super and sub-transfer) in a similar way as the study of long-time excitation decay reveals super and sub-radiance, where sub-radiance implies a change of slope in the decay of the survival probability. For instance a time dependent diffusion coefficient might be an experimental signature of super and sub-transfer.

Even if we assumed thermal equilibrium in our structural analysis, it is possible that out-of-equilibrium processes can have an important role in molecular nanotubes. Indeed cooperative effects can induce time scales in a system which are faster or comparable with thermal relaxation time scales. We believe that the assumption of thermal equilibrium made in this chapter is adequate to assess the structural robustness of molecular nanotubes. Indeed thermal equilibrium represents a worst case scenario for coherence and out-of-equilibrium processes should be characterized by even larger excitonic coherence lengths. For instance the initial state after the absorption of light is characterized by a very large coherence length due to the large wave-length (≈ 700 nm) of the absorbed light with respect to the size of molecular nanotubes (≈ 200 nm). After absorption the coherence length will decrease due to thermal relaxation, reaching its minimal value at thermal equilibrium. Thus processes which occurs out-of-equilibrium will be characterized by a larger coherence length.

The analysis presented in this chapter is structural, and it has been made under the assumption of thermal equilibrium. The emergence of a macroscopic coherence length in molecular nanotubes even at room temperature is likely to have important consequences at the functional level. Indeed a large coherence length allows for excitonic giant dipoles to superabsorb light and to supertransfer excitations, thus enhancing the exciton diffusion coefficient. These effects have been studied in several realistic systems and are thought to play an important functional role in natural photosynthetic complexes. The results presented in this chapter could explain the large efficiency of some natural photosynthetic complexes and inspire the engineering of efficient molecular aggregates for energy transport and light-harvesting. In perspective we plan to assess the functional role of macroscopic coherence in molecular aggregates both in equilibrium and out-of-equilibrium processes.

3.8 Appendix

3.8.1 Geometry of the models

We analyzed five different cylindrical models with fixed radius ($R = 60$ Å) and total number of chromophores N, as shown in Figure 3.12(A). These models differ for the geometrical arrangement of the chromophores (dipoles) along the cylindrical surface.

In order to describe how the dipoles are placed on the cylindrical surface let us wrap it up on a rectangular plane. In this plane the dipoles are disposed on the vertices of a lattice. The unit cell of the lattice in all structures is created starting from two lattice parameters a and b arranged in such a way that the angle between them is γ, see Figure 3.12(B). Depending on the particular arrangement of the unit cell in the lattice the dipoles can be arranged into vertical chains or placed onto equal horizontal and coaxial rings. We assume that, in each of these structures, the shortest distance

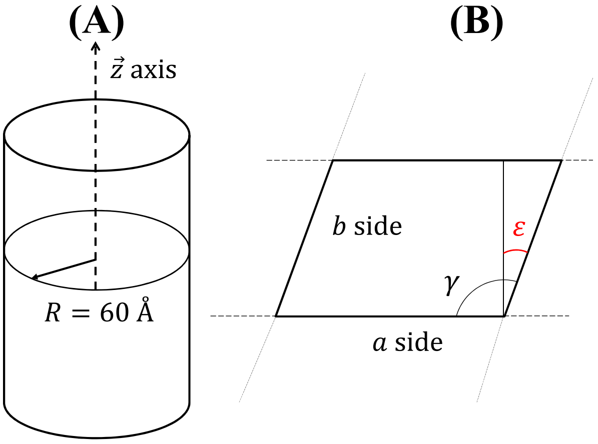

Figure 3.12: (A) Schematic cylindrical structure of each model. The cylindrical axis corresponds to the $\vec{z}$ axis and the radius is $R = 60$ Å. (B) Fundamental unit cell of the analyzed aggregates. One may obtain each of the models varying the three parameters a, b and γ. In our models we consider only the cases in which a and $\vec{z}$ are orthogonal or parallel.

between two chromophores located on the same ring is $r_1 = 6.28$ Å. In our scheme all chromophores can be treated as dipoles with a constant squared dipole moment $|\mu|^2 = 30\,\mathrm{D}^2$ [100]. This corresponds to a dipole length $L_d = 1.14$ Å [3]. The ratio $L_d/r_1 \simeq 0.18$ is relatively small so that the dipole approximation can be successfully applied for the nearest-neighbor coupling.

In the following subsections we will analyze in details the geometrical structures associated with each model.

MT model

The MT model proposed here coincides with the Chlorobium Tepidum bchQRU triple mutant investigated in other studies ([92, 93, 95]).

In the MT cylindrical structure, the total number N of chromophores is organized into N_1 equal, horizontal and coaxial rings, see Figure 3.1(A). Each ring contains $N_2 = 60$ chromophores and two consecutive rings are separated by a vertical distance $h = 8.3$ Å. In the unit cell, shown in Figure 3.13(A), h is parallel while a is perpendicular to the

---

[3] In terms of ESU-CGS and Gaussian units one may observe that $1\ \mathrm{D} = 10^{-6}\ \mathrm{cm\ g}^{1/2}\ \mathrm{s}^{-1}\ \mathrm{Å}^{3/2}$ and the elementary charge is $|e^-| = 4.80320425 \cdot 10^{-10}\ \mathrm{cm}^{3/2}\ \mathrm{g}^{1/2}\ \mathrm{s}^{-1}$. From the relation $L_d = \mu/e^-$ we obtain $L_d = 1.14$ Å.

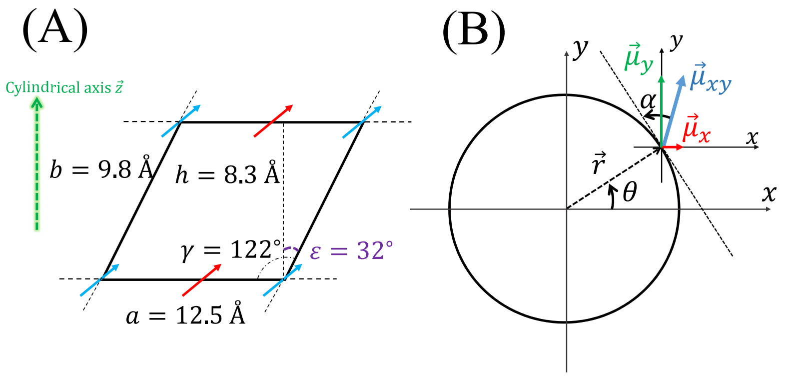

Figure 3.13: (A) Unit cell for the MT model. Here $h = 8.3$ Å is the vertical distance between two consecutive rings. The cylindrical axis $\vec{z}$ is represented by the green arrow on the left and is perpendicular to the a side. Note that the alternation between the colours of two consecutive dipoles along the a and the b sides is due to the alternation $\alpha = \pm 4°$.(B) View from above of the single ring of the MT type. $\vec{\mu}_{xy}$ is the projection of the dipole $\vec{\mu}$ onto the xy plane.

cylindrical axis $\vec{z}$. Any chromophore along the surface will be labelled as the n_2^{th} dipole on the n_1^{th} ring (where $n_1 = 1, ..., N_1$ and $n_2 = 1, ..., N_2$). Since we keep the radius R fixed, the density of chromophores along each ring is also fixed: $\rho_s = (2\pi \text{Å})^{-1}$. The position of each dipole onto the cylindrical surface is characterized by two cylindrical coordinates. Nevertheless it is useful to introduce three angles (the latter being dependent on the first and second):

- $\varphi = 360°/N_2 = 6°$ is the azimuthal angle between two adjacent dipoles in the same ring,
- $\xi = h \tan \varepsilon / R \simeq 4.956°$ is the shift angle between two successive dipoles located onto neighbour rings,
- $\theta = n_1 \xi + n_2 \varphi$ is the angle between the position $\vec{r}$ of the dipole and the x axis.

In this way we have :

$$\begin{aligned} r_x &= R \cos \theta \\ r_y &= R \sin \theta \\ r_z &= h n_1 \end{aligned} \tag{3.21}$$

The components of the dipole moment $\vec{\mu}$ can be expressed through two angles:

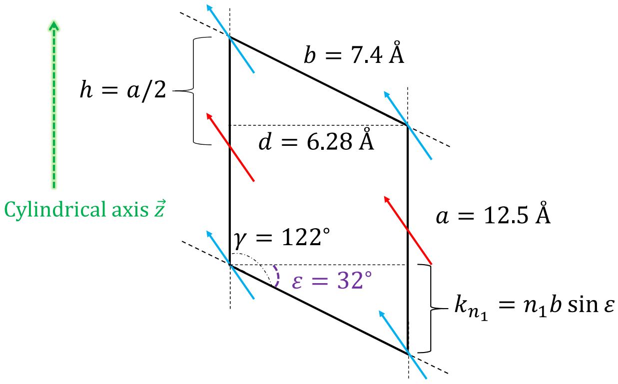

Figure 3.14: Unit cell for the WT model. Here k_{n_1} refers to the vertical shift of two dipoles belonging to two nearest-neighbour chains, while d is the distance between two chains. Two consecutive dipoles on the same chain are separated just by a quantity equal to $a/2$. One can notice that this unit cell is the rotation by 90° around $\vec{z}$ of the previous unit cell for the MT model (Figure 3.13), but with different parameters. The alternation of two colours of two consecutive dipoles along the a and the b direction represents the typical alternation $\alpha = \pm 4°$.

- $\alpha = 4°$, between the projection of the dipole moment onto the plane of the ring and the plane tangent to the cylindrical surface, see Figure 3.13(B).
- $\beta = 55°$, is the angle created by the single dipole moment with the cylindrical axis.

Assuming the n_2^{th} dipole with an angle $\alpha = +4°$, the $(n_2+1)^{th}$ dipole will have $\alpha = -4°$, the $(n_2+2)^{th}$ dipole $\alpha = +4°$ and so on. This alternation is valid along the a direction and makes consecutive dipoles to point inward ($\alpha = +4°$) and outward ($\alpha = -4°$) respectively. Generally, we have that the generic dipole moment $\vec{\mu}$ has the following normalized components expressed in terms of spherical coordinates:

$$\begin{aligned} \mu_x &= -\sin\beta \sin(\theta + (-1)^{n_2} \cdot \alpha) \\ \mu_y &= \sin\beta \cos(\theta + (-1)^{n_2} \cdot \alpha) \\ \mu_z &= \cos\beta \end{aligned} \tag{3.22}$$

WT model

The WT model [92, 93, 95] shows a deep structural difference compared to the other structures. Indeed it can be thought as organized into N_1 vertical chains and each of them with N_2 molecules. So one can talk about the n_2^{th} chromophore on the n_1^{th} chain with $n_1 = 1, ..., N_1$ and $n_2 = 1, ..., N_2$. Dipoles moments on adjacent chains do not have the same height but they are shifted by a quantity $k_{n_1} = n_1 b \sin \varepsilon$ to originate a helical structure, as shown in Figure 3.1(B). The lattice has the following parameters: $a = 12.5$ Å, $b = 7.4$ Å, $\gamma = 122°$ and $\varepsilon = 32°$. The unit cell of the WT type is similar to that of the MT, but it is rotated by an angle 90° around the $\vec{z}$ direction, so the vertical distance between two dipoles on the same chain measures $h = a/2 = 6.25$ Å. Moreover $\varphi = 360°/N_1 = 6°$ will be intended as the azimuthal angle between adjacent chains, and $\theta = n_2 \varphi$ as the angle between the position vector $\vec{r}$ and the x axis. The position of the generic dipole on the surface can be expressed in cylindrical coordinates as follows:

$$\begin{aligned} r_x &= R \cos \theta \\ r_y &= R \sin \theta \\ r_z &= h n_2 + k_{n_1} \end{aligned} \tag{3.23}$$

The components of each dipole moment are given by equation (3.22) with $\alpha = 4°$, $\beta = 35°$. Also in the WT model there is the alternation $\alpha = +4°$ and $\alpha = -4°$ between consecutive dipoles.

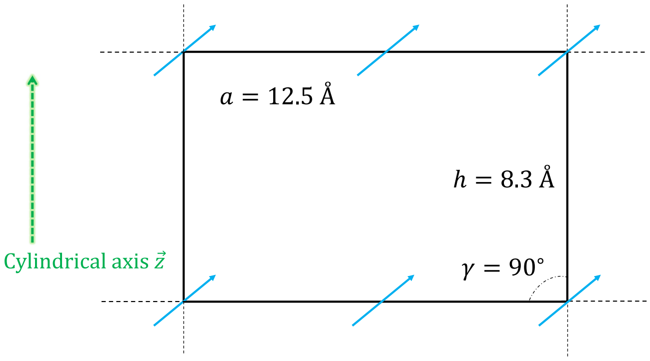

Figure 3.15: Unit cell for the PD, TD and RD models. Here the parameter b coincides with the vertical distance h between two consecutive rings. The cylindrical structure is obtained wrapping this rectangular unit cell around the direction of $\vec{z}$, which is perpendicular to the a side.

PD, TD and RD models

These models, shown in Figure 3.1(C, D, E), do not exist in nature and they have been introduced only for comparison with the natural systems. They exhibit a different lattice compared to the natural complexes, since the unit cell is a rectangle. As shown in Figure 3.15 we have $\gamma = 90°$, $a = 12.5$Å and $b = h = 8.3$ Å. The cylindrical axis $\vec{z}$ is perpendicular to the a side and one could build each of the three structures wrapping up the lattice around it. The three cylinders have again the same radius $R = 60$ Å and the same number of molecules N. Also, they are arranged into N_1 equal, horizontal and coaxial rings such that each of them carries N_2 dipoles. Once again a particular dipole moment will be indicated as the n_2^{th} chromophore on the n_1^{th} ring ($n_1 = 1, ..., N_1$ and $n_2 = 1, ..., N_2$). The three models differ for the values of α, β in the following way:

- in the PD structure, $\beta = 0°$ and $\alpha = 0°$,
- in the TD structure, $\beta = 90°$ and $\alpha = 0°$,
- in the RD structure, the angles are uniformly distributed such that $\alpha \in [0, 2\pi]$ and $\beta \in [0, \pi]$.

3.8.2 Comparison between dipole strengths and radiative decay widths

In Figure 3.16 the comparison between the dipole strengths $|D_n|^2$ (obtained using the Hamiltonian H_r (3.7)) and the rescaled radiative widths Γ_n/γ (obtained diagonalizing the Non-Hermitian Hamiltonian H (3.1)) is shown for all the eigenstates of the MT, WT, TD and PD models for $N = 6000$ dipoles. As one can see the two quantities can be considered to be the same (compare symbols with the dashed lines, which represent the behaviour $|D_n|^2 = \Gamma_n/\gamma$).

3.8.3 Comparison between radiative and dipole approximations

In order to understand the validity of the dipole approximation in the range of sizes of the natural systems considered, we have compared the dipole Hamiltonian, see equation (3.8), with the radiative Hamiltonian, see equation (3.7), which we used in this chapter. For instance comparing the dipole strength and the energy of the superradiant state we have found that the dipole approximation is good for both quantities, with a relative error which increases with the system size, but it remains small up to the value of $L/\lambda_0 \approx 0.3$ where the relative error of the dipole strength is 0.1% and the relative error of the energies is 0.02%. Nevertheless in other quantities, such as the energy gap between the ground state and the first excited state, the error can be as large as 20%, see Figure 3.17. Thus, we can say that while the dipole approximation seems to be well justified for the typical sizes of natural nanotubes, nevertheless non-negligible deviations can be found in some relevant quantities. For this reason here we used the radiative Hamiltonian which is more accurate. Moreover, one should not forget that the errors increase with the system size.

3.8.4 Participation ratio of the eigenstates

As a measure of delocalization of the eigenstates of the different nanotubular structures, we analyze the participation ratio (PR) of the eigenstates. Let us take into account the expression in equation (3.5) of the n^{th} energy eigenstate on the site basis: the coefficient

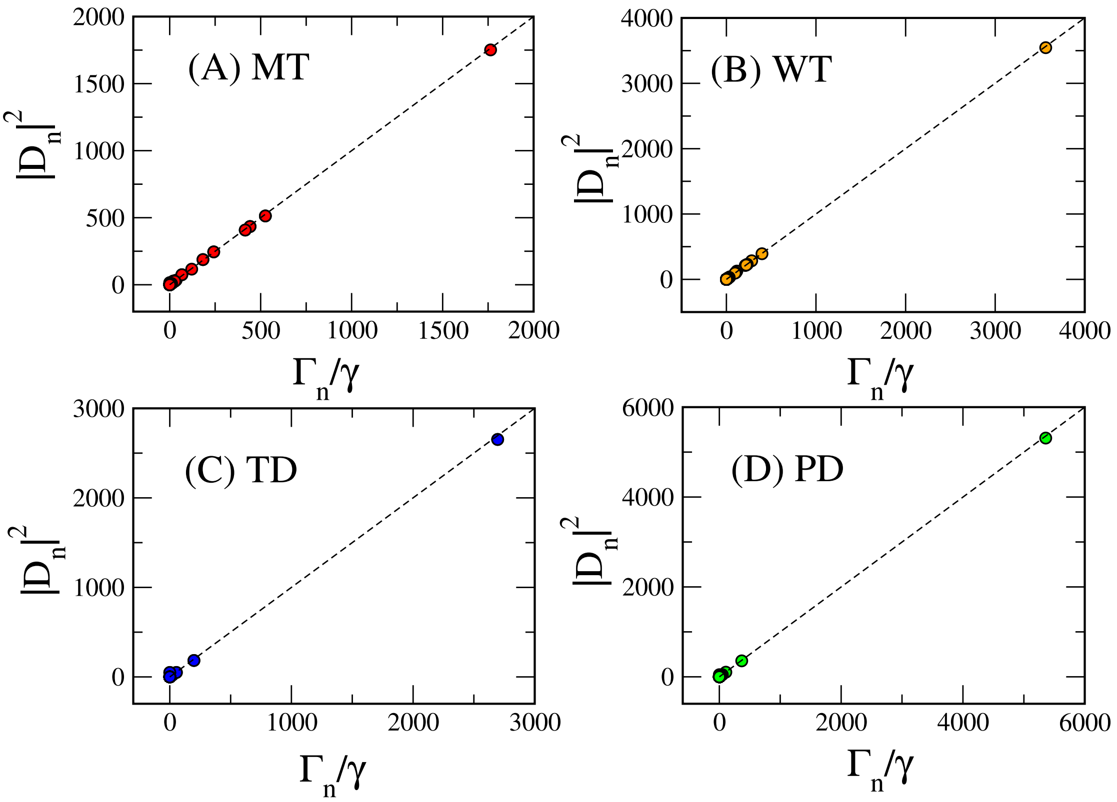

Figure 3.16: (A) - (D) Squared dipole strength $|D_n|^2$ obtained using the real Hamiltonian H_r (3.7) as a function of the radiative decay Γ_n/γ obtained diagonalizing the Non-Hermitian Hamiltonian H (3.1), for a total number of dipoles $N = 6000$. The trend is manifestly linear in each model as it can be noticed from the superposition with the line $|D_n|^2 = \Gamma_n/\gamma$. This matter of fact confirms that the imaginary part of the Hamiltonian given in equation (3.1) is perturbative indeed. Using the real Hamiltonian equation (3.7) would not result in any significant difference.

C_{ni} indicates its component on the i^{th} site. The PR of the n^{th} eigenstate is defined as follows:

$$PR_n = \frac{1}{\sum_{i=1}^{N} |C_{ni}|^4}. \tag{3.24}$$

Generally speaking, $PR_n \sim o(N)$ stands for a suitable degree of delocalization of the n^{th} eigenstate, while we have $PR = 1$ for a state fully localized on a single site. Figure 3.18 shows how the PR of each eigenstate depends on the eigenstate index in the six cylindrical models examined so far. All models but the RD (E) exhibit a participation ratio of the same order, such that $PR_n \sim o(N)$. One may observe indeed a difference of about one order of magnitude between the RD aggregate and the other structures. The presence of low degree of delocalization in the RD model is expected since the random

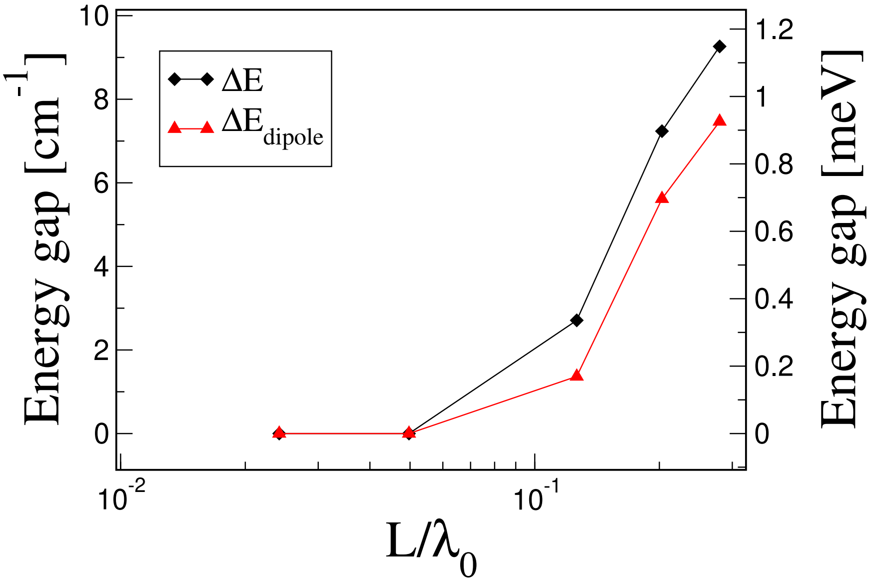

Figure 3.17: Energy gap between the ground state and the first excited state, computed for the radiative Hamiltonian (black squares), see equation (3.7), and the dipole Hamiltonian (red triangles), see equation (3.8).

coupling matrix elements between molecules can induce Anderson localization [109].

Note that the expression of L_ρ in equation (3.9) is not equivalent to the PR even for the case of a density matrix describing a pure state. Nevertheless both L_ρ and the PR are a measure of delocalization.

3.8.5 Super-Transfer in the WT model

The WT model is more complicated than the other models since the dipoles are not arranged into rings, but rather into helical structures. Nevertheless a very highly symmetrical disposition of the dipoles is also present in this case and one can think that the super-transfer coupling between the eigenstates of sub-units of the whole cylinder might influence the lowest part of the spectrum even for this model. To show that we have split the whole cylinder along the axis direction (the z direction) into smaller cylindrical structures. Each smaller cylinder contains a variable number of dipoles N_U. The projection of the SRS of a cylinder of 9600 dipoles on the eigenstates of these sub-units is shown in Figure 3.19 for different values $N_U = 240, 480, 960$. For a WT cylinder of 9600 dipoles the SRS lies in the lower part of the spectrum and it corresponds to the second excited state with a dipole strength directed along the z-axis. As one can see from Figure 3.19 the SRS of the whole cylinder has components mainly on one eigenstate for each sub-unit. We checked that such eigenstate corresponds to a superradiant state SRS of each sub-unit with a dipole strength directed along the z-axis. Since the SRSs of

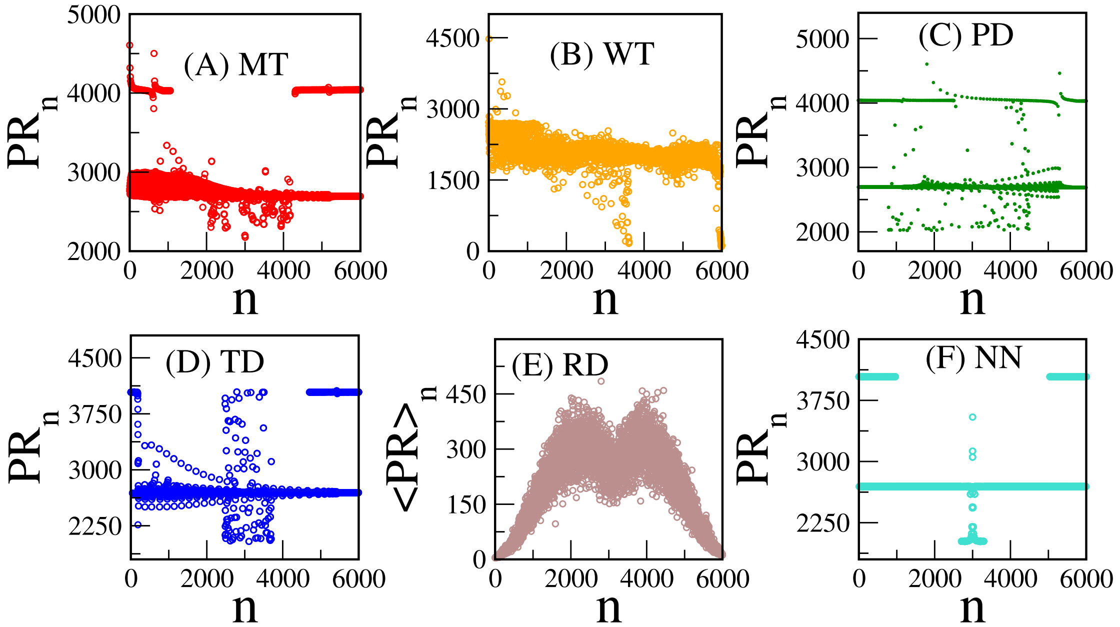

Figure 3.18: (A) - (F) PR of the eigenstates as a function of the eigenstate index. Most structures, both natural and artificial, show a PR of the same order of magnitude of the total number of dipoles N. An exception to this trend is represented by the RD model (panel (E)), in which the PR is smaller of about one order of magnitude. Note that in this case we speak of $\langle PR \rangle$, since the PR has been calculated for 10 random realizations. In all cases we considered $N = 6000$ dipoles.

each sub-unit have a giant dipole strength they couple by super-transfer. This shows that also for the WT model the super-transfer coupling inside the cylindrical structure might be responsible for the low density of states close to the ground state energy, see Figure 3.3(B). Nevertheless further analysis is needed to confirm this conjecture for the WT model. Let us note that the fact that the decomposition in sub-units of different sizes show a similar pattern, is a signature of the self similar behaviour present in such structures, which has been observed also in other molecular nanotubes [68]. Clearly if one chooses too small subunits the self-similar behaviour disappears. For instance in our case if we take a block of 60 molecules the superradiant state of the whole structure is not concentrated mostly on one eigenstate of the block.

3.8.6 Robustness to Static Disorder

In order to study the robustness of the thermal coherence length as defined in Eqs. (3.9), (3.11) to other sources of noise, here we consider the effect of static disorder, i.e. time-independent and space-dependent fluctuations of the excitation energies of the molecules comprising the molecular nanotube. Specifically, we consider that the excitation energies are uniformly distributed around the initial value e_0, between $e_0 - W/2$

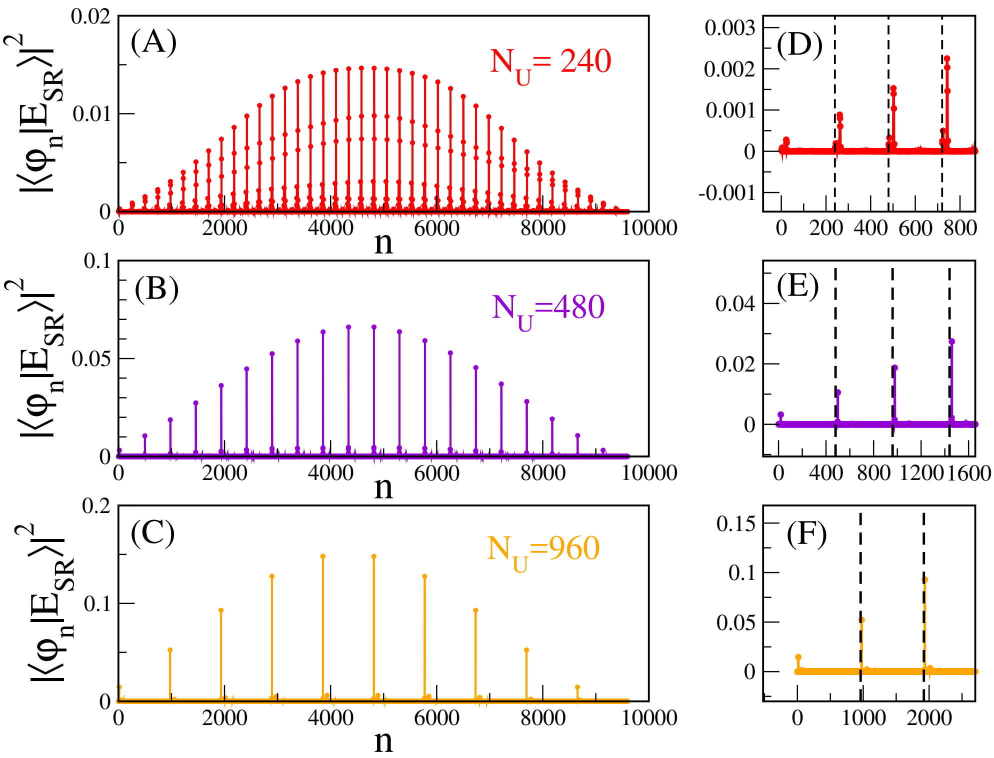

Figure 3.19: Projections of the most SRS of the whole cylinder $|E_{SR}\rangle$ for the WT model composed of 9600 dipoles over the eigenstates $|\varphi_n\rangle$ of smaller cylinders composing the whole one. The smaller cylinder has been obtained by dividing the whole cylinder in smaller sub-units along its main axis length. The length of the sub-units has been varied as follows: $N_U = 240$ (A), $N_U = 480$ (B) and $N_U = 960$ (C). In the case considered in this figure the SRS corresponds to the second excited state $|E_3\rangle$. Panels (D,E,F) are enlargements of (A,B,C) respectively. The vertical dashed lines indicates where each sub-unit ends.

and $e_0 + W/2$, so that W represents the strength of the static disorder. It is well known that static disorder induces localization of the system eigenstates, a phenomenon known as Anderson localization [109]. Due to this effect, for large disorder, the probability to find the excitation is concentrated on very few sites, eventually on one site only, for extremely large disorder. Anderson localization usually occurs in presence of short-range interactions, which is not our case, since interaction results from a complicated power law, see Eq. (3.1). Therefore the results of our analysis are in principle not obvious. In Fig. (3.20) the thermal coherence length for $T = 300K$ is shown as a function of the static disorder strength, normalized to k_BT with $T = 300$ K. As one can see the natural models (MT and WT) retain their larger thermal coherence length even in presence of static disorder up to $W \approx 10k_BT$. This energy scale is much larger than the static disorder expected in natural systems which is of the order of $k_B T$. Thus, our preliminary results, even if cylinders with only 6000 dipoles have been considered, show that such structures are able to sustain a large thermal coherence length even in presence of static disorder.

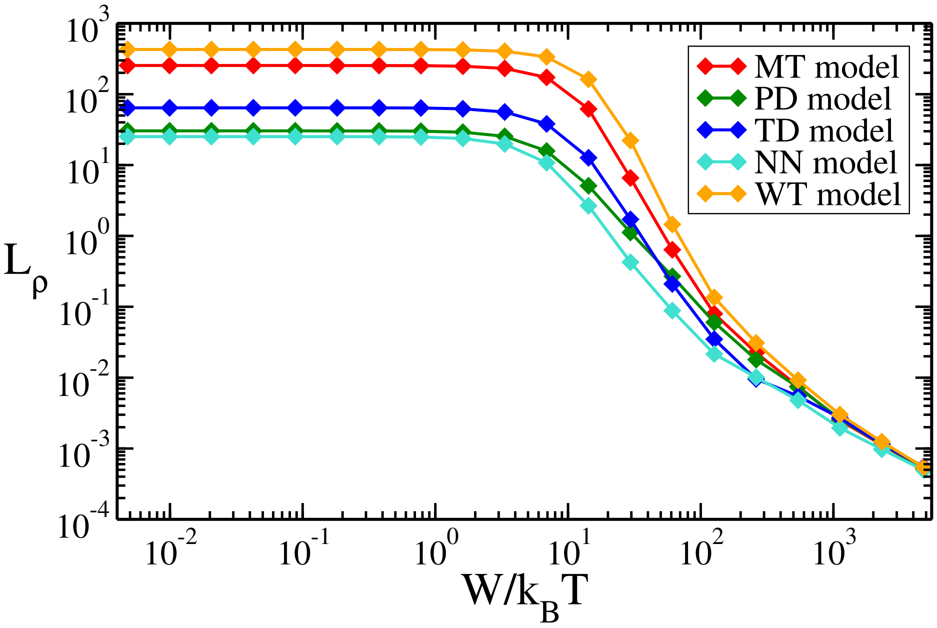

Figure 3.20: Thermal coherence length *vs* the normalized strength of static disorder $W/k_B T$, with $T = 300K$ for different models as indicated in the legend. In all models we considered $N = 6000$ dipoles. Average over 20 realizations of disorder have been done for each disordered strength.

3.8.7 Concentric cylinders

Let us emphasize that the fact that the coherence length for the four concentric cylinders is larger than the single cylinder is highly non trivial. Indeed, in the case of four concentric cylinders we have many more states and the density of states is larger than that of a single cylinder having the same length. In order to explain better this point, let us compute the density of states $\delta(k_B T)$ in a unit of thermal energy $k_B T$ for different numbers of dipoles N, see equation (3.12). This is shown in Figure 3.21 for both the concentric cylinders model and the MT, see Figure 3.21(A). As one can see the density of states is exactly the same for the two models as a function of the number of dipoles N. Nevertheless for the same fixed length, the density of states for the four concentric cylinders is larger than the density of the single cylinder. Despite all that, a large thermal delocalization length for the concentric cylinder case can be explained by the fact that the eigenstates for the 4 concentric cylinders are delocalized over a larger number of molecules as it is shown in Figure 3.21(B).

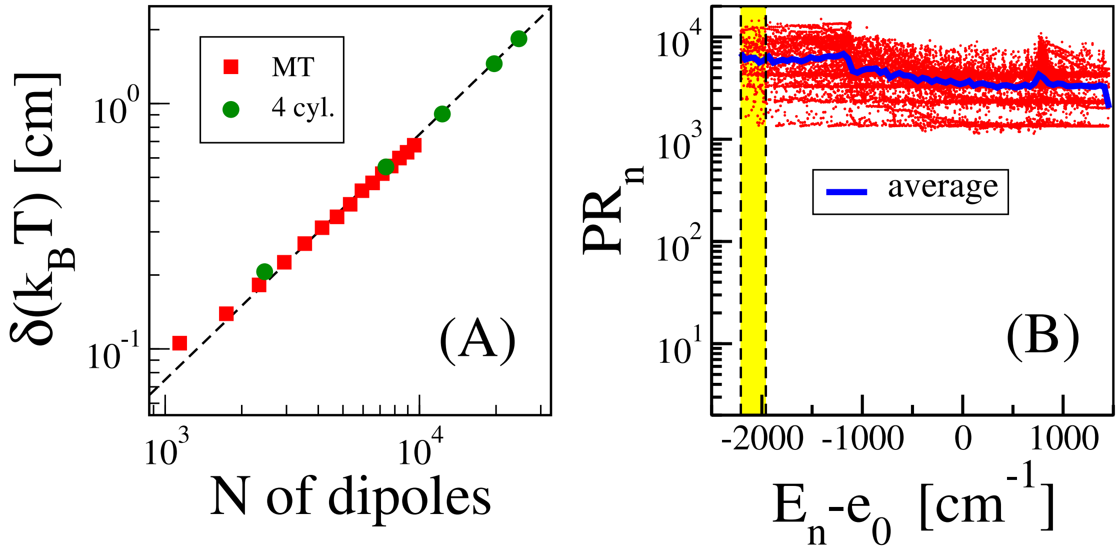

Figure 3.21: (A) Density of states (number of states per unit of thermal energy $k_B T$ at room temperature $T = 300K$, as a function of the total number of dipoles for the MT model (red squares) and for the four concentric cylinders (green circles). Dashed line stands for $\delta(k_B T) \propto N$. (B) Participation ratio as a function of the shifted eigenenergy (red points). Blue curve represents the average. Yellow region indicates the width of the thermal region $k_B T$. Here we have 100 layers, corresponding to $N = 24600$ dipoles.

Chapter 4

Applications of superradiance in photosynthetic molecular aggregates to sunlight-pumped lasers

In this chapter we propose an application of the cooperative effects present in natural molecular aggregates. Specifically, we address the technical issues that limit sunlight-pumped lasers, by proposing a laser medium inspired by well-studied natural photosynthetic Purple Bacteria. Results from this chapter are available as a preprint at: Francesco Mattiotti, William M. Brown, Nicola Piovella, Stefano Olivares, Erik M. Gauger, and G. Luca Celardo, "Bio-inspired sunlight-pumped lasers", arXiv:2007.04314 (2020). I contributed by co-ideating the project, deriving the laser equations for a large aggregate starting from the full Bloch-Redfield Master Equation, solving the rate equations at the steady state and discussing the results.

Even though sunlight is by far the most abundant renewable energy source available to humanity, its dilute and variable nature has kept efficient ways to collect, store, and distribute this energy tantalisingly out of reach. Turning the incoherent energy supply provided by the Sun into a coherent laser beam would overcome several of the practical limitations inherent in using sunlight as a source of clean energy: laser beams travel nearly losslessly over large distances, and they are effective at driving chemical reactions which convert sunlight into chemical energy. Here we propose a bio-inspired blueprint for a novel type of laser with the aim of upgrading unconcentrated natural sunlight into a coherent laser beam. Our proposed design constitutes an improvement of several orders of magnitude over existing comparable technologies: state-of-the-art solar pumped lasers operate above 1000 suns (corresponding to 1000 times the natural sunlight power). In order to achieve lasing with the extremely dilute power provided by natural sunlight, we here propose a laser medium comprised of molecular aggregates inspired by the architecture of natural photosynthetic complexes. Such complexes, by exploiting a highly symmetric arrangement of molecules organized in a hierarchy of energy scales, exhibit a

very large internal efficiency in harvesting photons from a power source as dilute as natural sunlight. Specifically, we consider substituting the reaction center of photosynthetic complexes in purple bacteria (*Rhodobacter Sphaeroides*) with a suitably engineered molecular dimer composed of two strongly coupled chromophores. We show that if pumped by the surrounding photosynthetic complex, which efficiently collects and concentrates solar energy, the core dimer structure can reach population inversion, and reach the lasing threshold under natural sunlight. The design principles proposed here will also pave the way for developing other bio-inspired quantum devices.

4.1 Introduction

One of the most remarkable aspects of many natural molecular aggregates is their ability to efficiently process extremely weak sources of energy or signals for biological purposes. Examples of this include the ability of avian magneto-receptors to sense the extremely weak geomagnetic field [110–113], or the ability of aquatic bacterial photosynthetic systems to harvest sunlight in deep murky waters, where incident light levels are much reduced beyond the already dilute level on land [3, 5]. For instance, purple bacteria have the ability to exploit extremely weak light sources [3, 5] (less than 10 photons per molecule per second) and some species of green sulfur bacteria even perform photosynthesis with geothermal radiation from deep-sea hydrothermal vents at about 400°C [114]. This incredible ability of bacterial photosynthetic systems to utilise weak sources of incoherent light stems from highly symmetric molecular aggregates organized in hierarchical structures which have evolved to harvest light and funnel the collected energy to specific molecular aggregates [34, 35]. In this chapter, inspired by the design of the photosynthetic apparatus of purple bacteria [3, 5], we show that biomimetic molecular aggregates hold the promise of significantly lowering the threshold requirements for sunlight-pumped lasers.

Sunlight is by far the most abundant renewable energy source on Earth (a single hour of sunlight provides all the energy humanity uses in a whole year). Despite this, there remain significant limitations in utilising sunlight as it is both dilute and variable. Therefore, efficient storage and distribution of energy harvested from sunlight is paramount. In this respect, sunlight-pumped lasing is an extremely promising technology for energy harvesting, distribution and storage of solar energy [8]. Sunlight-pumped lasers transform natural incoherent sunlight into intense beams of coherent light, which can be used to efficiently distribute the collected energy and drive chemical reactions as a way to efficiently store solar energy. Indeed, sunlight-pumped lasers have been proposed as essential elements in several renewable energy technologies such as the magnesium cycle [9–11].

Since the power density in natural sunlight is very dilute, typically concentrated sunlight is needed to cross the lasing threshold. Experimentally, a concentration of 10^5 'suns' (1 sun = 0.14 W/cm^2) is reachable, but clearly the smaller the 'number of suns' required for reaching the lasing threshold the better, since this lowers cost, technical demand, and increases efficiency. The first sunlight-pumped laser was realized in 1963 [8] and current state-of-the-art sunlight-pumped lasers operate above 1000 suns [115], however, proposals for sunlight-pumped lasers operational at few hundreds suns have been developed [115]. Typically, the concentration of sunlight relies on imaging or non-imaging concentrators. One of the most efficient way to concentrate sunlight is through black-body cavity pumping, where concentrated sunlight collected by a mirror heats a black-body cavity to temperatures which range from 1000 K to 3000 K [8].

Inspired by natural photosynthetic complexes, we propose a bio-mimetic molecular architecture to achieve efficient sunlight-pumped lasers capable of operating at pumping intensities as low as 1 sun. Photosynthetic antenna complexes [2–5, 44, 52, 53, 85, 86, 116] are comprised of a network of chlorophyll molecules which are typically modelled as two-level systems (2LS) capable of absorbing radiation and transporting the resulting electronic excitation to the reaction center where charge separation occurs, a process which precedes and drives all other photosynthetic steps. Each 2LS has an associated transition dipole moment (TDM) which determines its coupling with both the electromagnetic field and also with other proximal chlorophyll molecules. Owing to the low solar photon density, photosynthetic aggregates operate in the single-excitation regime, meaning at most one excitation is present in the system at any one time. The design principles which allow natural photosynthetic complexes to be so efficient rely on several levels of organization. On the lower level, single molecular aggregates feature a high degree of symmetry which favours the formation of bright (superradiant) or dark (subradiant) states with, respectively, large or small dipole strength [3, 5, 116, 117]. On a higher level, photosynthetic systems assemble many of these symmetric aggregates into hierarchical structures to maximize light-harvesting and energy transport. For instance, in purple bacteria, symmetric rings of chlorophyll molecules (LHI and LHII) surround the reaction center. These rings are J-aggregates with superradiant bright states which favor the absorption of light and the transfer of the excitation between each other [3, 5].

Many molecular aggregates, both naturally occurring as well as artificially synthesized, display bright and dark states in their single-excitation manifold [118–121]: J-aggregates are characterized by a bright state below the energy of the monomer absorption peak, while H-aggregates are characterized by a bright state above the energy of the monomer absorption peak. Cooperative properties, such as those seen in photosynthetic aggregates, have inspired many proposals for engineering artificial light-harvesting devices [1, 122–128]. The lasing properties of molecular aggregates, such as organic crystals (3D molecular aggregates) which display strong cooperative effects in the form of H- or J-aggregates, have been widely investigated [129–131].

Our proposed bio-inspired molecular architecture has at its core a suitably engineered molecular H-dimer. In an H-dimer the interaction between the excited states of each molecules create a bright state at high energy and a dark state at low energy. Under illumination, energy is absorbed mainly by the bright high-energy state and quickly transferred by thermal relaxation to the lower-energy state, which, being dark, loses energy by re-emission very slowly. Thus, an H-dimer is an ideal candidate to achieve population inversion (which is a main requirement for lasing) and its lower dark excitonic state can be exploited for the lasing transition. Nevertheless, natural sunlight is so weak that the required level of darkness of the lower excitonic state to achieve lasing would be unrealistically high. Indeed, the very long required excitonic lifetime of the lowest-excited state in the single-excitation manifold might be difficult to achieve in practice, due to disorder and competing non-radiative decay processes. In order to increase the pumping on the bright dimer state, so that the requirement on the darkness of the lower excitonic state can be relaxed, we consider substituting the reaction center of photosynthetic complexes in purple bacteria ”Rhodobacter Sphaeroides” with a suitably engineered H-dimer [playing a role similar to the special pair in the reaction center [3, 5]]. Indeed, natural antenna systems are extremely efficient precisely at collecting and funneling natural sunlight energy to specific locations. We show that a randomly positioned ensemble of such molecular aggregates inside a double-mirror cavity can lase under weak black-body radiation pumping (delivered by a surrounding black-body cavity that is heated by concentrated sunlight), and even under natural sunlight illumination.

We proceed by first deriving lasing equations for a generic molecular aggregate. We then consider lasing from an ensemble of isolated H-dimers. We show that placing the H-dimer at the center of a purple bacteria LHI ring lowers the lasing threshold and allows for less restrictive requirements on the darkness of the subradiant state of the H-dimer, with further advantages when adding additional LHII rings as occurs in the natural template. While we mainly focus on an aggregate inspired by photosynthetic apparatus of purple bacteria, we also consider a molecular architecture inspired by the photosynthetic complex of green sulfur bacteria [93] in the Appendix.

4.2 Lasing equations for molecular aggregates

We begin with the derivation of lasing equations for a generic ensemble of molecular aggregates, each made of N identical molecules, that are placed in an optical lasing cavity with suitably chosen frequency. The Hamiltonian of the molecular aggregate is written with the usual Pauli operators as

$$\hat{H}_S = \sum_{j=1}^{N} \frac{\hbar\omega_A}{2} \hat{\sigma}_j^z + \sum_{i,j} \Omega_{i,j} \left(\hat{\sigma}_i^+ \hat{\sigma}_j^- + \hat{\sigma}_j^+ \hat{\sigma}_i^- \right) , \tag{4.1}$$

where $\Omega_{i,j} = (\vec{\mu}_i \cdot \vec{\mu}_j)/r_{ij}^3 - 3(\vec{\mu}_i \cdot \vec{r}_{ij})(\vec{\mu}_j \cdot \vec{r}_{ij})/r_{ij}^5$ is the dipolar inter-molecular coupling [68, 116, 117] with $\vec{\mu}_j$ being the TDM of the j-th molecule in the aggregate and $\vec{r}_{ij}$ the vector between the i-th and the j-th molecule[1]. Equation (4.1) represents a molecular aggregate where each molecule is approximated as a 2LS with splitting ω_A. Under the relatively weak pumping conditions considered here, rather than retaining the full

---

[1] Closely spaced molecules require a modification of the dipole interaction term which is then not solely determined by the TDM [2, 4].

Hilbert space of dimension 2^N it suffices to limit our analysis to the overall aggregate ground state $|G\rangle$ and the single-excitation manifold comprised of N states $|j\rangle$ where the j-th molecule is excited while all the other ones are in their respective ground states.

We capture thermal relaxation by coupling each molecule to an independent bath of harmonic oscillators, and for simplicity we here neglect vibronic effects [121]. The interaction of the molecular aggregate with black-body radiation and phonons is then governed by the master equation

$$\frac{d\hat{\rho}(t)}{dt} = -\frac{i}{\hbar}\left[\hat{H}_S, \hat{\rho}(t)\right] + \mathcal{D}_{BB}[\hat{\rho}(t)] + \mathcal{D}_T[\hat{\rho}(t)]\,, \tag{4.2}$$

where $\mathcal{D}_{BB}$ and $\mathcal{D}_T$ are the Bloch-Redfield dissipators for the coupling to the black-body cavity and phonon environments, respectively (see Appendix). In our simulations phonon bath parameters have been chosen in order to effect thermal relaxation within few picoseconds, typical of molecular aggregates [3, 5].

Equation (4.2) can be largely simplified under well-motivated assumptions: first, as we check and validate numerically in the Appendix, we may safely secularise and reduce our master equation to Lindblad form [49]. Moreover, since thermal relaxation is typically the fastest time scale for molecular aggregates at room temperature (RT), we can assume that the populations in the single-excitation manifold are always at thermal equilibrium. Let us define the total probability for the aggregate to be excited as $P_e = \sum_k P_k$, where P_k is the probability of the $|k\rangle$ single excitation eigenstate to be excited. Neglecting higher excitation manifolds, we write $P_G + P_e = 1$, where P_G is the probability to be in the ground state. Then, assuming thermal equilibrium, we have

$$P_k = P_e p_k \quad \text{with} \quad p_k = \frac{e^{-E_k/k_B T}}{\sum_n e^{-E_n/k_B T}}\,, \tag{4.3}$$

where E_k is the energy of the k-th excitonic eigenstate, and we assume henceforth $T = 300$ K.

The coupling with the black-body photon bath is well-approximated by rate equations for the populations (see Appendix and Ref. [132]), with absorption rates between the $|G\rangle$ and the single-excitation states $|k\rangle$ given by

$$R_k = n_T^k \gamma_k\,, \quad \text{with} \quad \gamma_k = \frac{\mu_k^2 \omega_k^3}{3\pi\epsilon_0 \hbar c^3}$$
$$\text{and} \quad n_T^k = \frac{1}{e^{E_k/k_B T_{BB}} - 1}\,, \tag{4.4}$$

where γ_k is the spontaneous decay rate of the k-th state, ω_k and μ_k its transition frequency and TDM, respectively, and n_T^k the photon occupancy at the black-body temperature T_{BB}.

As our laser gain medium, we consider an ensemble of molecular aggregates randomly distributed with density n_A inside a lasing cavity of frequency ω_c and containing a classical oscillating field $\vec{E} = E_0 \hat{e} \cos(\omega_c t)$. The aggregate's single-excitation states $|k\rangle$

couple coherently to the cavity mode with Rabi frequencies $\Omega_k = (\vec{\mu}_k \cdot \hat{\epsilon})E_0/\hbar$ that depend on the cavity polarization $\hat{\epsilon}$ and field amplitude E_0. In molecular aggregates under weak pumping, the Rabi frequency is typically smaller than the interband excitonic dephasing rate, $\Gamma_\phi \gg \Omega_k$. Therefore, instead of coherent Rabi oscillations we obtain incoherent transition rates proportional to Ω_k^2, as derived in the Appendix and Ref. [81]. The field intensity $I = \epsilon_0 |E_0|^2 c/2$ can also be written as $I = \hbar\omega_c nc/V$, where n is the number of photons in the cavity, V the cavity volume, and c the speed of light. This allows us to express the cavity-induced transition rate between $|G\rangle$ and $|k\rangle$ state in terms of the number of cavity photons n as

$$nB_k = n\,\frac{1}{3}\,\frac{|\mu_k|^2\omega_c}{V\hbar\epsilon_0}\,\frac{\Gamma_\phi}{\Gamma_\phi^2 + (\Delta_k/\hbar)^2} = \frac{\Omega_k^2}{2}\,\frac{\Gamma_\phi}{\Gamma_\phi^2 + (\Delta_k/\hbar)^2}\,, \tag{4.5}$$

where $\Delta_k = (E_k - \hbar\omega_c)$ is the energy detuning between the single-excitation state k and the cavity mode. The factor 1/3 derives from averaging over the random aggregate orientations.

Under the above assumption we can write lasing rate equations that couple the populations of the molecular aggregates with the number of photons in the cavity. For this purpose, let us define the density of aggregates in the excited states as $N_e = n_A P_e$, the density of aggregates in the ground state as $N_G = n_A P_G$, and the population difference per unit volume as $D = N_e - N_G$. This gives the lasing equations

$$\begin{aligned}\frac{dD}{dt} =& -D[R_d + R_u + (B_{tot} + \langle B\rangle)n] + \\ & + n_A[R_u - R_d + n(B_{tot} - \langle B\rangle)] \qquad (4.6a)\\ \frac{dn}{dt} =&\ V(B_{tot} + \langle B\rangle)\frac{nD}{2} - V(B_{tot} - \langle B\rangle)\frac{nn_A}{2} - \kappa n\,, \qquad (4.6b)\end{aligned}$$

where $R_u = \sum_k R_k$ is the total absorption rate and $R_d = \sum_k (R_k + \gamma_k)p_k$ is the spontaneous and stimulated emission rate from the single-excitation manifold. Further, $B_{tot} = \sum_k B_k$ and $\langle B\rangle = \sum_k B_k p_k$ are, respectively, the total upwards and downwards transition rates between $|G\rangle$ and the single-excitation manifold which is induced by the coupling to the cavity mode.

From Eq. (4.6) we obtain the stationary values of the population difference per unit volume D_0 and the stationary number of photons n_0 in the cavity

$$\begin{aligned}D_0 =& \frac{2\kappa}{V(B_{tot} + \langle B\rangle)} + n_A\bar{B}\,, \qquad (4.7a)\\ n_0 =& \frac{V(n_A D_{eq} - D_0)}{2\kappa}(R_u + R_d)\,, \qquad (4.7b)\end{aligned}$$

where $\bar{B} = (B_{tot} - \langle B\rangle)\,/\,(B_{tot} + \langle B\rangle)$ and $D_{eq} = (R_u - R_d)/(R_u + R_d)$ is the equilibrium population difference in absence of driving from the cavity. Above the lasing threshold, i.e. having $n_0 > 0$ stationary photons in the cavity, the laser intensity and output power will be, respectively,

$$I = \frac{\hbar\omega_c c}{V} n_0 \,, \tag{4.8a}$$

$$P_{out} = \frac{\kappa V}{c} I = \kappa\hbar\omega_c n_0 \,. \tag{4.8b}$$

We turn to the question under which conditions we achieve lasing. Imposing $n_0 > 0$ in Eq. (4.7) we require $n_A D_{eq} - D_0 > 0$, which can be written as

$$n_A(D_{eq} - \bar{B}) > \frac{2\kappa}{V(B_{tot} + \langle B \rangle)} \,. \tag{4.9}$$

Using the definitions of R_u and R_d and for $n_T^k \ll 1$,

$$D_{eq} \approx \frac{\sum_k \chi_k n_T^k - \langle \chi \rangle}{\sum_k \chi_k n_T^k + \langle \chi \rangle} \,, \tag{4.10}$$

where $\chi_k = \gamma_k/\gamma_0$ indicates the relative brightness of the state $|k\rangle$ and $\langle \chi \rangle = \sum \chi_k p_k$ is the thermal average of the relative decay rates of all the single-excitation states. Moreover, $\gamma_0 = (\mu^2\omega_A^3)/(3\pi\epsilon_0\hbar c^3)$ is the spontaneous decay rate of a single molecule. We reiterate that Eq. (4.10) is generically valid subject to fast thermal relaxation and with negligible occupation of states containing more than one excitation. Both assumptions are realistic for molecular aggregates under black-body radiation pumping.

Equation (4.9) determines the critical density of molecular aggregates to achieve lasing, implying

$$D_{eq} > \bar{B} \,. \tag{4.11}$$

Since $\bar{B} \geq 0$ by definition, unsurprisingly we require population inversion, $D_{eq} > 0$, to achieve lasing. Considering Eq. (4.11) with Eq. (4.10) and recalling that $R_u = \gamma_0 \sum_k \chi_k n_T^k$, implies $\langle \chi \rangle \leq \frac{R_u}{\gamma_0}\frac{1-\bar{B}}{1+\bar{B}}$, which can be recast as:

$$\langle \chi \rangle \leq \frac{R_u}{\gamma_0}\frac{\langle B \rangle}{B_{tot}} \,. \tag{4.12}$$

Equation (4.12) clearly shows that given a non-zero (but realistically small) value for $\langle \chi \rangle$, two conditions need to be met for lasing: (i) the ratio $\langle B \rangle / B_{tot}$ should be as large as possible, given $\langle B \rangle \leq B_{tot}$ this is maximized for $\langle B \rangle \approx B_{tot}$. This condition can be realised by a lasing state that is well-gapped (w.r.t. $k_B T$ at RT) below all other states in its excitation manifold; (ii) the absorption rate R_u should be as large as possible. Lasing under very weak pumping requires a highly dark aggregate (i.e. small $\langle \chi \rangle$), even if $\langle B \rangle \approx B_{tot}$. This is not easy to achieve, and the situation is compounded by non-radiative losses typically present in molecular aggregates. As we shall show in the following, a bio-inspired molecular architecture can help to mitigate this stringent demand and make lasing achievable.

Throughout this chapter, when considering black-body optical pumping, we choose a temperature $T_{BB} = 3000$ K which is attainable using sunlight concentrated by a mirror of a few m^2 [8] with an input power into the black-body cavity of few kW. To compute the laser output power we assume a typical gain medium volume of $V = 11.3$ cm^3 (radius of 6 mm and length of 10 cm). The densities of the laser medium are chosen to be lower than 1 aggregate/(10 nm)^3, corresponding to realistic densities for dye lasers: $n_A^{(\max)} = 10^{18}$ cm^{-3} $= 1.6$ mmol/L [133]. This choice ensures that direct interactions between the molecular aggregates can be neglected. Moreover, it also keeps the output power below 1 kW, so that thermal balancing with the black-body cavity under realistic sunlight pumping can be maintained. To remove the need for and complexity of sunlight concentration we shall also consider the possibility to achieve lasing under direct natural sunlight illumination. To model natural sunlight we consider pumping under a black-body at $T_{BB} \approx 5800$ K but with rates in Eq. (4.4) reduced by a factor f_S representing the solid angle of the Sun as seen on Earth [134],

$$f_S = \frac{\pi r_S^2}{4\pi R_{ES}^2} = 5.4 \times 10^{-6}\,, \tag{4.13}$$

with r_S being the radius of the Sun and R_{ES} the Sun-to-Earth distance. In this case we limit the output power to 1 W since the incident power on our chosen lasing cavity is just a few W.

4.3 Lasing with dimers

Let us consider a dimer comprising two identical chromophores. Each molecule (labeled $j = 1, 2$) has one relevant optical transition, so that we may model it as a 2LS with ground state $|g_j\rangle$ and excited state $|e_j\rangle$. Excitation energy $\hbar\omega_A$ and magnitude μ of the electric TDM are identical between the molecules, while the direction of the optical dipole $\vec{\mu}_j$ depends on the orientation of its chromophores and may differ.

For this dimer system the Hamiltonian in Eq. (4.1) is diagonalized by a set of four states (see Fig. 4.1a): $|G\rangle = |g_1\rangle|g_2\rangle$, where both molecules are in their respective ground state; $|L\rangle$ and $|H\rangle$ are the lowest and highest single-excitation states, where only one excitation is present in the system, delocalised over both molecules; these states span the single-excitation manifold and they correspond to the symmetric and anti-symmetric states $(|g_1\rangle|e_2\rangle \pm |e_1\rangle|g_2\rangle)/\sqrt{2}$. Finally, $|F\rangle = |e_1\rangle|e_2\rangle$ has both molecules in their respective excited state. The corresponding energies are shown in Fig. 4.1a.

Optical transitions between the levels are determined by the relative orientation of the single molecules. We indicate the transition dipoles between the ground state $|G\rangle$ and the states $|L\rangle$ and $|H\rangle$ with $\vec{\mu}_L$ and $\vec{\mu}_H$, respectively, see Fig. 4.1a. The conservation of total oscillator strength demands that $\mu_L^2 + \mu_H^2 = \mu_1^2 + \mu_2^2 = 2\mu^2$ and we have an H-dimer if $\mu_L < \mu$ while if $\mu_L > \mu$ we have a J-dimer. The coupling Ω between molecules can either have a dipolar or a different origin, see Appendix. Typical H-dimers feature splittings between their bright and dark states of several $k_B T$, and the lower state may be many hundreds times less bright than the upper state [118–121]. Here, we consider a dimer with excitation energy in the near-infrared $\hbar\omega_A = 1.17$ eV ($\lambda \approx 1060$ nm),

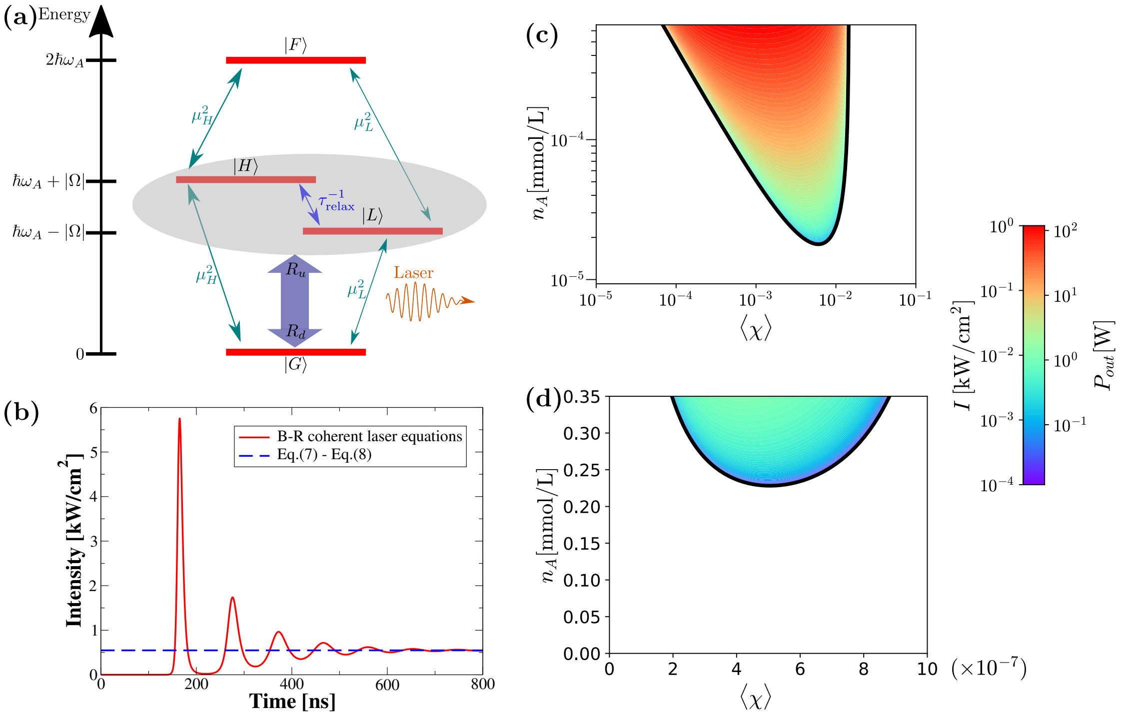

Figure 4.1: **(a)** Eigenstates of the dimer Hamiltonian $\hat{H}_S$ [Eq. (4.1)] and transition rates between them. Optical rates (green arrows) are proportional to the squared dipole strengths [see Eq. (4.4)], while the thermal relaxation rate (blue arrow) is $\tau_{\text{relax}}^{-1} \approx 1\ \text{ps}^{-1}$. All these transitions obey detailed balance, i.e. upwards and downwards rates are proportional to the Bose-Einstein occupation number $n_T(\hbar\omega)$ and $[1+n_T(\hbar\omega)]$, respectively. The thick double arrow represents the resulting effective rates linking the ground state $|G\rangle$ to the single-excitation manifold (grayed area), as utilised in Eq. (4.6a). The $|L\rangle - |G\rangle$ transition is further coupled to a resonant lasing cavity. **(b)** Temporal evolution of the laser intensity under black-body pumping: Bloch-Redfield model (solid red) for dimers that are coherently coupled to the lasing cavity (details in the Appendix), and steady-state solution (dashed blue) of our lasing equations, Eqs. (4.7)-(4.8). Parameters: $\mu = 10.157$ D, $\hbar\omega_A = 1.17$ eV, $\Omega = 2000\ \text{cm}^{-1}$, $T_{BB} = 3000$ K, $\Gamma_\phi = 1/(10\ \text{ps})$, $\kappa/(2\pi) = 50$ MHz, $\langle\chi\rangle = 0.005$, $n_A = 5\times10^{-4}$ mmol/L, and a lasing cavity volume $V = 11.3\ \text{cm}^3$ (cylindrical shape of radius $R = 6$ mm and length $L = 10$ cm). **(c)-(d)** Laser intensity and output power for the same parameters as (b) except for $\langle\chi\rangle$ (thermal average of the relative brightness of single-excitation states with respect to a single molecule) and n_A (dimer density in millimol/L) which are varied along the axes. The black line represents the lasing threshold [Eq. (4.9)]. In (c) optical pumping occurs via a black body radiation at $T_{BB} = 3000$ K, whereas in (d) the lasing medium is illuminated by natural sunlight.

transition dipole of $\mu = 10.157$ D (as for the bacteriochlorophyll-a molecule) and a coupling $\Omega = 2000\ \mathrm{cm}^{-1}$ as in similar H-dimers [135].

Under black-body illumination, primarily the bright state $|H\rangle$ undergoes excitation, followed by rapid thermal relaxation to the lower dark $|L\rangle$ state. The large energetic separation between $|H\rangle$ and $|L\rangle$ makes this relaxation one-way, preventing environmental re-excitation into $|H\rangle$. In the Appendix we show that it is possible to achieve population inversion provided the absorption rate $|G\rangle \rightarrow |H\rangle$ dominates over the spontaneous emission rate $|L\rangle \rightarrow |G\rangle$. We proceed to couple the $|L\rangle \rightarrow |G\rangle$ transition to a resonant lasing cavity and evaluate the lasing performance of the system using the equations derived in the previous section. Figure 4.1b shows the resulting laser intensity: once the stationary regime has been reached, there is perfect agreement between the intensity predicted by Eq. (4.6) with our numerically obtained results from a coherent Bloch-Redfield model. The latter, derived in Eqs. (4.50) and (4.56) of the Appendix, treats both photon and phonon environments in the Bloch-Redfield formalism, includes the doubly excited state, and – as its main assumption – treats the laser field semi-classically, but nonetheless coherently coupled to the aggregates similarly to Refs. [136, 137]. In Fig. 4.1c we show the dependence of the laser intensity and power output on n_A and $\langle\chi\rangle$ based on realistic choices for all other parameters (see caption). The white area highlights the region below the laser threshold Eq. (4.9) (black continuous line), where the dimer density n_A is too low to permit lasing. As one can see, an intensity of up to 1 $\mathrm{kW/cm}^2$ can be reached with a very low dimer concentration.

To assess the possibility of lasing under direct natural sunlight illumination (i.e. without a black-body cavity heated by concentrated sunlight), we show the lasing threshold and output power for this scenario in Fig. 4.1d. Clearly, lasing is still theoretically possible but only for very low values of $\langle\chi\rangle$. In practice, this is challenging due to the competition of non-radiative decays and other sources of noise in realistic situations. Nevertheless, as we show in the next section, the critical value of $\langle\chi\rangle$ increases by orders of magnitude if the dimer is placed inside a purple bacteria molecular aggregate. Finally, note that for lasing we require a small yet finite value of $\langle\chi\rangle$. In the case of a homodimer (where for parallel TDMs the $|L\rangle$ dimer state would be fully dark) this can either arise as a consequence of the relative orientation of the TDMs, or through the presence of structural or energetic disorder.

4.4 Bio-inspired lasers

Whilst lasing with a gain medium composed of suitable H-dimers is realistic under black-body cavity pumping, achieving the extremely high optical darkness (small $\langle\chi\rangle$) for direct sunlight-pumped operation is a tall order. According to Eq. (4.12) $\langle\chi\rangle$ is upper-bounded by the pumping rate in units of γ_0 (assuming that we have the favourable ratio $\langle B\rangle/B_{tot} \approx 1$). Thus increasing the effective pumping rate reduces the stringency of required darkness. A possible way of increasing pumping is to surround the dimer by a molecular aggregate that is capable of efficiently absorbing photons and transferring the resulting energy excitations to the $|H\rangle$ dimer state. The ag-

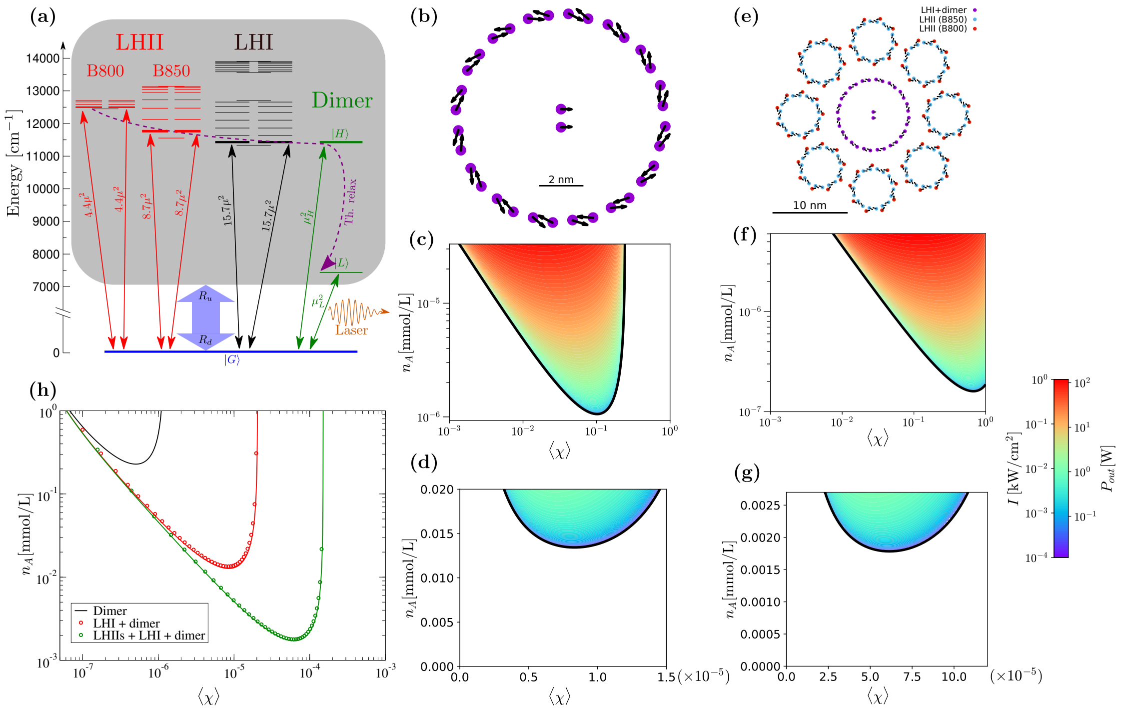

Figure 4.2: **(a)** Single-excitation eigenstates of the LHII complex (with a distinction between the B800 and the B850 subunits), LHI complex, and H-dimer. The strongest optical rates, proportional to the squared dipole strengths, are indicated alongside the two-headed arrows. As before, the thick double arrow represents the resulting effective rates linking the ground state $|G\rangle$ to the single-excitation manifold (grayed area) and the $|L\rangle - |G\rangle$ dimer transition is also coupled to a lasing cavity. The H-dimer parameters are: $\mu = 10.157$ D, $\hbar\omega_A = 1.17$ eV, $\Omega = 2000$ cm^{-1}. Further, $\Gamma_\phi = 1/(10 \text{ ps})$, $\kappa/(2\pi) = 50$ MHz, and $V = 11.3$ cm^3. **(b), (e)** Positions of the chromophores (circles) and transition dipole orientations (arrows) for the bio-mimetic complexes. Excitation energies and nearest-neighbour couplings for bio-mimetic aggregates are taken from Refs. [2, 4, 34, 138, 139]. **(c), (d), (f), (g)** Laser intensity and output power for an LHI ring surrounding an H-dimer (c,d) and with eight additional B800/850 LHII rings surrounding the LHI ring (f,g). On the axes we vary $\langle\chi\rangle$ of the H-dimer and n_A (the aggregate density in mmol/L). In all panels the black line represents the lasing threshold [Eq. (4.9)]. In (c,f) we have black-body pumping at temperature $T_{BB} = 3000$ K, whereas (d,g) are for natural sunlight illumination. **(h)** Lasing threshold density under natural sunlight for a bare dimer, one LHI surrounding the dimer as in (b), and eight LHIIs around an LHI ring containing the dimer as in (e). The red and green continuous curves are for a dimer with a re-scaled R_u pumping rate: by a factor of 17 (red curve) and by a factor of 125 (green curve), corresponding to an enhancement factor $N/2$ with N being the number of chromophores in the aggregate. The circles are obtained from the full set of optical transitions as indicated in (a).

gregate should absorb at an energy larger than the $|H\rangle$ dimer state energy in order to preserve the gap which separates the dimer lasing state from other states, so that $\langle B\rangle/B_{tot} \approx 1$. Note that under this condition $\langle\chi\rangle$ of the whole aggregate can remain very close to $\langle\chi\rangle$ of the dimer alone. Here we consider a dimer surrounded by the antennae complex of purple bacterial photosynthetic systems that thrive in very low light intensity [3, 5, 34, 35, 139]. Moreover, in the Appendix a green sulfur bacteria antenna complex is used to increase the pumping of the dimer $|H\rangle$ state even further.

Purple bacteria feature a hierarchical structure of symmetric molecular aggregates which absorb light and direct the collected energy to the specific molecular aggregate of the reaction center (RC). The purple bacteria RC contains a bacteriochlorophyll (BChl) dimer called the special pair, and is surrounded by an LHI (Light-Harvesting system I) ring comprising 32 BChl molecules. The LHI ring is a J-aggregate with two superradiant states at 875 nm that are polarized in the ring plane and close to the lowest excitonic state. The LHI ring is surrounded by several LHII rings, each featuring the B850 ring, a J-aggregate composed of 18 BChl molecules with two superradiant states at 850 nm, and the B800 ring composed of 9 BChl molecules with main absorption peak at 800 nm. This hierarchical structure is able to absorb photons at different frequencies and guide the collected energy down an energetic funnel to the RC through a process dubbed supertransfer, resulting from the coupling between the LHII-LHI superradiant states and the LHI-RC aggregates [3, 5, 34, 35].

We propose substituting the special pair in the purple bacteria reaction center with an H-dimer whose $|H\rangle$ state is resonant with the superradiant states of LHI. Photons absorbed by the LHI ring would then contribute to the pumping of the dimer's $|H\rangle$ state, with the strong coupling between $|H\rangle$ and the bright state of the LHI complex ensuring fast transfer. The geometrical arrangement for this envisioned aggregate is shown in Fig. 4.2b [2, 4, 138, 139] (for full details see the Appendix). Starting from a realistic model for the antenna system coupled to the dimer (see the Appendix for details) we obtain the eigenvalues and the TDMs of all the energy states by direct Hamiltonian diagonalization, which allows evaluating the lasing equations (4.6) under the already discussed assumptions of negligible non-radiative losses and fast thermal relaxation. The latter is valid in this aggregate owing to supertransfer throughout the aggregate which entails thermal relaxation on the order of tens of picoseconds [2, 4]: this is much faster than optical pumping, which range from a few nanoseconds (large aggregates, high black-body temperature) down to milliseconds (small aggregates, natural sunlight) and spontaneous decay, which is of the order of a nanosecond for the brightest states. Moreover, other relevant timescales are the transition rate due to the coupling to the lasing cavity field which we estimate to be larger than hundreds of picoseconds (for the parameters considered here), and the realistic extraction rate κ from the cavity of about three nanoseconds which we considered. In summary, thermal relaxation is clearly the fastest process, justifying the use of Eq. (4.6) for analyzing the lasing response of such bio-inspired aggregates. Moreover, in the Appendix, results of incoherent laser equations Eqs. (4.75) in the Appendix, which do not assume quasi-instantaneous thermalization, are shown to be in excellent agreement with Eq. (4.6).

The calculated lasing intensity and output power for a disordered ensemble of such aggregates (LHI+H-dimer) is shown in Fig. 4.2c for black-body cavity pumping, and in Fig. 4.2d for natural sunlight illumination. Comparing Fig. 4.1c-d with Fig. 4.2c-d, the critical aggregate density to cross the lasing threshold is greatly lowered, and more importantly, the required level of the dimer darkness for the natural sunlight case is reduced by more than an order of magnitude. We obtain a further improvement when surrounding our LHI ring with eight LHII rings, see Fig. 4.2e. The B800/850 LHII aggregate level structure next to that of the LHI and H-dimer is shown in Fig. 4.2a. As shown in Fig. 4.2f-g this larger aggregate architecture achieves a further lowering of the lasing threshold, i.e. increase of the critical value of $\langle \chi \rangle$ for the H-dimer below which lasing is possible. Interestingly, in Fig. 4.2f, the addition of the rings has increased the effective pumping of the H-dimer to the extent where the dimer no longer has to feature a dark state to lase: indeed in this case lasing is possible even for $\langle \chi \rangle = 1$.

We have established that surrounding an H-dimer with purple bacteria LHI and LHII rings not only lowers the necessary threshold density but also enables lasing with much less dark H-dimers. To better understand and visualise these trends, we map out the lasing transition as a function of threshold density and average brightness of the H-dimer for natural sunlight pumping in Fig. 4.2h[2]. This uses an H-dimer system described by Eqs. (4.9) and (4.10) but with effective pumping R_u increased by the factor $N/2$, where N is the number of molecules in the bio-inspired aggregate including the H-dimer. This is a simplified approach of approximating enhanced pumping compared to the approach above based on the known TDMs of LHI/LHII states. Interestingly, the resulting threshold lines in Fig. 4.2h perfectly reproduce those obtained in the presence of the whole aggregate (symbols). This confirms that the crucial role of adding bio-inspired aggregates is to increase the effective pumping rate. Moreover, it suggests that our proposed architecture is scalable and an even lower lasing threshold could be achieved with larger J-aggregates surrounding the H-dimer, as we discuss in the Appendix, where we consider another bio-inspired architecture where the antenna complex of the green sulfur bacteria pumps the dimer $|H\rangle$ state. Nevertheless, caution is necessary when applying the lasing equations derived here to very large aggregates, where the assumption of thermalization occurring on the fastest relevant timescale can become invalid, in which case an incoherent laser equation might be more appropriate as discussed in the Appendix.

4.5 Conclusions and perspectives

Efficient sunlight-pumped lasers could revolutionize renewable energy technologies, nevertheless lasing under natural sunlight illumination is still well beyond reach. By mimicking the architecture of photosynthetic antenna complexes, here we have shown how lasing with natural sunlight pumping can be achieved.

We first considered an ensemble of molecular H-dimers inside an optical cavity

---

[2] The case of a black body pumping at $T_{BB} = 3000$ K is discussed in the Appendix.

pumped by black-body cavity radiation. When considering realistic values of the H-dimer darkness, lasing is possible for high black-body temperatures which can be achieved by heating up a cavity with concentrated sunlight. Nevertheless, lasing with H-dimers under natural sunlight would require a very high level of darkness, which is very difficult to achieve. The main limitation is due to the very weak pumping produced by natural sunlight. Larger molecular H-aggregates might be able to lower the lasing threshold by absorbing more light and thus increasing the pumping. On the other hand, if not properly designed, large aggregates have an increased density of states which would suppress the thermal population of the lasing state. This effect would compete with the advantage gained by more absorbed light. In order to increase the absorbed light without suppressing the population of the lasing state, one possibility is to consider an aggregate which absorbs light on a hierarchy of energy scales and which is able to efficiently funnel the absorbed energy to a low energy lasing state which is well-gapped below other excitonic states. In this way, its thermal population will not be suppressed. These are precisely the features which characterize many natural antenna photosynthetic systems. Our proposed bio-inspired molecular aggregate serving as the lasing medium is composed of an H-dimer operating at low energy, surrounded by LHI and LHII rings of the purple bacteria antenna complex, which absorb at higher energy and efficiently funnel the absorbed energy to the H-dimer. In this configuration, we show that lasing should be possible even under natural sunlight illumination.

The specific bio-inspired parameters we have analysed would implement a short wavelength infrared laser, which has the advantage of being able to efficiently distribute converted solar energy due to the low dispersion in this wavelength range [135], which is also why this spectral regime is used in optical fiber communications. As an interesting prospect, our bio-mimetic molecular aggregates should be able to lase in nanocavities with volume of $(\lambda/20)^3$ [140] and could thus be engineered into sun-light pumped nanolasers [141].

Our idea can be generalized to other bio-inspired molecular architectures where molecular (J-)aggregates efficiently pump the bright state of a homo-dimer; this would allow lasing in other spectral regimes, and utilising other photosynthetic systems, e.g. the chlorosome of green sulfur bacteria [55] (as discussed in the Appendix) or photosynthetic membranes such as in Photosystem II [142] to feed excitations into $|H\rangle$ and make them available for the lasing transition.

4.6 Appendix

4.6.1 A possible geometry for an H-dimer

Here we introduce a possible configuration for an H-dimer with dipolar coupling. This serves as a simple example for how to achieve the level configuration presented in Fig. 4.1a.

Let us consider the orientation shown pictorially in Fig. 4.3a: the optical transition dipoles of two identical molecules lie in the (x, y) plane and they have an opposite inclination angle θ with respect to the x axis. The corresponding transition dipole moment (TDM) for each molecule can be expressed as

$$\vec{\mu}_1 = \mu \sin\theta \hat{x} - \mu \cos\theta \hat{y} \, , \tag{4.14a}$$
$$\vec{\mu}_2 = \mu \sin\theta \hat{x} + \mu \cos\theta \hat{y} \, . \tag{4.14b}$$

The dipole-dipole coupling between the two molecules at distance r_{12} is

$$\Omega = -\frac{\mu^2}{r_{12}^3} \left(1 + \cos^2\theta\right) \, , \tag{4.15}$$

and is negative for any value of θ. Note that the dipole coupling is valid only when the distance between the molecules is larger than the charge displacement producing the TDM. For smaller distances, the whole charge distribution should be taken into account to compute the coupling [143]. For this reason in this chapter the coupling is considered as an input parameter or a realistic value has been chosen.

Since the two molecules have the same excitation energy $\hbar\omega_A$ and the coupling Ω is negative, the eigenstates and the corresponding eigenvalues (relative to the dimer ground state) are

$$|G\rangle := |g_1\rangle |g_2\rangle \, , \qquad E_G = 0 \, , \tag{4.16a}$$
$$|L\rangle := \frac{|g_1\rangle |e_2\rangle + |e_1\rangle |g_2\rangle}{\sqrt{2}} \, , \qquad E_L = \hbar\omega_A - |\Omega| \, , \tag{4.16b}$$
$$|H\rangle := \frac{|g_1\rangle |e_2\rangle - |e_1\rangle |g_2\rangle}{\sqrt{2}} \, , \qquad E_H = \hbar\omega_A + |\Omega| \, , \tag{4.16c}$$
$$|F\rangle := |e_1\rangle |e_2\rangle \, , \qquad E_F = 2\hbar\omega_A \, . \tag{4.16d}$$

Optical transitions between the eigenstates are proportional to the TDM, defined as the matrix element of the dipole operator

$$\hat{\vec{\mu}} = \sum_{j=1}^{2} \vec{\mu}_j \left(\hat{\sigma}_j^+ + \hat{\sigma}_j^-\right) \, . \tag{4.17}$$

The only non-vanishing elements of the TDM $\langle k| \hat{\vec{\mu}} |k'\rangle$ between two generic dimer eigenstates $|k\rangle$ and $|k'\rangle$ are:

$$\vec{\mu}_L := \langle G|\,\hat{\vec{\mu}}\,|L\rangle = \langle L|\,\hat{\vec{\mu}}\,|F\rangle = \frac{\vec{\mu}_2 + \vec{\mu}_1}{\sqrt{2}} = \sqrt{2}\mu \sin\theta\,\hat{x}\,, \tag{4.18a}$$

$$\vec{\mu}_H := \langle G|\,\hat{\vec{\mu}}\,|H\rangle = \langle H|\,\hat{\vec{\mu}}\,|F\rangle = \frac{\vec{\mu}_2 - \vec{\mu}_1}{\sqrt{2}} = \sqrt{2}\mu \cos\theta\,\hat{y}\,. \tag{4.18b}$$

Note that TDMs obey the conservation law $\mu_L^2 + \mu_H^2 = \mu_1^2 + \mu_2^2 = 2\mu^2$.

4.6.2 The Bloch-Redfield master equation

Here we sketch the derivation of the master equation introduced in Eq. (4.2). For convenience we reprint this master equation, which describes the interaction of a molecular aggregate with a collective photon and individual phonon baths:

$$\frac{d\hat{\rho}(t)}{dt} = -\frac{i}{\hbar}\left[\hat{H}_S, \hat{\rho}(t)\right] + \mathcal{D}_{BB}[\hat{\rho}(t)] + \mathcal{D}_T[\hat{\rho}(t)]\,, \tag{4.19}$$

where $\mathcal{D}_{BB}$ and $\mathcal{D}_T$ are Bloch-Redfield dissipators for the coupling to photons and phonons, respectively.

The photon dissipator is based on the assumption that the molecular absorbers are positioned close together relative to relevant optical wavelengths ($\sim 2\pi c/\omega_A$), so that all dipoles interact with the same shared optical field via the following collective interaction Hamiltonian:

$$\hat{H}_{I,\mathrm{opt}} = \sum_i \vec{\mu}_i \hat{\sigma}_i^x \otimes \sum_k f_k(\hat{a}_k + \hat{a}_k^\dagger)\,, \tag{4.20}$$

where f_k and $\hat{a}_k^{(\dagger)}$ are, respectively, the coupling strength and annihilation (creation) operator for the optical mode k. We then couple local phonon baths to each 2LS with repeated spin-boson interaction Hamiltonians:

$$\hat{H}_{I,\mathrm{vib}} = \sum_i \hat{\sigma}_i^z \otimes \sum_q g_{i,q}(\hat{b}_{i,q} + \hat{b}_{i,q}^\dagger)\,, \tag{4.21}$$

where $g_{i,q}$ and $\hat{b}_{i,q}^{(\dagger)}$ are, respectively, the coupling strength and annihilation (creation) operator for the vibrational mode q for the bath linked to site i.

The optical and vibrational Bloch-Redfield dissipators both take the form [49]

$$\begin{aligned}\mathcal{D}_\alpha = \sum_{n,m} C_n C_m \Big(& A_m(\omega_m)\rho_S(t)A_n^\dagger(\omega_n)\Gamma_{nm}(\omega_m) + A_n(\omega_n)\rho_S(t)A_m^\dagger(\omega_m)\Gamma_{nm}^\dagger(\omega_m) \\ & - \rho_S(t)A_m^\dagger(\omega_m)A_n(\omega_n)\Gamma_{nm}^\dagger(\omega_m) - A_n^\dagger(\omega_n)A_m(\omega_m)\rho_S(t)\Gamma_{nm}(\omega_m)\Big)\,,\end{aligned} \tag{4.22}$$

where the n, m summation is taken over all pairwise combinations of elements in each of the system interaction matrices from Eq. (4.20) and Eq. (4.21), i.e. the set of $\hat{\sigma}_i^x$ and $\hat{\sigma}_i^z$, respectively. The weighting terms, C_n, are determined by the transformation of these

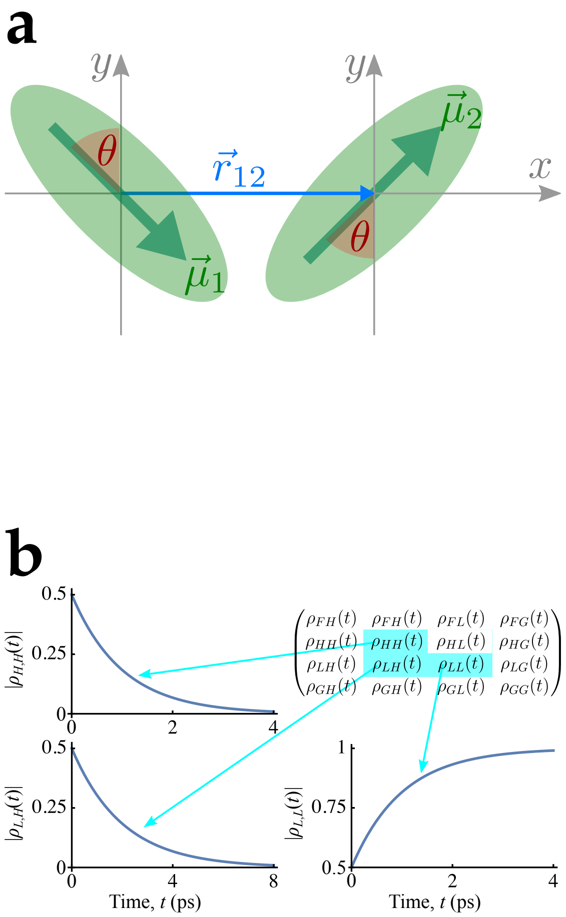

Figure 4.3: **(a)** Dimer geometry described in Eq. (4.14a). Each green ellipse represents a molecule. Orientation of the transition dipole moments (green arrows), vector joining the dipoles (blue arrow) and directions of the x, y axes (grey arrows) and θ angle are indicated. **(b)** Plots of the density matrix component evolution for the populations of, and coherence between $|H\rangle$ and $|L\rangle$. The dimer is only connected to independent phonon baths. The timescale for the relaxation of population in the single excitation manifold and for dephasing between $|H\rangle$ and $|L\rangle$ are both on the order of picoseconds. The dimer parameters are the same from the previous part of the chapter: ($\hbar\omega_A$ = 1.17 eV and optical lifetime, $1/\gamma_0$ = 36.8 ns), with θ = 0.07 rad and coupling Ω = 2000 cm^{-1} (0.25 eV). The initial density matrix is given by Eq. (4.26).

interaction matrices to the system eigenbasis (for example, the dipole contributions for transitions between different eigenstates in the optical case) [49]. Only the real part of the spectral correlation tensor is kept, leading to a solely dissipative contribution to the dynamics. This means that Lamb shifts and any other Hamiltonian renormalisation effects are assumed to have already been accounted for when setting up $\hat{H}_S$ (Eq. (4.1)). Further, we assume a flat optical spectral density, yielding optical environment correlation functions

$$\Gamma_{nm}(\omega) = \frac{1}{2}\kappa_{\text{opt}}\omega^3\big(1+n(\omega)\big)\,, \tag{4.23}$$

where the prefactor κ_{opt} is determined by the lifetime of an isolated 2LS, and $n(\omega)$ is the Bose-Einstein occupancy of modes, given by

$$n(\omega) = \frac{1}{e^{\beta\hbar\omega}-1}\,, \tag{4.24}$$

with $\beta = 1/k_B T_{BB}$, where T_{BB} is the photon black-body bath temperature and k_B is Boltzmann's constant. For photon processes the transition frequencies will be of the order of single molecule excitation frequency ω_A, and the factor ω^3 arises from the density of modes [49].

For simplicity and in the absence of detailed information about the nature of the vibrational environment we also keep the phonon spectral density flat and equal at each site, this results in vibrational environment correlation terms of the form

$$\Gamma_{nm}(\omega) = \frac{1}{2}\kappa_{\text{vib}}\omega\big(1+n(\omega)\big)\,, \tag{4.25}$$

where the prefactor κ_{vib} will be fixed by imposing a characteristic phonon spontaneous emission relaxation timescale of 1 picosecond. For instance for the dimer parameters we consider in the rest of the chapter, $\Omega = 2000\ \text{cm}^{-1} = 0.25$ eV, we set $\kappa_{\text{vib}} = 1.3\times10^{-3}$, unitless to obtain a relaxation of the order of 1 ps between the $|H\rangle$ and $|L\rangle$ states of the dimer. The Bose-Einstein occupation number $n(\omega)$ is here taken at room temperature (300 K). Phonon transition frequencies will be of order of the coupling Ω. In Fig. 4.3b we show that the timescale of evolution for the populations of, and dephasing between, states connected by phonons, is indeed picoseconds in a dimer system identical to what was considered in the rest of the chapter and coupled only to phonon baths with an initial state given by

$$\begin{pmatrix} 0 & 0 & 0 & 0 \\ 0 & 0.5 & 0.5 & 0 \\ 0 & 0.5 & 0.5 & 0 \\ 0 & 0 & 0 & 0 \end{pmatrix}\,. \tag{4.26}$$

4.6.3 From Bloch-Redfield to Lindblad master equation

The coupling to the photon bath is typically much weaker than the level spacing within the system. This allows the secular approximation to be applied to the Bloch-Redfield dissipator $\mathcal{D}_{BB}$, simplifying it to the Lindblad form [49]. In the eigenbasis, with transitions labelled by k, this yields

$$\begin{aligned}\mathcal{D}_{BB}[\hat{\rho}] =& \sum_k \gamma_k(\omega)\,(1+n_T(\omega))\left[\hat{\sigma}_k^- \hat{\rho}\hat{\sigma}_k^+ - \frac{1}{2}\left\{\hat{\sigma}_k^+\hat{\sigma}_k^-, \hat{\rho}\right\}\right] \\ &+ \sum_k \gamma_k(\omega) n_T(\omega)\left[\hat{\sigma}_k^+ \hat{\rho}\hat{\sigma}_k^- - \frac{1}{2}\left\{\hat{\sigma}_k^-\hat{\sigma}_k^+, \hat{\rho}\right\}\right] , \end{aligned} \tag{4.27}$$

where the optical rates are

$$\gamma_k(\omega) = \frac{\mu_k^2 \omega^3}{3\pi\epsilon_0 \hbar c^3} \tag{4.28}$$

with the transition dipoles μ_k^2 and universal constants ϵ_0 (vacuum permittivity), $\hbar$ (reduced Planck constant), and c (speed of light). We will now focus on a dimer system with optical transition frequencies $\omega_L = \omega_A - |\Omega|/\hbar$, $\omega_H = \omega_A + |\Omega|/\hbar$ and with the eigenstates $|G\rangle, |L\rangle, |H\rangle$ and $|F\rangle$ defined in Eq. (4.16). The thermal population of black-body photons at frequency ω is defined using Eq. (4.24). The curly brackets in Eq. (4.27) indicate the anticommutator, and the raising/lowering operators $\hat{\sigma}_k^{\pm}$ in it act on the eigenstates as shown in the following scheme

$$\begin{tikzcd}
|G\rangle \arrow[r, shift left, "\hat{\sigma}_L^+"] & |L\rangle \arrow[l, shift left, "\hat{\sigma}_L^-"] \arrow[r, shift left, "\hat{\sigma}_L^+"] & |F\rangle \arrow[l, shift left, "\hat{\sigma}_L^-"] \\
|G\rangle \arrow[r, shift left, "\hat{\sigma}_H^+"] & |H\rangle \arrow[l, shift left, "\hat{\sigma}_H^-"] \arrow[r, shift left, "\hat{\sigma}_H^+"] & |F\rangle \arrow[l, shift left, "\hat{\sigma}_H^-"] .
\end{tikzcd} \tag{4.29}$$

To make Eq. (4.27) more explicit, we first compute the transition rates between the populations of each eigenstate. We do that by projecting the black-body dissipator onto each eigenstate Eq. (4.16), obtaining

$$\begin{aligned}
\langle G|\,\mathcal{D}_{BB}[\hat{\rho}]\,|G\rangle =& \gamma_L(\omega_L)\,[1+n_T(\omega_L)]\,\rho_{LL} + \gamma_H(\omega_H)\,[1+n_T(\omega_H)]\,\rho_{HH} \\
&- \gamma_L(\omega_L) n_T(\omega_L)\rho_{GG} - \gamma_H(\omega_H) n_T(\omega_H)\rho_{GG} , && \text{(4.30a)} \\
\langle L|\,\mathcal{D}_{BB}[\hat{\rho}]\,|L\rangle =& \gamma_L(\omega_H)\,[1+n_T(\omega_H)]\,\rho_{FF} - \gamma_L(\omega_L)\,[1+n_T(\omega_L)]\,\rho_{LL} \\
&+ \gamma_L(\omega_L) n_T(\omega_L)\rho_{GG} - \gamma_L(\omega_H) n_T(\omega_H)\rho_{LL} , && \text{(4.30b)} \\
\langle H|\,\mathcal{D}_{BB}[\hat{\rho}]\,|H\rangle =& \gamma_H(\omega_L)\,[1+n_T(\omega_L)]\,\rho_{FF} - \gamma_H(\omega_H)\,[1+n_T(\omega_H)]\,\rho_{HH} \\
&+ \gamma_H(\omega_H) n_T(\omega_H)\rho_{GG} - \gamma_H(\omega_L) n_T(\omega_L)\rho_{HH} , && \text{(4.30c)} \\
\langle F|\,\mathcal{D}_{BB}[\hat{\rho}]\,|F\rangle =& \gamma_L(\omega_H) n_T(\omega_H)\rho_{LL} + \gamma_H(\omega_L) n_T(\omega_L)\rho_{HH} \\
&- \gamma_L(\omega_H)\,[1+n_T(\omega_H)]\,\rho_{FF} - \gamma_H(\omega_L)\,[1+n_T(\omega_L)]\,\rho_{FF} . && \text{(4.30d)}
\end{aligned}$$

As one can see, the dynamics of the populations are coupled only to the populations of the other states (ρ_{kk}) and not to the coherences ($\rho_{kk'}$ with $k \neq k'$). This allows to write a set of rate equations (i.e. a Pauli master equation) for photon absorption and spontaneous emission for the populations of the four eigenstates.

Similarly, the dissipator describing the coupling of the dimer to a phonon bath can also be approximated in the Lindblad form and it produces dynamics where the populations are decoupled from the coherences. Specifically, for a dimer system, we have

$$\begin{aligned}
\langle G|\,\mathcal{D}_T[\hat{\rho}]\,|G\rangle &= 0\,, && (4.31\text{a})\\
\langle L|\,\mathcal{D}_T[\hat{\rho}]\,|L\rangle &= \Gamma_\Omega\,(1+n_\Omega)\,\rho_{HH} - \Gamma_\Omega n_\Omega \rho_{LL}\,, && (4.31\text{b})\\
\langle H|\,\mathcal{D}_T[\hat{\rho}]\,|H\rangle &= -\Gamma_\Omega\,(1+n_\Omega)\,\rho_{HH} + \Gamma_\Omega n_\Omega \rho_{LL}\,, && (4.31\text{c})\\
\langle F|\,\mathcal{D}_T[\hat{\rho}]\,|F\rangle &= 0\,, && (4.31\text{d})
\end{aligned}$$

where the thermal relaxation rate $\Gamma_\Omega = 2|\Omega|\kappa_{\text{vib}}$ is proportional to the bath spectral density at the energy $2|\Omega|$ (with Ω being the coupling between the molecules) and the thermal population is defined with Eq. (4.24), with $T = 300$ K being the phonon temperature.

Combining the sunlight and phonon contributions, we have the rate equation for a dimer system

$$\begin{aligned}
\frac{d\rho_{GG}}{dt} =& \gamma_L(\omega_L)\,[1+n_T(\omega_L)]\,\rho_{LL} + \gamma_H(\omega_H)\,[1+n_T(\omega_H)]\,\rho_{HH}\\
&- \gamma_L(\omega_L) n_T(\omega_L)\rho_{GG} - \gamma_H(\omega_H) n_T(\omega_H)\rho_{GG}\,, && (4.32\text{a})\\
\frac{d\rho_{LL}}{dt} =& \gamma_L(\omega_H)\,[1+n_T(\omega_H)]\,\rho_{FF} - \gamma_L(\omega_L)\,[1+n_T(\omega_L)]\,\rho_{LL}\\
&+ \gamma_L(\omega_L) n_T(\omega_L)\rho_{GG} - \gamma_L(\omega_H) n_T(\omega_H)\rho_{LL}\\
&+ \Gamma_\Omega\,[1+n_\Omega]\,\rho_{HH} - \Gamma_\Omega n_\Omega \rho_{LL}\,, && (4.32\text{b})\\
\frac{d\rho_{HH}}{dt} =& \gamma_H(\omega_L)\,[1+n_T(\omega_L)]\,\rho_{FF} - \gamma_H(\omega_H)\,[1+n_T(\omega_H)]\,\rho_{HH}\\
&+ \gamma_H(\omega_H) n_T(\omega_H)\rho_{GG} - \gamma_H(\omega_L) n_T(\omega_L)\rho_{HH}\\
&- \Gamma_\Omega\,[1+n_\Omega]\,\rho_{HH} + \Gamma_\Omega n_\Omega \rho_{LL}\,, && (4.32\text{c})\\
\frac{d\rho_{FF}}{dt} =& -\gamma_L(\omega_H)\,[1+n_T(\omega_H)]\,\rho_{FF} - \gamma_H(\omega_L)\,[1+n_T(\omega_L)]\,\rho_{FF}\\
&+ \gamma_L(\omega_H) n_T(\omega_H)\rho_{LL} + \gamma_H(\omega_L) n_T(\omega_L)\rho_{HH}\,, && (4.32\text{d})
\end{aligned}$$

based on treating the influence of the environments on the dimer dynamics to second order and the Born-Markov approximation (both inherent in the Bloch-Redfield formalism), and the additional secular simplification of each dissipator to its Lindblad form.

We can compare the Bloch-Redfield approach (Eq. (4.22)) – solved numerically – against the rate equations arising from the four-level Lindblad dissipators as presented above. For the parameter ranges we consider, we find the two results are consistent to machine precision. This is do be expected due to the large energy splitting we consider between the two single-excitation eigenstates (but we would expect the results to begin diverging when considering near-degenerate terms from much smaller or vanishing coupling between 2LSs). Note that the validity of the Lindblad master equation approximation for the populations of a molecular aggregate is the basis of our laser equations in this chapter.

4.6.4 Lasing equations for molecular aggregates

In this section we expand on the derivation the lasing equations that is given in the main part of the chapter.

For convenience and ease of readability, we here duplicate most of the key equations, beginning with the Hamiltonian for a generic molecular aggregate N molecules, written with the usual Pauli operators as

$$\hat{H}_S = \sum_{j=1}^{N} \frac{\hbar\omega_A}{2}\hat{\sigma}_j^z + \sum_{i,j}\Omega_{i,j}\left(\hat{\sigma}_i^+\hat{\sigma}_j^- + \hat{\sigma}_j^+\hat{\sigma}_i^-\right) , \tag{4.33}$$

where $\Omega_{i,j}$ is the inter-molecular coupling, which here we describe through a dipole-dipole interaction [68, 116, 117] (see also the sections about Bio-inspired aggregates), apart from very close-by molecules for which the interaction is not determined by the transition dipole of the molecule alone. Eq. (4.33) represents a molecular aggregate where each molecule is described as a two-level system. As mentioned in the main part of the chapter (and for the case of a dimer validated in Fig. 4.4), we can limit our analysis to the ground state $|G\rangle$, which represent a state in which all molecules are in their ground state, and the single excitation manifold made of N states $|j\rangle$ which represent a state in which the j-th molecule is excited while all the others are in the ground state. The interaction of the molecular aggregate with black-body radiation and phonons is then governed by the master equation Eq. (4.19). As established above, Eq. (4.19) can be safely secularised and simplified to Lindblad form [49]. Thus the coupling with the phonon bath and the black-body photon bath can be described by rate equations for the populations.

In order to have lasing, we consider an ensemble of molecular aggregates randomly distributed inside the cavity volume with density n_A. We consider a cavity mode at frequency ω_c filled with a classical field. The coupling of the molecular aggregate single excitation eigenstate $|k\rangle$ to the resonant cavity mode is described by incoherent transition rates for large enough dephasing as discussed in the main part of the chapter. Below we report the rates induced by the cavity field for convenience,

$$B_k n = n\frac{|\mu_k|^2\omega_c}{3V\hbar\epsilon_o}\frac{\Gamma_\phi}{\Gamma_\phi^2 + (\Delta_k/\hbar)^2} , \tag{4.34}$$

where $\Delta_k = (E_k - \hbar\omega_c)$ is the energy detuning between the single excitation state k and the mode of the cavity, μ_k is the transition dipole moment of the single excitation state $|k\rangle$, Γ_ϕ is the dephasing rate and n is the number of photons in the cavity mode. The factor 3 in the denominator comes from the average over the aggregate orientations. For a derivation of Eq. (4.34), see Eq. (4.68) and the analysis in the same section.

Let us first focus on the population of the ground state P_G. Due to the optical pumping from the black-body radiation there will be a transition rate from the ground state to the single excitation states given by $R_k = n_T(\omega_k)\gamma_k(\omega_k)$, where $\gamma_k(\omega_k)$ is given by Eq. (4.28) and is the spontaneous decay rate of the k-th eigenstate. Moreover, the cavity mode will drive transitions from the ground state to the states $|k\rangle$, given by the rate $B_k n$. Thus, for the population of the ground state we can write

$$\frac{dP_G}{dt} = -\sum_k R_k P_G + \sum_k [R_k + \gamma_k(\omega_k)] P_k - \sum_k B_k n P_G + \sum_k B_k n P_k \,.$$

The total population in the single excitation manifold can be written as $P_e = \sum_k P_k$ and since we assume the other manifolds are not populated we can write $P_G + P_e = 1$. Assuming thermal relaxation in the single excitation manifold to be the fastest time scale, the populations in the single excitation manifold are always at thermal equilibrium so that we have

$$P_k = P_e p_k \quad \text{with} \quad p_k = \frac{e^{-E_k/k_B T}}{\sum_j e^{-E_j/k_B T}} \,,$$

where E_k is the energy of the excitonic state $|k\rangle$. We consider a room temperature vibration environment by fixing $T = 300$ K. Under these assumptions the population of the ground state obeys the following equation,

$$\frac{dP_G}{dt} = -P_G \sum_k R_k + P_e \sum_k [R_k + \gamma_k(\omega_k)] p_k - n P_G \sum_k B_k + n P_e \sum_k B_k p_k \,.$$

We can now define

$$R_u = \sum_k R_k \quad \text{and} \quad R_d = \sum_k [R_k + \gamma_k(\omega_k)] p_k \,,$$

and we further introduce:

$$B_{tot} = \sum_k B_k \quad \text{and} \quad \langle B \rangle = \sum_k B_k p_k \,,$$

where p_k is the Boltzmann occupation probability at thermal equilibrium of the state $|k\rangle$.

With these definitions, and defining the density of aggregates in the excited states as $N_e = n_A P_e$ and the density of aggregates in the ground state as $N_G = n_A P_G$, the laser equations coupling the population in the single excitation manifold of the molecular aggregates and the number of photons in the cavity become

$$\frac{dN_e}{dt} = -R_d N_e + R_u N_G - \langle B \rangle n N_e + B_{tot} n N_G \,, \tag{4.35a}$$

$$\frac{dn}{dt} = V \langle B \rangle n N_e - V B_{tot} n N_G - n\kappa \,, \tag{4.35b}$$

where VN_e and VN_G are the total numbers of molecular aggregates in the excited and ground manifold respectively. Finally by defining the population difference per unit volume between the population in the single-excitation manifold and the population in the ground state as $D = N_e - N_0$ we obtain the laser equations reported in Eq. (4.6).

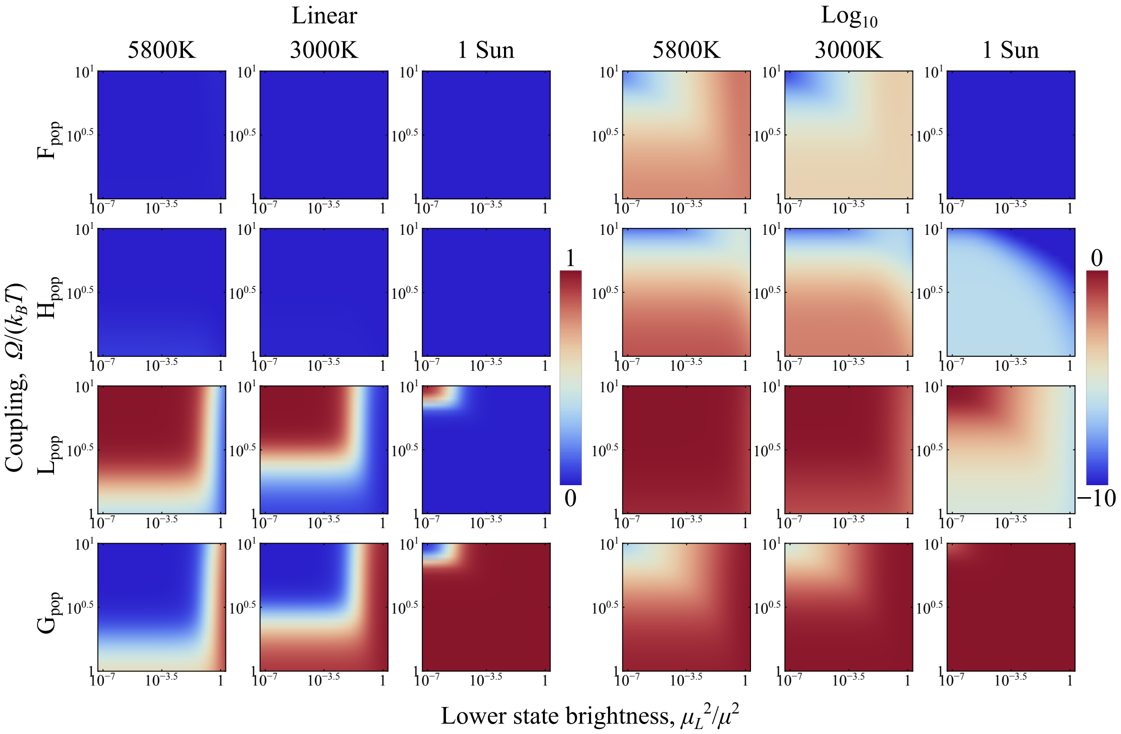

Figure 4.4: Total population of all four states of the dimer system at the steady-state, solving with the Bloch-Redfield approach Eq. (4.19). A linear scale on the color bar (left panels) is used to show population inversion in the lower states, while a logarithmic scale (right panels) shows the order of magnitude of the population in the higher energy states. We use the following dimer parameters: the single molecule excitation energy is $\hbar\omega_A = 1.17$ eV and the spontaneous optical lifetime for the absorbers was fixed at $1/\gamma_0 = 36.8$ ns. Phonon bath at 300 K, and phonon decay rate defined to match a picosecond spontaneous decay rate for $\theta = 0.07$ rad, where θ determines the relative orientation of the TDMs of the molecules in the dimer, see Fig. (4.3 a). No cavity is attached. Comparison of cases with photon bath at 5800 K, 3000 K, and natural '1 sun' (natural sunlight illumination).

4.6.5 Population inversion for a dimer

Here we analyze the parameter region for obtaining population inversion for a dimer under black-body pumping using the full Bloch-Redfield master equation. Moreover we check the validity of the analytical expression given in Eq. (4.10), for the population difference at the steady-state.

In Fig. 4.4 we plot the populations of the dimer eigenstates at the steady-state, by solving the Master Equation Eq. (4.19) varying the parameters Ω an μ_L^2 in three cases. We remind that μ_L is the TDM of the $|L\rangle$ state of the dimer. We set photon bath temperatures at $T_{BB} = 5800$ K, $T_{BB} = 3000$ K, and also consider a '1 sun' case, where $T_{BB} = 5800$ K, but all photon thermal population terms are reduced by the factor f_S, see Eq. (4.13), to account for the solid angle of the Sun as observed from Earth. We plot the populations of all four states using both linear and logarithmic scales. The results presented here show that population inversion is possible for large enough coupling Ω in sufficiently dark dimers (as measured by μ_L^2/μ^2). Moreover, we see that the doubly excited state $|F\rangle$ can always be neglected, justifying the approximations used in the main part of the chapter to limit our considerations to the single excitation manifold.

We now compare the results of the full Bloch-Redfield model Eq. (4.19) against Eq. (4.10). In Fig. 4.5 we consider the same photon temperatures that were used in Fig. 4.4 and plot the the population difference between the single excitation manifold and the ground state. The results of the Bloch-Redfield model (full curves) are compared with the analytical expression given in Eq. (4.10) (dashed curves). Moreover their differences are shown in the lower panels for the three different black-body temperatures. While there are some discrepancies between the two approaches there is generally very good agreement. Note that as the temperature of the photon bath is reduced, larger couplings, as well as weaker lower state brightness values are required to achieve population inversion.

4.6.6 Coupling dimer to a cavity: modification of the Hamiltonian

In this section we describe the coupling of the dimer to a cavity mode at frequency $\omega_c = \omega_L$, where ω_L is the transition frequency between the $|G\rangle$ and $|L\rangle$ states of the dimer.

To couple a cavity resonant with the energy of $|L\rangle$ to the dimer we begin with the laboratory frame dimer Hamiltonian in the site basis, $\hat{H}_S$ [Eq. (4.1)]. In this section we set $\hbar = 1$ for simplicity. We describe the interaction between the dimer and the cavity field by adding the time-dependent matrix elements $\vec{\mu}_j \cdot \vec{E}(t)$ to $\hat{H}_S$. Such matrix elements describe the interaction energy of each single-molecule TDM ($\vec{\mu}_j$, $j = 1, 2$) with the time-dependent cavity electric field $\vec{E}(t) = \vec{E}_0 \cos(\omega_L t)$, which has a fixed polarization (determined by the direction of $\vec{E}_0 = E_0\hat{\epsilon}$) and oscillates at frequency $\omega_c =$

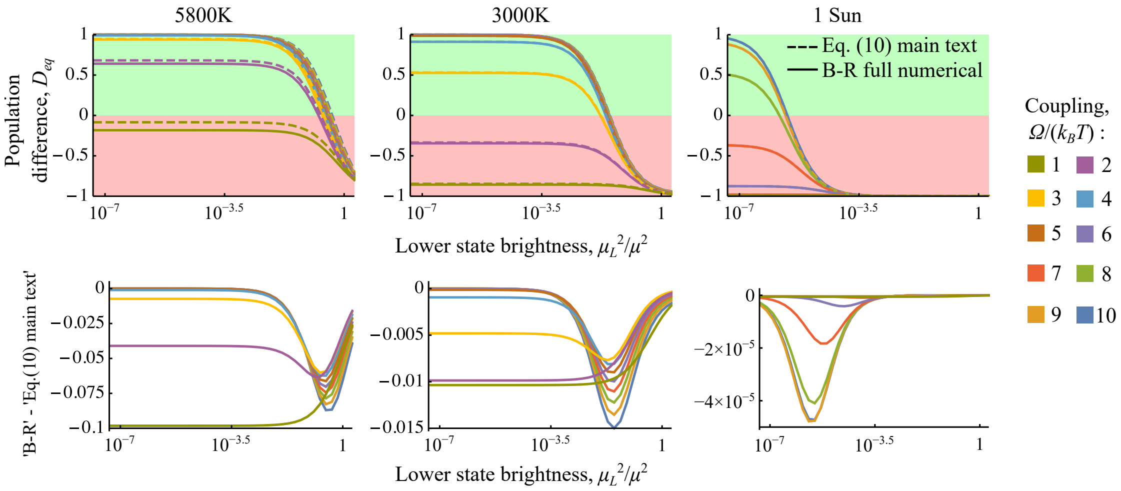

Figure 4.5: Comparison between the approximate steady-state solution given by Eq. (4.10) and the exact solution of Eq. (4.19) for different values of the coupling, $\Omega/(k_BT)$ (with $T = 300$ K), and lower state brightness. Shown below: the differences between the results of the two methods. Dimer parameters: $\hbar\omega_A = 1.17$ eV and single-molecule spontaneous optical lifetime fixed at $1/\gamma_0 = 36.8$ ns. Phonon bath at 300 K, and phonon decay rate defined to match a picosecond thermal relaxation time. No cavity is attached. Comparison of cases with photon bath at 5800 K, 3000 K, and '1 sun'.

ω_L. The resulting Hamiltonian is:

$$\hat{H} = \begin{pmatrix} 2\omega_A & \vec{\mu}_1\cdot\vec{E}_0\cos(\omega_L t) & \vec{\mu}_2\cdot\vec{E}_0\cos(\omega_L t) & 0 \\ \vec{\mu}_1\cdot\vec{E}_0\cos(\omega_L t) & \omega_A & \Omega & \vec{\mu}_1\cdot\vec{E}_0\cos(\omega_L t) \\ \vec{\mu}_2\cdot\vec{E}_0\cos(\omega_L t) & \Omega & \omega_A & \vec{\mu}_2\cdot\vec{E}_0\cos(\omega_L t) \\ 0 & \vec{\mu}_1\cdot\vec{E}_0\cos(\omega_L t) & \vec{\mu}_2\cdot\vec{E}_0\cos(\omega_L t) & 0 \end{pmatrix}, \quad (4.36)$$

written in the site basis

$$\{\,|e_1\rangle\,|e_2\rangle\,,\,|e_1\rangle\,|g_2\rangle\,,\,|g_1\rangle\,|e_2\rangle\,,\,|g_1\rangle\,|g_2\rangle\,\}\,. \quad (4.37)$$

The $\vec{\mu}_1\cdot\vec{E}_0$ and $\vec{\mu}_2\cdot\vec{E}_0$ terms account for the alignment of the single-molecule dipole moments with the orientation of the cavity containing the field, and are, respectively, now relabelled to E_1 and E_2. We then choose the unitary transformation matrix

$$\hat{U} = \begin{pmatrix} e^{i2\omega_L t} & 0 & 0 & 0 \\ 0 & e^{i\omega_L t} & 0 & 0 \\ 0 & 0 & e^{i\omega_L t} & 0 \\ 0 & 0 & 0 & 1 \end{pmatrix}, \quad (4.38)$$

to move to a frame rotating at the frequency of the lasing transition with the transformed (prime) Hamiltonian given by

$$\hat{H}' = \hat{U}\hat{H}\hat{U}^\dagger + i\hat{U}\frac{d\hat{U}^\dagger}{dt}\,. \quad (4.39)$$

The transformation gives

$$\hat{H}' = \begin{pmatrix} 2\omega_A - 2\omega_L & \frac{E_1}{2}(1+e^{i2\omega_L t}) & \frac{E_2}{2}(1+e^{i2\omega_L t}) & 0 \\ \frac{E_1}{2}(1+e^{-i2\omega_L t}) & \omega_A - \omega_L & \Omega & \frac{E_1}{2}(1+e^{i2\omega_L t}) \\ \frac{E_2}{2}(1+e^{-i2\omega_L t}) & \Omega & \omega_A - \omega_L & \frac{E_2}{2}(1+e^{i2\omega_L t}) \\ 0 & \frac{E_1}{2}(1+e^{-i2\omega_L t}) & \frac{E_2}{2}(1+e^{-i2\omega_L t}) & 0 \end{pmatrix}. \tag{4.40}$$

We then drop the fast oscillating terms $e^{i2\omega_L t}$ (oscillating at twice the lasing frequency) to leave

$$\hat{H}' \approx \begin{pmatrix} 2\omega_A - 2\omega_L & \frac{E_1}{2} & \frac{E_2}{2} & 0 \\ \frac{E_1}{2} & \omega_A - \omega_L & \Omega & \frac{E_1}{2} \\ \frac{E_2}{2} & \Omega & \omega_A - \omega_L & \frac{E_2}{2} \\ 0 & \frac{E_1}{2} & \frac{E_2}{2} & 0 \end{pmatrix}. \tag{4.41}$$

The next step is to move to the eigenbasis of the dimer. We temporarily drop the field terms to have

$$\hat{H}'_S = \begin{pmatrix} 2\omega_A - 2\omega_L & 0 & 0 & 0 \\ 0 & \omega_A - \omega_L & \Omega & 0 \\ 0 & \Omega & \omega_A - \omega_L & 0 \\ 0 & 0 & 0 & 0 \end{pmatrix}. \tag{4.42}$$

Using $\omega_L = \omega_A - |\Omega|$, we have that $\hat{H}'_S$ diagonalises (tilde) to

$$\tilde{\hat{H}}'_S = \begin{pmatrix} 2\omega_A - 2\omega_L & 0 & 0 & 0 \\ 0 & \omega_A - \omega_L + |\Omega| & 0 & 0 \\ 0 & 0 & \omega_A - \omega_L - |\Omega| & 0 \\ 0 & 0 & 0 & 0 \end{pmatrix} = \begin{pmatrix} 2|\Omega| & 0 & 0 & 0 \\ 0 & 2|\Omega| & 0 & 0 \\ 0 & 0 & 0 & 0 \\ 0 & 0 & 0 & 0 \end{pmatrix}. \tag{4.43}$$

In the rotating frame, the two lower energy states $|L\rangle$, and $|G\rangle$ appear degenerate since they are linked by a transition which is driven by the resonant lasing field in the cavity.

Finally, the interaction matrix elements with the cavity field (in the rotating frame),

$$\begin{pmatrix} 0 & \frac{E_1}{2} & \frac{E_2}{2} & 0 \\ \frac{E_1}{2} & 0 & 0 & \frac{E_1}{2} \\ \frac{E_2}{2} & 0 & 0 & \frac{E_2}{2} \\ 0 & \frac{E_1}{2} & \frac{E_2}{2} & 0 \end{pmatrix}, \tag{4.44}$$

need to be moved to the newfound dimer diagonal basis, becoming

$$\frac{1}{\sqrt{8}} \begin{pmatrix} 0 & E_1 + E_2 & \frac{\Omega}{|\Omega|}(-E_1 + E_2) & 0 \\ E_1 + E_2 & 0 & 0 & E_1 + E_2 \\ \frac{\Omega}{|\Omega|}(-E_1 + E_2) & 0 & 0 & \frac{\Omega}{|\Omega|}(-E_1 + E_2) \\ 0 & E_1 + E_2 & \frac{\Omega}{|\Omega|}(-E_1 + E_2) & 0 \end{pmatrix}. \tag{4.45}$$

In general, we obtain the full field-coupled Hamiltonian by adding Eq. (4.45) to Eq. (4.43), that can be written as

$$\hat{H}_{S-C} := \hat{H}' = \begin{pmatrix} 2|\Omega| & g_H E_0 & g_L E_0 & 0 \\ g_H E_0 & 2|\Omega| & 0 & g_H E_0 \\ g_L E_0 & 0 & 0 & g_L E_0 \\ 0 & g_H E_0 & g_L E_0 & 0 \end{pmatrix} , \tag{4.46}$$

where $g_{L,H}$ are coupling constants and $E_0 = |\vec{E}_0|$ is the magnitude of the cavity electric field. This Hamiltonian will be substituted into Eq. (4.19), to find the evolution of the dimer and field.

We will be mostly interested in the case where the lasing mode of the cavity is matched to the frequency of the $|L\rangle \leftrightarrow |G\rangle$ transition and the orientation of the molecular aggregate is random w.r.t the cavity field polarization. In this case we may set $g_H E_0 = \mu_H E_0/(2\sqrt{3})$ and $g_L E_0 = \mu_L E_0/(2\sqrt{3})$. In the case where the lasing mode of the cavity is matched to the frequency and polarisation of the $|L\rangle \leftrightarrow |G\rangle$ transition, in we may set $g_H E_0 = 0$ and $g_L E_0 = \mu_L E_0/2$ through requiring $\vec{\mu}_1 \cdot \vec{E} = -\vec{\mu}_2 \cdot \vec{E}$.

4.6.7 Including dephasing and the coupling to the cavity in the Bloch-Redfield master equation

In Eq. (4.19), dephasing between the ground state and higher excitation manifolds is not properly included (rather, such a Bloch-Redfield approach only captures vibrationally driven dephasing within each manifold). Therefore, in the absence of introducing additional dephasing Lindblad operators, dephasing between different excitation subspaces only occurs on optical (nanosecond) timescales. However, much faster electronic dephasing will be present in any realistic situation, typically on a (sub)-picosecond timescale. For this reason, we supplement our master equation Eq. (4.19) with additional pure dephasing Lindblad operators as described below. We shall see that this dephasing plays a crucial role in that it gives rise to effectively incoherent energy exchange with the resonantly cavity, provided it is faster than the Rabi frequency.

We illustrate the inclusion of pure dephasing using the example of a dimer system with the usual eigenbasis

$$\{\, |F\rangle \,,\, |H\rangle \,,\, |L\rangle \,,\, |G\rangle \,\} \,. \tag{4.47}$$

Specifically, we introduce phenomenological dephasing processes between each pair of eigenstates, apart from the $|H\rangle - |L\rangle$ pair. Indeed, we do not include a phenomenological operator linking the two single-excitation states as dephasing (as well as relaxation) between these states is already included by the phonon dissipator, as is evidenced in the decay of coherence seen in Fig. 4.3b. We constructed a range of dephasing Lindblad dissipators

$$\mathcal{D}_\phi[\hat{\rho}] = \frac{2}{7}\Gamma_\phi \sum_k \hat{L}_k \hat{\rho} \hat{L}_k^\dagger - \frac{1}{2}\{\hat{L}_k^\dagger \hat{L}_k, \hat{\rho}\} \tag{4.48}$$

using the following $\hat{L}_k$ operators:

$$\begin{pmatrix}1 & 0 & 0 & 0\\ 0 & -1 & 0 & 0\\ 0 & 0 & 0 & 0\\ 0 & 0 & 0 & 0\end{pmatrix}, \begin{pmatrix}1 & 0 & 0 & 0\\ 0 & 0 & 0 & 0\\ 0 & 0 & -1 & 0\\ 0 & 0 & 0 & 0\end{pmatrix}, \begin{pmatrix}1 & 0 & 0 & 0\\ 0 & 0 & 0 & 0\\ 0 & 0 & 0 & 0\\ 0 & 0 & 0 & -1\end{pmatrix},$$
$$\begin{pmatrix}0 & 0 & 0 & 0\\ 0 & 1 & 0 & 0\\ 0 & 0 & 0 & 0\\ 0 & 0 & 0 & -1\end{pmatrix}, \begin{pmatrix}0 & 0 & 0 & 0\\ 0 & 0 & 0 & 0\\ 0 & 0 & 1 & 0\\ 0 & 0 & 0 & -1\end{pmatrix}. \tag{4.49}$$

We plot the evolution of our coherence term of interest, $\rho_{G,L}(t)$, for various dephasing rates in Fig. 4.6a, using the Bloch-Redfield equation given in Eq. (4.19) with the addition of $\mathcal{D}_\phi[\hat{\rho}]$ and without the coupling with the photon bath. With the inclusion of these phenomenological dissipators we observe decay in the coherence term at the anticipated rapid timescales. The factor of $2/7$ in Eq. (4.48) ensures that the observed decoherence of $\rho_{G,L}(t)$ decays as $e^{-\Gamma_\phi t}$.

Finally we can write the Bloch-Redfield master equation which includes both the dephasing terms and the Hamiltonian of the system-cavity coupling, Eq. (4.46). Adding the new dissipative terms to Eq. (4.19) we obtain

$$\frac{d\hat{\rho}(t)}{dt} = -\frac{i}{\hbar}\left[\hat{H}_{S-C}, \hat{\rho}(t)\right] + \mathcal{D}_{BB}[\hat{\rho}(t)] + \mathcal{D}_T[\hat{\rho}(t)] + \mathcal{D}_\phi[\hat{\rho}(t)]\,. \tag{4.50}$$

4.6.8 Full 4-level Bloch-Redfield: coherent laser equations

In the following, we write a closed system of laser equations for the dimer coupled to the cavity field, in the frame of a semi-classical description. As far as the dimer is concerned, its dynamics is described by the master equation Eq. (4.50). Note that the electric field magnitude $E_0 = E_0(t)$ is a time-dependent quantity, because it exchanges energy with the dimers and loses energy out of the cavity. For this reason Eq. (4.50) must be extended by an equation determining the evolution of the electric field.

The evolution of the classical field in the cavity derives from Maxwell Equations [136],

$$\nabla^2\vec{E}(t) - \frac{1}{c^2}\frac{\partial^2}{\partial t^2}\vec{E}(t) = -\frac{1}{\epsilon_0 c^2}\frac{\partial^2}{\partial t^2}\vec{P}(t)\,, \tag{4.51}$$

where $\vec{E}(t) = E_0(t)\,\hat{e}\cos(\omega_L t)$ is the oscillating electric field in the cavity with polarization $\hat{e}$ and $\vec{P}(t) = P_0(t)\hat{e}\cos(\omega_L t)$ is the oscillating polarization per unit volume, where $E_0(t)$ and $P_0(t)$ are their slowly-varying envelopes. Since they vary on timescales that are much slower than $\sim 2\pi/\omega_L$, we can apply the slowly-varying envelope approximation (SVEA) [136], so that Eq. (4.51) becomes

$$\frac{dE_0}{dt} = \frac{i\omega_L}{2\epsilon_0}P_0\,. \tag{4.52}$$

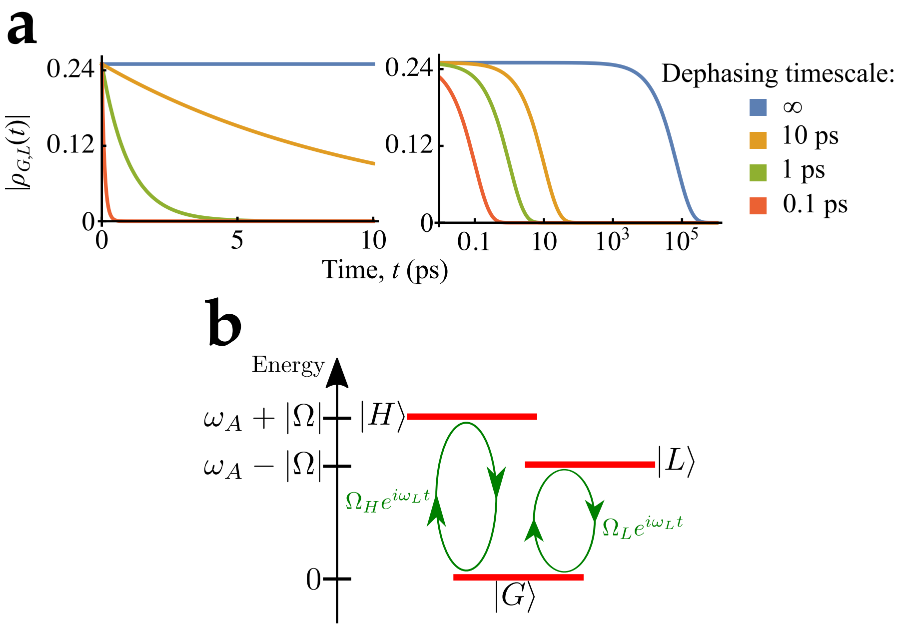

Figure 4.6: **(a)** Plots of the decay of the $\rho_{G,L}(t)$ coherence term in a dimer connected to a 3000 K photon bath for solar proccesses and local phonon baths but no cavity. Phenomenological dephasing operators are added at varying rates and this produces the expected decay on picosecond timescales. The parameters match those used in Fig. 4.3b. **(b)** Dimer levels excluding the double-excitation $|F\rangle$ state, with a coherent coupling (curves) induced by the cavity field. Here $\hbar = 1$ and the cavity frequency is $\omega_L = \omega_A - |\Omega|$. The Rabi frequencies are $\Omega_L = \mu_L E_0/(2\sqrt{3})$ and $\Omega_H = \mu_H E_0/(2\sqrt{3})$, where $\mu_{L,H}$ are the magnitudes of the TDMs, $\sqrt{3}$ comes from an average over the dimer orientations and E_0 is the amplitude of the cavity field.

We consider an ensemble of dimers with density n_A in a volume V, so that the polarization component parallel to the field is $P_0 = 2n_A\langle\left(\hat{\vec{\mu}}\cdot\hat{\epsilon}\right)\rangle$. Here the average TDM is the expectation value of the dipole operator averaged over the dimer orientations, $\langle\left(\hat{\vec{\mu}}\cdot\hat{\epsilon}\right)\rangle = \langle\mathrm{Tr}[\left(\hat{\vec{\mu}}\cdot\hat{\epsilon}\right)\hat{\rho}]\rangle_{\mathrm{or}}$, and the TDM operator in the dimer eigenbasis is

$$\hat{\vec{\mu}} = \begin{pmatrix} 0 & \vec{\mu}_H & \vec{\mu}_L & 0 \\ \vec{\mu}_H & 0 & 0 & \vec{\mu}_H \\ \vec{\mu}_L & 0 & 0 & \vec{\mu}_L \\ 0 & \vec{\mu}_H & \vec{\mu}_L & 0 \end{pmatrix}. \tag{4.53}$$

Taking the trace $\mathrm{Tr}[\left(\hat{\vec{\mu}}\cdot\hat{\epsilon}\right)\hat{\rho}]$ we have

$$P_0 = 2n_A\langle[(\vec{\mu}_L\cdot\hat{\epsilon})\,(\rho_{LG}+\rho_{FL}) + (\vec{\mu}_H\cdot\hat{\epsilon})\,(\rho_{HG}+\rho_{FH})]\rangle_{\mathrm{or}}\,, \tag{4.54}$$

where the subscript "or" accounts for the average over different dimer orientations. Replacing Eq. (4.54) into Eq. (4.52) we have

$$\frac{dE_0}{dt} = \frac{i\omega_L n_A}{\epsilon_0}\langle[(\vec{\mu}_L\cdot\hat{\epsilon})\,(\rho_{LG}+\rho_{FL}) + (\vec{\mu}_H\cdot\hat{\epsilon})\,(\rho_{HG}+\rho_{FH})]\rangle_{\mathrm{or}}\,. \tag{4.55}$$

Now we proceed by performing the orientational averaging. It can be shown [see Eq. (4.64) in the following section] that the coherence terms are proportional to the corresponding TDM, for example $(\rho_{LG}+\rho_{FL}) \propto (\vec{\mu}_L\cdot\hat{\epsilon})$. For this reason, the average over dipole orientations is proportional to the squared amplitude of the TDM along $\hat{\epsilon}$, namely $\langle(\vec{\mu}_L\cdot\hat{\epsilon})(\rho_{LG}+\rho_{FL})\rangle_{\mathrm{or}} \propto \langle(\vec{\mu}_L\cdot\hat{\epsilon})^2\rangle_{\mathrm{or}}$, and similarly for the $(\vec{\mu}_H\cdot\hat{\epsilon})$ term. When the dimers are randomly oriented, $\langle(\vec{\mu}_L\cdot\hat{\epsilon})^2\rangle_{\mathrm{or}} = \mu_L^2/3$. Finally, we add the term $-\kappa E_0/2$ accounting for the losses from the cavity, so that we have

$$\frac{dE_0}{dt} = -\frac{\kappa E_0}{2} - i\alpha n_A\left[g_H(\rho_{F,H}+\rho_{H,G}) + g_L(\rho_{F,L}+\rho_{L,G})\right]\,, \tag{4.56}$$

where κ is the field loss rate, $\alpha = 2\omega_L/\epsilon_0$ and $g_{L,H} = \mu_{L,H}/(2\sqrt{3})$. Note that in the case of an ordered ensemble of dimers, with $\vec{\mu}_L$ TDMs parallel with the cavity electric field, it should be $g_L = \mu_L/2$ and $g_H = 0$. Thus the final laser equations are given by the two coupled equations Eq. (4.50) and Eq. (4.56). Before showing the results of these full coherent laser equations, we introduce in the following sections further approximations leading to the working set of rate equations.

4.6.9 Results with 4-level Bloch-Redfield static field model

While the most complete version of our model considers a cavity field that is coupled dynamically to the molecular aggregates, see Fig. 4.1b, considering the coupling of an ensemble of molecular aggregates with a non-evolving static field allows us to focus on a few more subtle behavioural aspects.

In the main part of the chapter, the laser equations [see Eqs. (4.7) and Eqs. (4.8)], have been derived under the assumption that the population of the double excited state $|F\rangle$ of the dimer can be neglected and that the dephasing rate between $|L\rangle$ and $|G\rangle$ is larger than the Rabi frequency induced by the coupling of the $|L\rangle \leftrightarrow |G\rangle$ transition with the cavity mode. Nevertheless, when a strong intensity field is present in a cavity, this could also induce transitions between $|L\rangle$ and $|F\rangle$, despite the fact that this transition is detuned from the cavity frequency by 2Ω and hence suppressed. In particular, the suppression will cease to be effective once the cavity field is sufficiently intense and the Rabi frequency approaches the detuning.

Moreover, if the polarisation of the cavity lasing mode is not quite parallel with the dipole moment of the $|L\rangle \leftrightarrow |G\rangle$ transition, it can additionally induce an off-resonant transition between $|G\rangle$ and $|H\rangle$ and a resonant transition between $|H\rangle$ and $|F\rangle$. Nevertheless we do not consider the case of disordered ensemble of molecular aggregates here.

In order to understand when it is possible to neglect the $|F\rangle$ state even in presence of a cavity field, we consider the coupling of the dimer molecule to an ideally aligned cavity [i.e. we set $g_H = 0$ and $g_L = \mu_L/2$ in Eq. (4.46)]. To relate the Rabi frequency of the field to the intensity we use ($\hbar = 1$)

$$\Omega_L = 2\frac{\mu}{\sqrt{\epsilon_0 c}} \sin\theta \sqrt{I(\infty)}\,, \tag{4.57}$$

where (using our assumed default dipole parameters)

$$\frac{\mu}{\sqrt{\epsilon_0 c}} = 4.106 \times 10^{-9} \frac{\mathrm{eV}}{(\mathrm{W/m^2})^{1/2}}\,. \tag{4.58}$$

In Fig. 4.7 we show the steady-state populations of the dimer eigenstates as a function of the dimer angle, θ, and intensity of the cavity field, I. The results show, while the $|H\rangle$ state is always negligible (for the intensity range considered), the fully excited state $|F\rangle$ can mostly be ignored, and only for very large intensities (larger than we use in our results) do we approach a regime where the transition linking $|L\rangle$ to $|F\rangle$ becomes important. We also note that the larger the dephasing is, the larger the needed intensity in the cavity to excite the dimer becomes.

We also note that there is a minimum intensity level, below which behaviour is dominated by the phonon and photon dissipators rather than the coupling to the cavity. Once the cavity coupling takes over population is evenly distributed between the states coupled by lasing transitions, namely $|G\rangle$, $|L\rangle$ and occasionally $|F\rangle$.

4.6.10 Electric field with strong dephasing: incoherent rates

In the main part of the chapter we derive the lasing equations assuming that dephasing is much stronger than the coupling to the cavity. Here we show in detail how a master equation reduces to a rate equation under that assumption.

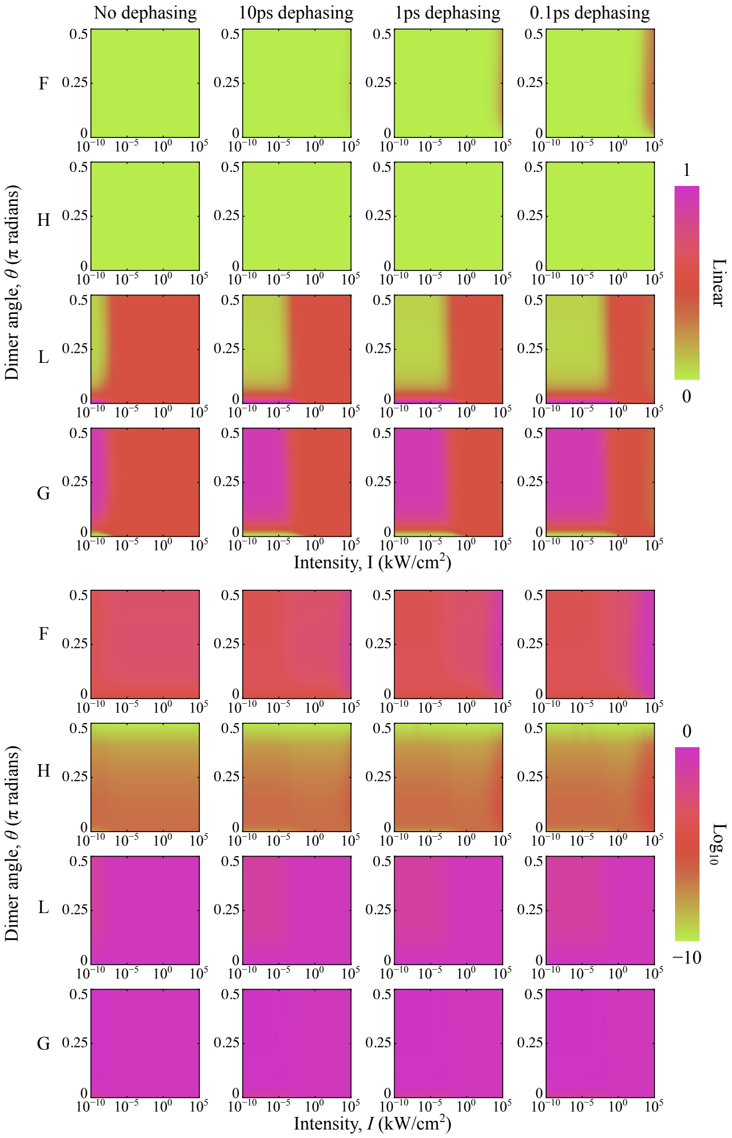

Figure 4.7: Parameter scan of steady states using the static field model. Results are displayed in linear and logarithmic scales. The intensity of the coupled static field, I, and the dimer angle θ are varied across the parameter scan. The range of dephasing rates for phenomenological dephasing dissipators matches those used in other models. We use parameters from the rest of the chapter: $\hbar\omega_A = 1.17$ eV and the spontaneous optical lifetime for the absorbers was fixed at $1/\gamma_0 = 36.8$ ns. Photon bath at 3000 K, phonon bath at 300 K, and phonon decay rate defined to match a picosecond spontaneous decay rate for $\theta = 0.07$ rad.

At first we derive an expression for the transition rate between the ground state and single-excitation manifold states induced by the cavity field. For simplicity, we neglect the $|F\rangle$ state but our results are nonetheless valid more generally. Let us introduce an Hamiltonian coupling induced by the cavity, as given in Eq. (4.46) and shown pictorially in Fig. 4.6b ($\hbar = 1$). We relabel the coupling strength (Rabi frequency) as $\Omega_{L,H} := g_{L,H}E_0$. The cavity field is resonant with the $|L\rangle - |G\rangle$ transition at frequency $\omega_L = \omega_A - |\Omega|$, and it is therefore detuned from the frequency of the $|H\rangle - |G\rangle$ transition.

Following the same approach described in the previous sections [see Eq. (4.38) and following], we write the Hamiltonian in the rotating frame as

$$\hat{H}_{S-C} = \begin{pmatrix} 2|\Omega| & 0 & \Omega_H \\ 0 & 0 & \Omega_L \\ \Omega_H & \Omega_L & 0 \end{pmatrix} , \tag{4.59}$$

represented in the basis $\mathcal{B} = \{|H\rangle, |L\rangle, |G\rangle\}$. For the current purpose, we may consider a simplified master equation without thermal relaxation and coupling to the photon bath,

$$\frac{d\hat{\rho}}{dt} = -i\left(\hat{H}_{S-C}\hat{\rho} - \hat{\rho}\hat{H}_{S-C}\right) + \mathcal{D}_\phi[\hat{\rho}] , \tag{4.60}$$

where the density matrix and the dephasing operator are, respectively,

$$\hat{\rho} = \begin{pmatrix} \rho_{HH} & \rho_{HL} & \rho_{HG} \\ \rho_{LH} & \rho_{LL} & \rho_{LG} \\ \rho_{GH} & \rho_{GL} & \rho_{GG} \end{pmatrix} , \qquad \mathcal{D}_\phi[\hat{\rho}] = \begin{pmatrix} 0 & -\Gamma_{HL}\rho_{HL} & -\Gamma_{GH}\rho_{HG} \\ -\Gamma_{HL}\rho_{LH} & 0 & -\Gamma_{GL}\rho_{LG} \\ -\Gamma_{GH}\rho_{GH} & -\Gamma_{GL}\rho_{GL} & 0 \end{pmatrix} . \tag{4.61}$$

The dephasing rates Γ_{HL}, Γ_{GH} and Γ_{GL} describe the decay of coherence due to energy fluctuations and interaction with the (vibrational) environment. Eq. (4.60) reads explicitly

$$\frac{d\rho_{GL}}{dt} = -i\Omega_L\left(\rho_{LL} - \rho_{GG}\right) - i\Omega_H\rho_{HL} - \Gamma_{GL}\rho_{GL} , \tag{4.62a}$$

$$\frac{d\rho_{HL}}{dt} = -i\Omega_H\left(\rho_{GL} - \rho_{HG}\right) - 2i|\Omega|\rho_{HL} - \Gamma_{HL}\rho_{HL} , \tag{4.62b}$$

$$\frac{d\rho_{GH}}{dt} = -i\Omega_H\left(\rho_{HH} - \rho_{GG}\right) - i\Omega_L\rho_{LH} + 2i|\Omega|\rho_{GH} - \Gamma_{GH}\rho_{GH} , \tag{4.62c}$$

$$\frac{d\rho_{LL}}{dt} = -i\Omega_L\left(\rho_{GL} - \rho_{LG}\right) , \tag{4.62d}$$

$$\frac{d\rho_{HH}}{dt} = -i\Omega_H\left(\rho_{GH} - \rho_{HG}\right) , \tag{4.62e}$$

where $\Omega_{L,H} = \mu_{L,H}E_0/(2\sqrt{3})$ with $\mu_{L,H}$ being the magnitudes of the TDMs, and $\sqrt{3}$ arising from orientational averaging. When decoherence is very fast, namely

$$\min\{\Gamma_{HL}, \Gamma_{GH}, \Gamma_{GL}\} \gg \max\{\Omega_H, \Omega_L\} , \tag{4.63}$$

we can assume that coherences ($\rho_{k\neq k'}$) will adiabatically follow populations ρ_{kk}. Thus, setting the first three derivatives to zero, we have

$$\rho_{GL} \approx -i\frac{\Omega_L}{\Gamma_{GL}}\left(\rho_{LL}-\rho_{GG}\right) - i\frac{\Omega_H}{\Gamma_{GL}}\rho_{HL}\,, \tag{4.64a}$$

$$\rho_{HL} \approx -i\frac{\Omega_H}{\Gamma_{HL}+2i|\Omega|}\left(\rho_{GL}-\rho_{HG}\right)\,, \tag{4.64b}$$

$$\rho_{GH} \approx -i\frac{\Omega_H}{\Gamma_{GH}-2i|\Omega|}\left(\rho_{HH}-\rho_{GG}\right) - i\frac{\Omega_L}{\Gamma_{GH}-2i|\Omega|}\rho_{LH}\,. \tag{4.64c}$$

On the right-hand sides of Eq. (4.64), the terms involving coherences are of the order $|\rho_{k\neq k'}| \sim \Omega_{H,L}/\Gamma_{kk'} \ll 1$, whereas populations have larger values, $\rho_{kk} \sim 1$. Therefore, we can safely drop the coherence terms from those right-hand sides and substitute the resulting simplified relationship back into the population equations Eq. (4.62). This yields

$$\frac{d\rho_{LL}}{dt} \approx -2\frac{\Omega_L^2}{\Gamma_{GL}}\left(\rho_{LL}-\rho_{GG}\right)\,, \tag{4.65a}$$

$$\frac{d\rho_{HH}}{dt} \approx -2\frac{\Omega_H^2}{\Gamma_{GH}}\frac{1}{1+(2|\Omega|/\Gamma_{GH})^2}\left(\rho_{HH}-\rho_{GG}\right)\,. \tag{4.65b}$$

Consequently, the full master equation for the time evolution of the entire density matrix is very well-approximated by just two rate equations for the populations

$$\frac{d\rho_{LL}}{dt} \approx -T_{GL}\left(\rho_{LL}-\rho_{GG}\right)\,, \tag{4.66a}$$

$$\frac{d\rho_{HH}}{dt} \approx -T_{GH}\left(\rho_{HH}-\rho_{GG}\right)\,, \tag{4.66b}$$

with the resonant and off-resonant transition rates given by, respectively,

$$T_{GL} = 2\frac{\Omega_L^2}{\Gamma_{GL}}\,, \qquad T_{GH} = 2\frac{\Omega_H^2}{\Gamma_{GH}}\frac{1}{1+(2|\Omega|/\Gamma_{GH})^2}\,. \tag{4.67}$$

Note that these expressions are more generally valid and applicable between weakly coupled levels (both resonant and detuned) in the presence of fast dephasing, as is shown in Ref. [45]. Indeed, in general we can write

$$T_{kk'} = 2\frac{\Omega_{kk'}^2}{\Gamma_{kk'}}\frac{1}{1+(\Delta_{kk'}/\Gamma_{kk'})^2}\,, \tag{4.68}$$

where $T_{kk'}$ is the incoherent transition rate between the states $|k\rangle$ and $|k'\rangle$, $\Omega_{kk'}$ is the coherent coupling between the states, $\Gamma_{kk'}$ is the dephasing rate between them and $\Delta_{kk'} = \omega_{kk'} - \omega_c$ is the detuning between the $|k\rangle - |k'\rangle$ transition frequency and the cavity frequency ω_c. Here $\omega_{kk'} = |E_k - E_{k'}|/\hbar$ and $E_{k,k'}$ is the energy of the $|k\rangle\,,|k'\rangle$-th state.

Note that including photon and phonon (Bloch-Redfield) dissipators to the master equation (which can be done additively within second order perturbation expansions) only affects the precise values of the dephasing terms $\Gamma_{kk'}$ and will not alter the form and validity of Eq. (4.68).

4.6.11 Electric field with strong dephasing: incoherent laser equation

In the following, we use the incoherent rates of Eq. (4.68) to derive a set of rate equations for the dimer levels driven by the cavity under strong dephasing, including also the effect of photons and phonons. We start from the approximate Lindblad master equation Eq. (4.32) comprising a set of rate equations for photon absorption, spontaneous emission and phonon-induced thermal relaxation. We include the effect of the cavity by adding semi-classical transition rates Eq. (4.68) between the levels $|G\rangle - |L\rangle$, $|H\rangle - |F\rangle$ (resonant transitions) and $|L\rangle - |F\rangle$, $|G\rangle - |H\rangle$ (non-resonant transitions, with a detuning frequency $|2\Omega|/\hbar$), assuming for simplicity that the dephasing rate has the same value $\Gamma_{kk'} = \Gamma_\phi$ for all transitions. Moreover, we derive a rate equation for the intensity of the cavity field $I = \epsilon_0 |E_0|^2/2$: we start from Eq. (4.56) and we replace the coherence terms with the approximate expressions that we derived in Eq. (4.64) dropping higher-order terms proportional to the coherences, under the assumption of strong dephasing. The resulting system of coupled equations reads

$$\begin{aligned}
\frac{d\rho_{GG}}{dt} =& \gamma_L(\omega_L)\left[1+n_T(\omega_L)\right]\rho_{LL} + \gamma_H(\omega_H)\left[1+n_T(\omega_H)\right]\rho_{HH} \\
&- \gamma_L(\omega_L)n_T(\omega_L)\rho_{GG} - \gamma_H(\omega_H)n_T(\omega_H)\rho_{GG} \\
&+ T_{GL}(I)\left[\rho_{LL}-\rho_{GG}\right] + T_{GH}(I)\left[\rho_{HH}-\rho_{GG}\right] \; , \qquad (4.69a) \\
\frac{d\rho_{LL}}{dt} =& \gamma_L(\omega_H)\left[1+n_T(\omega_H)\right]\rho_{FF} - \gamma_L(\omega_L)\left[1+n_T(\omega_L)\right]\rho_{LL} \\
&+ \gamma_L(\omega_L)n_T(\omega_L)\rho_{GG} - \gamma_L(\omega_H)n_T(\omega_H)\rho_{LL} \\
&+ \Gamma_\Omega\left[1+n_\Omega\right]\rho_{HH} - \Gamma_\Omega n_\Omega \rho_{LL} + T_{GL}(I)\left[\rho_{GG}-\rho_{LL}\right] + T_{LF}(I)\left[\rho_{FF}-\rho_{LL}\right] \; , \qquad (4.69b) \\
\frac{d\rho_{HH}}{dt} =& \gamma_H(\omega_L)\left[1+n_T(\omega_L)\right]\rho_{FF} - \gamma_H(\omega_H)\left[1+n_T(\omega_H)\right]\rho_{HH} \\
&+ \gamma_H(\omega_H)n_T(\omega_H)\rho_{GG} - \gamma_H(\omega_L)n_T(\omega_L)\rho_{HH} \\
&- \Gamma_\Omega\left[1+n_\Omega\right]\rho_{HH} + \Gamma_\Omega n_\Omega \rho_{LL} + T_{GH}(I)\left[\rho_{GG}-\rho_{HH}\right] + T_{HF}(I)\left[\rho_{FF}-\rho_{HH}\right] \; , \qquad (4.69c) \\
\frac{d\rho_{FF}}{dt} =& -\gamma_L(\omega_H)\left[1+n_T(\omega_H)\right]\rho_{FF} - \gamma_H(\omega_L)\left[1+n_T(\omega_L)\right]\rho_{FF} \\
&+ \gamma_L(\omega_H)n_T(\omega_H)\rho_{LL} + \gamma_H(\omega_L)n_T(\omega_L)\rho_{HH} \\
&+ T_{LF}(I)\left[\rho_{LL}-\rho_{FF}\right] + T_{HF}(I)\left[\rho_{HH}-\rho_{FF}\right] \; , \qquad (4.69d) \\
\frac{dI}{dt} =& b(I)\left\{\frac{\mu_L^2}{\mu^2}\left[\rho_{LL}-\rho_{GG}+\frac{\rho_{FF}-\rho_{LL}}{1+(2|\Omega|/\hbar\Gamma_\phi)^2}\right]\right. \\
&\left. + \frac{\mu_H^2}{\mu^2}\left[\rho_{FF}-\rho_{HH}+\frac{\rho_{HH}-\rho_{GG}}{1+(2|\Omega|/\hbar\Gamma_\phi)^2}\right]\right\} - \kappa I \, , \qquad (4.69e)
\end{aligned}$$

where we have introduced the transition rates

$$T_{GL}(I) = \frac{\mu_L^2 I}{3\hbar^2 \epsilon_0 c \Gamma_\phi}, \quad T_{LF}(I) = \frac{\mu_L^2 I}{3\hbar^2 \epsilon_0 c \Gamma_\phi [1 + (2\Omega/\hbar\Gamma_\phi)^2]}, \quad T_{HF}(I) = \frac{\mu_H^2 I}{3\hbar^2 \epsilon_0 c \Gamma_\phi},$$
$$T_{GH}(I) = \frac{\mu_H^2 I}{3\hbar^2 \epsilon_0 c \Gamma_\phi [1 + (2\Omega/\hbar\Gamma_\phi)^2]}, \quad b(I) = \frac{n_A \mu^2 \omega_L I}{3\hbar \epsilon_0 \Gamma_\phi}, \tag{4.70}$$

which all depend on the field intensity I. The approximations leading to Eq. (4.69) are allowed only if the dephasing rate is much faster than the coherent oscillations induced by the laser field in the cavity. We now proceed to write the condition of validity for the rate equations Eq. (4.63) in terms of the field intensity. Approximating $\max\{\Omega_H, \Omega_L\} \approx \Omega_H \approx \mu E_0/(\sqrt{6}\hbar)$ for $\mu_L^2 \ll \mu^2$, we define the parameter

$$\eta = \frac{\max\{\Omega_L, \Omega_H\}}{\Gamma_\phi} = \sqrt{\frac{I}{\tilde{I}}} \qquad \text{where} \qquad \tilde{I} \approx \frac{3c\epsilon_0 \hbar^2 \Gamma_\phi^2}{\mu^2}. \tag{4.71}$$

According to the condition Eq. (4.63), the rate equation description is valid when $\eta \ll 1$, that is when $I \ll \tilde{I}$. For the parameters used in the main part of the chapter, $\mu = 10.157$ D and $\Gamma_\phi = 1/(10\text{ ps})$, we have $\tilde{I} = 80\text{ kW/cm}^2$ which is larger than the stationary values of the intensities considered in the main part of the chapter.

4.6.12 Comparing coherent and incoherent laser equations

In this section we compare the full Bloch-Redfield coherent laser equations Eq. (4.50) and Eq. (4.56) with the incoherent laser equation Eq. (4.69). Both will be contrasted against the (stationary) laser equation presented in Eq. (4.7) and Eq. (4.8). Note that the incoherent laser equations are the most general (and also most difficult to solve), while the incoherent laser equations assumed strong dephasing so that energy exchange with the cavity can be considered incoherent. Finally, the laser equation presented in Eq. (4.7) and Eq. (4.8) not only assumed strong dephasing as in the incoherent laser equation, but they also assume fast thermal relaxation which has not been assumed in deriving Eq. (4.69).

In order to validate the laser equation presented in Eq. (4.7) and Eq. (4.8) we have computed the evolution of the intensity as a function of time starting with the following initial conditions for the dimer density matrix

$$\rho(t=0) = \begin{pmatrix} 0 & 0 & 0 & 0 \\ 0 & 0 & 0 & 0 \\ 0 & 0 & 0.5 & 0 \\ 0 & 0 & 0 & 0.5 \end{pmatrix}, \tag{4.72}$$

where only the $|G\rangle, |L\rangle$ states are initially equally populated and as initial value of the field in the cavity we set $E_0(t=0) = 868\text{ Vm}^{-1}$. Only the case of disordered dimers is considered. A first comparison between the fully coherent model and the laser equation

(a) $\Gamma_\phi = 1/(10\text{ ps})$, $n_A = 5 \times 10^{-4}$ mmol/L, $\tilde{I} = 80$ kW/cm^2

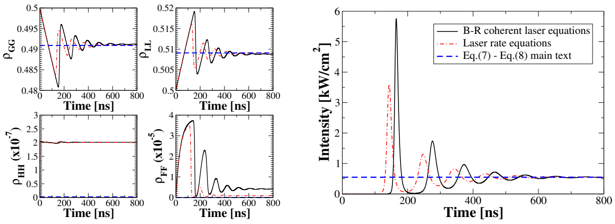

(b) $\Gamma_\phi = 1/(1\text{ ps})$, $n_A = 5 \times 10^{-3}$ mmol/L, $\tilde{I} = 8$ MW/cm^2

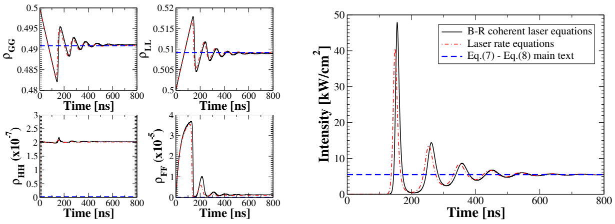

(c) $\Gamma_\phi = 1/(100\text{ fs})$, $n_A = 5 \times 10^{-2}$ mmol/L, $\tilde{I} = 800$ MW/cm^2

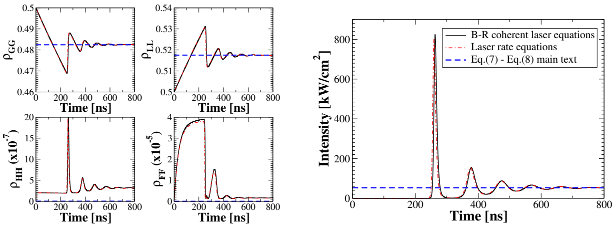

(d) no dephasing, $n_A = 5 \times 10^{-4}$ mmol/L, $\tilde{I} = 5.7$ mW/cm^2

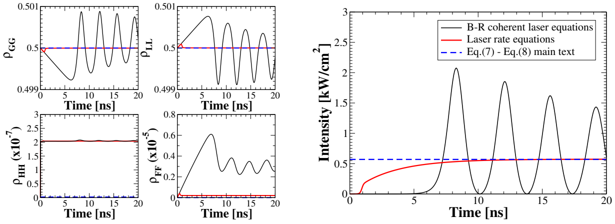

Figure 4.8: Level populations and laser intensity obtained with the Bloch-Redfield (B-R) coherent model Eq. (4.50)-Eq. (4.56) and with the laser rate equations Eq. (4.69). The blue dashed lines represent the steady-state solution of the laser equations Eq. (4.7)-Eq. (4.8). $\tilde{I}$ is the maximal intensity for which the rate equations are expected to work, see Eq. (4.71). In panel (d), for the "laser rate equation" and "Eq. (4.7)-Eq. (4.8)" cases we set the dephasing rate from the spontaneous emission timescale ($\Gamma_\phi = 1/(36.78\,\text{ns})$). Parameters: $\mu = 10.157$ D, $\hbar\omega_A = 1.17$ eV, $\Omega = 2000\ \text{cm}^{-1}$, $T_{BB} = 3000$ K, $\kappa/(2\pi) = 50$ MHz, $\langle\chi\rangle = 0.005$.

is presented in Fig. 4.1b for the case of a black body pumping of $T = 3000$ K. In the following, we shall also limit our consideration to the same black-body temperature.

In Fig. 4.8 we plot the populations of all the four levels and the laser intensity against time. In panel (a) the parameters ensure a stationary laser intensity of 0.5 $\mathrm{kW/cm^2}$ at $T_{BB} = 3000$ K and $\tilde{I} = 80\ \mathrm{kW/cm^2}$, which implies $\eta = 0.08$, so that the rate equation approximation Eq. (4.69) is valid. By comparing the rate equations Eq. (4.69) results (red dash-dotted lines) with the full Bloch-Redfield coherent laser equations results (black continuous lines), one can see that they are very similar. Moreover, the stationary intensity reached by both approaches is also equal to Eq. (4.7) and Eq. (4.8), see horizontal dashed line. The laser equations derived in Eq. (4.7) and Eq. (4.8) remain valid also for shorter dephasing times, as we show in panels (b,c), where higher dephasing values are used (1 ps and 0.1 ps), so that $\tilde{I} = 8\ \mathrm{MW/cm^2}$ (panel b) and $\tilde{I} = 800\ \mathrm{MW/cm^2}$ (panel c). Note that in panels (b,c) we also use higher densities than panel (a), in order to reach the lasing threshold. With these parameters we obtain a stationary laser intensity of 5 $\mathrm{kW/cm^2}$ (panel b), implying $\eta = 0.03$, and intensity of 50 $\mathrm{kW/cm^2}$ (panel c), implying $\eta = 0.008$ so that the rate equations (red dash-dotted lines) remain valid in these two cases. Finally, in panel (d) we consider the case with “no dephasing”, in the sense that no extra dephasing is included in the system, and the main source of decoherence is due to the coupling to the photons. Therefore, we compare the full Bloch-Redfield coherent laser equations results with the rate equations Eq. (4.69), where we choose $\Gamma_\phi = \gamma_0$, that is we assume that the dephasing rate is given only by spontaneous decay. From panel (d) one can see that the coherent model has a very different dynamics from the rate equations. The coherent model shows non-damped oscillations (we verified that there is no damping up to 650 ns), while the rate equations quickly reach their steady-state values in few nanoseconds. For the parameters in panel (d) we obtain an average stationary laser intensity of 0.5 $\mathrm{kW/cm^2}$ with $\tilde{I} = 5.7\ \mathrm{mW/cm^2}$, implying $\eta = 296$, so that the rate equations are not expected to be valid.

The results presented in this section thus confirm the validity of our laser equations, see Eq. (4.7) and Eq. (4.8), under the assumption of strong dephasing and quick thermal relaxation. Both these assumptions are realistic in molecular aggregates at room temperature.

Finally we would like to note that the timescale required for reaching the stationary regime strongly depends on the black-body temperature. For instance, for $T_{BB} = 3000$ K equilibrium is reached in ~ 100 ns, while for natural sunlight timescales up to 10 ms are needed to reach the equilibrium lasing intensity. As this would require heavy numerical simulations, we are not showing this case here. In general, the equilibration timescale is given by $\max\left\{[(R_u + R_d)(n_A/2n_A^{th})]^{-1}, 1/\kappa\right\}$, with the threshold density n_A^{th} given implicitly by Eq. (4.9).

Moreover, within the considered range of parameters the double-excitation $|F\rangle$ state never acquires any significant population. Therefore, when $\eta \ll 1$ and the 4-level rate-equation description is valid, we can also safely ignore the $|F\rangle$ state and assume thermal relaxation within the single-excitation manifold, obtaining the main-text theory. In other words, the $\eta \ll 1$ condition is enough to justify the approximations made in our theory in Eq. (4.7) and Eq. (4.8).

Finally we would like to comment on the effect of faster dephasing as considered here. The main effect of faster dephasing is to lower the incoherent driving of the cavity, thus inducing a larger critical threshold density for lasing. As for the level of darkness required to have lasing, Eq. (4.12) establishes an upper bound for the brightness, in order to have lasing. The only dependence on dephasing in Eq. (4.12) is in the rates $\langle B \rangle, B_{tot}$. In any case, when the aggregate has only one transition that is resonant with the cavity (and all others are well detuned with energy differences larger than $\hbar\Gamma_\phi$), then $\langle B \rangle \approx B_{tot}$ and the upper bound for the dimer brightness is dephasing-independent. In all of our calculations we indeed focused to such regime.

On the other hand, the threshold density Eq. (4.9) always depends on Γ_ϕ, since the right-hand side of Eq. (4.9) increases proportionally to Γ_ϕ [see Eq. (4.5) neglecting the contribution of the off-resonant states].

4.6.13 Bio-inspired aggregate: Purple Bacteria

In Fig. 4.2 we apply our lasing theory to a bio-mimetic molecular aggregate inspired by the antenna complex of purple bacterium *Rhodobacter Sphaeroides*. Here we describe in detail the structure and the Hamiltonian of the aggregate. Purple bacteria antenna complexes are formed by bacteriochlorophyll-a (BChl) molecules, aggregated in different kinds of ring-like structures [35, 139]. The most common BChl aggregates are those called light-harvesting complex II (LHII). These are either 9-fold [35] or 8-fold [3, 5] structures, formed by two stacked rings. Here we consider the 9-fold structure, which is subdivided into a lower ring made of 18 BChl molecules and an upper ring made of nine molecules. The lower ring is called B850 since it has a fluorescence peak at 850 nm, while the upper ring is called B800 because it emits at 800 nm. The LHII rings are distributed on bacterial membranes, surrounding the larger light-harvesting I (LHI) complexes. LHI can have a ring structure [139] made of 32 molecules or an S-like shape [35] made of 56 molecules. Here we consider the ring-like structure for LHI, also called B875 for its emission peak at 875 nm. Around the LHI complex we place 8 equally spaced LHII aggregates (see Fig. 4.9) mimicking natural antennae. The minimal distance between neighboring LHII aggregates is 22.4 Å as in Ref. [35], while the minimal distance between LHII and LHI is 25.3 Å. At the center of the LHI we place a homo-dimer, where the two molecules are separated by 8 Å (similarly to BChls in the special pair of purple bacteria reaction centers [3, 5]) and their transition dipoles have an equal component $\cos\theta$ on the ring plane and an opposite component $\pm\sin\theta$ out of plane. Controlling θ and keeping the coupling between the dimer molecules fixed, we can change the dimer brightness $\langle \chi \rangle$, so that we go from an H-dimer ($\theta \approx 0$, $\langle \chi \rangle \approx 0$) to a J-dimer ($\theta \approx \pi/2$, $\langle \chi \rangle \approx 1$). We chose the excitation frequency of the molecules in the dimer to be 1.17 eV corresponding to ≈ 1060 nm, which is in the near infrared wavelength. Since the coupling in the dimer is 2000 cm^{-1} the dimer $|H\rangle$ state has an excitation wavelength of about 875 nm at resonance with the superradiant states of the LHI aggregate. This choice will ensure a large supertransfer coupling and fast thermal relaxation between the LHI and the dimer. Indeed due to the symmetric arrangement (the dimer is at the center of the LHI ring) the coupling between the $|H\rangle$ state of the dimer and the super-radiant states of the LHI ring will be enhanced by a factor $\approx \sqrt{32}$ [3].

In Fig. 4.9 we show a top-view of the aggregate, while in Table 4.1 we report the positions of the molecules and the unit vectors for their transition dipole moment.

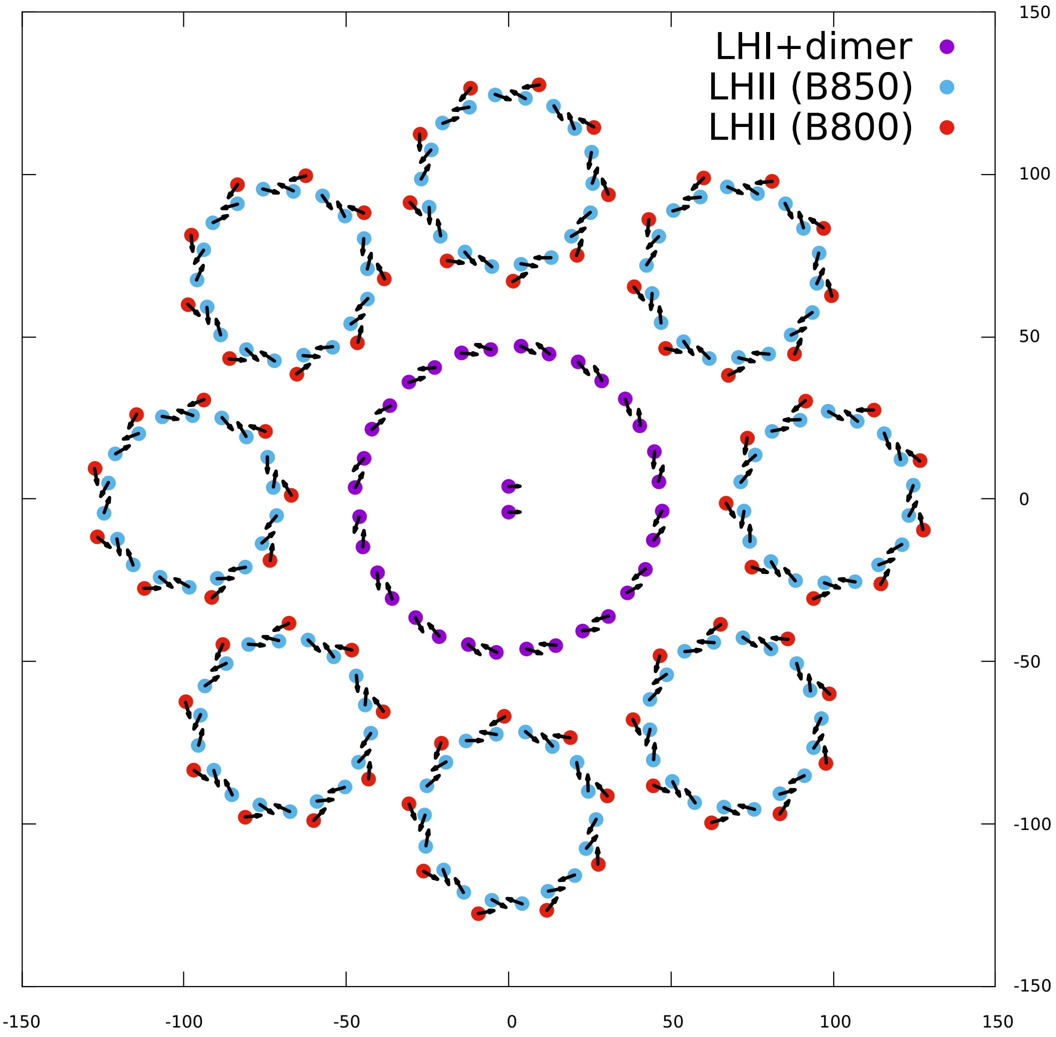

Figure 4.9: Positions (circles) and transition dipole orientations (arrows) for all the molecules in the aggregate (see also Table 4.1). View from top. The axes are in Å units.

Following Ref. [3, 5], we describe the excitation transfer between the molecules of the aggregate using the single-excitation Hamiltonian

$$\hat{H}_S = \sum_j \hbar\omega_j |j\rangle \langle j| + \sum_{i,j} \Omega_{i,j} |i\rangle \langle j| \ , \tag{4.73}$$

Subunit	Site energy [cm^{-1}]	Nearest-neighbor coupling [cm^{-1}]
LHII (B850)	12532, 12728 (alternate)	363, 320 (alternate)
LHII (B800)	12555	dipole-dipole
LHI	12911	806, 377 (alternate)
Dimer	9437	2000
Transition dipole	10.157 D	

x [Å]	y [Å]	z [Å]	μ_x/μ	μ_y/μ	μ_z/μ
LHII (B850)					
123.289	-5.157	-0.06	0.48	0.865	0.147
124.618	4.179	0.067	-0.33	-0.934	0.136
120.678	12.253	-0.047	-0.182	0.972	0.145
115.707	20.304	0.043	0.34	-0.93	0.143
107.485	23.988	-0.056	-0.76	0.633	0.146
98.534	26.991	0.055	0.862	-0.489	0.135
89.822	24.479	-0.06	-0.989	-0.017	0.147
81.072	20.962	0.067	0.974	0.182	0.136
76.05	13.513	-0.047	-0.751	-0.644	0.145
71.563	5.183	0.043	0.635	0.759	0.143
72.483	-3.78	-0.056	-0.168	-0.975	0.146
74.358	-13.033	0.055	-0.007	0.991	0.135
80.889	-19.322	-0.06	0.509	-0.848	0.147
88.31	-25.141	0.067	-0.644	0.753	0.136
97.272	-25.766	-0.047	0.933	-0.328	0.145
106.73	-25.487	0.043	-0.975	0.171	0.143
114.032	-20.208	-0.056	0.928	0.342	0.146
121.108	-13.958	0.055	-0.855	-0.502	0.135
LHII (B800)					
126.628	11.769	16.843	-0.771	0.619	0.149
112.396	27.476	16.751	-0.987	-0.013	0.162
91.382	30.349	16.774	-0.754	-0.643	0.131
73.494	18.908	16.843	-0.151	-0.977	0.149
67.007	-1.271	16.751	0.504	-0.848	0.162
75.026	-20.906	16.774	0.934	-0.332	0.131
93.878	-30.677	16.843	0.922	0.358	0.149
114.597	-26.205	16.751	0.482	0.861	0.162
127.592	-9.443	16.774	-0.18	0.975	0.131

x [Å]	y [Å]	z [Å]	μ_x/μ	μ_y/μ	μ_z/μ
LHI					
44.706	-12.591	-0.099	0.634	0.76	0.147
47.167	-3.677	0.099	-0.452	-0.886	0.098
46.122	5.475	-0.099	0.295	0.944	0.147
44.984	14.653	0.099	-0.079	-0.992	0.098
40.515	22.709	-0.099	-0.089	0.985	0.147
35.952	30.752	0.099	0.307	-0.947	0.098
28.741	36.485	-0.099	-0.459	0.876	0.147
21.448	42.169	0.099	0.646	-0.757	0.098
12.591	44.706	-0.099	-0.76	0.634	0.147
3.677	47.167	0.099	0.886	-0.452	0.098
-5.475	46.122	-0.099	-0.944	0.295	0.147
-14.653	44.984	0.099	0.992	-0.079	0.098
-22.709	40.515	-0.099	-0.985	-0.089	0.147
-30.752	35.952	0.099	0.947	0.307	0.098
-36.485	28.741	-0.099	-0.876	-0.459	0.147
-42.169	21.448	0.099	0.757	0.646	0.098
-44.706	12.591	-0.099	-0.634	-0.76	0.147
-47.167	3.677	0.099	0.452	0.886	0.098
-46.122	-5.475	-0.099	-0.295	-0.944	0.147
-44.984	-14.653	0.099	0.079	0.992	0.098
-40.515	-22.709	-0.099	0.089	-0.985	0.147
-35.952	-30.752	0.099	-0.307	0.947	0.098
-28.741	-36.485	-0.099	0.459	-0.876	0.147
-21.448	-42.169	0.099	-0.646	0.757	0.098
-12.591	-44.706	-0.099	0.76	-0.634	0.147
-3.677	-47.167	0.099	-0.886	0.452	0.098
5.475	-46.122	-0.099	0.944	-0.295	0.147
14.653	-44.984	0.099	-0.992	0.079	0.098
22.709	-40.515	-0.099	0.985	0.089	0.147
30.752	-35.952	0.099	-0.947	-0.307	0.098
36.485	-28.741	-0.099	0.876	0.459	0.147
42.169	-21.448	0.099	-0.757	-0.646	0.098
Dimer					
0.0	-4.0	0.0	$\cos\theta$	0.0	$\sin\theta$
0.0	4.0	0.0	$\cos\theta$	0.0	$-\sin\theta$

Table 4.1: Parameters for the aggregate Hamiltonian, positions and normalized transition dipole vectors for the LHI complex, the dimer and one of the eight LHII complexes forming the aggregate in Fig. 4.9.

where $|j\rangle$ is a state where only the j-th molecule is excited and all the other ones are in their ground state, and the off-diagonal elements are the inter-molecular couplings. For pairs of molecules that are sufficiently far apart, we follow Ref. [2] using a dipole-dipole coupling

$$\Omega_{i,j} = \frac{1}{4\pi\epsilon_0}\left[\frac{\vec{\mu}_i \cdot \vec{\mu}_j}{r_{i,j}^3} - 3\frac{(\vec{\mu}_i \cdot \vec{r}_{i,j})(\vec{\mu}_j \cdot \vec{r}_{i,j})}{r_{i,j}^5}\right] \tag{4.74}$$

with the unit vectors $\vec{\mu}_i/\mu$ given in Table 4.1 and the distance vectors $\vec{r}_{i,j} = \vec{r}_j - \vec{r}_i$ obtained from the positions in Table 4.1. The dipole-dipole coupling is a good approximation only when the molecules are far apart, though. This excludes the nearest-neighbor molecules in the LHII B850 ring and the nearest-neighbor pairs in LHI. Therefore, we replace the B850 nearest-neighbor couplings with the values reported in Ref. [35] and the LHI couplings with the ones in Ref. [3, 5]. The transition dipole μ for the dipole-dipole couplings Eq. (4.74) is taken from Ref. [3, 5], while the site energies are set to match the main fluorescence peaks at 800 nm (B800), 850 nm (B850) and 875 nm (LHI). All these parameters are reported in Table 4.1.

By diagonalizing the Hamiltonian Eq. (4.73) for the whole bio-inspired aggregate, we obtain the energies and TDMs for all eigenstates of the system. This information allows us to use our laser equations (4.6),(4.7) and (4.8), under the assumption of quasi-instantaneous thermal relaxation and incoherent driving induced by the cavity field. We would like to stress that, while incoherent driving induced by the cavity field is well justified, the fast thermal relaxation assumption might fail in very large systems. Nevertheless here we show that this assumption remains valid for the large aggregates considered in this section. Indeed, due to the cooperative coupling between the superradiant states of the LHII-LHI complex and LHI-dimer system, thermalization is estimated to occur in tens of picoseconds [2]. We now proceed by estimating the remaining relevant timescales: the driving rate induced by the cavity coupling and the optical rates (spontaneous and stimulated emission) induced by the photon field. Specifically, from Eq. (4.5) we can estimate the cavity-induced transition rate as $n(B_{tot} + \langle B\rangle)$. When the $|L\rangle$ state of the dimer is well-gapped below the rest of the single excitation manifold, its Boltzmann occupation is close to 1 and we have $B_{tot} \approx \langle B\rangle \approx B_L$. Owing to Eq. (4.5) we also have $n(B_{tot} + \langle B\rangle) \approx 2nB_L = \Omega_L^2/\Gamma_\phi = \mu_L^2 I/(\hbar^2 c\epsilon_0\Gamma_\phi)$. For the parameters used here ($\mu = 10.157$ D, $\Gamma_\phi = 1/(10\text{ ps})$) and the maximal intensity that we consider ($I = 1\text{ kW/cm}^2$), we obtain $n(B_{tot} + \langle B\rangle) \approx 7.78(\mu_L/\mu)^2\text{ ns}^{-1}$. In the extreme case $\mu_L = \mu$ we have $n(B_{tot} + \langle B\rangle) \approx 1/(126\text{ ps})$. In most cases $\mu_L \ll \mu$ and the intensity is less than 1 kW/cm^2, so laser-induced transitions occur on a timescale slower than 126 ps. Moreover, as explained before in this chapter, thermal relaxation is certainly faster than optical pumping and decay rates, which range from a few nanoseconds (large aggregates, high black-body temperature) down to milliseconds (small aggregates, natural sunlight). Another relevant timescale is the realistic extraction rate κ from the cavity of about three nanoseconds which we considered. Finally, note that under natural sunlight pumping (where the maximal laser intensity considered is 10 W/cm^2) these other timescales are considerably longer and thus Eqs. (4.6), (4.7) and (4.8) retain their validity for larger aggregates.

These estimates justify the use of the laser equations (4.6), (4.7) and (4.8) for the bio-inspired aggregate considered here. To further validate this and to show how to extend our analysis to even larger aggregates, where thermal relaxation might not be the fastest timescale, here we analyze a set of incoherent laser equations, similar to Eq. (4.69), where instantaneous thermalization is not assumed.

For this purpose we focus on the LHI-Dimer aggregate, composed of a total of 34 molecules, 32 for the LHI and two for the dimer. In this case we will consider the eigenstates of the LHI aggregate and the dimer aggregate separately. Let us define P_k as the population of one of these 34 states: $k = 1, \ldots, 32$ for the LHI eigenstates and $k = 33, 34$ for the dimer eigenstates ($|L\rangle$ and $|H\rangle$). This separation is motivated from the fact that thermalization on the LHI or dimer aggregate alone will be faster (few picoseconds) than the thermalization over the whole LHI-Dimer aggregate. This is because the coupling within the aggregates (of the order of several hundreds of cm^{-1}) is much stronger than the coupling between the aggregates (few cm^{-1}). Moreover, let us define P_G as the probability to be in the ground state and n the number of photons in the cavity, so that the incoherent laser equations read

$$\frac{dP_G}{dt} = -\sum_k R_k P_G + \sum_k [R_k + \gamma_k(\omega_k)] P_k - \sum_k B_k n P_G + \sum_k B_k n P_k \,, \tag{4.75a}$$

$$\frac{dP_k}{dt} = R_k P_G - [R_k + \gamma_k(\omega_k)] P_k + B_k n P_G - B_k n P_k + \sum_j \left(T_{k,j} P_j - T_{j,k} P_k \right) \,, \tag{4.75b}$$

$$\frac{dn}{dt} = V \sum_k B_k n P_k - V \sum_k B_k n P_G - n\kappa \,, \tag{4.75c}$$

where the definitions of $R_k, \gamma_k(\omega_k), B_k$ and κ can be found in the previous subsections of the Appendix. The rates $T_{j,k}$ between the eigenstates of each aggregate are taken from Eq. (4.25),

$$T_{j,k} = \frac{\kappa_{\mathrm{vib}} \omega_{j,k}}{1 - e^{-\hbar \omega_{j,k}/(k_B T)}} \qquad \text{with} \qquad \omega_{j,k} = \frac{E_k - E_j}{\hbar}$$

where $\kappa_{\mathrm{vib}} = 1.3 \times 10^{-3}$ has the same value that we used when studying the dimer in the previous sections. The coupling between the LHI and the dimer is taken into account by considering only the coupling of one superradiant state of the LHI with the $|H\rangle$ dimer state. Indeed, these two states are resonant and the coupling between all other states is either much smaller or largely off-resonant. Starting from [144], the thermal transfer rate between the LHI ring and the special pair of the RC system has been estimated to be $\approx 1/(16\ \mathrm{ps})$. The thermal transfer rate between two aggregates is defined as $K = \sum_{n,m} = p_n T_{n,m}$, where n labels the eigenstates of the first aggregate and m labels the eigenstates of the second aggregate, p_n is the thermal population of the n-th eigenstate and $T_{n,m}$ is the transfer rate between the n-th eigenstate of the first aggregate and the $m-$th eigenstate of the second aggregate. For the case of the LHI-dimer complex, only the coupling between one superradiant state of the ring and the $|H\rangle$ dimer state is relevant, so that $K = p_2 T_{2,34}$. Given that $p_2 \approx 0.212$ at room temperature, we consider only the coupling $T_{2,34} = T_{34,2} = 1/(p_2 \times 16\ \mathrm{ps})$ [144] and set all the other couplings between the eigenstates of LHI and the dimer to zero. The value of the coupling between the superradiant state of the LHI aggregate and the $|H\rangle$ dimer state has been chosen to be identical to that estimated for natural structures between the LHI aggregate and the special pair [2]. The laser intensity can now be obtained from the number of photons n using Eq. (4.8).

In Fig. 4.10 we compare the numerical solutions obtained from Eq. (4.75) with the theoretical prediction for stationary values obtained from Eqs. (4.6), (4.7) and (4.8). As one can see, both the stationary population difference (upper panel) and the stationary laser intensity (lower panel) obtained with Eq. (4.75) are in excellent agreement with our theoretical predictions obtained assuming instantaneous thermal relaxation over the whole aggregate. This figure shows the case of black-body pumping at 3000 K. For natural sunlight irradiation, since the pumping and the coupling to the cavity is much weaker, we expect that our assumption of fast thermal relaxation will be valid even for much larger aggregates than the one considered in Fig. 4.10.

Whilst the rate equation model presented above will naturally not capture some of the more subtle details of the excitation dynamics of an LHI ring, it nonetheless resolves the thermalization process dynamically and is thus more realistic than assuming instant thermalization. Moreover, finer details in the dynamics will not affect the lasing predictions and efficiency, provided thermalization does indeed occur sufficiently quickly, as is captured by the above rate equations.

4.6.14 Threshold density at 3000 K for purple bacteria bio-inspired aggregates

In Fig. 4.2h we compare the threshold density under natural sunlight pumping for a dimer and two aggregates (LHI + dimer and LHIIs + LHI + dimer). We show that the threshold density of the aggregates is mapped to the threshold density of a dimer whose R_u pumping factor is multiplied by $N/2$, where N is the total number of molecules in the whole aggregate. Here, we show the same effect under pumping from a 3000 K black-body source. In Fig. 4.11 the threshold density is plotted for a dimer and for the two aggregates. The maximal $\langle\chi\rangle$ required for lasing increases with the aggregate size, and the threshold density decreases with increasing N. Similarly to the natural sunlight case (shown in Fig. 4.2), we can reproduce the aggregate threshold density using a dimer with an enhanced R_u factor. However, differently to the natural sunlight case, now the scaling factor is smaller than $N/2$. Specifically, we reproduce the "LHI + dimer" case using a dimer with $0.85(N/2)R_u$ and the "LHIIs + LHI + dimer" case using a dimer with $0.45(N/2)R_u$. The scaling here is not as simple as the natural sunlight case because of energy-dependent terms contained within R_u. Specifically, $R_u = \sum_k \gamma_k(\omega_k)n_T(\omega_k)$ is the sum of the dipole strengths of the eigenstates (contained in γ_k) multiplied by the black-body spectrum of the source. In the natural sunlight case ($T_{BB} = 5800$ K) the black-body spectrum is basically flat over the energy range of the aggregate, so that R_u scales as N, the sum of all the dipole strengths in the aggregate. In the $T_{BB} = 3000$ K case, instead, the black-body spectrum decreases with the

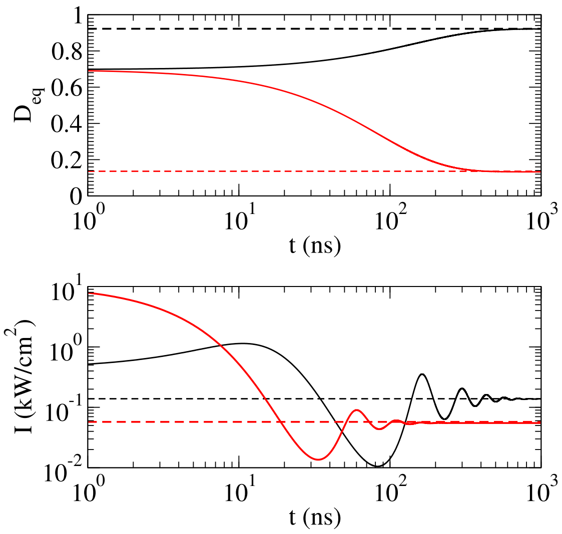

Figure 4.10: Comparison between theoretical prediction of Eqs. (4.6), (4.7) and (4.8) and incoherent rate laser equations Eq. (4.75) for the of the LHI-dimer aggregate (Fig. 4.2b). Initial conditions for both panels: $P_G(t = 0) = 0.15$, $P_{34}(t = 0) = 0.85$ (initial population of the $|H\rangle$ dimer state), $P_{k\neq 34}(t = 0) = 0$ and $n(t = 0)/V = 10^{11}$ cm^{-3}. Upper panel: population difference D_{eq} *vs.* time: the horizontal dashed lines correspond to Eq. (4.10), whereas the solid lines have been obtained from Eq. (4.75) in absence of the coupling to the cavity. Lower panel: laser intensity *vs* time: the horizontal dashed lines correspond to Eq. (4.8) whereas the solid lines to Eq. (4.75). In both panels we consider black body pumping at $T_{BB} = 3000$ K, and an aggregate density of $n_A = 10^{-5}$ mmol/L. Two different values of the dimer brightness are shown: $\langle\chi\rangle = 9.7 \times 10^{-3}$ (black curves) and $\langle\chi\rangle = 0.185$ (red curves). The other dimer and LHI parameters are discussed in the main body.

energy in the aggregate range. So, the additional dipole strength that is provided by the LHIIs in the aggregate is proportionally less effective and needs to be multiplied by a correction factor accounting for the reduced spectral intensity. This explains why the enhancement is smaller than $N/2$ at this temperature.

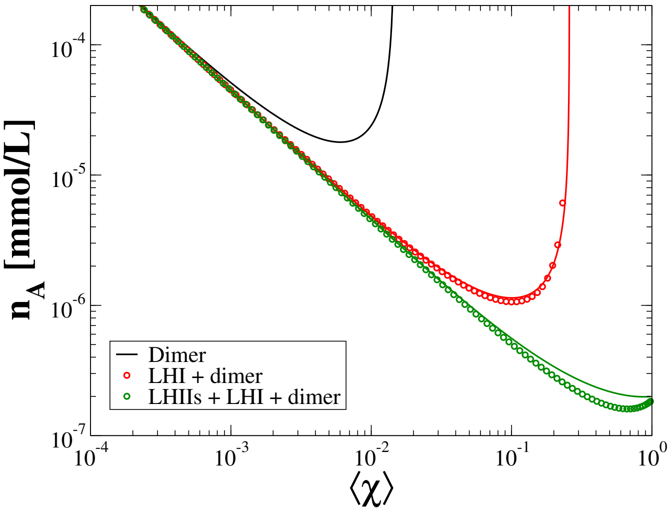

Figure 4.11: Threshold density for dimer, LHI+dimer and LHIIs+LHI+dimer aggregates. The red line is a dimer with R_u rescaled by $0.85(34/2)$ where 34 is the number of molecules in the LHI + dimer aggregate. The green line is a dimer with R_u rescaled by $0.45(250/2)$, where 250 is the number of molecules in the LHIIs + LHI + dimer aggregate. The parameters are the same as in Fig. 4.2h, apart from the black-body temperature, here $T_{BB} = 3000$ K.

4.6.15 Bio-inspired aggregate: Green Sulfur Bacteria

While in the main part of this chapter we considered a bio-inspired aggregate which mimics the architecture of purple bacterium antennae, here we consider a different bio-inspired aggregate which mimics the architecture of another natural photosynthetic complex: the green sulfur bacteria (GSB) antenna complex [93]. We are motivated in doing so since, as we pointed out in the main part of this chapter, the lasing efficiency of the bio-inspired aggregate increases with the number of molecules composing the aggregate; the GSB antenna photosynthetic complex is the largest and most efficient antenna complex present in nature [93]. Indeed, GSB antenna complexes can contain up to 250,000 BChl molecules. Even if the precise structure of the GSB antenna complex is not fully known and it can vary a lot in natural samples, one of the most important molecular structures present in GSB antennae are certainly constituted by self-aggregated BChl-c nanotubular structures [117]. Typically in GSB an ensemble of molecular structures (molecular nanotubes and lamellae) absorb sunlight and transfer excitation to a two-dimensional aggregate called "baseplate", which lies below the

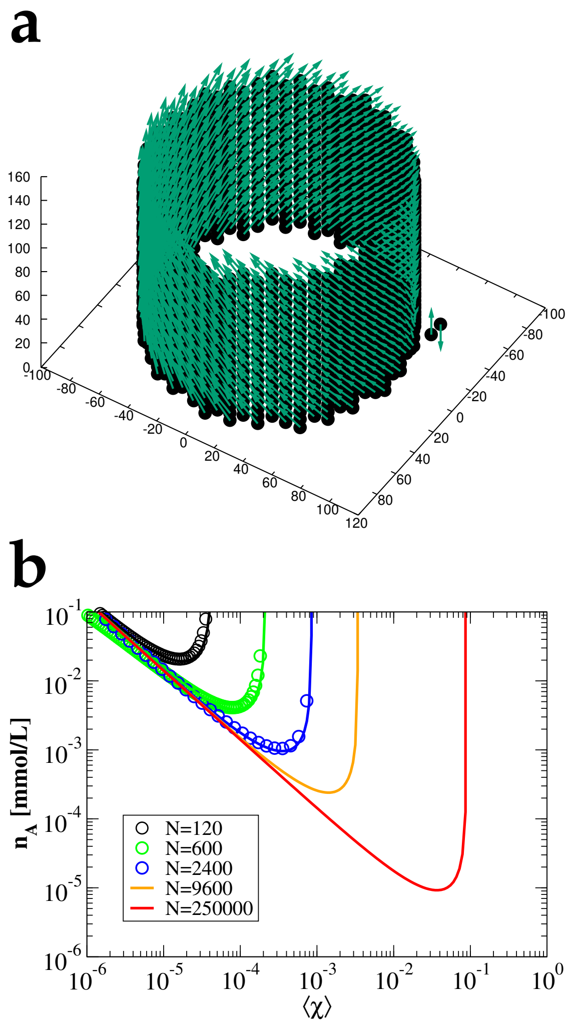

Figure 4.12: **(a)** Positions of the chromophores (circles) and transition dipole orientations (arrows) for the bio-mimetic complexes inspired to the GSB antenna complex considered in this section. Excitation energies, position, TDM orientation for this bio-mimetic aggregate are taken from Refs. [56, 96, 117]. **(b)** Lasing threshold density under natural sunlight for a dimer coupled to a green sulfur bacteria nanotube. Symbols have been obtained by diagonalizing the whole aggregate Hamiltonian and using Eq. (4.9). Continuous curves have been obtained using the lasing equation, Eq. (4.9), for the dimer only with a modified pumping $R_u \to NR_u/2$, where N is the total number of chromophores in the aggregate composed of a nanotube and a dimer. System sizes up to $N = 250,000$, corresponding to a realistic number of molecules in the whole green sulfur bacteria chlorosome [56, 96, 117], have been considered. However, as we discuss in the text, aggregate sizes $N \gtrapprox 4,000$ stretch the validity of the assumptions of our laser equations, and are thus of indicative rather than literal value.

nanotubular structures. Attached to the baseplate there are the FMO complexes which transfer the excitation from the antenna system to the reaction center.

Here we propose to enhance the pumping of the dimer $|H\rangle$ state by placing a natural nanotubular BChl-c aggregate close to the H-dimer as shown in Fig. 4.12a, where the positions and TDM orientations of the molecules composing the nanotubular structures and the dimers are shown. The nanotube structure is described in [117] and references therein. The nanotube is composed by BChl-c molecules which have an excitation energy of 1.9 eV and a TDM of $\sqrt{30}$ D. The coupling between the BChl molecules in the nanotube produces a superradiant excitonic state state around 750 nm [117]. As for the dimer, we place it 3 nm from the wall of the nanotube (the same distance of the baseplate). The excitation frequency of the molecules composing the dimer (1.4 eV) and their coupling 2000 cm^{-1} are chosen so that the dimer $|H\rangle$ state is close in energy to the superradiant state of the nanotube.

As was done for the purple bacteria, we diagonalize the appropriate Hamiltonian, as reported in Ref. [117], to obtain the eigenvalues and the TDM of the eigenstates of the whole aggregate and we then use Eq. (4.9) to obtain the threshold density of lasing as a function of the brightness $\langle \chi \rangle$ of the dimer under natural sunlight pumping. The results are shown in Fig. 4.12b, where symbols refer to the threshold density obtained from Eq. (4.9). The threshold density is shown for different nanotube lengths which contains different number of molecules N, see figure. The continuous lines represent the density threshold of a dimer alone whose R_u pumping factor is multiplied by $N/2$, where N is the total number of molecules in the whole aggregate (nanotube plus dimer).

As one can see, the effect of this different bio-inspired aggregate is similar to the Purple Bacteria molecular aggregate, which is to increase the pumping of the dimer by a factor $N/2$. The curves corresponding to the largest aggregates sizes ($N = 9600, 250000$) have been obtained only using the dimer equations with enhanced pumping. The results presented are very promising since they indicate the possibility to achieve lasing under natural sunlight for relatively large dimer brightness $\langle \chi \rangle \sim 10^{-1}$ (which is easy to reach experimentally [118]).

Notwithstanding the promising results in Fig. 4.12b for larger GSB aggregates, a word of caution is in order: as discussed in the following, applying our lasing equations to very large aggregates stretches the assumptions we have made in deriving Eqs. (4.6), (4.7), (4.8) and (4.9) beyond its strict regime of validity. This renders quantitative conclusions unreliable, however, we believe the extrapolation can nonetheless give an indicative picture of the expected qualitative trend.

Specifically, we expect the implicit assumption that thermalization in the overall system Hamiltonian eigenbasis is the fastest timescale to break for very large aggregates. On the one hand, it could be argued that disorder in large structures will lead to more localised states and the picture of completely delocalised eigenstates becomes questionable. On the other hand – and neglecting disorder for now – collective enhancements in the radiative rates will at some point change the hierarchy of timescales. To discuss this issue we now compare the fluorescence and the thermalization timescales: in large aggregates the dipole strength $|\mu_{SR}/\mu|^2$ of the superradiant state in the nanotube scales with the number of molecules as $|\mu_{SR}/\mu|^2 \approx 0.6N$ [117]. This means that the decay time of the superradiant state is $\tau_{fl} = \tau_0/|\mu_{SR}/\mu|^2$, where $\tau_0 \approx 3 \times 10^4$ ps is the decay time of a single molecule. The overall thermalization timescale is given by the thermalization on the nanotube followed by the excitation transfer time from the nanotube to the dimer. Since the latter can be enhanced by lowering the distance between the dimer and the nanotube, we will solely focus on the nanotube thermalization time in the following. An upper bound for the thermalization timescale τ_{th} can be obtained from the diffusion coefficient $D \approx 200\ \text{nm}^2/\text{ps}$ as estimated for the GSB nanotubes in [145], through the relationship $\tau_{th} = L^2/D$, where L is the length of the nanotube. For the natural nanotube considered here we have $L \approx N(0.01\ \text{nm})$. The given estimates of thermalization and fluorescence times suggest that for a nanotube of $N \approx 4000$ molecules we obtain $\tau_{th} \approx \tau_{fl}$. We would therefore expect the laser equations derived in Eqs. (4.6), (4.7) and (4.8) to become quantitatively unreliable for $N \gtrapprox 4000$.

Adequately capturing the dynamics of larger aggregates with an explicit model is beyond the scope of the current work, and would require the derivation of lasing equations without the assumption of quasi-instantaneous vibrational thermalization, while keeping the large dephasing assumption inducing incoherent cavity driving. This means that one should use incoherent laser equations for these larger aggregates similar to Eq. (4.75), used in the previous Section.

For the above reason, we only show circled data points for nanotubes up to $N = 2400$ in Fig. 4.12b. Up to this point the required lasing dimer threshold brightness approaches 10^{-3}, and we note that this value is still almost an order of magnitude better than the best result shown in Fig. 4.2h using the purple bacteria bio-inspired aggregate. However, we believe the solid extrapolation curves shown in Fig. 4.12b for larger N will nevertheless capture the trend for longer nanotubes, not least since much larger photosynthetic aggregates are known to be highly efficient at channelling energy excitations over long distances to the reaction centers. This extrapolation suggests that larger photosynthetic structures can indeed further significantly lower the lasing threshold requirements in terms of molecular density and dimer brightness.

Chapter 5

Superradiance in quantum dot superlattices

In this chapter we analyze the interplay of superradiance and noise in a solid state system. The results presented in this chapter have been published at: Francesco Mattiotti, Masaru Kuno, Fausto Borgonovi, Boldizsár Jankó, and G. Luca Celardo, "Thermal decoherence of superradiance in lead halide perovskite nanocrystal superlattices", Nano Lett. **20***, 7382–7388 (2020). I contributed by performing all the calculations, both numerical and analytical.*

Recent experiments by Rainò et al. [47] have documented cooperative emission from $CsPbBr_3$ nanocrystal superlattices, exhibiting the hallmarks of low temperature superradiance. In particular, the optical response is coherent and the radiative decay rate is increased by a factor of three, relative to that of individual nanocrystals. However, the increase is six orders of magnitude smaller than what is theoretically expected from the superradiance of large assemblies, consisting of 10^6 to 10^8 interacting nanocrystals. Here we develop a theoretical model of superradiance for such systems and show that thermal decoherence is largely responsible for the drastic reduction of the radiative decay rate in nanocrystal superlattices. Our theoretical approach explains the experimental results [47] and provides insight into the design of small nanocrystal superlattices, able to show a four orders of magnitude enhancement in superradiant response. These quantitative predictions pave the path towards observing superradiance at higher temperatures.

5.1 Introduction

Spontaneous emission is a basic quantum mechanical effect due to the coupling of an excited electronic state with the vacuum state of the electromagnetic field. In an ensemble of identical emitters, cooperative radiation emerges. Called superfluorescence [146], or superradiance (SR) by Dicke, who first proposed the phenomenon in 1954 [15], this effect arises from the excitation of an ensemble of individual dipole emitters and results in an emissive, macroscopic quantum state. SR has been observed in a variety of systems [17], with some of the most recent examples being cold atomic clouds [18], photosynthetic antenna complexes [19], molecular aggregates [20, 21], quantum dots [22, 23] and nitrogen vacancies in nanodiamonds [24]. This effect is relevant in enhancing absorption and energy transfer, which has been proposed to improve the efficiency of light-harvesting systems [1–5]. SR also leads to spectrally ultranarrow laser beams [6].

In an exciting new development, SR-like behavior has recently been observed at low temperature ($T = 6$ K) in a solid state superlattice of $CsPbBr_3$ perovskite nanocrystals (NCs) [47]. These superlattices consist of $\sim 10^6 - 10^8$ individual cubic NCs self-assembled into ordered cubic arrays with dimensions on the order of microns. Lead halide perovskite NC superlattices distinguish themselves from analogous semiconductor NC superlattices [147, 148] in that $CsPbBr_3$ NCs have very high emission quantum yields and very short radiative lifetimes [149]. This high sensitivity to incoming photons makes $CsPbBr_3$ NCs ideal candidates for building photon sensors and quantum devices. For this reason, recent experimental evidence of SR in $CsPbBr_3$ NC superlattices [47] represents an exciting development.

Apparent $CsPbBr_3$ NC superlattice SR distinguishes itself from the normal band edge emission of $CsPbBr_3$ NCs in that it exhibits a 2.7 times faster radiative lifetime. Most importantly, the emission is coherent as seen through first- and second-order correlation measurements.

Despite these highly suggestive results, there are notable discrepancies in the experimental observations [47] from what is expected of SR behavior. Our primary concern is the reported 2.7 times radiative rate enhancement. This is because SR radiative rate enhancements scale as N, the number of interacting dipoles [17, 27, 146]. Given that there are approximately $N \sim 10^6 - 10^8$ NC emitters in the superlattice, the observed factor of 2.7 enhancement easily differs by six orders of magnitude from what is expected at low temperature (6 K). For instance, at similar temperatures, SR enhancement in molecular systems is hundreds of times larger [20, 21].

5.2 Model, results and discussion

We have now developed an open quantum model [117], based on the use of well-known non-Hermitian radiative Hamiltonians [44], to rationalize SR-like emission from NC superlattices in the weak excitation regime. Our model specifically applies to the low fluence (500 nJ cm^{-2}) fluorescence measurements of Ref. [47] (see Appendix 5.4.1). This regime is also relevant for renewable energy applications, involving light harvesting, and has previously been invoked when modeling the SR of molecular aggregates [44] and cold atom gases [150, 152].

We model the $CsPbBr_3$ NC band edge electronic structure using a four-level system, which accounts for the main isotropic $s - p$ transitions of single NCs [149]. In the low fluence regime, we limit our considerations to the single excitation manifold, spanned by the states $|n, \alpha\rangle = \hat{a}^\dagger_{n,\alpha} |G\rangle$, where one excitation is present on the $\alpha = x, y, z$ state of the nth NC, while all the other NCs are in their ground states. Here, $|G\rangle$ is the ground

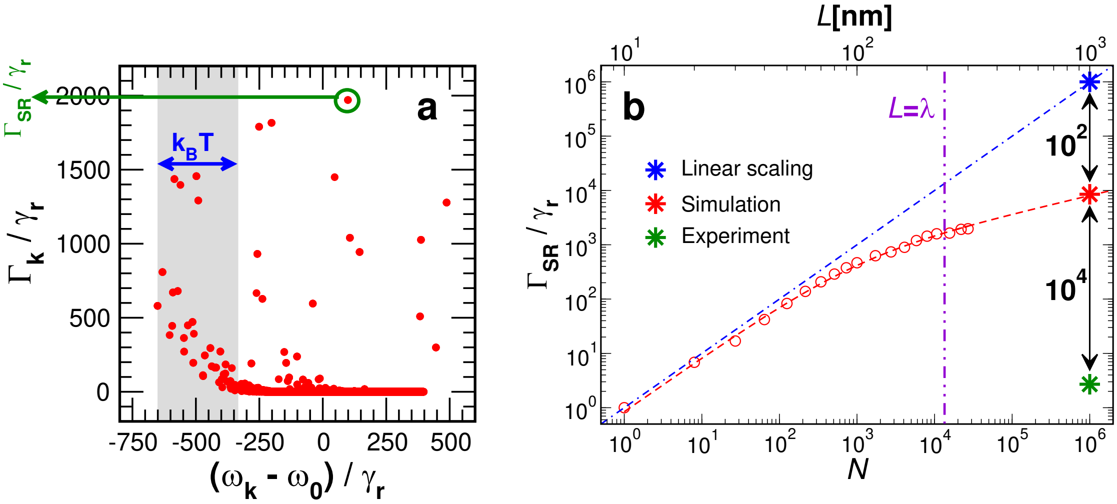

Figure 5.1: **a** Eigenvalues in the complex plane of the Hamiltonian $\hat{H}$ (see Eq. (5.1)) for a cubic superlattice of $N = 30^3$ NCs. $\hat{H}$ has dimensions $3N \times 3N = 6.561 \times 10^9$. The SR rate, Γ_{SR}, corresponding to the maximal decay rate, is circled green. The grayed region denotes the energy range within k_BT of the ground state energy at $T = 6$ K. **b** Plot of Γ_{SR}/γ_r versus N. The dashed blue line represents the maximal SR rate theoretically achievable. The violet vertical dash-dotted line indicates where L equals the wavelength λ of emitted light within the material. Simulation data (circles) have been fit (dashed red line) to the function $\Gamma_{SR}/\gamma_r = CN/(N^{2/3} + N_{cr}^{2/3})$ (fit parameters: $C = 81.2$ and $N_{cr} = 932$), that interpolates between the $\sim N$ behavior (expected for $L \ll \lambda$) and $\sim N^{1/3}$ (expected for $L \gtrsim \lambda$) [150, 151]. The green symbol marks the experimental results of Ref. [47]. Parameters for **a**,**b**: single NC radiative lifetime $1/\gamma_r = \tau_r = 0.4$ ns, single NC band edge energy $\hbar\omega_0 = 2.38$ eV, relative dielectric constant at optical frequencies $\epsilon_r = 4.8$ and NC edge length, $l = 9$ nm.

state of the whole system, where no excitation is present, and $\hat{a}^{\dagger}_{n,\alpha}$ is an operator that creates an excitation on the αth state of the nth NC. The label $\alpha = x, y, z$ denotes the three angular momentum states of the p orbital. In our simulations, we consider an ensemble of N NCs, each of edge length l, forming a cubic superlattice of edge length $L \gg l$. The center-to-center distance between neighboring NCs is $l^{'} = l + b$, which accounts for the presence of surface ligands. In our simulations, $b = 1$ nm, as commonly seen in superlattices[153].

The following $3N \times 3N$ non-Hermitian, radiative Hamiltonian

$$\begin{aligned}\hat{H} = &\sum_{n=1}^{N} \sum_{\alpha=x,y,z} E_n \left|n,\alpha\right\rangle \left\langle n,\alpha\right| \\ &+ \sum_{\alpha,\beta} \sum_{n\neq m} J^{\alpha\beta}_{mn} \left|m,\alpha\right\rangle \left\langle n,\beta\right| \end{aligned} \tag{5.1a}$$

accounts for interactions between individual NCs and their common light field [44, 150] where point-dipole couplings have been implicitly assumed (see Appendix 5.4.2). Furthermore, $E_n = \hbar\left(\omega_0 - i\frac{\gamma_r}{2}\right)$ is the complex self-energy of the nth NC, where $\hbar\omega_0 = 2.38$ eV is the NC transition energy [47] and $\gamma_r = \mu^2\omega_0^3\sqrt{\epsilon_r}/(3\pi\epsilon_0\hbar c^3) = 2.5\ \mathrm{ns}^{-1}$ is the radiative decay rate of a single NC [47] (with $\mu = 23$ D being the single NC transition dipole moment, $\epsilon_r = 4.8$ the relative dielectric permittivity at frequency ω_0 [149], ϵ_0 the vacuum permittivity and c the speed of light). Moreover, $J^{\alpha\beta}_{mn} = \Omega^{\alpha\beta}_{mn} - \frac{i}{2}\Gamma^{\alpha\beta}_{mn}$ with the real and imaginary parts given by

$$\begin{aligned}\Omega^{\alpha\beta}_{mn} = &\frac{\hbar\gamma_r}{2}\Big\{ y_0\left(k_0 r_{mn}\right) \hat{e}_\alpha \cdot \hat{e}_\beta \\ &- \frac{y_2\left(k_0 r_{mn}\right)}{2}\left[\hat{e}_\alpha \cdot \hat{e}_\beta - 3\left(\hat{e}_\alpha \cdot \hat{r}_{mn}\right)\left(\hat{e}_\beta \cdot \hat{r}_{mn}\right)\right]\Big\},\end{aligned} \tag{5.1b}$$

$$\begin{aligned}\Gamma^{\alpha\beta}_{mn} = &\hbar\gamma_r\Big\{ j_0\left(k_0 r_{mn}\right) \hat{e}_\alpha \cdot \hat{e}_\beta \\ &- \frac{j_2\left(k_0 r_{mn}\right)}{2}\left[\hat{e}_\alpha \cdot \hat{e}_\beta - 3\left(\hat{e}_\alpha \cdot \hat{r}_{mn}\right)\left(\hat{e}_\beta \cdot \hat{r}_{mn}\right)\right]\Big\}.\end{aligned} \tag{5.1c}$$

Here, $y_0(x)$, $y_2(x)$, $j_0(x)$, and $j_2(x)$ are spherical Bessel functions, $k_0 = \omega_0\sqrt{\epsilon_r}/c$ is the transition wavenumber, $\hat{e}_\alpha$ is the unit vector along the α direction, r_{mn} is the distance between the mth and nth NC and $\hat{r}_{mn}$ is the unit vector joining them. $J^{\alpha\beta}_{mn}$ describes the full radiative coupling between different NC transition dipoles in the superlattice.

A similar approach has recently been proposed to model two-dimensional $\mathrm{CsPbBr_3}$ NC superlattices. [154] The employed dipolar near-field coupling, however, is not valid for distances larger than λ, the NC band edge transition wavelength inside the material. This means that collective radiation cannot be analyzed for typical experimental system sizes where $L \approx 5\lambda$ (see Appendix 5.4.1). Within our approach interference between different emitters is implicitly accounted for by $J^{\alpha\beta}_{mn}$ even for distances larger than λ. Diagonalizing $\hat{H}$, in turn, yields complex eigenenergies $E_k = \hbar\left(\omega_k - i\frac{\Gamma_k}{2}\right)$ where the imaginary part is related to the radiative lifetime $\tau_k = \Gamma_k^{-1}$ of the kth eigenstate.

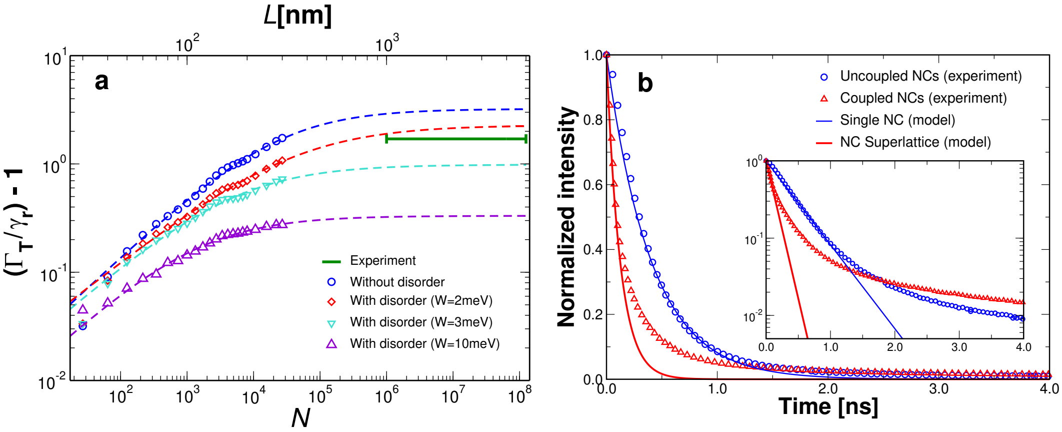

Figure 5.2: **a** Thermal average of the normalized radiative decay, $(\Gamma_T/\gamma_r) - 1$, (Eq. (5.2)) versus N. Note that we subtract one from the normalized thermal radiative rate to improve the visibility at small decay rates. The 2.7 enhancement reported in Ref. [47] is shown in solid green. Symbols are obtained from numerical diagonalization of Eq. (5.1). Dashed lines are best fits using the function $(\Gamma_T/\gamma_r) - 1 = AN^B/(N^B + N_{sat}^B)$, with fit parameters A, B, N_{sat} (values in Appendix 5.4.6). **b** Comparison of the experimental [47] NC superlattice SR radiative decay rate to theory, accounting for thermalization and static disorder ($W = 2$ meV). Temperature is 6 K. "Coupled NCs" refers to the decay of coupled NCs in a superlattice, while "Uncoupled NCs" refers to the measured decay of isolated, non-interacting NCs. Inset: same data on a logarithmic y-scale. In both **a,b**, $\hbar\omega_0 = 2.38$ eV, $\gamma_r = 2.5$ ns^{-1}, $\epsilon_r = 4.8$ and $l = 9$ nm.

Figure 5.1a shows the typical complex spectrum for a superlattice of $N = 30^3 = 27,000$ NCs with individual NC edge lengths of $l = 9$ nm and an associated center-to-center distance of $l^{'} = 10$ nm. Here both the decay widths ($\hbar\Gamma_k$) and the real energies ($\hbar\omega_k$) are normalized with the single NC decay width $\hbar\gamma_r \approx 1.6$ μeV. We identify the SR decay, Γ_{SR}, as the maximal decay rate predicted (cf. circle in Figure 5.1a), since time evolution from a generic initial state is dominated by $\sim \exp(-\Gamma_{SR} t)$, assuming $T = 0$ K (see Appendix 5.4.3). Note that the energy of the maximal SR state is highly dependent on the superlattice geometry, dimension and on the ratio L/λ, see Appendix 5.4.4.

Given that the system size we consider, $N = 30^3$, is two orders of magnitude smaller than that used experimentally [47] ($N \sim 10^6 - 10^8$), we study how Γ_{SR} scales with N and extrapolate its value to experimentally-relevant superlattice sizes using the well-established relationship [150, 151]: $\Gamma_{SR} \propto N$ for $L \ll \lambda$ and $\Gamma_{SR} \propto N/(L/\lambda)^2$ for for $L \gtrsim \lambda$, which implies $\Gamma_{SR} \propto N^{1/3}$ for a fixed NC superlattice density of N/L^3.

By extrapolating Γ_{SR} to large N, our model predicts a SR lifetime of order $\tau_{SR} \sim 0.04$ ps for a NC superlattice of similar size to the one studied experimentally [47] (see Figure 5.1b and Appendix 5.4.3). Thus we predict at least $\Gamma_{SR}/\gamma_r \sim 10^4$ for the experimental NC and superlattice size, which is four orders of magnitude larger than the enhancement observed in Ref. [47].

At this point, we suggest that what prevents agreement between theory and experiment is the absence of an explicit consideration of the sensitivity of SR to thermalization-induced coherence losses and structural disorder. Indeed, thermal noise suppresses quantum coherence, especially when $k_B T$ becomes comparable to the spectral width of the interacting ensemble (typically of the same order as the nearest-neighbor coupling J). This can lead to highly suppressed SR in the regime experimentally investigated [47], since at 6 K $k_B T = 0.5$ meV, which is ~ 3 times larger than the estimated $J = 0.14$ meV coupling between nearest NC neighbors.

We therefore account for thermalization effects on NC superlattice SR by taking thermal averages of all superradiant and subradiant eigenstate emission rates [155, 156], namely

$$\Gamma_T = \frac{1}{Z} \sum_k \Gamma_k e^{-\hbar\omega_k/(k_B T)} \,, \tag{5.2}$$

where $Z = \sum_k e^{-\hbar\omega_k/(k_B T)}$ is the partition function. From Equation (5.2), a corresponding emission intensity is $I(t) \propto \exp(-\Gamma_T t)$, with Γ_T the thermal decay rate. Thermalization therefore suppresses SR so that $\Gamma_T \approx \gamma_r$ (with $\gamma_r = \tau_r^{-1}$) if $k_B T$ is comparable to the spectral width of the coupled system. Note that in using Equation (5.2) we implicitly assume that thermal relaxation dominates all other relaxation processes in the material (see details in Appendix 5.4.5).

Figure 5.2a shows that by taking thermal averages for different superlattice sizes (blue circles), we observe an initial fast increase of Γ_T for small N, followed by a slower increase at large N. Assuming saturation in the limit $N \to \infty$ (see Appendix 5.4.7), we estimate $\Gamma_T/\gamma_r \approx 4.2$ for $N \sim 10^6 - 10^8$. This is in excellent agreement with the experimental results [47] where $\Gamma_{EXP}/\gamma_r \approx 2.7$.

An even better correspondence is found by taking into account structural disorder in the superlattice, stemming from NC size heterogeneities [47, 157] as well as inhomogeneities in NC positions and orientations. To estimate the impact this structural disorder has on SR, we consider excitation energy fluctuations, which we model by adding an on-site disorder of strength W (see also Appendix 5.4.8). This form of disorder has previously been used [25] to model the effects of different sources of time-independent disorder in various systems.

By introducing such disorder and extrapolating the results to experimentally-relevant superlattice sizes, we find excellent agreement with experiment [47] for W between 2 meV and 3 meV, see Figure 5.2a where the experimental [47] result is shown in green. Note these values of W are several times larger than the nearest-neighbor coupling $J = 0.14$ meV ($W/J \approx 15$).

Figure 5.2b now compares the theoretical decay, Γ_T, for $W = 2$ meV (red line) to the experimental emission intensity decay reported in Ref. [47] (red triangles). Our theoretical emission intensity accounts for $\sim 70\%$ of the experimental intensity decay. A discrepancy between theory and experiment is visible at long times (see also inset). This likely reflects omissions in the theory, namely not accounting for non-radiative processes in NCs that lead to non-unity emission quantum yields [158]. This interpretation is confirmed by the non-exponential decay of the emission from an ensemble of uncoupled NCs (blue circles, Figure 5.2b). Modelling such processes is highly non trivial since they should account for dynamical transitions between radiative and non-radiative channels, possibly including activation/deactivation processes for non-radiative channels that induce blinking [159, 160]. At this point, however, our proposed theoretical framework, which accounts for thermalization and structural disorder, generally rationalizes the superradiant accelerated PL decay reported in Ref. [47].

In Ref. [47] it was also observed that the emission spectrum of single superlattices consists of several emission peaks, with the SR emission band being redshifted relative to the emission of uncoupled NCs by 64 ± 6 meV (an average across 10 superlattices). This redshift cannot be explained by dipolar couplings between NCs in our model, which at best induces a few meV redshift to the SR emission, see Appendix 5.4.9.

While the origin of a redshifted emission from superlattices remains debated [161–167], (see Appendix 5.4.9), we conjecture here that the SR redshifted emission observed in Ref. [47] arises from the existence of sub-domains, composed of larger NCs, within individual superlattices. In fact, this has already been suggested by the authors of Ref. [47]. Supporting this are $CsPbBr_3$ NC size-dependent band energies that change by hundreds of meV when NC edge lengths change from $l = 3$ nm to $l = 12.8$ nm [157]. Consequently, large NC SR-active sub-domains will show a sizable redshift relative to uncoupled and smaller NCs present in the same NC superlattice. It is of note that larger NCs have an inherently higher likelihood of realizing uniform SR-active sub-domains, due to their smaller relative edge length fluctuations [157], see Appendix 5.4.9.

Indeed, assuming that l varies between 8 nm and 12 nm, which is consistent with the size fluctuations reported in Ref. [47], a 50 meV redshift is readily realized between larger NCs and their smaller NC counterparts within a given superlattice's residual size

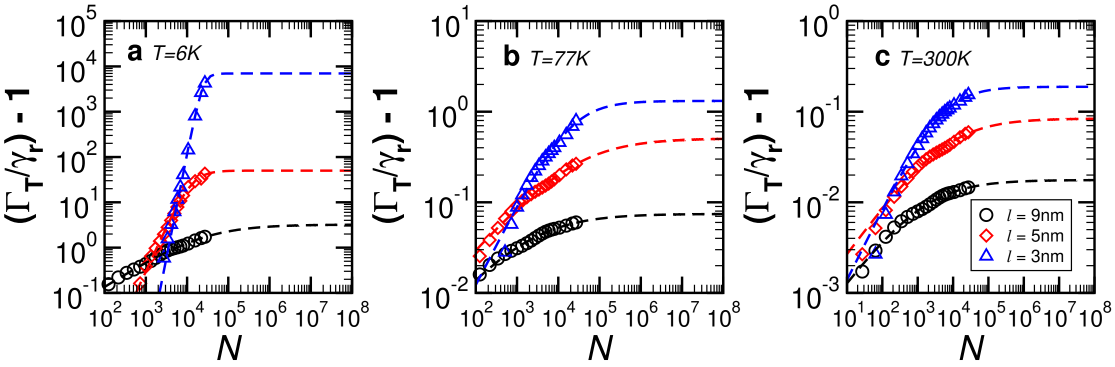

Figure 5.3: Thermal average of the normalized radiative decay (Eq. (5.2)) versus N for different temperatures (T = 6 K, 77 K, 300 K). In each panel, the temperature is fixed and each color represents a different NC size (l = 3 nm, 5 nm, 9 nm, see the legend). Dashed lines are best fits with the function $(\Gamma_T/\gamma_r) - 1 = AN^B/(N^B + N_{sat}^B)$, with fit parameters A, B, N_{sat} (values in Appendix 5.4.6). In all panels, the excitation energy is $\hbar\omega_0 = 2.38$ eV and the transition dipole moment is $\mu = 23$ D. The relative dielectric constant of NC superlattice effective medium is $\epsilon_r = 4.8$.

distribution (see details in the Appendix 5.4.9). The existence of sub-domains made of larger NCs within a superlattice thus rationalize large redshifts of the SR emission.

How large are the sub-domains? In considering this, we note that thermal decoherence, which occurs on the several picoseconds timescale in CsPbBr$_3$ NCs [168], cannot be neglected when considering their radiative decay, a process that occurs on the hundred picosecond timescale. This ultimately implies that the aforementioned SR sub-domains must be composed of at least $N = 10^4$ NCs to attain a superradiant decay compatible with experiment, see Fig. 5.2a.

The existence of SR-active sub-domains also explains the large SR linewidth seen in Ref. [47]. Namely, Ref. [47] shows SR to have an inhomogeneous linewidth of tens of meV. This exceeds the estimated static disorder in our model by at least an order of magnitude, see Fig. 5.2a. The discrepancy, however, can be rationalized by the presence of *multiple* SR-active sub-domains within a given superlattice, which is consistent with the presence of substructures in the SR emission band, as noted in Ref. [47]. Namely, provided that these sub-domains are composed of NCs with different average edge lengths, inhomogeneous broadening of the experimetal SR will be seen. In whole, the existence SR sub-domains within a given superlattice, where each sub-domain is composed of large NCs, with an average size that differs from sub-domain to sub-domain, self-consistently rationalizes three observations made in Ref. [47]: (1) large 64 ± 6 meV redshifts, (2) large 15 ± 4 meV SR inhomogeneous linewidths and (3) SR emission spectral substructure. For more details, see the discussion in Appendix 5.4.10.

Finally, our theoretical framework points to ways of enhancing the SR effect in NC superlattices. Specifically, our model suggests that superlattices made of smaller, tightly packed NCs will exhibit stronger couplings, implying enhanced SR decays and better prospects for realizing high temperature SR.

We demonstrate this by decreasing component NC edge lengths, l, below CsPbBr$_3$'s exciton Bohr diameter of 7 nm [149, 157]. In what follows, a NC transition dipole moment of $\mu = 23$ D and a radiative decay rate of $\gamma_r = 2.5$ ns^{-1} is assumed since both parameters are weakly size-dependent in the range of NC sizes explored [149, 157, 169]. Near-field dipole coupling strengths, in contrast, increase due to smaller inter-NC separations. This stems from nearest-NC neighbor couplings scaling as $J \approx \mu^2/(l')^3$ (see Appendix 5.4.2).

We consider NCs as small as $l = 3$ nm, compatible with the current lower bound for size-controlled CsPbBr$_3$ NCs [157]. In the case of $l = 3$ nm, the estimated coupling between NCs is $J \approx 2.1$ meV. This is 15 times larger than that in the $l = 9$ nm NC superlattice studied in Ref. [47].

Figure 5.3 shows the dependence of Γ_T with NC superlattice size, for superlattices made of $l = 3$ nm and $l = 5$ nm NCs. The $l = 9$ nm case is included for comparison purposes. Each panel in Figure 5.3 considers a different temperature ($T = 6$ K, 77 K, 300 K). It is clear that decreasing l enhances the SR effect at all temperatures. The largest enhancement occurs at $T = 6$ K for $l = 3$ nm.

By assuming enhancement saturation at large N, we estimate Γ_T for realistically large superlattices ($N \sim 10^8$) made of $l = 3, 5, 9$ nm NCs. At $T = 6$ K, we predict $\Gamma_T/\gamma_r \approx 4.2$ for $l = 9$ nm, in excellent agreement with experiment [47]. For $l = 5$ nm and $l = 3$ nm, we find $\Gamma_T/\gamma_r \approx 50$ and $\Gamma_T/\gamma_r \approx 7000$ respectively at $T = 6$ K. The latter $l = 3$ nm enhancement is three orders of magnitude larger than that reported in Ref. [47].

The modeling therefore suggests that small NCs can be used to significantly increase the temperature range where it is possible to observe NC superlattice SR. To illustrate this, Figure 5.3b shows that the expected SR decay rate enhancement for a $l = 3$ nm NC superlattice is $\Gamma_T/\gamma_r \approx 2.3$ at liquid nitrogen temperature ($T = 77$ K). This raises exciting prospects for realizing robust NC superlattice SR at significantly higher temperatures than 6 K in the near future.

Before concluding, it is important to consider the role of static disorder for different NCs sizes. Indeed, band edge transition energies vary with size, especially at small l [157]. This, in turn, implies that small NCs will exhibit energy disorder parameters larger than those of their larger NC counterparts for identical size distributions. Nevertheless, as shown in Appendix 5.4.10, the ratio W/J (where W is the disorder strength and J is the coupling between neighbor NCs) remains almost constant as NC sizes are varied between $l = 3$ nm and $l = 9$ nm. Consequently, since realistic disorder has a minor effect for large NC sizes and for $W/J \approx 15$, we expect a minor effect for small NCs so long as W/J remains of the same order.

5.3 Conclusions

In summary, we have developed a theoretical model that explicitly accounts for the effects of thermal decoherence and structural disorder on NC superlattice SR and which rationalizes the SR effect recently observed [47]. Our proposed model also estimates the effects of NC size and temperature on superlattice SR, revealing that superlattices made of smaller, tightly packed NCs will exhibit stronger couplings. Indeed, we predict a SR enhancement of at least three orders of magnitude, using NCs with edge lengths of $l = 3$ nm. This points to the possibility of observing NC superlattice SR at liquid nitrogen temperatures instead of at $T = 6$ K.

We note that our model is generally applicable to other NC assemblies. The only input parameters needed are NC band-edge transition energies, lifetimes, and NC positions within assemblies. Future iterations of the model will account for non-radiative processes in NCs [158] (i.e. non unity emission quantum yields) as well as higher excitation fluences.

5.4 Appendix

5.4.1 Non-Hermitian Hamiltonian for NC superlattices

Here we describe in detail the radiative hamiltonian $\hat{H}$ (Eq. (5.1)), introduced to rationalize SR-like emission from NC superlattices focusing on the low fluence regime (weak excitation).

In order to build a model able to reproduce the system response to electromagnetic radiation, the features of the NC emitter must be established. The unit element of the superlattice under study is the cubic CsPbBr$_3$ perovskite NC [149]. Because of its cubic symmetry, optical transitions in a CsPbBr$_3$ NC involve three degenerate states (labelled as $\alpha = x, y, z$), each with a transition dipole moment (TDM) equal in magnitude ($\mu_\alpha = \mu$) and perpendicular to the others. A similar situation is found in many atomic systems with isotopic response to electromagnetic excitation [150, 152]. Thus we model each NC as a four-level system, with a ground state $|g\rangle$ and three degenerate excited states $|x\rangle$, $|y\rangle$ and $|z\rangle$. Corresponding TDM matrix elements are $\left\langle \alpha \middle| \hat{\vec{\mu}} \middle| g \right\rangle = \mu \hat{e}_\alpha$, with $\alpha = x, y, z$ and the Cartesian unit vectors defined as $\hat{e}_\alpha$.

Here we consider an ensemble of cubic NCs and, in particular, focus on a regular cubic superlattice. Since excitons are bound inside each NC, we do not include any overlap interaction between different NCs and the only interaction between NCs is mediated by the light field. We thus propose to describe the NC cubic superlattice using the following $3N \times 3N$ radiative Hamitonian [150, 152], which takes the vectorial nature of light into account,

$$\hat{H} = \hbar \left(\omega_0 - i \frac{\gamma_r}{2} \right) \sum_{\alpha \in \{x,y,z\}} \sum_{n=1}^{N} |n, \alpha\rangle \langle n, \alpha| + \sum_{\alpha,\beta \in \{x,y,z\}} \sum_{\substack{m,n=1 \\ (m \neq n)}}^{N} J_{mn}^{\alpha\beta} |m, \alpha\rangle \langle n, \beta| \,, \tag{5.3}$$

where $\hbar\omega_0 = 2.38$ eV is the NC transition energy [47] and $\gamma_r = \mu^2 \omega_0^3 \sqrt{\epsilon_r} / (3\pi\epsilon_0\hbar c^3) = 2.5\ \text{ns}^{-1}$ is the radiative decay rate of a single NC [47] (with $\mu = 23$ D being the single NC TDM, $\epsilon_r = 4.8$ the relative dielectric permittivity at frequency ω_0 [149], ϵ_0 the vacuum permittivity and c the speed of light). In Eq. (5.3), $|n, \alpha\rangle$ represents a quantum state where the nth NC is excited in its αth state, while all the other NCs are in their ground state. Interaction terms are non-Hermitian, namely $J_{mn}^{\alpha\beta} = \Omega_{mn}^{\alpha\beta} - \frac{i}{2}\Gamma_{mn}^{\alpha\beta}$ with the real and imaginary parts given, respectively, by

$$\Omega_{mn}^{\alpha\beta} = \frac{\hbar\gamma_r}{2} \left\{ y_0\left(k_0 r_{mn}\right) \hat{e}_\alpha \cdot \hat{e}_\beta - \frac{y_2\left(k_0 r_{mn}\right)}{2} \left[\hat{e}_\alpha \cdot \hat{e}_\beta - 3\left(\hat{e}_\alpha \cdot \hat{r}_{mn}\right)\left(\hat{e}_\beta \cdot \hat{r}_{mn}\right) \right] \right\} \,, \tag{5.4a}$$

$$\Gamma_{mn}^{\alpha\beta} = \hbar\gamma_r \left\{ j_0\left(k_0 r_{mn}\right) \hat{e}_\alpha \cdot \hat{e}_\beta - \frac{j_2\left(k_0 r_{mn}\right)}{2} \left[\hat{e}_\alpha \cdot \hat{e}_\beta - 3\left(\hat{e}_\alpha \cdot \hat{r}_{mn}\right)\left(\hat{e}_\beta \cdot \hat{r}_{mn}\right) \right] \right\} \,. \tag{5.4b}$$

In Eq.s (5.4), $y_0(x)$, $y_2(x)$, $j_0(x)$, and $j_2(x)$ are spherical Bessel functions, $k_0 = \omega_0 \sqrt{\epsilon_r} / c$ is the transition wavenumber, ϵ_r is the refractive index at the optical frequency ω_0, r_{mn} is the distance between the mth and nth NC and $\hat{r}_{mn}$ is the unit vector joining them.

Being non-Hermitian, Eq. (5.3) has complex eigenvalues $E_k = \hbar\left(\omega_k - i\frac{\Gamma_k}{2}\right)$ that represent the self-energies of eigenstates. Each eigenstate has a finite lifetime $\tau_k = 1/\Gamma_k$ that is inversely proportional to the imaginary part $(-\hbar\Gamma_k/2)$ of the eigenvalue.

Our model specifically applies to the weak excitation regime, where the physics can be described by considering that only one excitation is present in the system. This regime is relevant for the fluorescence measurements in Ref. [47] at low excitation fluence (500 nJ cm^{-2}). Indeed, multiplying the fluence by the area of a superlattice face ($\sim$ 1 μm^2) and dividing by the photon energy (3 eV, see Ref. [47]), indicates that, for this fluence value, only $\sim 10^4$ photons are hitting the superlattice. This is a small fraction ($\sim$ 1%) of the number of NCs present in the superlattice, $N \sim 10^6$. The single-excitation approximation is thus appropriate for describing the experiment. The main advantage of the single-excitation approximation is that the Hilbert space scales as N in contrast to the 2^N dimension of the full system. This allowed us to numerically study superlattices containing up to $N = 30^3$ NCs, with an Hamiltonian matrix dimension of $3N \times 3N = 6.561 \times 10^9$. In general, by exploiting the translational invariance of superlattices, even larger sizes could be studied by employing a Bloch-like eigenbasis for the superlattice [154, 170]. Nevertheless, we found that the Bloch-like analytical wavefunctions as employed in Ref. [154] for two-dimensional lattices are not the correct choice in our three-dimensional case, since long-range couplings between NCs do not allow to neglect boundary effects (see more details in section 5.4.1). Note that the effect of the long-range $1/r_{mn}^2$ and $1/r_{mn}$ terms in the Hamiltonian, Eq. (5.4), is stronger in three dimensions than in lower dimensions.

Discrepancies with the Bloch basis

We introduced the radiative hamiltonian $\hat{H}$ (Eq. (5.1)) describing the collective interaction of a CsPbBr$_3$ NC superlattice with the common radiation field. As we discuss in the previous sections, a similar approach has been introduced in Ref. [154] to model two-dimensional NC superlattices. A common problem to model these systems is that they are made of a very large number of NCs ($N \gtrsim 10^6$), so that it is not possible to deal numerically with the full Hamiltonian matrix, of order N. In Ref. [154] this "size problem" is solved in an elegant way by using the periodicity of the superlattice. As one can see from Eq. (5.4), the matrix elements of $\hat{H}$ depend on the positions of the NCs in the superlattice, which are periodic. Therefore, if one neglects the boundary effects, the Hamiltonian becomes translation-invariant on the Bravais lattice $\vec{n}l' = (n_x l', n_y l', n_z l')$ (with $n_{x,y,z}$ integers) and the Bloch Theorem could be applied[170], implying that the eigenfunctions would have the form

$$\langle \vec{n}, \alpha | \psi_{\vec{k},u} \rangle = \frac{e^{i\vec{k}\cdot\vec{n}}}{\sqrt{N}} c_u^{(\alpha)}(\vec{k}) \,, \qquad \alpha \in \{x, y, z\} \,, \qquad u = 1, 2, 3 \,. \tag{5.5}$$

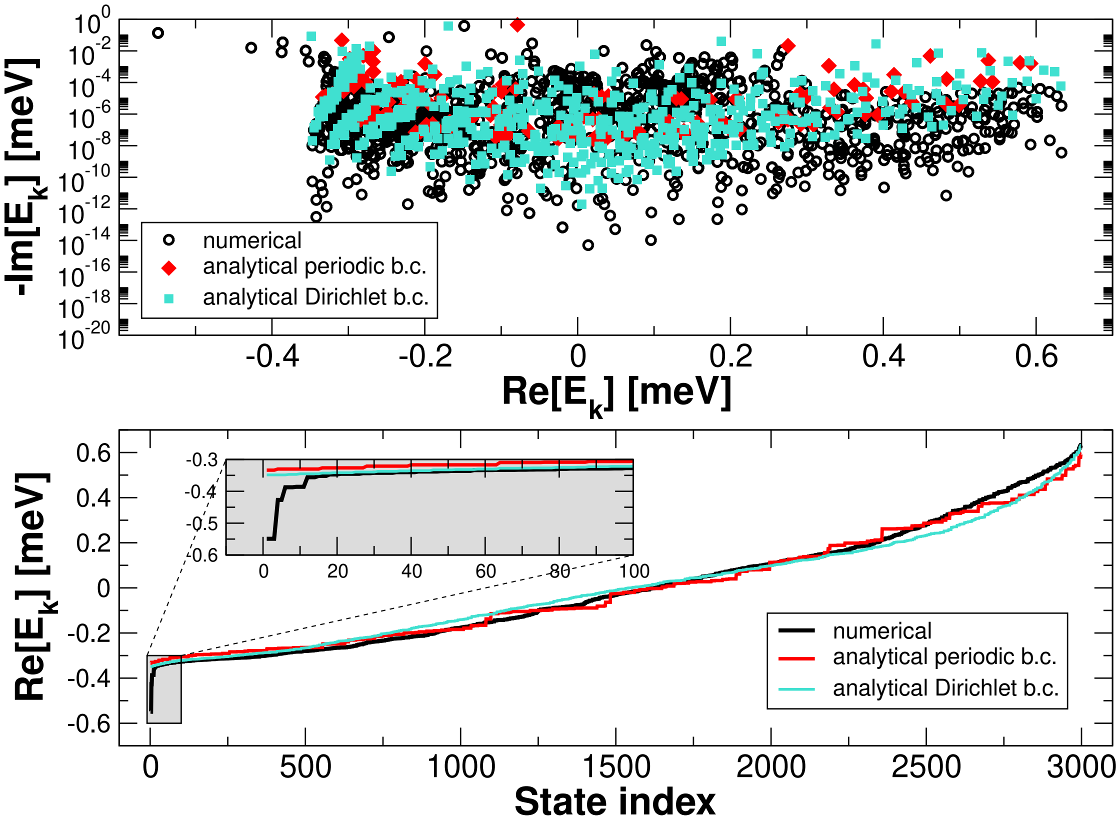

Figure 5.4: Complex eigenvalues of $\hat{H}$ in the complex plane (upper panel) and their real parts (lower panel), computed from numerical diagonalization and as expectation values $\langle \psi_{\vec{k},u} | \hat{H} | \psi_{\vec{k},u} \rangle$ of the Bloch wavefunctions, Eq. (5.5). For the analytical wavefunctions, two different boundary conditions have been considered (see text). Parameters: $\hbar\omega_0 = 2.38$ eV, $\gamma_r = 2.5\ \text{ns}^{-1}$, $\epsilon_r = 4.8$, $N = 1000$, $l = 9$ nm.

In Eq. (5.5) the vector $\vec{k}$ has N possible values, determined by the boundary conditions, while the $c_u^{(\alpha)}(\vec{k})$ coefficients can be found by diagonalizing a 3×3 matrix for each $\vec{k}$,

$$h_{\alpha\beta}(\vec{k}) = \langle \psi_{\vec{k},\alpha} | \hat{H} | \psi_{\vec{k},\beta} \rangle = \sum_{\vec{m}} \sum_{\vec{n}} \frac{e^{i\vec{k}\cdot(\vec{m}-\vec{n})}}{N} \langle \vec{n}, \alpha | \hat{H} | \vec{m}, \beta \rangle \ . \tag{5.6}$$

The coefficients $c_u^{(\alpha)}(\vec{k})$ in Eq. (5.5) are the coefficients that allow to diagonalize $h_{\alpha\beta}(\vec{k})$, and they arise from the coupling between Bloch wavefunctions having the same eigenmode $\vec{k}$ but different polarizations $\alpha, \beta = x, y, z$.

Such approach works very well in presence of nearest-neighbor coupling only, for which boundary effects are negligible, as we verified (data not shown). When boundary effects are negligible, it is convenient to employ periodic boundary conditions to the Hamiltonian, like it has been done in Ref. [154], where the authors use dipolar couplings on a two-dimensional superlattice, so that the couplings are short-range. On the other hand, this approach might not work in our case, that is a cubic superlattice larger than the transition wavelength λ, with long-range radiative couplings scaling as r_{nm}^{-3}, r_{nm}^{-2} and even r_{nm}^{-1} (see Eq. (5.4)). In such case, the boundary effects can become important and the choice of the boundary conditions (for example, periodic boundary conditions *vs.* Dirichlet boundary conditions) can lead to different results.

In order to show this, in the following we compare results from exact diagonalization with those obtained using analytical, translational-invariant eigenstates obtained imposing different boundary conditions. In Fig. 5.4 we plot the complex spectrum of $\hat{H}$, that is the real and imaginary parts of the complex eigenvalues $E_k = \hbar \left(\omega_k - i\frac{\Gamma_k}{2} \right)$. We use a cubic superlattice of $N = 1000$ NCs with size $l = 9$ nm. We compare the numerical results obtained from the diagonalization of $\hat{H}$ (black circles) to the expectation values $\langle \psi_{\vec{k},u} | \hat{H} | \psi_{\vec{k},u} \rangle$ of the Bloch wavefunctions, using two different boundary conditions (b.c.): periodic b.c. ($e^{i\vec{k}\cdot\vec{n}} = e^{i2\pi\vec{m}_k\cdot\vec{n}/\sqrt[3]{N}}$, with $\vec{m}_k$ vector of integers) and Dirichlet b.c. ($\frac{1}{\sqrt{N}} e^{i\vec{k}\cdot\vec{n}} \to \left(\frac{2}{1+\sqrt[3]{N}} \right)^{3/2} \sin\left(\frac{\pi m_k^x n_x}{1+\sqrt[3]{N}} \right) \sin\left(\frac{\pi m_k^y n_y}{1+\sqrt[3]{N}} \right) \sin\left(\frac{\pi m_k^z n_z}{1+\sqrt[3]{N}} \right)$, with $m_k^{x,y,z} = 1, \dots, \sqrt[3]{N}$, integers). As one can see from the upper panel of Fig. 5.4, the estimation of the eigenvalues with the Bloch wavefunctions ("analytical") are different from the numerical results. Specifically, there are large differences for the few eigenvalues that have the lowest real part $\mathrm{Re}[E_k]$. These last eigenvalues are particularly important because, once the system reaches thermal equilibrium, most of the population is concentrated at low energy. This discrepancy is also shown in the lower panel of Fig. 5.4, where the real part of the eigenvalues is plotted against the state index, ordering the eigenvalues according to their real parts. There is a clear discrepancy of about 0.2 meV (that is 40% of $k_B T$ with $T = 6$ K) for the first 10 to 20 eigenvalues (see also the blow-up).

If the discrepancy originates from long-range couplings, then it will increases with N. To check this point, in Fig. 5.5 we plot the main figure of merit of SR in this work, that is the thermal average of the decay rates (defined in Eq. (5.2)), as a function of the sys-

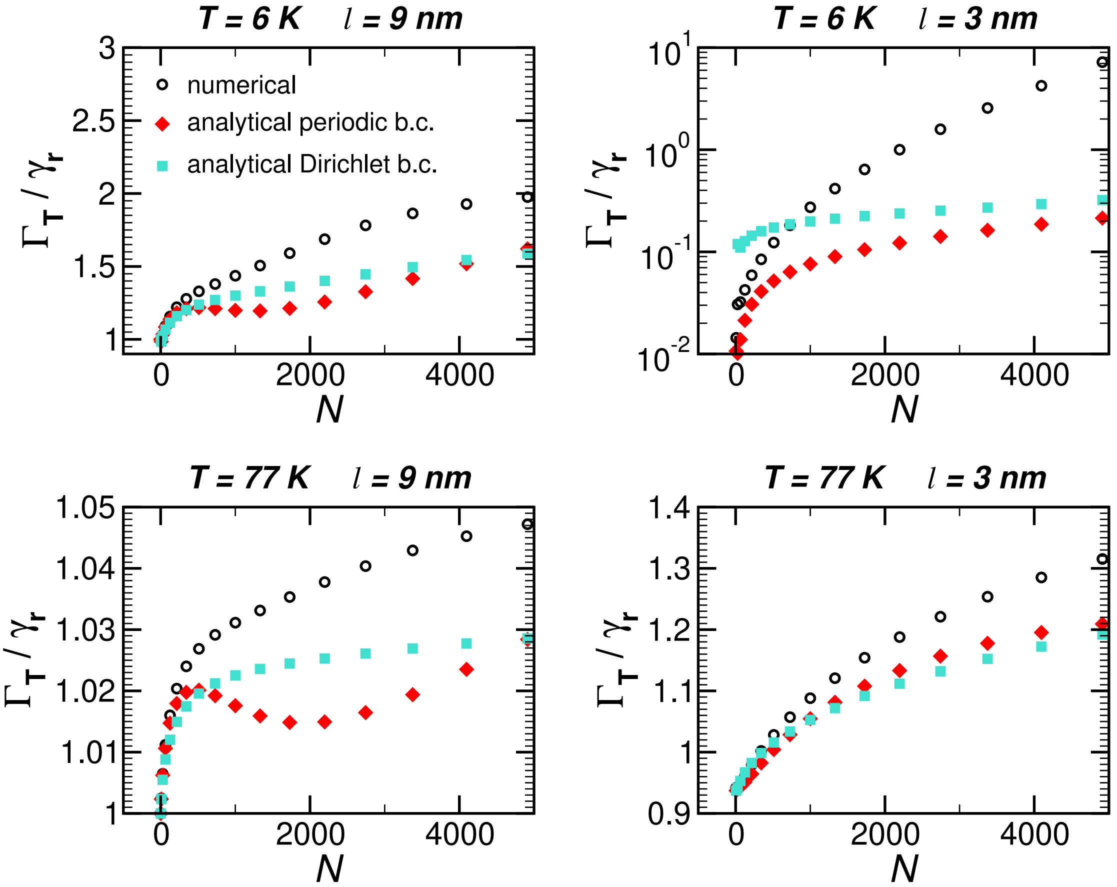

Figure 5.5: Thermal average of the decay rates (see Eq. (5.2)) as a function of the number of NCs in the superlattice. Comparison between numerical eigenvalues and expectation values of $\hat{H}$ over the Bloch wavefunctions, Eq. (5.5). Temperature (T) and NC side length (l) indicated over each panel. Parameters: $\hbar\omega_0 = 2.38$ eV, $\gamma_r = 2.5\,\text{ns}^{-1}$, $\epsilon_r = 4.8$.

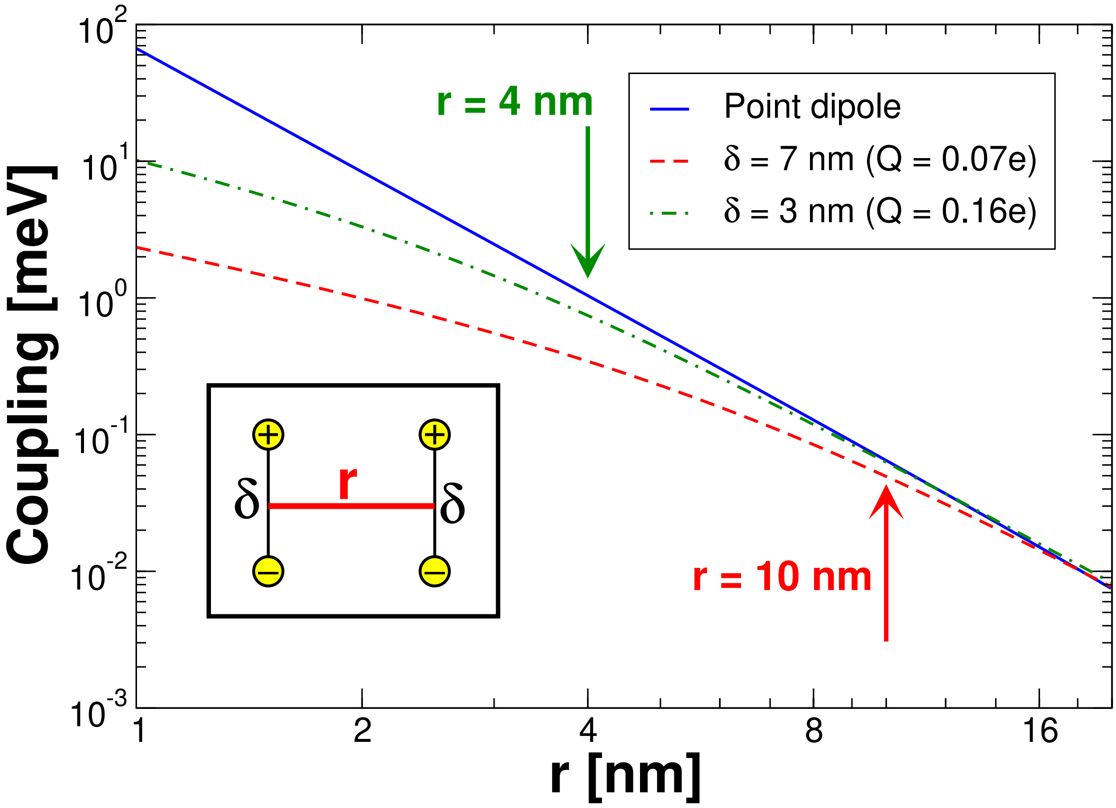

Figure 5.6: Extended dipole coupling between the TDMs of two NCs (see Eq. (5.7)). The relative positions of the partial charges $\pm Q$ are shown pictorially inside the plot. The point dipole coupling is given by Eq. (5.8). Parameters: $\mu = 23$ D, $\epsilon_r = 4.8$.

tem size N for different temperatures ($T = 6$ K, 77 K) and different NC sizes ($l = 3$ nm, 9 nm). As one can see, the results obtained using the analytical Bloch wavefunctions differ from the numerical results and the discrepancy increases with N, indeed. These results suggest that the Bloch basis is not suitable to describe the system at thermal equilibrium.

5.4.2 Point dipole validity

The radiative Hamiltonian introduced in section 5.4.1 describes the couplings between the TDMs of the NCs treating them as point dipoles. Here we justify such approximation.

In general, the coupling between two excited states localized on different NCs can be described in terms of the Coulomb interaction between the excited state wavefunctions [143]. In most practical cases, the Coulomb coupling between two extended wavefunctions can be mapped to the so-called "extended dipole coupling" [143], that is the Coulomb interaction between four effective charges (two for each wavefunction, with opposite sign). The extended dipole coupling has the form

$$V_{mn} = \frac{Q^2}{4\pi\epsilon_0\epsilon_r}\left(\frac{1}{r_{++}} + \frac{1}{r_{--}} - \frac{1}{r_{+-}} - \frac{1}{r_{-+}}\right) \tag{5.7}$$

where $r_{++} = |\vec{r}_{m+} - \vec{r}_{n+}|$, $r_{--} = |\vec{r}_{m-} - \vec{r}_{n-}|$, $r_{+-} = |\vec{r}_{m+} - \vec{r}_{n-}|$ and $r_{-+} = |\vec{r}_{m-} - \vec{r}_{n+}|$. The position of the "±" charge in the nth dipole is $\vec{r}_{n\pm} = \vec{r}_n \pm (\delta/2)\hat{e}_n$, where $\hat{e}_n$ is the unit vector of the nth dipole, δ is the effective charge displacement in the dipole and Q is the partial charge, that is an effective point charge used to describe the coupling. These parameters must satisfy the constraint $\mu = Q\delta$, where μ is the magnitude of the TDM.

If the charge displacement is small with respect to the distance between the dipoles, i.e. $\delta \ll |\vec{r}_m - \vec{r}_n|$, the extended dipole coupling is approximated by the near-field point-dipole coupling, that is

$$V_{mn} \approx \frac{\mu^2\left[\hat{e}_m \cdot \hat{e}_n - 3\left(\hat{e}_m \cdot \hat{r}_{mn}\right)\left(\hat{e}_n \cdot \hat{r}_{mn}\right)\right]}{4\pi\epsilon_0\epsilon_r|\vec{r}_m - \vec{r}_n|^3} \tag{5.8}$$

where $\hat{r}_{mn} = (\vec{r}_m - \vec{r}_n)/|\vec{r}_m - \vec{r}_n|$.

In the case of NCs, the excitons are bound inside the NC volume due to quantum confinement [171]. Therefore, the charge displacement is bounded by l, that is the edge length of the NC, and by the exciton Bohr diameter $2a_B$ (where a_B is the exciton Bohr radius).

In Fig. 5.6 we plot the extended dipole coupling, see Eq. (5.7), for a pair of TDMs against their center-to-center distance r, comparing it to the point dipole coupling, Eq. (5.8). We employ the typical parameters of $CsPbBr_3$ NCs, that is the magnitude $\mu = 23$ D and dielectric constant $\epsilon_r = 4.8$, and we consider a pair of TDMs oriented perpendicularly to the joining vector (see the pictorial representation in the box inside Fig. 5.6), but a similar result can be obtained with different orientations. For the charge displacement δ we consider two typical situations: $\delta = 2a_B = 7$ nm, that is the maximal charge displacement for large NCs, and $\delta = 3$ nm, corresponding to the maximal charge displacement for the smallest NC side length that we considered in Fig. 5.3. As one can see from Fig. 5.6, the extended dipole coupling is well approximated by the point dipole if r is larger than some value, proportional to δ. For a fixed value of r, the agreement with the point dipole approximation is better for smaller charge displacement δ. In particular, we checked the difference in the couplings between nearest neighbour NCs in two cases: (a) $\delta = 7$ nm and $r = 10$ nm, that is NCs with $l = 9$ nm (red arrow), and (b) $\delta = 3$ nm and $r = 4$ nm, corresponding to NCs with $l = 3$ nm (green arrow). In both cases the point dipole coupling overestimates the extended dipole coupling by $\sim 30\%$.

We conclude that the point dipole coupling captures correctly the order of magnitude of the nearest neighbor couplings, assuming the maximal charge displacement in typical cases. The accuracy of the point dipole approximation improves on decreasing the charge displacement, and since we obtain a discrepancy of $\sim 30\%$ for the maximal δ, the actual charge displacement in these NCs is likely smaller than what we considered, implying a better accuracy.

5.4.3 Time-resolved fluorescence at T = 0 K without disorder

Here we proceed to use the Hamiltonian $\hat{H}$, see Eq. (5.1), to compute the time evolution of an excitation initially absorbed by the superlattice.

At $T = 0$ K, the dynamics of the system are governed by the time-dependent Schrödinger equation

$$i\hbar\frac{d}{dt}\left|\psi\left(t\right)\right\rangle = \hat{H}\left|\psi\left(t\right)\right\rangle . \tag{5.9}$$

The non-Hermiticity of $\hat{H}$ results in a non-unitary time evolution of the excitation in the superlattice[44]. As an example, if the initial state is an eigenstate $\left|\psi\left(0\right)\right\rangle = \left|k\right\rangle$ of $\hat{H}$ satisfying

$$\hat{H}\left|k\right\rangle = \hbar\left(\omega_k - \frac{i}{2}\Gamma_k\right)\left|k\right\rangle , \tag{5.10}$$

then the total excitation of the system at time t, as quantified by the squared norm of the time-evolved state $|\psi(t)\rangle$, decays exponentially,

$$\left\langle\psi\left(t\right)|\psi\left(t\right)\right\rangle = e^{-\Gamma_k t} . \tag{5.11}$$

The decay time $\tau_k = 1/\Gamma_k$ is inversely proportional to the imaginary part $(-\hbar\Gamma_k/2)$ of the eigenvalue.

Here we show the signature of SR in the dynamics, studying the time dependence of the emitted intensity using a master equation approach. As an initial state, we consider an incoherent statistical average of all NC levels. This corresponds to an excited state created by the absorption of an off-resonant photon[172, 173]. The state is described by the density operator

$$\hat{\rho}\left(0\right) = \frac{1}{3N}\sum_{\alpha\in\{x,y,z\}}\sum_{n=1}^{N}\left|n,\alpha\right\rangle\left\langle n,\alpha\right| , \tag{5.12}$$

which evolves under the generalized Liouville-Von Neumann master equation

$$i\hbar\frac{d}{dt}\hat{\rho}\left(t\right) = \hat{H}\hat{\rho}\left(t\right) - \hat{\rho}\left(t\right)\hat{H}^{\dagger} . \tag{5.13}$$

Eq. (5.13) is formally equivalent to the Schrödinger equation (Eq. (5.9)). Its formal solution is

$$\hat{\rho}\left(t\right) = e^{-i\hat{H}t/\hbar}\hat{\rho}\left(0\right)e^{i\hat{H}^{\dagger}t/\hbar} = \frac{1}{3N}\sum_{\alpha\in\{x,y,z\}}\sum_{n=1}^{N} e^{-i\hat{H}t/\hbar}\left|n,\alpha\right\rangle\left\langle n,\alpha\right| e^{i\hat{H}^{\dagger}t/\hbar} \tag{5.14}$$

from which we obtain the emitted intensity by taking the product of the excitation energy by the negative derivative of the excitation's survival probability

$$\begin{aligned} I\left(t\right) &= -\hbar\omega_0\frac{d}{dt}\mathrm{tr}\left[\hat{\rho}\left(t\right)\right] = -\frac{\hbar\omega_0}{3N}\frac{d}{dt}\sum_{\alpha,\beta\in\{x,y,z\}}\sum_{m,n=1}^{N}\left|\left\langle m,\beta\right| e^{-i\hat{H}t/\hbar}\left|n,\alpha\right\rangle\right|^2 \\ &= -\frac{\hbar\omega_0}{3N}\frac{d}{dt}\sum_{\alpha\in\{x,y,z\}}\sum_{n=1}^{N} P_{n,\alpha}\left(t\right) . \end{aligned} \tag{5.15}$$

In Eq. (5.15) tr $[\hat{\rho}\,(t)]$ is the trace of the density operator and we have defined the probability to find the excitation in the superlattice at time t starting from the NC state $|n,\alpha\rangle$ as

$$P_{n,\alpha}\,(t) = \sum_{\beta\in\{x,y,z\}} \sum_{m=1}^{N} \left| \langle m,\beta|\, e^{-i\hat{H}t/\hbar}\, |n,\alpha\rangle \right|^2 . \tag{5.16}$$

As a point of comparison, note that the survival probability of a single NC's excited state is $P_0(t) = e^{-\gamma_r t}$ which, in turn, yields an exponential decay of the emission intensity $I_0\,(t) = \hbar\omega_0\gamma_r e^{-\gamma_r t}$.

The result from Eq. (5.15) allows us to numerically compute the emitted intensity versus time by knowing the spectrum of $\hat{H}$. For the NCs considered here, $\lambda = \frac{\lambda_0}{n_r} =$ 238 nm where $\lambda_0 = 521$ nm is the band-edge transition wavelength in vacuum and $n_r = \sqrt{\epsilon_r} = 2.19$ is the refractive index of bulk $CsPbBr_3$ at the optical frequency ω_0 [149]. The other model parameters are a NC side length of 9 nm and a NC radiative lifetime of $1/\gamma_r = 400$ ps. Note that the radiative lifetime we chose in our model for the single NC is in good agreement with the experimental results for the intensity emission from single NC, compare blue line and blue symbols in Fig. 5.7. The blue circles are the experimental (6 K) excited state emission decay of an ensemble of non-interacting NCs, characterized by a short timescale, near exponential decay followed by a longer-lived component. The former is attributed to radiative decay while the latter is thought to stem from delayed trap-related emission.

Using this approach, we compute the intensity versus time by applying Eq. (5.15) to a $10 \times 10 \times 10$ NC superlattice. Fig. 5.7 shows the results of our simulations for the time evolution of the emitted intensity (solid red line), compared with the experimental intensity decays in time from Ref. [47] (red triangles). Of note is the faster initial decay observed experimentally for the case of coupled NCs (red triangles), which is approximately three times faster than the decay for the uncoupled NC measurements (blue circles). While our results for $T = 0$ K and $N = 10^3$ NCs in the superlattice (red curve) qualitatively reproduce the increased recombination rate seen experimentally, they overestimate the initial, short time experimental rate by nearly four orders of magnitude, according with what is observed in Fig. (5.1)b. As we discussed above, a number of possible reasons exists for this discrepancy. They center on the absence of thermalization and structural disorder in our model. In section 5.4.8, we refine the model in a way that incorporates static disorder.

5.4.4 Geometry dependence of the SR states position

In Fig. 5.1a the complex spectrum of the radiative Hamiltonian $\hat{H}$ (see Eq. (5.2)) is shown for a cubic superlattice. In this case the most SR state (circled in green in Fig. 1a) lies in the middle of the energy spectrum. In general, the exact energy of the most SR state in a system is exquisitely sensitive to the exact geometrical arrangement of emitting dipoles.

When the dipole is perpendicular to the joining vector between the emitters, the position of the most SR state is blueshifted with respect to the single emitter, as is typical

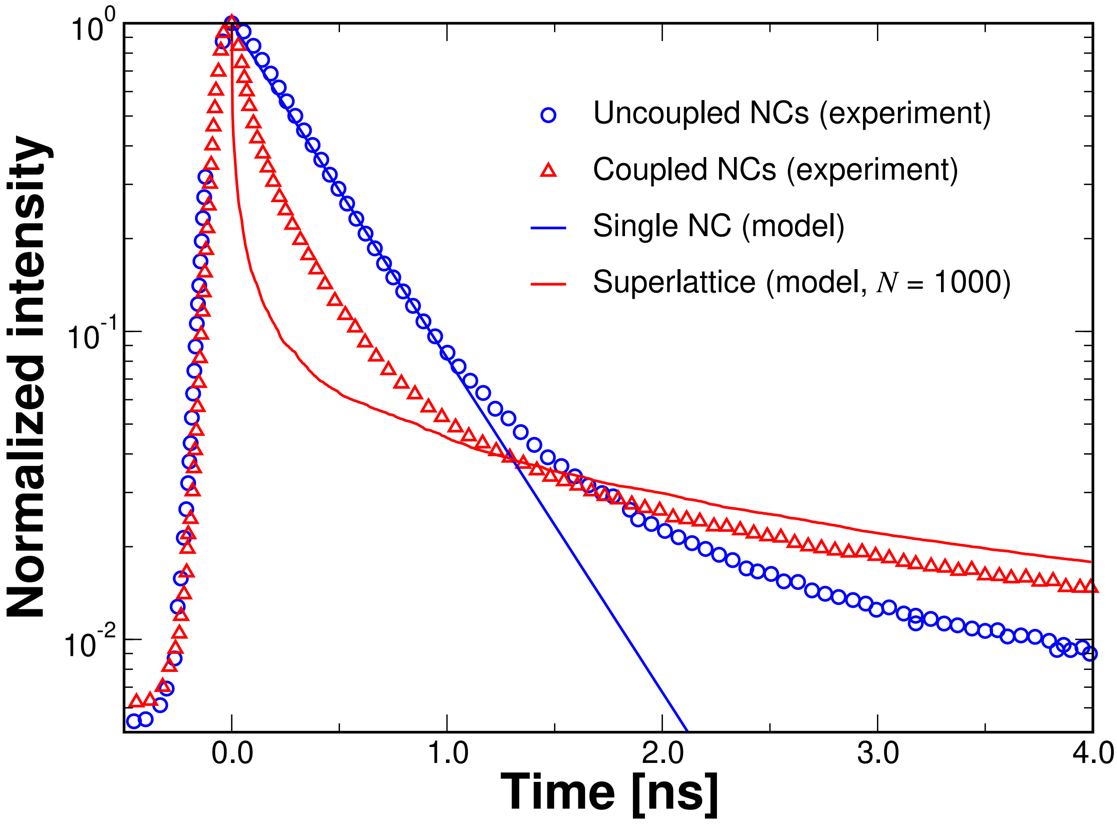

Figure 5.7: Theoretical emission intensity (see Eq. (5.15)) *vs.* time for a single NC (blue line) and for a superlattice of coupled NCs (red line). Parameters: $\hbar\omega_0 = 2.38$ eV, $\gamma_r = 2.5$ ns^{-1}, $\epsilon_r = 4.8$, $l = 9$ nm. Experimental time-resolved photoluminescence (TR-PL) decays from Ref. [47] shown by open symbols of the same color. Time=0 in PL experiments is determined as when the excitation pulse turns off.

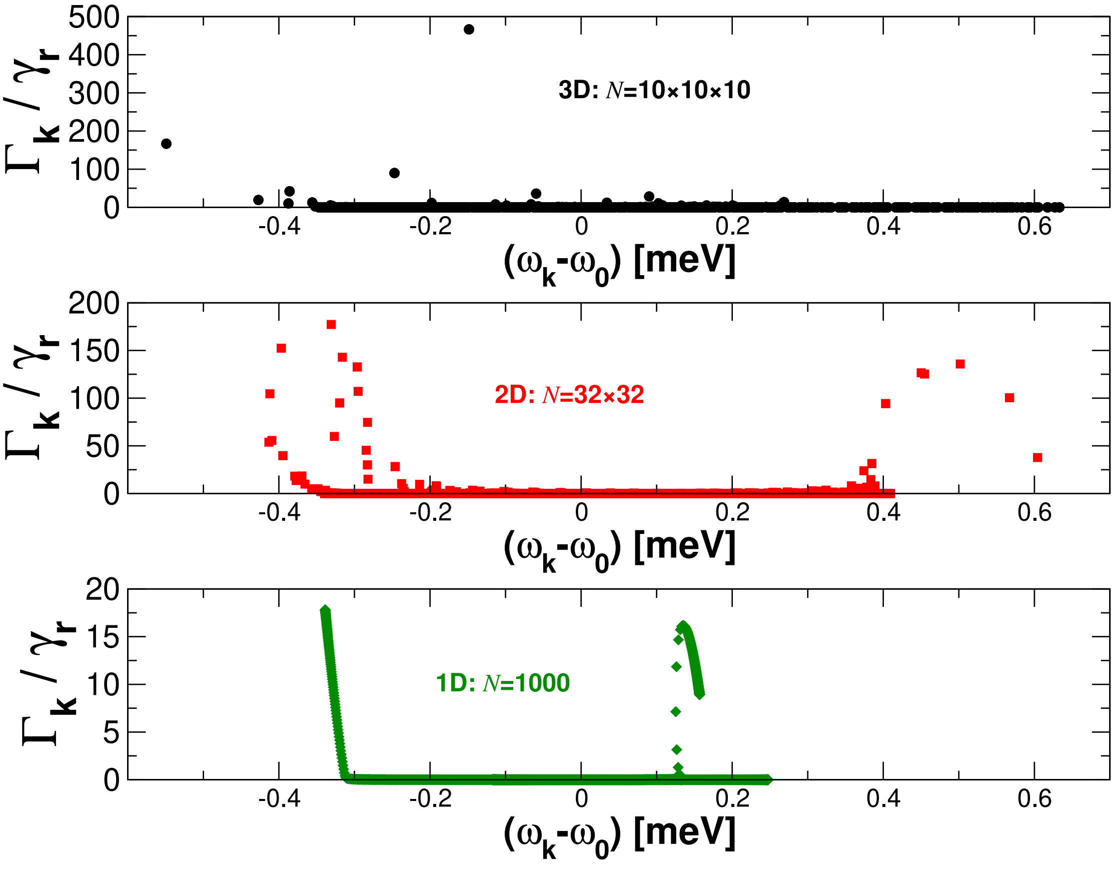

Figure 5.8: Complex eigenvalues of $\hat{H}$ in the complex plane for a superlattice of $N \approx 1000$ NCs. Each panel correspond to a different arrangement of the NCs in the superlattice: a perfect cube (upper panel), a two-dimensional square 'slab' (middle panel) and a chain (lower panel). Parameters: $\hbar\omega_0 = 2.38\,\text{eV}$, $\gamma_r = 2.5\,\text{ns}^{-1}$, $\epsilon_r = 4.8$, $l = 9\,\text{nm}$.

of H-aggregates [121]. On the other side, when the dipoles are parallel to the joining vector, one has a redshifted SR state, as is typical of J-aggregates [121]. The isotropic nature of the NCs considered here implies that, for each NC, three dipole directions have to be considered, each coupled to all the other NC dipole directions. Thus, there are both dipoles parallel to the joining vector between the NCs (i.e. $|\hat{e}_\alpha \cdot \hat{r}_{mn}| = 1$ in Eq. (5.1)), giving a redshift contribution, and also dipoles perpendicular to the joining vector (i.e. $|\hat{e}_\alpha \cdot \hat{r}_{mn}| = 0$), giving a blueshift contribution. Due to this mixture of redshift and blueshift contributions, it is not surprising that the most SR state is close to the middle of the spectrum.

The position of the most SR states is highly dependent on geometry. Indeed our preliminar results for a 1D and 2D superlattice (see Fig. 5.8) show that the most SR states are concentrated at the spectrum edges. This peculiar dependence on geometry is strongly determined by the presence of three degenerate TDMs for each NC, which implies a complicated mixture of redshift and blueshift contributions as explained above.

Finally, we note that identifying the energy of the highest SR state with respect to the thermal energy k_BT in an isotropic three-dimensional lattice is not trivial, as the energy of the highest SR state depends on different parameters. These include lattice geometry [117] and the coupling between distant NCs, which depends on the ratio of the superlattice edge length (L) to the emission wavelength (λ) in the superlattice, i.e. L/λ (see discussions in section 5.4.1 and section 5.4.7).

5.4.5 Time-resolved fluorescence with non-zero temperature

In order to estimate the effect of thermal decoherence on the decay rate of the NC superlattice, one can use the following common theoretical argument [156]. Let us consider the time evolution of an excitation initially present in the system, which is coupled to a thermal bath. Let us write a Pauli master equation [49] for the population $P_k(t)$ of each kth eigenstate,

$$\frac{dP_k(t)}{dt} = -\Gamma_k P_k\left(t\right) + \sum_{j=1}^{3N}\left[R_{kj}P_j(t) - R_{jk}P_k(t)\right] \ , \tag{5.17}$$

where R_{kj} are the thermalization rates between the eigenstates obeying the detailed balance relation $R_{kj} = R_{jk}e^{-\hbar(\omega_k-\omega_j)/(k_BT)}$, while Γ_k is the radiative decay rate of the $k-$th eigenstate. In typical situations, the radiative decay rates Γ_k are much smaller than the thermalization rates, namely $\Gamma_k \ll R_{kj}$. Since thermalization time is smaller than fluorescence time, one can describe time-resolved fluorescence assuming that the system is always at thermal equilibrium, i.e. the populations of the eigenstates follow $P_k(t) \approx P(t)e^{-\hbar\omega_k/k_BT}/Z$ at all times, where $P(t) = \sum_k P_k(t)$ is the excitation survival probability in the system and $Z = \sum_k e^{-\hbar\omega_k/(k_BT)}$ is the partition function. Under this ansatz, the second term in the right hand side of Eq. (5.17) is zero. Moreover, summing both sides of Eq. (5.17) over k, we have

$$\frac{dP\left(t\right)}{dt} = -\Gamma_T P\left(t\right) \ , \tag{5.18}$$

where we have defined the thermal rate

$$\Gamma_T = \frac{1}{Z}\sum_{k=1}^{3N}\Gamma_k e^{-\hbar\omega_k/(k_BT)} \ . \tag{5.19}$$

Eq. (5.18) has solution $P\left(t\right) = \exp\left(-\Gamma_T t\right)$. The emitted intensity at time t is related to the survival probability by $I\left(t\right) = -\hbar\omega_0\frac{dP(t)}{dt}$, so that we obtain $I\left(t\right) = \hbar\omega_0\Gamma_T\exp\left(-\Gamma_T t\right)$. When k_BT is much larger than the spectral width spanned by the real components $\hbar\omega_k$, thermal mixing of eigenstates suppresses coherence in the system, the thermal average is approximately the arithmetic average $\Gamma_T \simeq \gamma_r$ and the SR is effectively destroyed. This can be easily proven by letting k_BT tend to infinity in Eq. (5.19) and using the decay rate sum rule $\sum_{k=1}^{3N}\Gamma_k = 3N\gamma_r$, which stems from the conservation of total oscillator strength[174]. In the superlattice under consideration,

Temperature	NC sidelength (disorder)	A	B	N_{sat}
$T = 6$ K	$l = 9$ nm $(W = 0)$	3.22	0.58	21978
	$l = 9$ nm $(W = 2$ meV$)$	2.28	0.47	36954
	$l = 9$ nm $(W = 3$ meV$)$	0.96	0.53	5061
	$l = 9$ nm $(W = 10$ meV$)$	0.33	0.56	1424
	$l = 5$ nm	50	1.99	13075
	$l = 3$ nm	6977	4.58	24440
$T = 77$ K	$l = 9$ nm	0.0745	0.51	1816
	$l = 5$ nm	0.508	0.51	23290
	$l = 3$ nm	1.31	0.89	19280
$T = 300$ K	$l = 9$ nm	0.0176	0.52	1384
	$l = 5$ nm	0.084	0.53	6194
	$l = 3$ nm	0.188	0.79	5014

Table 5.1: Fit parameters for the data in Fig. 5.2a and Fig. 5.3, using Eq. (5.20).

the thermal energy at 6 K ($k_B T = 0.5$ meV, grayed area in Fig. 5.1a) is smaller but comparable to the spectral width.

In deriving Eq. (5.19) we implicitly assume that thermal relaxation, which is typically on the picosecond timescale [168], dominates all other relaxation processes in the material. Since at realistic sizes the maximal superradiant decay $\Gamma_{SR}^{-1} \approx \tau_r/10^4 \approx 40$ fs could be faster than other disorder-induced relaxation processes, this implies that our thermal decay rate constitutes a lower bound for the SR decay. Indeed, decay rates faster than thermal relaxation would result in an even faster initial SR decay.

5.4.6 Fitting parameters for the saturation function

In Fig. 5.2a and Fig. 5.3 we introduce the fitting function

$$\frac{\Gamma_T}{\gamma_r} - 1 = \frac{AN^B}{N^B + N_{sat}^B}\,, \tag{5.20}$$

where A, B, N_{sat} are fitting parameters. Here, in Table 5.1, we report the values of the fit parameters for all the data sets shown in Fig. 5.2a and Fig. 5.3.

5.4.7 The saturation assumption

In this chapter we assume that the thermal SR rate Γ_T saturates to a N-independent value, when the NC density N/L^3 is kept fixed. To justify this assumption, let us analyze the thermal decay rate Γ_T (see Eq. (5.2)) considering, for the moment, the following crude approximation for the Boltzmann occupation numbers,

$$\frac{e^{-\hbar\omega_k/(k_B T)}}{Z} \approx \begin{cases} 1/N_T & \text{for } \hbar(\omega_k - \omega_1) \le k_B T \\ 0 & \text{elsewhere} \end{cases}\,, \tag{5.21}$$

where N_T is the number of superlattice eigenstates having energy $\hbar(\omega_k - \omega_1) \leq k_B T$, with $\hbar\omega_1$ being the minimal energy in the spectrum. Under the approximation in Eq. (5.21), we can approximate Eq. (5.2) as

$$\frac{\Gamma_T}{\gamma_r} \approx \frac{1}{N_T} \sum_{\hbar(\omega_k - \omega_1) \leq k_B T} \frac{\Gamma_k}{\gamma_r} \,. \tag{5.22}$$

Moreover, as one can see from Fig. 5.1a, the sum of the Γ_k/γ_r for the states at low energy ($\hbar(\omega_k - \omega_1) \leq k_B T$) results in a large fraction of the total of the radiative decay rates in the system (which is $\sum_k \Gamma_k/\gamma_r = 3N$). Since the total of the Γ_k grows as the number N of NCs, we assume that also the sum in Eq. (5.22) grows as $\sim N$. We can estimate the number of states N_T at low energy assuming a constant density of states in the spectrum. This rough approximation is justified since $k_B T$ is comparable to the spectral width $\hbar\Delta\omega$. Therefore, $N_T \approx 3N \frac{k_B T}{\hbar\Delta\omega}$, that is the total number $3N$ of eigenstates multiplied by the fraction of $k_B T$ over the spectral width. Under these approximations, we predict that Γ_T/γ_r scales as

$$\frac{\Gamma_T}{\gamma_r} \sim \frac{\hbar\Delta\omega}{k_B T} \,. \tag{5.23}$$

Therefore, we proceed to estimate how $\Delta\omega$ scales with the superlattice parameters N and L. This will also allow us to estimate how Γ_T/γ_r scales with those parameters, thanks to Eq. (5.23).

Let us consider two limiting cases: (a) $L/\lambda \ll 1$ and (b) $L/\lambda \gg 1$. In case (a) it is known [117] that the coupling is dominated by dipole-dipole near-field terms. Since the dipole-dipole coupling decays as $1/r_{mn}^3$, the interaction is short-range. In such case, the spectral width scales proportionally to the nearest-neighbor coupling, namely $\hbar\Delta\omega \sim \mu^2/(l')^3 \sim N/L^3$, since the center-to-center distance is $l' = L/N^{1/3}$. Thus, thanks to Eq. (5.23), we estimate $\Gamma_T/\gamma_r \sim N/L^3$ for $L/\lambda \ll 1$. This estimate is valid in the case of $CsPbBr_3$ for realistic superlattice edge length, even if $L \approx 5\lambda$. In fact (see Fig. 5.9) $[(\Gamma_T/\gamma_r) - 1]$ is proportional to the density N/L^3 in a broad range of parameters and, specifically, in the experimental case where $l = 9$ nm (see vertical line in Fig. 5.9). Therefore, $[(\Gamma_T/\gamma_r) - 1]$ depends only on the density and it must saturate to a N-independent value when N is increased keeping the density fixed.

Nevertheless, this scaling is not true in general. For comparison, let us consider the opposite case (b), where the $1/r_{mn}^2$ and $1/r_{mn}$ terms in the hamiltonian (Eq. (5.4)) are much more relevant and one can expect a different scaling of the spectral width. The case of $L > \lambda$ has been studied in literature [150], for densities $N/(L/\lambda)^3 < 200$, much smaller tnan the superlattices analyzed in this work where $N/(L/\lambda)^3 > 10^4$. It has been found that the spectral widths in the complex plane (that is, the maximal imaginary part Γ_{SR} and the energy width $\hbar\Delta\omega$) scale proportionally to $N/(L/\lambda)^2$. Even if the atomic clouds in Ref. [150] are completely disordered, while superlattices are ordered, the conclusions of Ref. [150] are valid also for regular superlattices having the same low densities used for atomic clouds. Specifically, in Fig. 5.10a-b we find that both Γ_{SR} and $\Delta\omega$ scale proportionally to $N/(L/\lambda)^2$ for large volumes and small densities. Therefore,

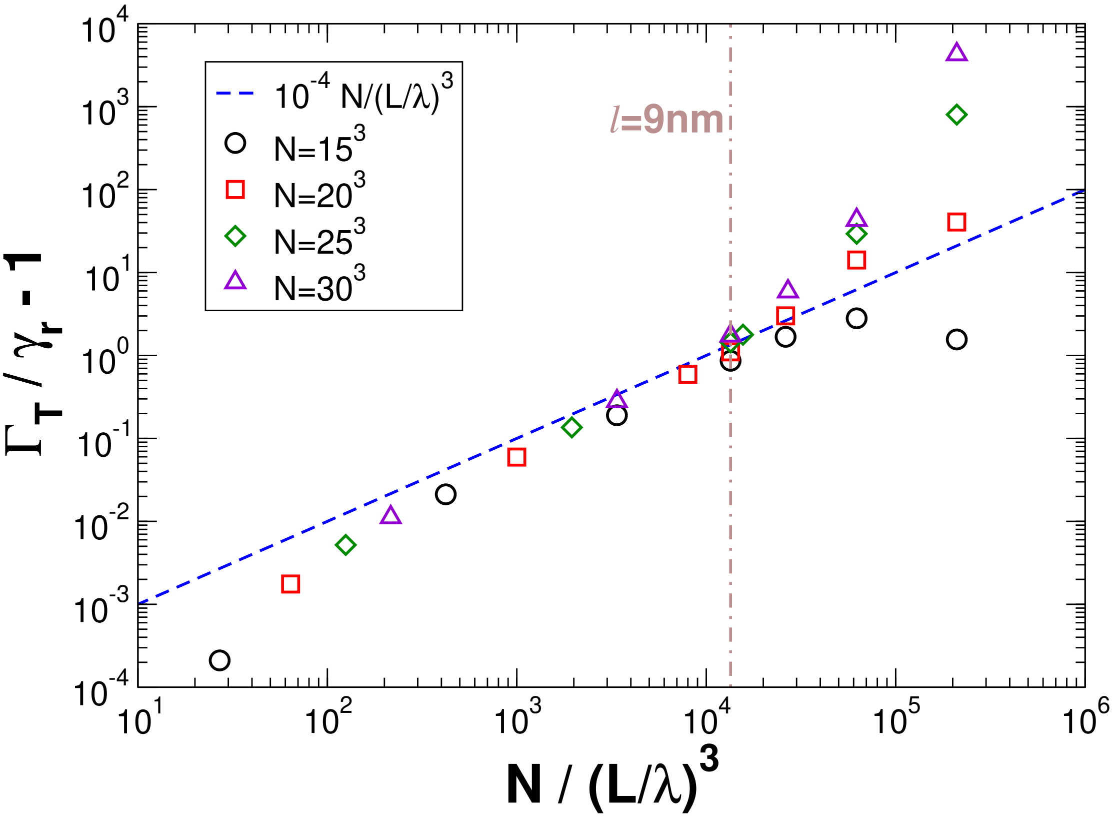

Figure 5.9: Thermal SR decay (see Eq. (5.2)) as a function of the NC density in the superlattice, at temperature $T = 6$ K. Parameters: $\hbar\omega_0 = 2.38$ eV, $\gamma_r = 2.5$ ns^{-1}, $\epsilon_r = 4.8$.

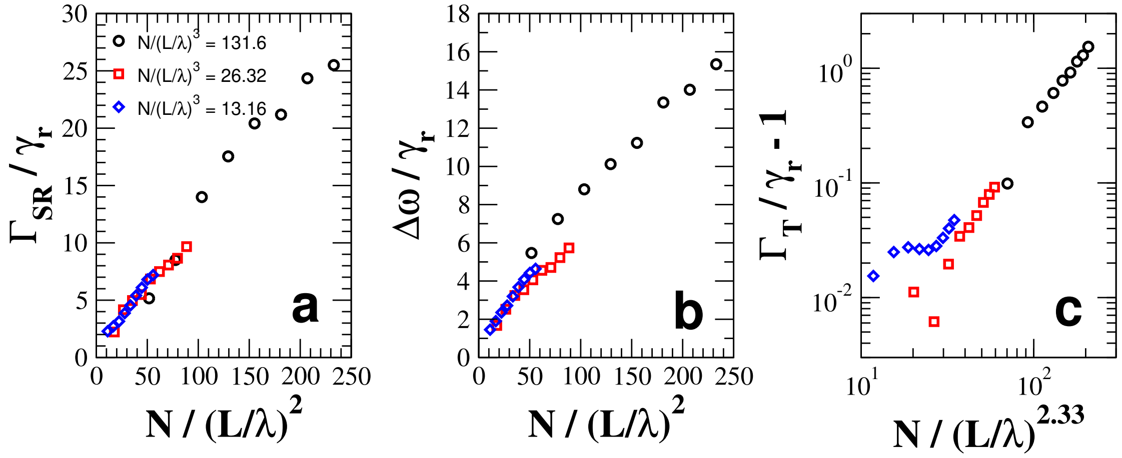

Figure 5.10: **a** Maximal decay rate for the superlattice eigenstates, **b** energy range spanned by the eigenvalues and **c** thermal decay rate ($T = 60$ mK) for superlattices (see Eq. (5.2)) at low density of NCs (see legend in panel (a)). Parameters: $\hbar\omega_0 = 2.38$ eV, $\gamma_r = 2.5\ \text{ns}^{-1}$, $\epsilon_r = 4.8$.

using Eq. (5.23), we predict $\Gamma_T/\gamma_r \sim N/(L/\lambda)^2$ in this regime. Then, we proceed to check such prediction for Γ_T/γ_r using the correct definition from Eq. (5.2), and for $T = 60$ mK, so that $(k_B T)/(\hbar\Delta\omega) \approx 1/3$ like in the superlattice considered in this work. The results are shown in in Fig. 5.10c where we plot $\Gamma_T/\gamma_r - 1$ for the same data shown in Fig. 5.10a-b. Optimizing the linear correlation, we find (see Fig. 5.10c) that the optimal scaling is established between $\Gamma_T/\gamma_r - 1$ and $N/(L/\lambda)^{2.33}$. Note that 2.33 is close to our rough prediction (2) and smaller than 3 (obtained above for the realistic, high-density case).

5.4.8 Time-resolved fluorescence at T = 0 K with static disorder

To further refine our model, we account for energetic heterogeneities as static disorder, parametrized by additional site-energy fluctuations in the Hamiltonian

$$\hat{H} \to \hat{H} + \sum_{\alpha\in\{x,y,z\}} \sum_{n=1}^{N} \delta_{n,\alpha} \left|n,\alpha\right\rangle \left\langle n,\alpha\right| \tag{5.24}$$

uniformly distributed within the range $-\frac{W}{2} \leq \delta_{n,\alpha} \leq \frac{W}{2}$. Static disorder is known to destroy SR [25]. Since our simulations in absence of disorder clearly overestimate SR (see Fig. 5.7), we may expect that the addition of static disorder would quench SR and therefore improve the accuracy of our model.

In Fig. 5.11 we plot the decay of the emitted intensity from a superlattice. The experiment has been conducted for $N \sim 10^6$, while we use $N = 1000$ in the simulations (continuous lines). The black line is the same as the model results from Fig. 5.7 in absence of disorder, while the blue and green lines have been obtained using different

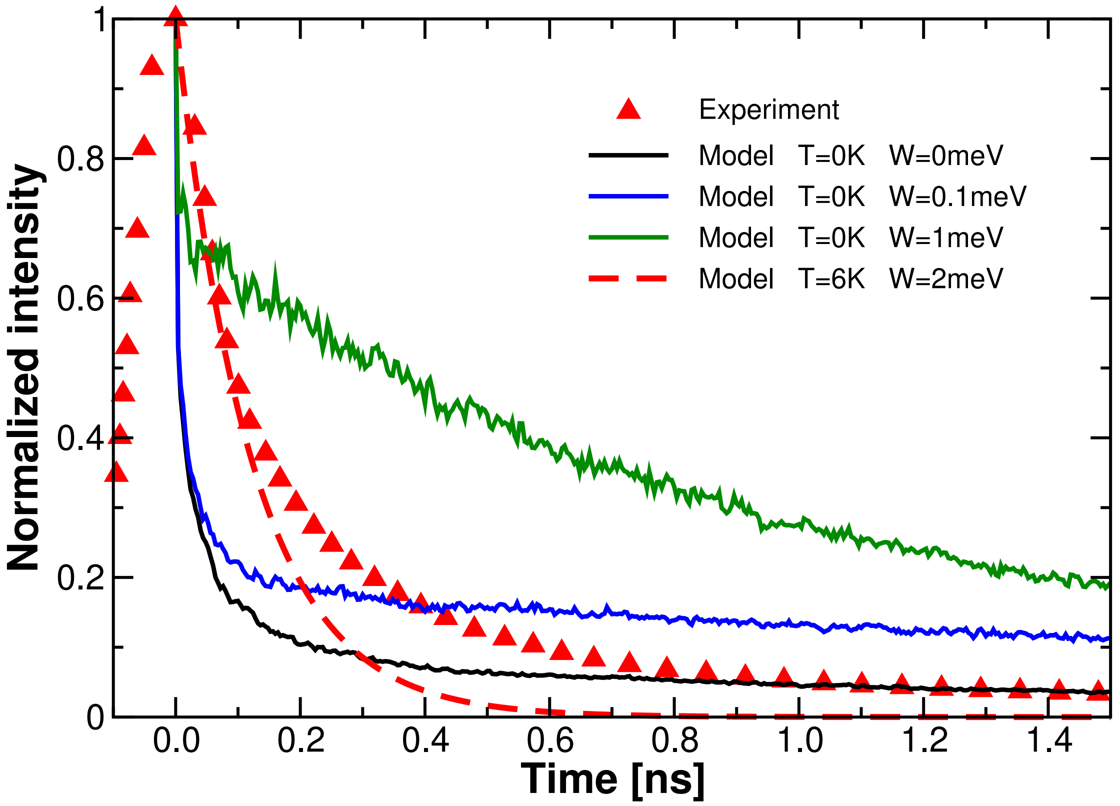

Figure 5.11: Decay of the emitted intensity in time. Experimental data taken from Ref. [47]. Model at $T = 0$ K computed using Eq. (5.15) with the Hamiltonian $\hat{H}$ (see Eq. (5.1)) corrected as in Eq. (5.24). Model at $T = 6$ K computed as discussed above. Parameters: $\hbar\omega_0 = 2.38$ eV, $\gamma_r = 2.5$ ns^{-1}, $\epsilon_r = 4.8$, $N = 1000$, $l = 9$ nm.

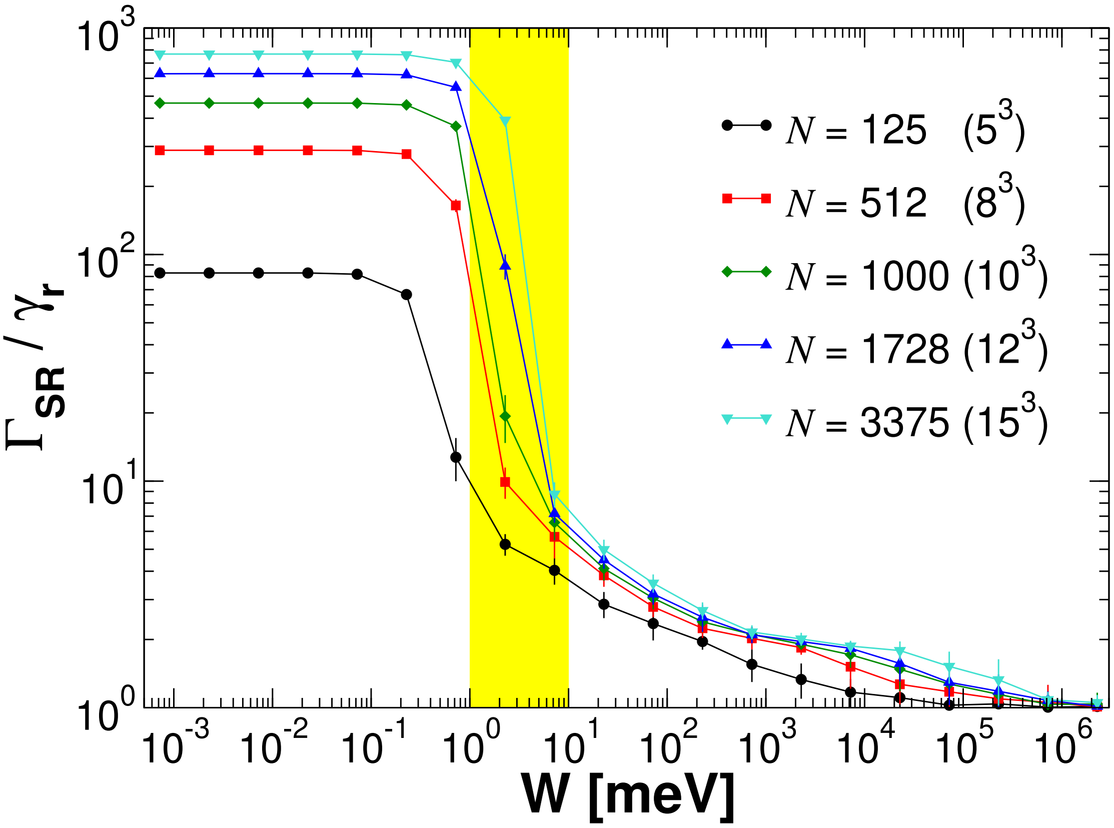

Figure 5.12: Normalized maximal absolute value of imaginary parts of the complex eigenvalues of $\hat{H}$ for a 3D cubic superlattice *vs.* the amplitude W of the static disorder (see Eq. (5.24)), measured in units of $\hbar\gamma_r$. Different values of the number N of nanocrystals are considered (see legend). The yellow region corresponds to a realistic range of disorder. Parameters: $\hbar\omega_0 = 2.38$ eV, $\gamma_r = 2.5$ ns^{-1}, $\epsilon_r = 4.8$ and $l = 9$ nm.

values of static disorder. Since the nearest-neighbor coupling is $J = 0.14$ meV, we consider a disorder value comparable to the coupling ($W = 0.1$ meV) and another much larger than J ($W = 1$ meV). In both cases, the agreement between the model and the experiment is not better than the case at $W = 0$: the initial decay is always much faster than the experiments and also the long-time behaviour is not captured.

As a comparison, we also plot (dashed line) the theoretical thermal decay that we derived, see Eq. (5.2), by considering thermal decoherence together with static disorder: as one can see, our predicted decay due to thermal decoherence and static disorder agrees with the experiment much better than modelling the emission intensity neglecting thermal decoherence and considering only static disorder.

At this point, one may wonder whether the agreement at $T = 0$ K with finite disorder may improve by increasing the system size. Since the initial, fast decay in the model is determined by $\Gamma_{SR} = \max\{\Gamma_k\}$, we analyzed how Γ_{SR} depends on the size for different values of disorder. The results of such analysis are shown in Fig. 5.12, where Γ_{SR} is plotted against disorder for different values of N. From Fig. 5.12 one can see that Γ_{SR} tends to γ_r for large W, i.e. SR is quenched by disorder. In the yellow region we mark the range of disorder between 1 meV and 10 meV, that is a realistic estimate of the effective disorder (as discussed in section 5.4.10). In such region, we can see that Γ_{SR} increases with N. Therefore, since Γ_{SR} determines the initial decay in Fig. 5.11, increasing N from 1000 (simulations in Fig. 5.11) up to $N = 10^6$ would not improve the agreement between the model and the experiments. On the contrary, an extrapolation of the model for large N would increase the overestimation of the initial decay with respect to the experiments. Therefore, we conclude that static disorder alone is not able to explain the quenched SR observed by Rainò et al. [47], and the effect of thermalization needs to be taken into account as explained in section 5.4.5.

5.4.9 Emission redshift

In Fig. 5.1a we show that the radiative coupling between NCs results in $3N$ superradiant and subradiant states, whose frequency ω_k is shifted with respect to the single NC emission frequency ω_0. Specifically, the largest redshift in Fig. 1a for $N = 30^3$ is $\sim 700\gamma_r \approx 1$ meV. Here we extrapolate the coupling-induced redshift to natural sizes (up to $N \sim 10^8$) and we compare our predictions with the experimental results.

In Fig. 5.13 we plot the predicted redshift (symbols) defined as $\max_k[\hbar(\omega_0 - \omega_k)]$ for parameters compatible with Ref. [47]. We observe that the redshift predicted by the simulations (symbols) increases slowly with N, following a power law trend $\sim N^{0.2}$ for large N. Once we extrapolate the results to $N = 10^8$, corresponding to the largest superlattices reported in Ref. [47], our model predicts a redshift of at most 7 meV at $N = 10^8$, that is an order of magnitude smaller than the average redshift of 64 meV measured experimentally in Ref. [47] averaging over 10 superlattices, see green line for comparison. Consequently there must be another origin to the large redshift observed in Ref. [47].

To begin with, we note that the PL spectrum (at temperature $T = 6$ K) of a single superlattice shown in Fig. 3a of Ref. [47] is composed of two main peaks: one at high energy, with a broad linewidth, assigned to an 'uncoupled' ensemble of NCs, and a second one, narrower and peaked at low energy, that is assigned to a 'coupled' ensemble of NCs. The low-energy 'coupled' peak produces the SR emission. The fact that at least two peaks are visible within the same superlattice can be attributed to the existence of different sub-domains within a single superlattice, as also suggested by Rainò et al. [47] Indeed the existence of several sub-domains, not only two, within a single superlattice is explicitly suggested in Ref. [47] to explain the observation of substructures in the redshifted emission band. In Ref. [47] it is also stressed that superlattices are made of NCs that are not identical in size, but have a certain size distribution. Another important fact to consider is that $CsPbBr_3$ NCs exhibit strong size-dependent emission [157]. Specifically, in Ref. [157] the emission energy measured at room temperature of $CsPbBr_3$ NCs (reproduced here in Fig. 5.14a) covers a range of about 300 meV when the side length

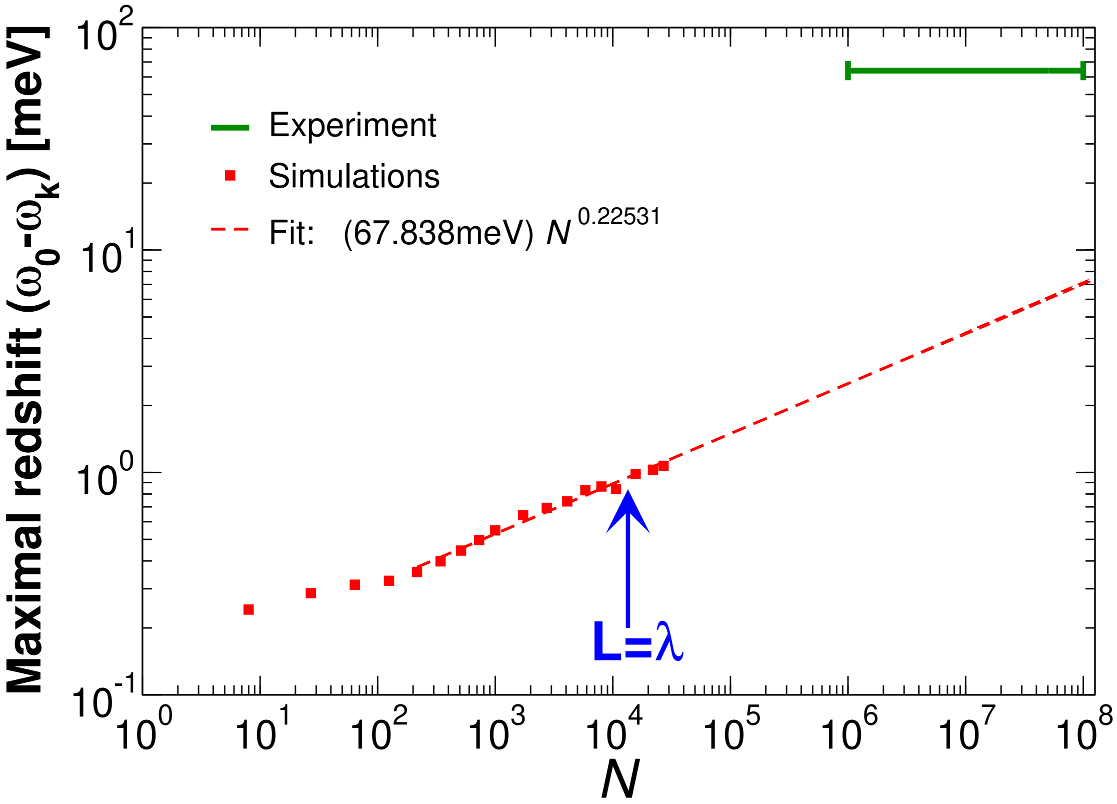

Figure 5.13: Maximal redshift, $\max_k[\hbar(\omega_0 - \omega_k)]$, with $\hbar\omega_k$ being real part of the eigenvalues of $\hat{H}$ (see Eq. (5.1)) and with the NC transition energy $\hbar\omega_0 = 2.38$ eV. The numerical results are fit with a power law and extrapolated to the natural size. "Experiment" refers to the average emission redshift 64 meV reported in Ref. [47]. Here, $\gamma_r = 2.5$ ns, $\epsilon_r = 4.8$ and $l = 9$ nm.

of the NCs is varied from $l = 3$ nm to $l = 12.8$ nm. The larger NCs possess the lowest, most redshifted emission energy.

Interestingly, from the data reported in Ref. [157], the side length fluctuations are independent of the NCs size, implying that the relative size fluctuations decreases as the NC size increases.

Therefore, we conjecture that the observed large redshifts in Ref. [47] are due to sub-domains made of larger than average NCs, which are more likely to form due to their smaller relative size fluctuations.

The NC size variation reported in Ref. [47] over 100 NCs in Extended Data Fig.1 ranges between 8.5 nm and 10.5 nm, which would cover an excitation energy range of 27 meV according to the data shown in Ref. [157]. This contribution, together with the coupling contribution of few meV, is only a factor of 2 different from the average observed redshift 64 ± 6 meV. Moreover the size distribution could be larger when the actual number of NCs (10^6-10^8) composing the superlattices is considered. For instance, a size distribution between 8 nm and 12 nm would cover an excitation energy range of about 50 meV, not too far from the observed 64 ± 6 meV redshift.

We stress, however, that the redshift seen in $CsPbBr_3$ NC superlattice emission remains debated with no consensus reached in literature [161–167]. Proposed explanations for such redshifts, which range from 10 meV to 96 meV, include variations in the dielectric constant [162, 166], photon recycling (i.e. reabsorption) [163], electronic coupling between NCs [164] and even bulk $CsPbBr_3$ "impurities" [161].

5.4.10 Static disorder and inhomogeneous linewidth

The emission spectra of SR superlattices reported in Ref. [47] are composed of at least two peaks: a SR redshifted, with an average inhomogeneous linewidth of 15 ± 4 meV, and an additional broader peak, corresponding to an ensemble of uncoupled NCs, with an average inhomogeneous linewidth of 49 ± 21 meV. On the other side, from our theoretical framework (see details in section 5.4.9), we predicted that the amount of disorder present in the SR sub-domain should be of the order of few meV, see Fig. 5.2a. This disorder strength cannot explain the inhomogeneous linewidths of the SR peak, that is on average 15 ± 4 meV. In order to explain this large linewidth we note that the existence of several sub-domains, not only two, is explicitly mentioned in Ref. [47]: "In most superlattices, we observe a substructure in this red-shifted emission band, which we attribute to the presence of several slightly different independent domains within the same individual superlattice". Thus, we explicitly considered the possibility of having several redshifted sub-domains each composed of NCs of different average sizes. In this way, one could easily explain the inhomogeneous linewidth of few tens of meV as due to different excitation energies corresponding to the different sizes in each sub-domain. Indeed, $CsPbBr_3$ NC emission energies are strongly size-dependent (see Ref.[157]) and the presence of multiple sub-domains within a single superlattice can readily yield an observed 15 ± 4 meV linewidth due to sub-domain induced inhomogeneous broadening.

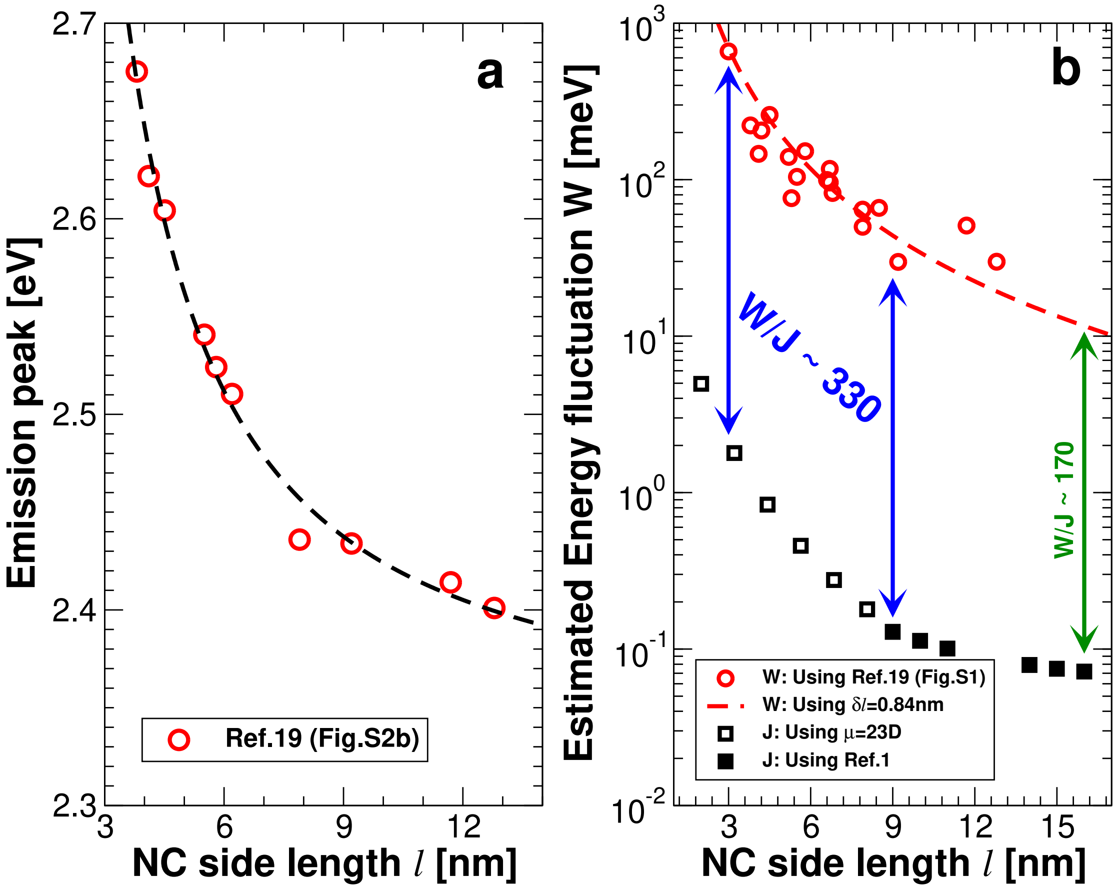

Figure 5.14: **a** Emission peak for $CsPbBr_3$ NCs of different side length l measured at room temperature (data taken from Ref. [157]). The dashed line is the best fit with the function in Eq. (5.25). **b** Estimated energy disorder (see Eq. (5.27)) against the NC side length using data from Ref. [157] (symbols) and setting a fixed side distribution $\delta l = 0.84$ nm (green dash-dotted line). For comparison, the dipole coupling J between nearest-neighbour NCs is also shown (squares), calculated with two different methods for $l \leq 9$ nm and $l \geq 9$ nm, see text.

To corroborate this point, following common theoretical predictions [149], we fit the measured emission energy obtained from Ref. [157] and reported in Fig. 5.14a with the function

$$E(l) = \frac{a}{l^2} + \frac{b}{l} + c \, , \tag{5.25}$$

obtaining the fit parameters $a = 2.07$ eV nm^2, $b = 0.763$ eV nm and $c = 2.33$ eV. Note that, assuming an SR emission band composed of several NCs sub-domains with mean edge length within 11 nm $< l <$ 13 nm, this would induce an inhomogeneous linewidth of 15 meV, in agreement with the observed inhomogenous linewidth.

Then, from Eq. (5.25) we estimate the corresponding energy disorder W for general values of the NC sizes distributed within $(l \pm \delta l)$, where δl is the standard deviation of the side length. Since $\delta l \ll l$, we have

$$\delta E = |E(l+\delta l) - E(l)| \approx \left| \frac{dE(l)}{dl} \right| \delta l = \left| \frac{2a}{l^3} + \frac{b}{l^2} \right| \delta l \, , \tag{5.26}$$

where δE represents the standard deviation of the energy fluctuations. Finally, we match the estimated δE parameter (standard deviation) to the model for energy disorder used in this chapter (see section 5.4.8), that entails random energies uniformly distributed within $(\hbar\omega_0 \pm W/2)$. Since the standard deviation in our model is $W/\sqrt{12}$, we obtain

$$W \approx \sqrt{12} \left| \frac{2a}{l^3} + \frac{b}{l^2} \right| \delta l \, . \tag{5.27}$$

In Fig. 5.14b the estimated energy disorder (see Eq. (5.27)) is plotted against the NC side length using values of $(l, \delta l)$ reported in Ref. [157] (symbols). As one can see, the estimated energy disorder W ranges between $\sim$ 20 meV and $\sim$ 700 meV, with the smallest energy disorder corresponding to the largest NCs. Also, the NC size fluctuations from Ref. [157] are independent of l, so that we evaluate Eq. (5.27) using the average size fluctuations $\delta l = 0.84$ nm from Ref. [157] (red dashed line in Fig. 5.14b) and we capture well the dependence between W and l. Note that the measurements in Ref. [157] were done at room temperature, while disorder is likely smaller at lower temperatures.

The conjecture of multiple redshifted sub-domains necessitates that in each sub-domain with SR emission, W cannot be larger than few meV to allow for SR emission to be observed, see Fig. 5.2a. This implies that sub-domains with SR emission should be characterized by a highly uniform size distribution which would favor the formation of a coherent sub-domain and it would allow to observe coherent emission.

Note that, since thermal decoherence occurs on few picoseconds timescales [168], while emission occurs on few hundreds of picoseconds, thermal decoherence cannot be neglected. Taking thermal decoherence into account implies that each sub-domain should be composed of at least $\sim 10^4$ NCs, see Fig. 5.2a.

In whole, the existence of SR sub-domains, where each sub-domain is composed of large NCs, with an average size differing from sub-domain to sub-domain, self-consistently rationalizes three observations made in Ref. [47]: (1) unexpected $\approx 64 \pm$

6 meV redshifts, (2) large $\approx 15 \pm 4$ meV SR inhomogeneous linewidths and (3) SR emission spectral substructure.

We also note that the predicted energy disorder increases as l is decreased (with δl independent of l). This may induce to think that small-l superlattices would be more sensitive to disorder, compared to their large-l counterparts. However, also the dipole coupling between nearest-neighbour NCs within a superlattice increases for small l (see black symbols in Fig. 5.14b). Here, following Ref. [149], we compute the nearest-neighbour coupling $J \approx \mu^2/(l^{'})^3$ accounting for the dependence of the TDM μ on the NC size. In the strong confinement regime ($l \ll 2a_B$, where a_B is the exciton Bohr radius) the TDM is independent from the NC side length, therefore here we use a constant TDM $\mu = 23$ D for $l \leq 9$ nm (open black squares in Fig. 5.14b). In the opposite regime (weak confinement, $l \gg 2a_B$) the calculated TDM scales as $\mu^2 \sim l^3$, implying that J is independent of the NC size for very large l. Finally, in the intermediate confinement regime (that we identify as 9 nm $\leq l \lesssim 16$ nm) we extract μ for the different NC sizes from Ref. [149]. Then we use μ to compute $J \approx \mu^2/(l^{'})^3$ and we multiply the coupling obtained this way by a factor 1.3 to match the data at $l = 9$ nm reported in Ref. [47], see filled black squares in Fig. 5.14b.

Since both W and J scale as $1/l^3$ for small l (see Eq. (5.27)) and μ is constant in such regime (as explained above), the ratio W/J is constant for $l \leq 9$ nm. Given that the effect of disorder is determined by the ratio W/J, we conclude that the effect of disorder on SR is independent of the NC size, for $l \lesssim 9$ nm. Note that the disorder values in Fig. 5.14b are much larger than the disorder estimated in Fig. 5.2a, i.e. $W/J \approx 15$. One possible reason for such discrepancy is that in Fig. 5.14b we use data measured at room temperature [157], while in Fig. 5.2a we compare to experiments at $T = 6$ K, where a smaller disorder is expected. Moreover, as we conjecture in section 5.4.9, the SR emission likely comes from very ordered, homogeneous sub-domains within the superlattice. The size distribution within such sub-domains is likely much smaller than 0.84 nm, rationalizing the smaller disorder $W/J \approx 15$ in Fig. 2a. Therefore, since disorder has a minor effect for NC sizes of $l = 9$ nm with $W/J \approx 15$ (as shown in Fig. 5.2a), the same minor effect could be expected for smaller NC sizes, provided that the size fluctuations can be controlled in order to keep the same ratio W/J.

On the other hand, if the size fluctuations could not be controlled for small NCs, disorder could be so large to completely quench SR. In such case, an alternative way to observe SR is to use large NCs ($l \gtrsim 9$ nm). In such regime the coupling J tends to a constant value, as discussed above (see black filled squares in Fig. 5.14b), while W always decreases with the NC size. Therefore the ratio W/J decreases for large NC sizes as shown in Fig. 5.14b, where W/J is nearly halved varying l from 9 nm to 16 nm. An even smaller reduction of W/J is expected for larger NCs, for example for $l = 25$ nm, J is expected to saturate above $l = 16$ nm, see Fig. 5.14b), and we would obtain a value of W/J, 5 times smaller than the its value for $l \leq 9$ nm. However, note that large NCs have couplings J weaker than small NCs (compare empty and filled black squares in Fig. 5.14b), so that smaller NCs are always more robust to thermal decoherence.

5.4.11 A remark on the role of the imaginary coupling in the robustness to disorder

At the beginning of this project we were considering a different model for perovskites superlattices, where all the dipoles were aligned along one direction. Moreover we did not consider the effect of the dielectric constant ϵ_r, so in our simulations $\lambda = 521$ nm instead of $\lambda = 238$ nm as in the previous chapters. In order to assess the relevance of the non-Hermitian coupling to induce robustness to disorder to the system, we analyzed the maximal decay width Γ_{SR}/γ_r (or the maximal dipole strength if only the Hermitian part was considered) as a function of static disorder for different system sizes. Three cases were considered: i) only Hermitian dipole-dipole interactions; ii) Hermitian radiative interactions; iii) full complex radiative interaction, including Hermitian and non-Hermitian terms. As one can see from Fig. 5.15 the robustness to disorder decreases with the systems size, unless the full non-hermitian interaction is considered. In the latter case, the robustness increases with the system size. This intriguing results shows the importance to consider the full non-Hermitian interactions in such systems.

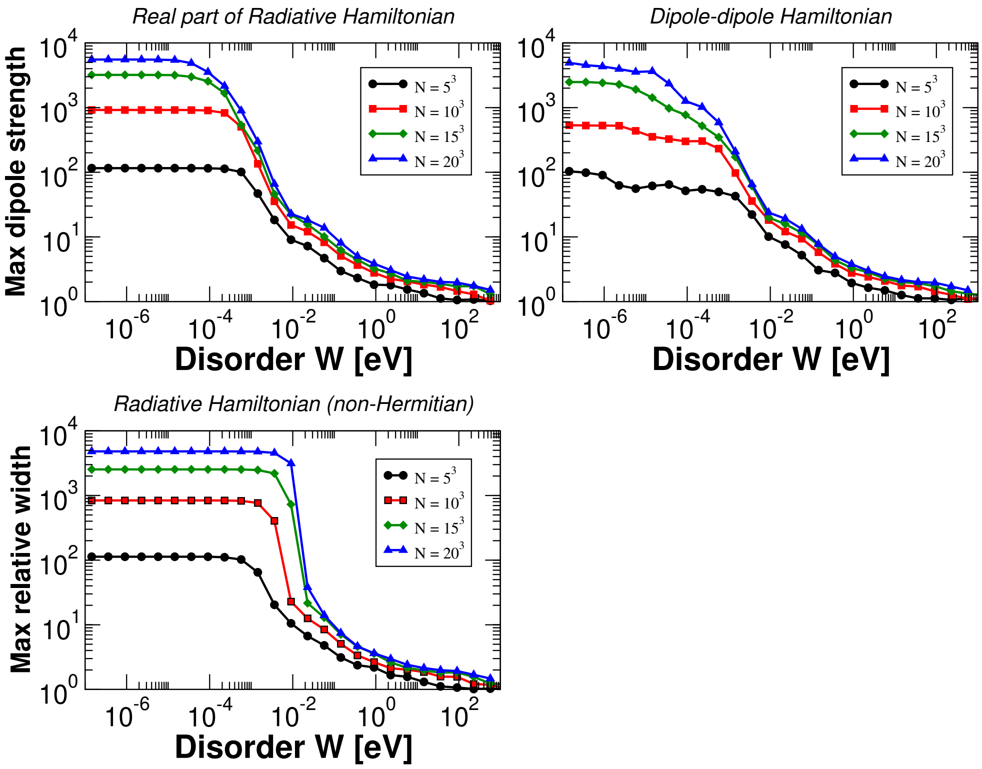

Figure 5.15: Maximal dipole strength (upper panels) and maximal decay width Γ_{SR}/γ_r (lower panel) against static disorder for a superlattice accounting only for one dipole per each NC, directed along the z axis. The dipole-dipole Hamiltonian is Eq. (5.8), while the Radiative hamiltonian is Eq. (5.1) in the case $\alpha = \beta = z$. Parameters: $\hbar\omega_0 = 2.38$ eV, $\gamma_r = 2.5\,\text{nm}^{-1}$, $l = 9$ nm, $\epsilon_r = 1$, $\mu \approx 34$ D.

Chapter 6

Real and imaginary energy gaps: a comparison between single excitation Superradiance and Superconductivity

In this chapter the superradiance transition is interpreted as a transition to a gapped regime, following the general framework introduced in Chapter 1. The results in this chapter have been published as: Nahum C. Chávez, Francesco Mattiotti, J. A. Méndez-Bermúdez, Fausto Borgonovi, and G. Luca Celardo, "Real and imaginary energy gaps: a comparison between single excitation superradiance and superconductivity and robustness to disorder", Eur. Phys. J. B **92***, 144 (2019). I contributed to all the analytical calculations and to the simulations about the robustness to disorder.*

A comparison between the single particle spectrum of the discrete Bardeen-Cooper-Schrieffer (BCS) model, used for small superconducting grains, and the spectrum of a paradigmatic model of Single Excitation Superradiance (SES) is presented. They are both characterized by an equally spaced energy spectrum (Picket Fence) where all the levels are coupled between each other by a constant coupling which is real for the BCS model and purely imaginary for the SES model. While the former corresponds to the discrete BCS-model describing the coupling of Cooper pairs in momentum space and it induces a Superconductive regime, the latter describes the coupling of single particle energy levels to a common decay channel and it induces a Superradiant transition. We show that the transition to a Superradiant regime can be connected to the emergence of an imaginary energy gap, similarly to the transition to a Superconductive regime where a real energy gap emerges. Despite their different physical origin, it is possible to show that both the Superradiant and the Superconducting gaps have the same magnitude in the large gap limit. Nevertheless, some differences appear: while the critical coupling at which the Superradiant gap

appears is independent of the system size N, for the Superconductivity gap it scales as $(\ln N)^{-1}$, which is the expected BCS result. The presence of a gap in the imaginary energy axis between the Superradiant and the Subradiant states shares many similarities with the "standard" gap on the real energy axis: the superradiant state is protected against disorder from the imaginary gap as well as the superconducting ground state is protected by the real energy gap. Moreover we connect the origin of the gapped phase to the long-range nature of the coupling between the energy levels.

6.1 Introduction

Cooperative effects, which are at the basis of emergent properties [175], are at the center of research investigations in a vast variety of fields: emergent properties in highly correlated materials [176], cooperative emission in superconducting qubits [177], Superradiance in cold atomic clouds [102], cooperative shielding in long range interacting systems [178], collective excitations in semiconductors [179], plasmonic Dicke effect [180], biophysical systems [3, 85] and proposal of quantum devices which exploits cooperative effects [1]. Despite the great importance of emergent properties, a general unifying framework and a full understanding of cooperative effects has not been found yet. One of the most interesting properties of cooperative effects is their robustness to the noise induced by external environments. A well known example is Superconductivity, but other quantum emergent effects, such as Single Excitation Superradiance (SES), have also been shown to be robust to noise [25, 26, 83, 181]. This suggests that emergent properties could play an essential role in the successful development of scalable quantum devices able to operate at room temperature. Since cooperative effects represent a common mechanism to all these emergent phenomena, we believe that finding links between different cooperative effects will be fundamental to progress our understanding of emergence. As was suggested by U. Fano [12] a common mechanism underlies several collective phenomena, such as Superconductivity, plasmon excitation and giant resonances in nuclei. In particular a possible connection between Superradiance and Superconductivity has been discussed by M. Scully [182, 183].

Here we perform a comparison between Superconductivity, i.e. the discrete Bardeen-Cooper-Schrieffer (BCS) model, and Single Excitation Superradiance (SES model). We show that in both cases we have the emergence of a "gap" in the energy spectrum. Superradiance is usually referred to the case of many excitations in an ensemble of N two level systems and to the existence of states which emit energy with an intensity proportional to N^2. On the other hand, SES refers to the possibility that a single excitation coherently shared by N two level systems can decay with a rate proportional to N, an effect defined as the Super of Superradiance in Ref. [28] due to the fact that SES involves a fully entangled state. Note that SES has been found experimentally in interacting two level system, such as cold atomic clouds [29] or in molecular aggregates [19].

Specifically, we analyze a paradigmatic model of SES, which has been studied

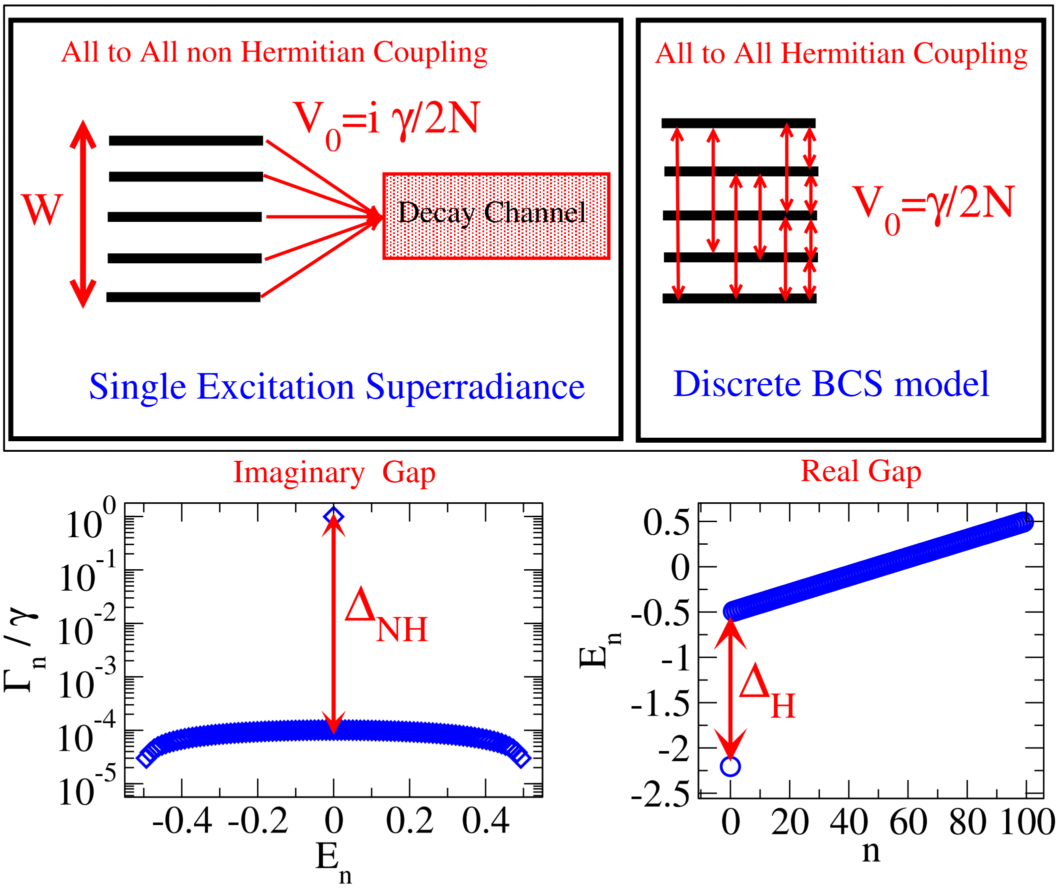

Figure 6.1: (Left upper panel) Paradigmatic model of SES: the coupling of equally spaced single particle energy levels to a common channel in the continuum induces a non-Hermitian all to all interaction between the energy levels described by the Hamiltonian in Eq. (6.1) with $V_0 = i\gamma/(2N)$. (Right upper panel) The discrete BCS model of Superconductivity where Cooper pair states are coupled by an all to all hermitian interaction, see arrows between levels, described by the Hamiltonian in Eq. (6.1) with $V_0 = \gamma/(2N)$. (Lower left panel) Complex eigenvalues $E_n - i\Gamma_n/2$ for the SES model and the imaginary energy gap are shown. (Lower right panel) The eigenvalues E_n and the real energy gap are shown for the BCS model. Parameters are: $N = 100$, $W = 1$, $\gamma = 10\gamma_{\text{cr}}^{\text{H,NH}}$, where $\gamma_{\text{cr}}^{\text{H,NH}}$ is the critical coupling for the BCS/SES transition.

in [184], see Fig. 6.1. In such model, the single excitation energy levels are assumed equally spaced and connected to a single decay channel in the continuum. Due to the fact that the system is open and the excitation can be lost in the common decay channel, the eigenvalues of the system are complex. When the resonances overlap, a Superradiance transition occurs: a Superradiant state acquires most of the decay width of the system, while the other $N-1$ subradiant states decrease their own widths on increasing the coupling strength with the common decay channel. In the limit of large coupling to the continuum only the Superradiant state can decay. Here we show that the Superradiance transition is connected with the emergence of an imaginary energy gap between the complex eigenvalues of the system. Our aim is to investigate and compare the energy gaps arising in such paradigmatic model of Superradiance [184–186] with the well-known energy gap present in a model of Superconductivity (the discrete BCS model [187–193]), paying main attention to the robustness to disorder induced by the presence of a gap and to the kind of interaction which originates the gap.

The discrete BCS model is widely used to analyze Superconductivity in small metallic grains [187–191]. Moreover, the single particle (single Cooper pair) sector of the discrete BCS model had been studied in several papers [192, 193]. In this case, the model is very similar to the model proposed by L. Cooper in his seminal paper [194] and its Hamiltonian reads:

$$H = H_0 + V = \sum_k E_k^0 \left|k\right\rangle \left\langle k\right| - V_0 \sum_{k,k'} \left|k\right\rangle \left\langle k'\right| \, , \tag{6.1}$$

where $|k\rangle$ is the Cooper pair state, E_k^0 is the unperturbed energy, usually taken as equally spaced (picket fence (PF) spectrum), and V_0 is the coupling between the Cooper pair states. The coupling is the same for all the states, similarly to what happens in models with an infinite range coupling in space, with the difference that here the coupling is in momentum space. The same model, see Fig. 6.1, is used to describe the Superradiance transition in a system where many levels are coupled to the same channel in the external environment [184]. The only but important difference is that for the case of Superradiance V_0 is a pure imaginary number. In this case $|k\rangle$ represents a single energy level or an atomic or molecular excitonic state in a specific point of the real space. For the case of Superradiance, the non-Hermitian Hamiltonian, originating from the imaginary coupling, takes into account the fact that the system can decay into the continuum but it also represents the coupling between the energy levels which modifies the spectral features of the system [195–199]. The limit of validity and the effectiveness of the effective non-Hermitian Hamiltonian description of the system has been investigated in Ref. [41, 46]. In such systems a transition to Superradiance occurs above a critical coupling strength. In the Superradiant regime, when one Superradiant state acquire most of the decay width of the system, a gap opens in the complex energy plane of the non-Hermitian Hamiltonian, see Fig. 6.1 lower left panel.

Note that the model presented in Eq. (6.1), apart from being relevant in studying cooperative effects, it is also relevant in describing realistic systems. For instance, for the hermitian case, this model can be reproduced in ion trap experiments with a tunable interaction range, including all-to-all coupling [178, 200–202]. On the other side, for the non-Hermitian case, this model is relevant in nuclear physics [195–199] and it could be also deviced in molecular systems [85].

In Sec. 6.2 we compare the imaginary gap present in the SES model with the real gap emerging in the discrete BCS model. We show that the Superradiance transition coincides with the opening of a gap in the complex energy plane. In the limit of large gap, the magnitude of the Superconducting gap is the same as the Superradiance gap. Nevertheless, our analytical results show that the critical coupling which determines the Superradiance transition scales with the system size differently from the critical coupling associated to the Superconductivity transition. In Sec. 6.3 we present a few numerical results showing the validity of our analytical equations. Then, in Sec. 6.4 we apply the perturbation theory (up to second order) to non-Hermitian systems and we show, also through numerical simulations, how the imaginary energy gap can protect the states from perturbations, such as static disorder, in the same way as a real energy gap does. This result is consistent with several results found in literature [25, 26, 83, 178, 181, 202] about the robustness of Superradiance to disorder. Finally, in Sec. 6.5 we analyze the role of the range of the interaction, showing that an energy gap emerges in the Hermitian system when the interaction is long-ranged. In the Conclusions the relevance of our analysis to realistic systems is discussed.

6.2 Analytical Results for N levels

Let us consider N equally spaced levels in an energy range W, coupled between each other with a constant coupling V_0, which can be real or imaginary. The Hamiltonian can thus be written as in Eq. (6.1), where for the energy we assume a PF distribution, namely

$$E_k^0 = k\delta = k\frac{W}{N}\,, \qquad k = -\frac{N}{2}, \dots, \frac{N}{2}\,, \tag{6.2}$$

where $\delta = W/N$ is the level spacing. First, for the sake of clarity, we present the derivation of the Gap Equation [16, 184, 194, 203], both for the Hermitian and non-Hermitian cases, which is equivalent to the Schrödinger Equation and it makes the computation of some eigenvalues much easier. For the derivation of the Gap Equation we follow [16, 203], which presents a simplified version of the famous derivation by L. Cooper in his seminal paper [194].

We want to solve the Schrödinger Equation

$$H\left|\Psi\right\rangle = E\left|\Psi\right\rangle, \tag{6.3}$$

where $|\Psi\rangle$ is an eigenstate of the full Hamiltonian H and it can be expanded as

$$\left|\Psi\right\rangle = \sum_k a_k \left|k\right\rangle, \tag{6.4}$$

where $|k\rangle$ are eigenstates of H_0, satisfying

$$H_0\left|k\right\rangle = E_k^0\left|k\right\rangle\,. \tag{6.5}$$

Eq. (6.3) can be rewritten as

$$(H - H_0)\left|\Psi\right\rangle = V\left|\Psi\right\rangle\,. \tag{6.6}$$

Then, using the expansion (6.4), we get

$$(H - H_0) \sum_{k'} a_{k'} \left| k' \right\rangle = V \sum_{k'} a_{k'} \left| k' \right\rangle = \sum_{k'} a_{k'} V \left| k' \right\rangle . \tag{6.7}$$

Now let us project Eq. (6.7) on the state $\langle k|$. Defining $V_{kk'} = \langle k|V|k'\rangle$ we have

$$\langle k| \sum_{k'} (E - E^0_{k'}) a_{k'} \left| k' \right\rangle = \sum_{k'} a_{k'} V_{kk'} . \tag{6.8}$$

Now, since $\langle k|k'\rangle = \delta_{k,k'}$ and $V_{kk'} = -V_0 \; \forall k, k'$ we get

$$\sum_{k'} (E - E^0_{k'}) a_{k'} \left\langle k|k' \right\rangle = (E - E^0_k) a_k = -V_0 \sum_k a_k . \tag{6.9}$$

Defining $C \equiv \sum_k a_k$ we have

$$a_k = -\frac{V_0 C}{E - E^0_k} \tag{6.10}$$

so that

$$C = \sum_k a_k = -V_0 \sum_k \frac{C}{E - E^0_k} . \tag{6.11}$$

Dividing by C we finally obtain the Gap Equation

$$1 = -V_0 \sum_k \frac{1}{E - E^0_k} . \tag{6.12}$$

Eq. (6.12) has been obtained by simple linear manipulations of the Schrödinger equation, and so they are equivalent. Given the unperturbed eigenvalues E^0_k, there are N possible values of E which satisfy Eq. (6.12), which are the eigenvalues of H.

The term Gap Equation comes from the fact that it is commonly used to compute the gap between the ground state and the excited states. In the next sections we will compute the gap for the case $V_0 = \gamma/(2N)$ real (for Superconductivity) and for $V_0 = i\gamma/(2N)$ complex (for Superradiance). Note that in both cases we rescale the coupling by N as it is found in the discrete BCS model [187–193]). The non rescaled case can be easily deduced by substituting γ with $N\gamma$ in the following results.

6.2.1 Hermitian case

Following Refs. [16, 192–194, 203], let us review the main results about the gap equation for the Hermitian case. Note that with respect to the BCS model, $1/\delta$ is the Density of States at the Fermi level, W in the Debye energy and V_0 the effective phonon mediated interaction. Let us now consider the Hermitian case, with $V_0 = \gamma/(2N)$. Recalling that the unperturbed spectrum is given by (6.2), we multiply both sides of (6.12) by $2W/\gamma$ to have

$$\frac{2W}{\gamma} = \sum_{k=-N/2}^{N/2} \frac{1}{k - E/\delta} . \tag{6.13}$$

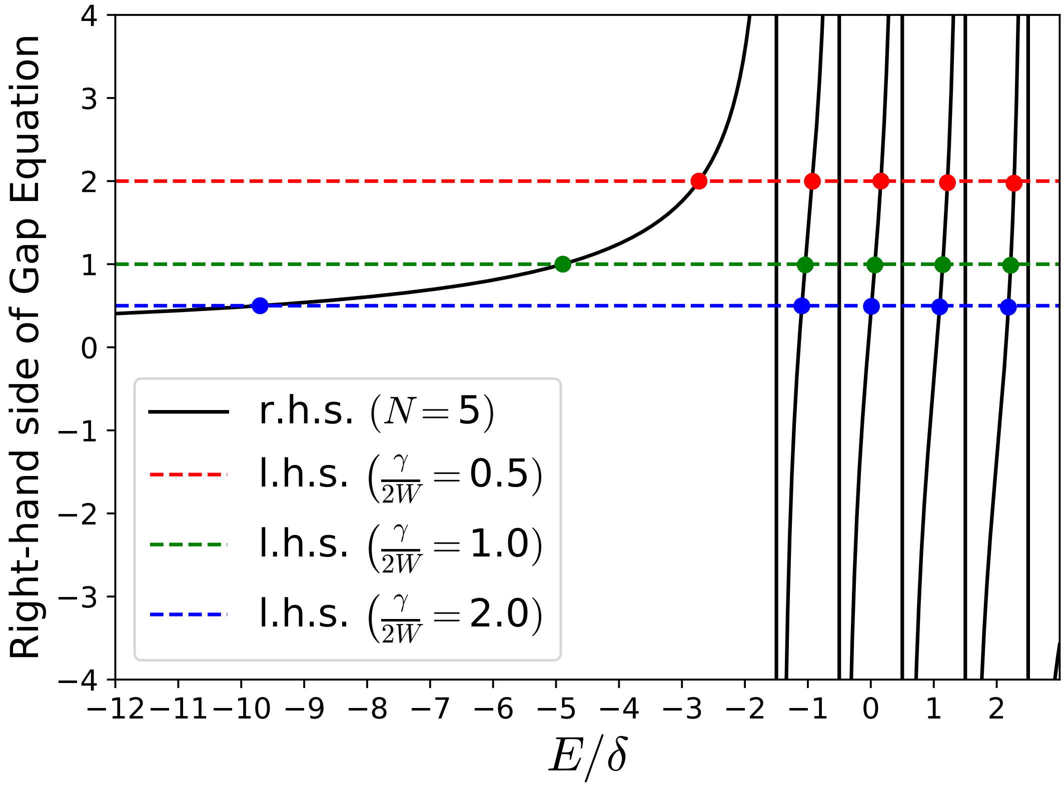

Figure 6.2: Graphical solution of Gap Equation (6.13) in the Hermitian case. The all-to-all coupling here is $V_0 = \gamma/(2N)$. We set $N = 5$.

A graphical solution of Eq. (6.13) is shown in Fig. 6.2 for $N = 5$. The r.h.s. of Eq. (6.13), shown as a continuous black line, is an unbounded function of E/δ having N asymptotes, corresponding to $E/\delta = -N/2, \ldots, N/2$ and shown as vertical black lines. The l.h.s., shown as dashed lines, is independent of E/δ. The solutions are given by the values of E where the r.h.s. intersects the l.h.s. and they are shown by full circles in Fig. 6.2.

From Fig. 6.2 one can see that there are $N = 5$ solutions to Eq. (6.13). Those solutions represent the eigenvalues E of the full Hamiltonian (6.1), divided by the level spacing $\delta = W/N$ of the unperturbed levels. Moreover, one can observe that, by increasing the ratio $\gamma/(2W)$ (so to increase the all-to-all coupling), the energy gap between the ground state and the first excited state increases, too. We are here interested in computing that gap in the limit $N \to \infty$ and keeping $W =$ const., so that the spacing δ of the unperturbed levels tends to 0. First of all, from Fig. 6.2 we can see that the energy of the excited states are all in the range $[-W/2, W/2]$ and, in particular, the first excited state lies in the interval $-W/2 + \delta < E_2 < -W/2 + 2\delta$. This implies that only the ground state energy E_1 can be less than $-W/2$ and that the energy of the first excited state E_2

tends to $-W/2$ when $\delta \to 0$. Now, let us focus on the energy of the ground state.

If $N \gg 1$, we can take the continuum limit for the Gap Equation (6.12)

$$1 = -\frac{\gamma}{2N} \int_{-W/2}^{W/2} \frac{N(x)dx}{E - x}, \tag{6.14}$$

where $N(x) = N/W$ is the density of states and it is constant for a PF level distribution. Then we can analytically solve the integral

$$1 = -\frac{\gamma}{2W} \int_{-W/2}^{W/2} \frac{dx}{E - x} = \frac{\gamma}{2W} \ln \frac{2E - W}{2E + W}, \tag{6.15}$$

noting that the above solution is valid only for $E < -W/2$. For what we stated before, the only state which satisfies this requirement is the ground state E_1. Then we have

$$E_1 = \frac{W}{2} \frac{1 + e^{2W/\gamma}}{1 - e^{2W/\gamma}}. \tag{6.16}$$

Now, let us recall that $E_2 \to -W/2$ when $N \to \infty$ and W does not depend on N (see [16, 203] and the previous considerations on Fig. 6.2). We can then define the Hermitian Gap between the ground state and the first excited state as

$$\Delta_{\mathrm{H}} = E_2 - E_1 = -\frac{W}{2} - E_1 = \frac{W}{e^{2W/\gamma} - 1}. \tag{6.17}$$

Note that the expression of the gap obtained is the same as the one obtained by L. Cooper [194], but it is slightly different from the BCS gap [187–193][1], In the limit $W \ll \gamma/2$ Eq. (6.17) is approximated as

$$\Delta_{\mathrm{H}} \approx \frac{\gamma}{2}. \tag{6.18}$$

On the other hand, when $W \gg \gamma/2$, Eq. (6.17) becomes

$$\Delta_{\mathrm{H}} \approx W e^{-2W/\gamma} \tag{6.19}$$

On increasing γ, the gap Δ_{H} increases as well and, for some $\gamma = \gamma_{\mathrm{cr}}^{\mathrm{H}}$ it becomes equal to the unperturbed level spacing $\delta = W/N$. By setting $\Delta_{\mathrm{H}} = \delta$, it is easy to find that for $N \gg 1$,

$$\gamma_{\mathrm{cr}}^{\mathrm{H}} = \frac{2W}{\ln(N+1)} \approx \frac{2W}{\ln N}, \tag{6.20}$$

which defines the critical coupling at which a gap opens in the BCS model.

---

[1] In the BCS theory [16, 203] and in Ref.s [178, 187–191, 202] the following expression for the gap is reported: $\Delta_{\mathrm{BCS}} = W/\sinh(2W/\gamma)$, which gives different results from Eq. (6.17) in some parameter range. In particular, when $W \gg \gamma/2$, Eq. (6.17) and Δ_{BCS} differ by a factor of 2, namely $\Delta_{\mathrm{H}} \approx W e^{-2W/\gamma}$ and $\Delta_{\mathrm{BCS}} \approx 2W e^{-2W/\gamma}$. On the other hand, in the opposite limit $W \ll \gamma/2$, both (6.17) and Δ_{BCS} have the same approximated expression $\Delta_{\mathrm{H}} \approx \Delta_{\mathrm{BCS}} \approx \gamma/2$. Nevertheless, both expressions predict that the gap closes in the limit $\gamma/W \to 0$.

6.2.2 Non-Hermitian case

Superradiant state (Gap Equation) Now, let us consider the non-Hermitian case $V_0 = i\gamma/(2N)$. Starting from Eq. (6.12) we obtain a gap equation

$$1 = -\frac{i\gamma}{2N}\sum_k \frac{1}{\mathcal{E} - E_k^0}, \tag{6.21}$$

where the eigenvalues are now complex,

$$\mathcal{E} = E - i\frac{\Gamma}{2}. \tag{6.22}$$

This complex equation splits into two real equations

$$\begin{cases} \sum_k \dfrac{E - E_k^0}{(E - E_k^0)^2 + \Gamma^2/4} = 0 \\ \sum_k \dfrac{\Gamma/2}{(E - E_k^0)^2 + \Gamma^2/4} = \dfrac{2N}{\gamma} \end{cases} \tag{6.23}$$

which have N solutions that depend on N and γ. In Fig. 6.3 we plot the eigenvalues (6.22) in the plane $(E/\delta, \Gamma/\gamma)$ for $N = 6$ (upper panel) and $N = 7$ (lower panel), as a function of γ. In particular, we plot the trajectories of the eigenvalues starting from $\gamma = (2W/\pi)/10$ (open circles) up to $\gamma = 10(2W/\pi)$ (full circles). The value $\gamma = 2W/\pi$ marks the Superradiance transition, as we will show here below. When γ is small (open circles in Fig. 6.3), the real parts of the eigenvalues are given by (6.2), while the imaginary part is $\Gamma_n \approx \gamma/N$ for all eigenvalues. On increasing γ, the spacing between the real parts of the eigenvalues decreases (a phenomenon called "pole attraction") up to a critical point γ_{SR}, where we see a different behaviour between $N = 6$ and $N = 7$.

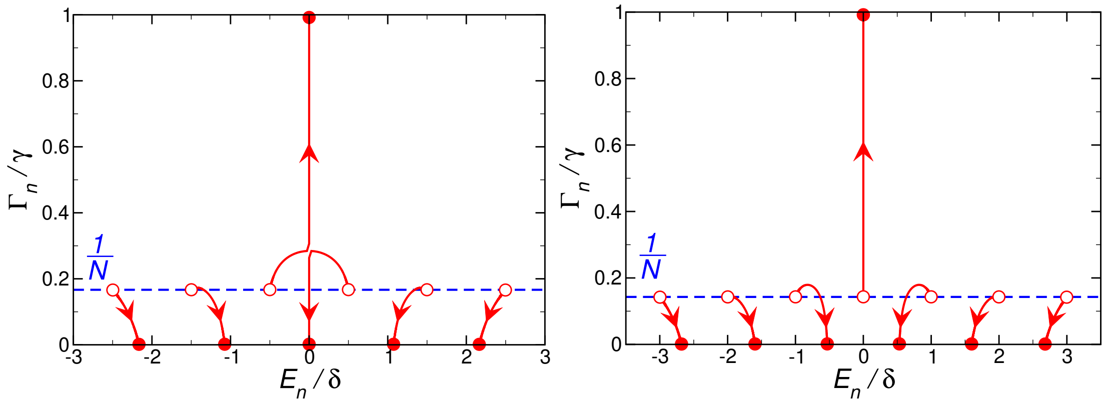

Figure 6.3: Complex eigenvalues (6.22) varying γ from $\gamma = (2W/\pi)/10$ (open circles) to $\gamma = 10(2W/\pi)$ (full circles). γ increases following the arrows. The dashed line marks the value $\Gamma_n = \gamma/N$. Parameters: $N = 6$ (left panel) and $N = 7$ (right panel).

For $N = 6$ (left panel of Fig. 6.3), the two eigenvalues whose real part is closer to 0 collapse to the imaginary energy axis (so that $E_n = 0$ for both of them) when $\gamma > \gamma_{\mathrm{SR}}$. The widths of those two eigenvalues, however, have a different behaviour because one increases with γ (and we call the respective state *Superradiant*) while the other one decreases with γ. For $\gamma \gg \gamma_{\mathrm{SR}}$ the total decay width of the system is concentrated in the superradiant state, while the other $N-1$ states have a negligible decay width, and thus they are called *subradiant*.

For $N = 7$ (right panel of Fig. 6.3) the behaviour is similar to that of $N = 6$ in that, on increasing γ, the real parts of the eigenvalues are attracted to each other and for $\gamma \gg \gamma_{\mathrm{SR}}$ the total decay width of the system is concentrated into one superradiant state. The difference here (with respect to $N = 6$) is that for $\gamma > \gamma_{\mathrm{SR}}$ only the Superradiant state has $E_{\mathrm{SR}} = 0$, while $E_n \neq 0$ for the subradiant states.

The same behaviour seen for $N = 6$ has been observed for all even values of N, while the behaviour observed for $N = 7$ has been seen for all odd values of N. In the following calculations we look for an analytical expression for the width Γ_{SR} of the superradiant state and for the critical coupling γ_{SR} and, based on the above discussion, we can set $E = 0$ in Eq. (6.23).

Moreover, in the limit $N \gg 1$ we approximate the PF spectrum (6.2) with a continuous energy distribution constant in the interval $[-W/2, W/2]$, so that we can solve the second equation in (6.23)

$$\frac{2N}{\gamma} = \frac{N}{W} \int_{-W/2}^{W/2} dx \frac{\Gamma/2}{x^2 + \Gamma^2/4} = \frac{2N}{W} \arctan \frac{W}{\Gamma}\,, \tag{6.24}$$

from which we get the width of the superradiant state

$$\Gamma_{\mathrm{SR}} = \frac{W}{\tan \frac{W}{\gamma}}\,. \tag{6.25}$$

This term is crucial to determine the gap in the complex plane between the superradiant and the closest subradiant state. Note that Γ_{SR} has to be positive, and this gives the condition of validity of Eq. (6.24), which is $\gamma \geq \frac{2W}{\pi}$. Therefore the superradiant state exists only above a critical coupling strength which coincides with the so-called Superradiance transition (at $\gamma = \gamma_{\mathrm{SR}}$), as we will show below.

Superradiant transition. In Ref. [184] the critical coupling at which a Superradiance transition occurs has been computed analytically by studying the dependence of the widths of the subradiant states on γ. Indeed below the Superradiance transition the widths of the subradiant states increase with γ, while above it, they decrease with γ. From Ref. [184] we have:

$$\gamma_{\mathrm{SR}} = \frac{2W}{\pi}\,. \tag{6.26}$$

Which is the same critical value of γ computed in the previous section.

Adapting the analytical results of Ref. [184] to our case (see Appendix 6.7.1 for details) the decay widths of all the eigenstates below the Superradiance transition are

$$\Gamma = \frac{W}{N\pi} \ln\left(\frac{1+\gamma/\gamma_{\mathrm{SR}}}{1-\gamma/\gamma_{\mathrm{SR}}}\right) \qquad \text{for } \gamma < \gamma_{\mathrm{SR}}\,, \tag{6.27}$$

while all the widths of the subradiant states above the Superradiance transition are

$$\Gamma_{\mathrm{sub}} = \frac{W}{N\pi} \ln\left(\frac{\gamma/\gamma_{\mathrm{SR}}+1}{\gamma/\gamma_{\mathrm{SR}}-1}\right) \qquad \text{for } \gamma > \gamma_{\mathrm{SR}}\,. \tag{6.28}$$

Note that the critical coupling parameter γ_{SR} is the point where the widths (6.27)-(6.28) are non-analytical.

Imaginary energy gap. The gap in the complex energy plane can be defined as

$$\Delta_{\mathrm{NH}} = \max_i \left\{ \min_{j\neq i} \left[\mathrm{dist}\left(\mathcal{E}_i, \mathcal{E}_j\right)\right] \right\}, \tag{6.29}$$

where the distance in the complex plane between two eigenvalues is

$$\mathrm{dist}\left(\mathcal{E}_i, \mathcal{E}_j\right) = \sqrt{\left(E_i - E_j\right)^2 + \frac{1}{4}\left(\Gamma_i - \Gamma_j\right)^2}\,. \tag{6.30}$$

We can use the previous analytical results given in Eqs. (6.27,6.28) to estimate such complex gap. For $\gamma < \gamma_{\mathrm{SR}}$, the widths of all the states are the same and the distance in real energy is constant and equal to δ, where δ is the level spacing in the PF model, see Eq. (6.2), so that we have $\Delta_{\mathrm{NH}} = \delta$ and no gap is present. On the other side in the superradiant regime $\gamma > \gamma_{\mathrm{SR}}$, we can estimate Δ_{NH} as the distance in the complex plane between the superradiant eigenstate $\mathcal{E}_{\mathrm{SR}}$ and the closest subradiant state $\mathcal{E}_{\mathrm{sub}}$, see Appendix 6.7.1 for details, namely

$$\Delta_{\mathrm{NH}} = \sqrt{\left(E_{\mathrm{SR}} - E_{\mathrm{sub}}\right)^2 + \frac{1}{4}\left(\Gamma_{\mathrm{SR}} - \Gamma_{\mathrm{sub}}\right)^2}\,. \tag{6.31}$$

When $N \to \infty$ we have $\left(E_{\mathrm{SR}} - E_{\mathrm{sub}}\right) \approx \delta \to 0$ and $\Gamma_{\mathrm{sub}} \to 0$ (see (6.28)), so that the gap Δ_{NH} is determined only by the decay width of the superradiant state (6.25),

$$\lim_{N\to\infty} \Delta_{\mathrm{NH}} = \frac{\Gamma_{\mathrm{SR}}}{2} = \frac{W}{2\tan\frac{W}{\gamma}}\,. \tag{6.32}$$

Now, we can define the critical value $\gamma_{\mathrm{cr}}^{\mathrm{NH}}$ as the value of γ at which the gap opens, i.e. by imposing $\Delta_{\mathrm{NH}} = \delta$. From Eq. (6.32), we then have

$$\gamma_{\mathrm{cr}}^{\mathrm{NH}} = \frac{W}{\arctan\frac{N}{2}}\,. \tag{6.33}$$

Note that this value is finite in the $N \to \infty$ limit,

$$\lim_{N\to\infty} \gamma_{\text{cr}}^{\text{NH}} = \frac{2W}{\pi}, \tag{6.34}$$

and it has the same value as γ_{SR} (see Eq. (6.26)). Our results demonstrate that the Superradiant transition, previously analyzed in Ref. [184], is equivalent to the emergence of a gap in the imaginary energy axis.

Moreover, we can approximate the gap for large γ, close to the transition and below the critical point, respectively, as

$$\Delta_{\text{NH}} \approx \frac{\gamma}{2} \qquad \text{for } \gamma \gg \gamma_{\text{SR}} \tag{6.35a}$$

$$\Delta_{\text{NH}} \approx \frac{\pi W}{4}\left(\frac{\gamma}{\gamma_{\text{cr}}^{\text{NH}}} - 1\right) \qquad \text{for } \gamma \gtrsim \gamma_{\text{SR}} \tag{6.35b}$$

$$\Delta_{\text{NH}} = 0 \qquad \text{for } \gamma \leq \gamma_{\text{SR}}\,. \tag{6.35c}$$

Note that for $\gamma \gg \gamma_{\text{SR}}$ the complex energy gap of the superradiant model is identical to the real energy gap of the superconductivity model, see Eq. (6.18). On the other side, in the limit of large system sizes, the critical coupling for the emergence of a gapped state goes to zero for the BCS model, while for the SES model it remains finite.

6.3 Numerical Results

Here we validate our previous analytical predictions with few numerical results.

In Fig. 6.4 the gap is shown, both for the Hermitian and non-Hermitian cases, as a function of γ for different system sizes N. For the non-Hermitian case we define the gap using the distance in the complex plane, see Eqs. (6.29,6.30). Similarly, for the Hermitian case we define the gap as

$$\Delta_{\text{H}} = \max_i \left\{ \min_{j\neq i} \left[\text{dist}\left(E_i, E_j\right) \right] \right\}, \tag{6.36}$$

where $\text{dist}\left(E_i, E_j\right) = |E_i - E_j|$ is the distance in the real axis (consistently with the non-Hermitian definition (6.30)). With this definition, the presence of a finite and N independent $\Delta_{\text{H,NH}}$ in some region of γ signals the existence of an energy gap in the spectrum. In contrast, we have no energy gap in the spectrum in the region of parameters where $\Delta_{\text{H,NH}}$ goes to zero as N increases.

The continuous blue curve in Fig. 6.4 indicates the analytical estimate of the gap $\Delta_{\text{H,NH}}$ for both cases: Eq. (6.17) for the Hermitian case and Eq. (6.32) for the non-Hermitian one. The critical couplings $\gamma_{\text{cr}}^{\text{H,NH}}$ can be identified graphically as the values of γ above which the numerical data for $\Delta_{\text{H,NH}}$ (symbols) coincide with the analytical estimates (continuous blue curves). In the figure our predictions of the critical couplings given in Eq. (6.34) (vertical dashed line in panel (a)) and Eq. (6.20) (arrows in panel (b)) are also shown.

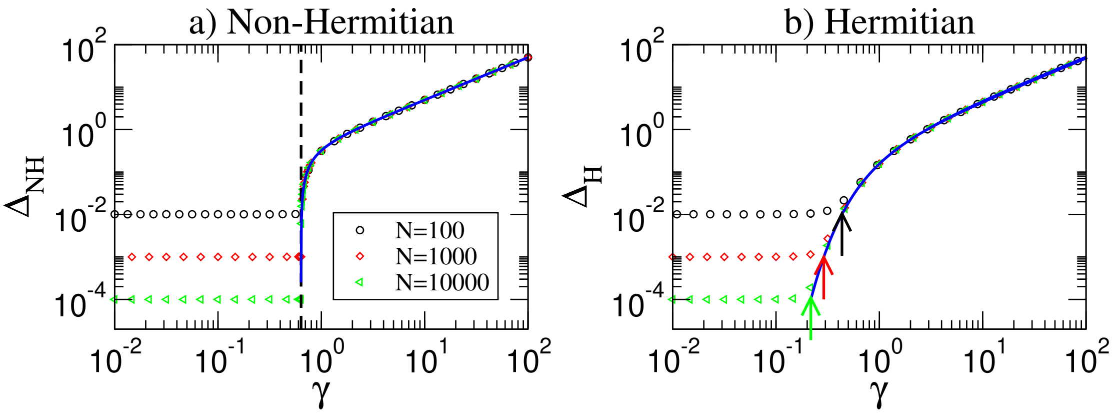

Figure 6.4: a) Gap Δ_{NH} *vs.* the coupling parameter γ. Symbols are given by (6.29)-(6.30), while the continuous blue curve shows the analytical estimate (6.32). The dashed vertical line marks the critical coupling $\gamma_{\mathrm{cr}}^{\mathrm{NH}}$ from Eq. (6.34). b) Gap Δ_{H} *vs.* the coupling parameter γ. Symbols are given by (6.36) while the continuous blue curve shows the analytical estimate (6.17). The arrows indicate the critical coupling $\gamma_{\mathrm{cr}}^{\mathrm{H}}$ from Eq. (6.20). Here, $W = 1$ and $N = \{100, 1000, 10000\}$.

Our analytical estimate for the gap works well above the critical γ for both Hermitian and non-Hermitian coupling, for all the values of N shown. Interestingly we find that the critical γ is independent of N for large N in the non-Hermitian case, as we predicted in Eq. (6.34), while it decreases with N in the Hermitian case, according to our prediction (6.20). Moreover from Fig. 6.4 one can see that the transition to a gapped phase in the non-Hermitian case is much sharper than the transition in the Hermitian case. Note that for $\gamma < \gamma_{\mathrm{cr}}^{\mathrm{H,NH}}$ our estimate predicts that $\Delta_{\mathrm{H,NH}} \to 0$ for $\gamma \to 0$, while the numerical simulations show that $\Delta_{\mathrm{H,NH}} \to \delta = W/N$. This is clearly a finite size effect and it is not relevant since δ goes to zero when $N \to \infty$.

6.4 Imaginary Energy gap and robustness to perturbations

We have shown the emergence of both Hermitian and non-Hermitian gaps in the spectrum of a Picket-Fence model. While, in the Hermitian case, it is well known that a gap between the ground state and the excited states makes the first more robust to perturbations, it is not trivial that an imaginary gap has the same effect on the gapped state. Thus, here we will apply perturbation theory to non-Hermitian systems and we will show how the distance in the complex plane is related to the robustness to perturbations. Then we will show numerically how the non-Hermitian gap makes the system robust to static disorder.

6.4.1 Non-Hermitian perturbative approach

Let us consider a perturbation D to the non-Hermitian Hamiltonian H, so that the total Hamiltonian of the system can be written as:

$$H_D = H + D\,, \tag{6.37}$$

where H is a generic non-Hermitian symmetric Hamiltonian.

Since H is non-Hermitian, its eigenfunctions are not orthogonal. First of all, let us define a "non-Hermitian bra", being the transpose of a ket

$$\langle\langle\psi| := (|\psi\rangle)^t\,. \tag{6.38}$$

Since the Hamiltonian is symmetric, the left eigenfunctions $\langle\langle\psi_i|$ are the "bra" of the right eigenfunctions $|\psi_i\rangle$, that is

$$H\,|\psi_i\rangle = \mathcal{E}_i\,|\psi_i\rangle \quad \text{and} \quad \langle\langle\psi_i|\,H = \mathcal{E}_i\langle\langle\psi_i|\,. \tag{6.39}$$

From here, the biorthogonality condition arises as

$$\langle\langle\psi_i|\psi_j\rangle = \delta_{ij}\,. \tag{6.40}$$

When the perturbation D is sufficiently small, a perturbative correction of the complex eigenvalues up to second order can be derived [25, 26], and it has the expression

$$\overline{\mathcal{E}}_n \approx \mathcal{E}_n + \langle\langle\psi_n|D|\psi_n\rangle + \sum_{m\neq n}\frac{\langle\langle\psi_n|D|\psi_m\rangle^2}{\mathcal{E}_n-\mathcal{E}_m}\,. \tag{6.41}$$

From Eq. (6.41) it is clear that the strength of the perturbation is determined by the ratio of two complex numbers $z_1 = \langle\langle\psi_n|D|\psi_m\rangle^2$, $z_2 = \mathcal{E}_n - \mathcal{E}_m$. This proves that a state separated by a gap in the complex plane from the rest of the spectrum is robust to perturbations as long as the gap is large compared to the modulus of the perturbations.

As a simple example of the above general calculations, let us consider a system made of two resonant sites, separated by a pure imaginary gap $i\gamma$, and perturbed with a coupling D. Note that this simple model has been used to describe experimental evidence of Dynamical "Quantum Phase Transition" in spin systems [204–207].

The corresponding non-Hermitian Hamiltonian is

$$H + D = \begin{pmatrix} E_0 & 0 \\ 0 & E_0 - i\gamma \end{pmatrix} + \begin{pmatrix} 0 & d \\ d & 0 \end{pmatrix}$$

and the eigenenergies $\overline{\mathcal{E}}_\pm$ of $H + D$ can be analytically obtained as

$$\overline{\mathcal{E}}_\pm = E_0 - \frac{i\gamma}{2} \pm \frac{i\gamma}{2}\sqrt{1-\frac{4d^2}{\gamma^2}}\,. \tag{6.42}$$

Now, let us consider the case when $2d \ll \gamma$, i.e. the complex gap γ is much larger than the coupling d between the sites. Under this assumption we can expand the eigenenergies (6.42) to obtain

$$\overline{\mathcal{E}}_{+} \approx E_0 - \frac{id^2}{\gamma}\,, \tag{6.43}$$

$$\overline{\mathcal{E}}_{-} \approx E_0 - i\gamma + \frac{id^2}{\gamma}\,. \tag{6.44}$$

The same result can be obtained by applying the perturbative expansion (6.41) and it shows that two unperturbed complex eigenenergies having the same real part but being distant in the imaginary axis can be robust to a perturbation, as long as the distance in the complex plane is much larger than the perturbation.

6.4.2 Robustness of superradiance to static diagonal disorder

In order to check that the previous results are valid in the model considered here beyond the perturbative regime, let us add to the the SES Hamiltonian

$$H = \sum_k E_k \left|k\right\rangle \left\langle k\right| - i\frac{\gamma}{2N}\sum_{k,k'} \left|k\right\rangle \left\langle k'\right|, \tag{6.45}$$

the static disorder

$$D = \sum_k \epsilon_k \left|k\right\rangle \left\langle k\right|\,, \tag{6.46}$$

where ϵ_k are random numbers uniformly distributed such that $\epsilon_k \in [-\xi/2, \xi/2]$. Here the parameter ξ is proportional to the standard deviation of the energy fluctuations introduced by D and it represents the disorder strength. In particular, our aim is to study the robustness of the superradiant state of the non-Hermitian case to such static disorder. In Fig. 6.5 (upper panel) the width of the superradiant state Γ_{SR} divided by the average width $\langle\gamma\rangle = \gamma/N$ is shown *vs.* the disorder strength ξ for different values of γ larger than the critical $\gamma_{\text{cr}}^{\text{NH}}$. As one can see, the width of the superradiant state is larger than $\langle\gamma\rangle$ for small disorder ξ. Then, beyond some critical value of ξ, the width start to decrease with ξ, ultimately reaching $\Gamma_{\text{SR}} = \langle\gamma\rangle = \gamma/N$ for $\xi \to \infty$. In order to quantify phenomenologically such critical disorder strength, let us define a critical value ξ_{cr} as the value of ξ beyond which the width of the superradiant state is less than 95% of its value without disorder. In this sense, ξ_{cr} is proportional to the disorder strength needed to destroy superradiance. In the lower panel of Fig. 6.5 ξ_{cr} is plotted *vs.* the ratio $\gamma/\gamma_{\text{cr}}^{\text{NH}}$. In the same panel, the gap (6.32) is plotted as a comparison. As one can see, apart from small deviations where $\gamma \simeq \gamma_{\text{cr}}^{\text{NH}}$, the critical disorder ξ_{cr} increases with γ and it is approximately proportional to the non-Hermitian gap. This shows that the non-Hermitian gap makes superradiance robust to static disorder.

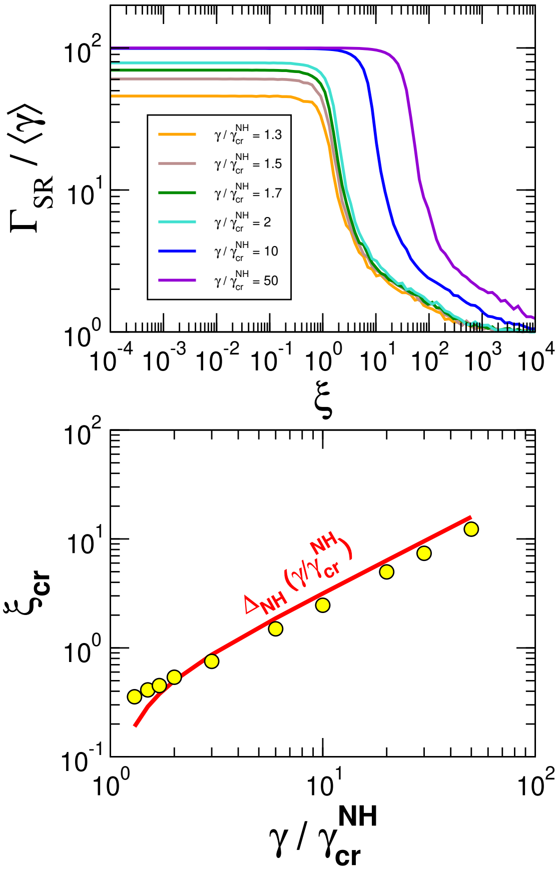

Figure 6.5: Upper panel: width of the superradiant state divided by the average width $\langle\gamma\rangle = \gamma/N$ *vs.* the disorder strength ξ as introduced in the Hamiltonian (6.37)-(6.45)-(6.46). Lower panel: the critical value ξ_{cr} (see text) is plotted *vs.* $\gamma/\gamma_{\text{cr}}^{\text{NH}}$ as circles. The red line is the gap, as defined in Eq. (6.32). Parameters in both panels are $N = 100$, $W = 1$ and an average over 100 realizations of static disorder is performed.

6.5 Relation between the gapped regime and the interaction range

In this section we want to extend our analysis to different ranges of interaction. In particular, we want to know if the emergence of the gap is a general outcome of long-range interactions in a PF model. Differently from the rest of the chapter, here we focus only on the Hermitian case. Note that the Hermitian model is relevant in many realistic situations, such as ion traps [178, 200–202], where one-dimensional systems with tunable interaction range can be emulated.

We model an interaction of range α by the Hamiltonian term

$$V = -\frac{\gamma}{2v_{N,\alpha}} \sum_{\substack{k,k' \\ k \neq k'}} \frac{|k\rangle \langle k'|}{|k-k'|^{\alpha}}, \tag{6.47}$$

where $v_{N,\alpha}$ is a normalization constant and, since we are dealing with a one-dimensional system, we speak about "long-range interaction" for $0 \leq \alpha < 1$ and about "short-range interaction" for $\alpha > 1$. Note that in ion trap experiments [200, 201] the exponent α can be tuned from 0 to 3. The case $\alpha = 1$ is critical because α equals the dimension of the system and thus we will analyze it separately. The normalization constant $v_{N,\alpha}$ has been added in order to have an extensive Hamiltonian energy and to fix the spectrum of V as large as $\gamma/2$. For the case $\alpha = 0$, for example, we have $v_{N,0} = N$, which is exactly the Hermitian case studied in the previous sections. For $\alpha \neq 0$, $v_{N,\alpha}$ is determined by numerically diagonalizing V, and it has the following scaling with the system size (see Appendix 6.7.2 for details):

$$v_{N,\alpha} \sim \begin{cases} N^{1-\alpha} & \text{for } \alpha < 1 \\ \ln N & \text{for } \alpha = 1 \\ \text{const.} & \text{for } \alpha > 1 \end{cases} . \tag{6.48}$$

In order to understand how the presence of a gap is connected to the range of the interaction, here we study numerically the presence of the gap Δ_{H} defined in Eq. (6.36). Let us remind that the presence of a finite and N-independent Δ_{H} in some region of γ signals the existence of an energy gap in the spectrum.

In Fig. 6.6 we plot Δ_{H}, defined as in Eq. (6.36), as a function of γ for $\alpha = \{1/3, 1, 5\}$. The case $\alpha = 1/3$ shown in panel (a) corresponds to a long-range interaction and one can see that, similarly to the case $\alpha = 0$ (see Fig. 6.4(b)), the gap is independent of the system size N for large γ. On the other hand, for short-range $\alpha = 5$ (panel (c)) Δ_{H} decreases with the system size for any value of γ and thus there is no gap for these two cases in the limit $N \to \infty$. For the critical range $\alpha = 1$ (panel (b)) the results are less clear and more analysis is needed to establish the non-existence of a gapped regime (as the data shown in the Figure seem to indicate).

From Fig. 6.6 one can see that $\gamma = 100$ represents a "strong-coupling" regime for the three values of α shown. Then, in Fig. 6.7 we plot Δ_{H} (symbols) *vs.* α for $\gamma = 100$ setting

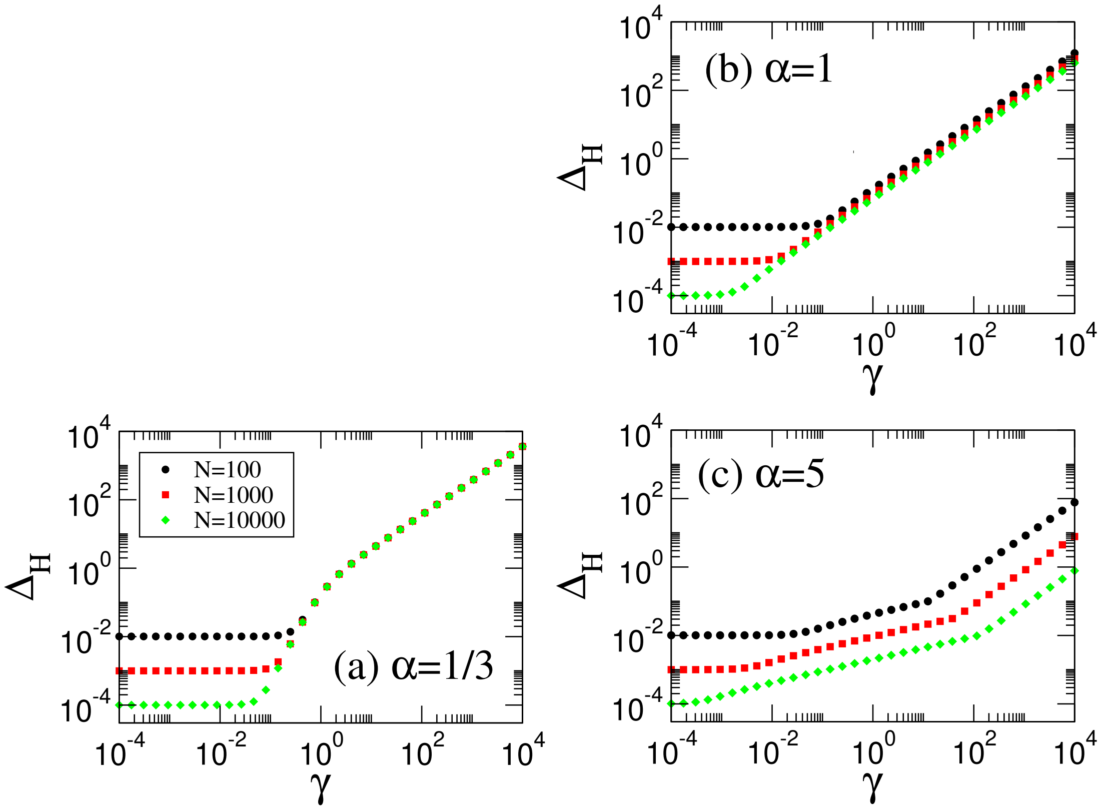

Figure 6.6: Gap Δ_{H}, as defined in (6.36), *vs.* the coupling parameter γ with the interaction (6.47). Here $W = 1$ and $N = \{100, 1000, 10000\}$.

the same parameters and the same values of N as in Fig. 6.6. In Fig. 6.7 one can see two different regimes: (i) for $\alpha < 1$ (long range)) Δ_{H} is independent of N, representing a gap in the $N \to \infty$ limit; (ii) for $\alpha \gtrsim 1$ (short range) Δ_{H} decreases with N, meaning that there is no gap in the thermodynamic limit. Note that we checked that in the long range regime ($\alpha < 1$) the gap arises between the ground state and the first excited state, i.e. $\Delta_{\mathrm{H}} = E_2 - E_1$.

As a final remark we note that in this section we have analyzed the role of the interaction range just in the Hermitian case, because adding a variable range of the interaction in the non-Hermitian case is more difficult. The generalization to different ranges that we used for the Hermitian case, in fact, cannot be performed as it is for the non-Hermitian case without loss of consistency. Indeed, an imaginary interaction $V_{k,k'} = -i\gamma|k - k'|^{-\alpha}$ would lead to both positive and negative decay widths, while the decay widths of a non-Hermitian Hamiltonian are required to be all positive. Nevertheless let us note that in realistic molecular system the non-Hermitian interaction can have a complicated power law decay with the distance [117].

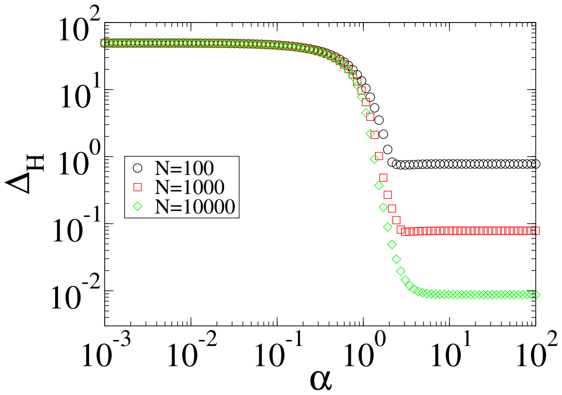

Figure 6.7: Gap $\Delta_{\rm H}$ *vs.* the range of interaction α for N={100,1000,10000}, where the symbols are given by Eq. (6.36). Here, $W = 1$ and $\gamma = 100$.

6.6 Conclusions and Perspectives

We have compared two paradigmatic models for Superconductivity and Superradiance, focusing on the emergence of an energy gap in the real and complex plane, respectively. We show that a gap arises also in the Superradiance model in the complex plane, and we give an analytical estimate of that gap which agrees very well with our numerical simulations. We show that the usual Superradiance transition can be interpreted as a transition to a gapped regime. Moreover in the large coupling limit the Superradiance and the Superconductivity gaps are mathematically the same, while they differ at the criticality. Indeed, while the critical value for the emergence of Superconductivity depends on the system size, the critical value for the emergence of Superradiance is independent of the system size. Finally we have also shown that a gap in the complex plane can induce robustness to perturbations in the system, similarly to a gap in the real axis. This result allows to interpret the robustness of Superradiance to disorder reported in several previous publications in literature as a consequence of the presence of an imaginary energy gap. In perspective, the relevance of these energy gaps to transport and other system properties will be analyzed. From a mathematical point of view, we have shown that the emergence of such gapped states can be connected with the long range nature of the interaction. Indeed both the discrete BCS model and the SES model share a distance independent coupling (all-to-all coupling). The connection of a gapped state with the long range of the interaction has been also pointed out in Ref. [178, 202].

Even if here we have analyzed very simple models amenable of analytic treatment, our results can be relevant for a variety of realistic systems, such as molecular chains [208, 209], ion traps [200, 201] and photosynthetic systems [117]. For instance the range of interaction can be controlled in ion trap experiments [200, 201] where the Hermitian Hamiltonian discussed here can be experimentally realized. Moreover a linear molecular chain interacting with an electromagnetic field can be modelled by non-

Hermitian Hamiltonians [117] very similar to the ones considered here. In perspectives we plan to analyze realistic models for quantum transport in presence of non-Hermitian and Hermitian interactions and to study the relevance of the gapped regime to the efficiency of transport. We expect that the existence of gapped extended states can act as a support for efficient energy transport.

6.7 Appendix

6.7.1 Non-Hermitian coupling: widths of the subradiant states

In the main text, discussing the case of a non-Hermitian coupling, we report the analytic expression of the widths of all the eigenstates for $\gamma < \gamma_{\text{SR}}$ (6.27) and of the widths of the subradiant states for $\gamma > \gamma_{\text{SR}}$ (6.28). Here we derive those expressions, as well as the critical coupling γ_{SR}, following [184].

Let us consider the case of odd N, so that we can write $N = 2M + 1$ with M an integer. Note that the limit $N \to \infty$ corresponds to $M \to \infty$ and in that limit there is no distinction between even or odd values of N. The Hamiltonian (6.1), with E_k given by (6.2) and $V_0 = i\gamma/(2N)$, can be mapped to

$$H = \delta \overline{H} = \delta \left(\sum_{k=-M}^{M} k \left|k\right\rangle \left\langle k\right| - i\alpha \sum_{k=-M}^{M} \sum_{k'=-M}^{M} \left|k\right\rangle \left\langle k'\right| \right) , \tag{6.49}$$

where the center of the unperturbed spectrum is assumed to be at $E_0 = 0$, without loss of generality, and the coupling parameter is

$$\alpha = \frac{\gamma}{2N\delta} = \frac{\gamma}{2W} . \tag{6.50}$$

We now proceed to compute the eigenvalues $\overline{\lambda}$ of $\overline{H}$, which are related to the eigenvalues λ of H by $\lambda = \delta\overline{\lambda}$. Thus, let us consider the matrix $\left\langle k\right| \overline{H} \left|k'\right\rangle$. By construction, all column and row vectors, respectively, of the non-Hermitian part of that matrix are linearly dependent. Summing $i\alpha$ times the central row ($k = 0$) to all the other rows ($k \neq 0$), one gets the following expression for the characteristic polynomial:

$$P_M(\overline{\lambda}) = \prod_{k=-M}^{M} (k - \overline{\lambda}) - i\alpha \sum_{k=-M}^{M} \prod_{\substack{j=-M \\ j\neq k}}^{M} (j - \overline{\lambda}) = 0 . \tag{6.51}$$

According to Eq. (6.51), $P_M(\overline{\lambda})$ is the sum of two polynomials,

$$P_M(\overline{\lambda}) = Q_M(\overline{\lambda}) - i\alpha R_M(\overline{\lambda}) \tag{6.52}$$

which are related in a simple manner,

$$R_M = -\frac{d}{d\overline{\lambda}} Q_M .$$

Taking the limit $M \to \infty$ and using the infinite product expansion of the sine function we have

$$P_\infty(\overline{\lambda}) = \sin[\pi\overline{\lambda}] + i\alpha\pi\cos[\pi\overline{\lambda}] = 0 \tag{6.53}$$

with $\overline{\lambda} = \overline{E} - \frac{i}{2}\overline{\Gamma}$. Then, we can substitute this expression of $\overline{\lambda}$ to get

$$P_\infty(\overline{\lambda}) = \sin\left[\pi\left(\overline{E} - \frac{i}{2}\overline{\Gamma}\right)\right] + i\alpha\pi\cos\left[\pi\left(\overline{E} - \frac{i}{2}\overline{\Gamma}\right)\right] = 0\,. \tag{6.54}$$

Separating real and imaginary parts one has

$$\begin{cases} \sin[\pi\overline{E}]\left[e^{\pi\overline{\Gamma}}(1-\alpha\pi) + (1+\alpha\pi)\right] = 0 \\ \cos[\pi\overline{E}]\left[e^{\pi\overline{\Gamma}}(1-\alpha\pi) - (1+\alpha\pi)\right] = 0 \end{cases}. \tag{6.55}$$

So there are two solutions:
i) $\sin[\pi\overline{E}] = 0$, $\overline{E} = n \in \mathbb{Z}$

$$e^{\pi\overline{\Gamma}} = \frac{1+\alpha\pi}{1-\alpha\pi}, \tag{6.56}$$

from which

$$\overline{\Gamma} = \frac{1}{\pi}\ln\left(\frac{1+\alpha\pi}{1-\alpha\pi}\right) \tag{6.57}$$

under the conditions $e^{\pi\overline{\Gamma}} > 0$, $\alpha < \frac{1}{\pi}$. This result represents the widths of all the eigenstates below the Superradiance transition.
ii) $\cos[\pi\overline{E}] = 0$, $\overline{E} = n + \frac{1}{2}, n \in \mathbb{Z}$

$$e^{\pi\overline{\Gamma}} = \frac{\alpha\pi+1}{\alpha\pi-1}, \tag{6.58}$$

which gives

$$\overline{\Gamma}_{\text{sub}} = \frac{1}{\pi}\ln\left(\frac{\alpha\pi+1}{\alpha\pi-1}\right) \tag{6.59}$$

under the conditions $e^{\pi\overline{\Gamma}} > 0$, $\alpha > \frac{1}{\pi}$. This result represents instead the widths of the subradiant states above the Superradiance transition. From these results a critical coupling parameter $\alpha_{\text{SR}} = 1/\pi$ emerges, which marks the Superradiance transition.

Now, let us map our expression for $\overline{\lambda}$ to $\lambda = E - \frac{i}{2}\Gamma$. Multiplying by δ we have

$$E_n = n\delta \qquad (n \in \mathbb{Z}) \tag{6.60a}$$

$$\Gamma = \frac{\delta}{\pi}\ln\left(\frac{1+\alpha/\alpha_{\text{SR}}}{1-\alpha/\alpha_{\text{SR}}}\right) \qquad \text{for } \alpha < \alpha_{\text{SR}} \tag{6.60b}$$

and

$$E_n = \left(n + \frac{1}{2}\right)\delta \qquad (n \in \mathbb{Z}) \tag{6.61a}$$

$$\Gamma_{\text{sub}} = \frac{\delta}{\pi}\ln\left(\frac{\alpha/\alpha_{\text{SR}}+1}{\alpha/\alpha_{\text{SR}}-1}\right) \qquad \text{for } \alpha > \alpha_{\text{SR}}\,, \tag{6.61b}$$

where we can use (6.50) to express the ratio between α and α_{SR} as

$$\frac{\alpha}{\alpha_{\mathrm{SR}}} = \frac{\gamma\pi}{2W} \,. \tag{6.62}$$

Thus, equations (6.60b) and (6.61b) can be rewritten in terms of the parameters of H as

$$\Gamma = \frac{W}{N\pi} \ln\left(\frac{1+\gamma/\gamma_{\mathrm{SR}}}{1-\gamma/\gamma_{\mathrm{SR}}}\right) \qquad \text{for } \gamma < \gamma_{\mathrm{SR}} \tag{6.63}$$

and

$$\Gamma_{\mathrm{sub}} = \frac{W}{N\pi} \ln\left(\frac{\gamma/\gamma_{\mathrm{SR}}+1}{\gamma/\gamma_{\mathrm{SR}}-1}\right) \qquad \text{for } \gamma > \gamma_{\mathrm{SR}} \,, \tag{6.64}$$

by defining the critical coupling

$$\gamma_{\mathrm{SR}} = \frac{2W}{\pi} \,. \tag{6.65}$$

6.7.2 Long and short-range interaction

In the text, we reported how the gap Δ_{H} changes with the range of the interaction for $\alpha = \{1/3, 1, 5\}$. Here, in Fig. 6.8, we show the dependence of Δ_{H} on γ for some additional values of the range of interaction, namely for $\alpha = \{1/10, 1/2, 3/2, 2\}$. We would like to point out also that the definition (6.36) is equal to $E_2 - E_1$ in the range of γ that we plotted in this figure and in the main text (Fig. 6.6).

As we reported in the Sec. 6.5, in order to obtain the gap Δ_{H} for different range of interaction α, the interaction (6.47) is normalized by the constant $v_{N,\alpha}$ defined as the difference between the maximum eigenenergy and minimal eigenenergy of the matrix V given in Eq. (6.47) without the prefactor $(\gamma/(2v_{N,\alpha}))$, i.e. $v_{N,\alpha} = V_{max} - V_{min}$. In Fig. 6.9 we plot $v_{N,\alpha}$ vs. N for different values of α and we show that the exact results obtained from the diagonalization of V (symbols) fit well the scaling (6.48) for all the values of α shown here.

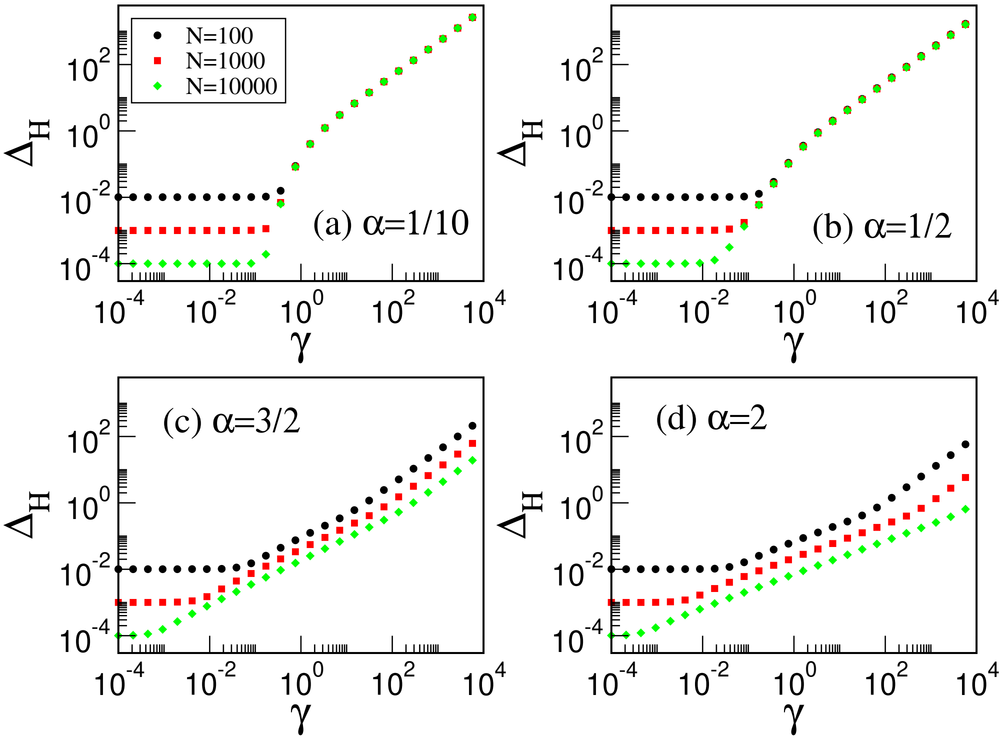

Figure 6.8: a) Gap Δ_{H}, as given by Eq. (6.36), *vs.* the coupling γ with the interaction (6.47) for different values of the interaction range α. Here we set $W = 1$.

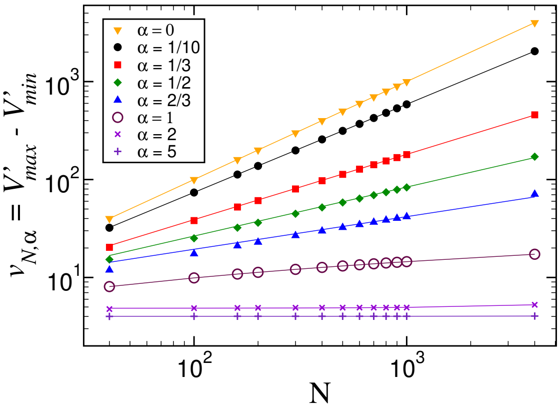

Figure 6.9: The energy range of the interaction $v_{N,\alpha}$ *vs.* the system size N for different $\alpha = \{0, 1/10, 1/3, 1/2, 2/3, 1, 2, 5\}$. Symbols are obtained by diagonalizing V (6.47) without the prefactor $\gamma/(2v_{N,\alpha})$, while lines are the best fits with the functions (6.48).

Chapter 7

Interplay of long-range interactions and disorder in energy transport

In this chapter we study the effect of long-range interactions on the transport properties of a paradigmatic system. The results in this chapter have been accepted for publication on Phys. Rev. Lett. (2021) as Editors' Suggestion and they are available as a preprint at: Nahum C. Chávez, Francesco Mattiotti, J. A. Méndez-Bermúdez, Fausto Borgonovi, and G. Luca Celardo, "Disorder-enhanced and disorder-independent transport with long-range hopping: application to molecular chains in optical cavities", arXiv:2010.08060 (2020). I contributed to this work by setting up the master equation simulations, mapping the master equation approach to the rate equation method, obtaining the average transfer time expression in terms of eigenvalues and eigenvectors of the non-Hermitian Hamiltonian, developing the perturbative approach in the gapped regime and discussing all the results.

Overcoming the detrimental effect of disorder at the nanoscale is very hard since disorder induces localization and an exponential suppression of transport efficiency. Here we unveil novel and robust quantum transport regimes achievable in nanosystems by exploiting long-range hopping. We demonstrate that in a 1D disordered nanostructure in presence of long-range hopping, transport efficiency, after decreasing exponentially with disorder at first, is then enhanced by disorder (Disorder-Enhanced Transport, DET regime) until, counter-intuitively, it reaches a Disorder-Independent Transport (DIT) regime, persisting over several orders of disorder magnitude in realistic systems. To enlighten the relevance of our results, we demonstrate that an ensemble of emitters in a cavity can be described by an effective long-range Hamiltonian. The specific case of a disordered molecular wire placed in an optical cavity is discussed, showing that the DIT and DET regimes can be reached with state-of-the-art experimental set-ups.

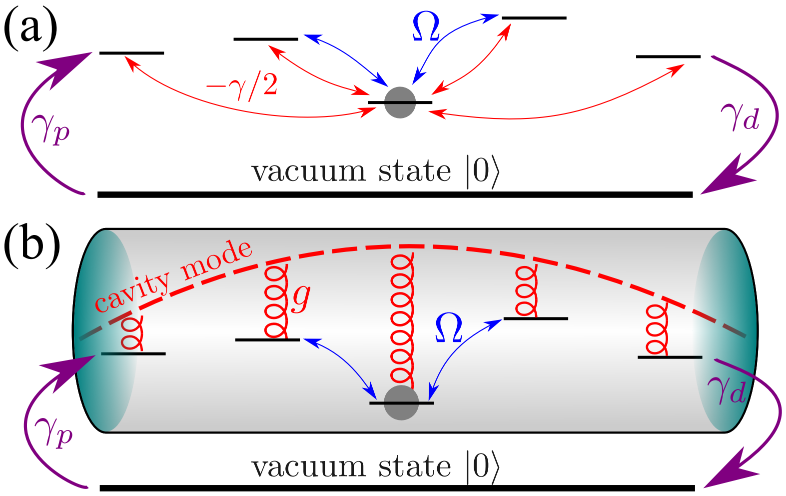

Figure 7.1: (a,b) Two different set-ups for a disordered chain with excitation pumping γ_p at one edge of the chain and draining γ_d at the opposite edge. Here, Ω is the hopping between nearest-neighbor sites. The arrows indicate the hopping paths available for an excitation (grey circle) present at the center of the chain. The energy of the sites is disordered. (a) A long-range coupling $-\gamma/2$ is present between each pair of sites. (b) The chain is placed inside an optical cavity, where g is the coupling of each site to the cavity mode.

7.1 Introduction

Achieving high efficiency for energy/charge transport in quantum wires is fundamental for quantum technologies related to quantum computation and basic energy science [208–218]. One of the main challenges is to control the detrimental effects of noise and disorder which naturally occur in realistic situations. It is well known that disorder induces localization [109, 219] and exponential suppression of transport in typical 1D nanostructures. One of the most ambitious goals in quantum transport is to achieve dissipationless quantum wires, able to transport energy/charge without suffering the detrimental effects of disorder and/or noise.

Here, to overcome disorder suppression of transport, we propose to exploit long-range interactions. Long-range interactions can arise due to microscopic interactions or by engineering the coupling to external degrees of freedom. They have been recently emulated in ion-traps [200] and are relevant in several realistic systems such as cold atomic clouds [151] and excitonic transport in molecular aggregates [3, 91, 117]. Long-range interactions present many contradictory features [178, 202, 220]. Specifically, the interplay of localization and long-range interactions is widely debated in literature [178, 202, 221–227]. Indeed, contrary to the common lore that long-range should destroy Anderson localization [228, 229], strong signatures of localization have been reported recently in long-range interacting systems [202, 221, 222], thus questioning their utility in achieving efficient transport. Here we demonstrate that localized states in long-range interacting systems have a hybrid character, with an exponentially localized peak and extended tail, which allows these states to support robust quantum transport.

Among the most important features of long-range systems, there is the emergence of a gapped ground state [42, 202]. In the gapped regime, while the ground state is extended and robust to disorder, the excited states present a hybrid nature with an exponentially localized peak superimposed to an extended tail [83, 181, 202]. While being very relevant to transport, since they constitute the vast majority of the states, due to their hybrid nature it is not clear what kind of transport they will be able to support. By using different standard figures of merit of transport efficiency, we unveil several regimes directly determined by the hybrid nature of the excited states. Indeed we demonstrate, in presence of long-range hopping, the emergence of extremely robust transport regimes arising as the disorder strength is increased: a Disorder-Enhanced-Transport (DET) regime and, at larger disorder strength, a Disorder-Independent-Transport (DIT) regime, where transport efficiency is independent of disorder over several orders of magnitude of disorder strength. The latter regime persists until disorder is so large to close the energy gap. We can explain the origin of this interesting behaviour by considering that in presence of an energy gap, disorder will mix the excited states, while leaving the ground state fully extended. The presence of an extended ground state imposes an orthogonality condition on the excited states which prevents their full single-site localization and generates an extended tail able to support robust transport over the whole energy spectrum.

In order to highlight the relevance of our findings, we analyze realistic set-ups consisting of an ensemble of emitters inside a cavity, focusing on the case of molecular chains in optical cavities. Recently these systems have been studied experimentally [216] and analyzed theoretically [208, 209, 230]. Here we show that, in the strong coupling regime [36, 40], the cavity induces an effective long-range hopping between the emitters, allowing to test our findings of both DET and DIT regimes in state-of-the-art experimental sets-ups.

7.2 The Model

As a paradigmatic model of a disordered chain in presence of long-range hopping, we analyze the 1D Anderson model [109] with all-to-all hopping [202], see Fig. 7.1(a),

$$H = H_0 + V \quad \text{with} \quad V = -\frac{\gamma}{2}\sum_{i\neq j} |i\rangle\langle j| \,, \tag{7.1}$$

where $|j\rangle$ is the site basis and γ is the strength of the distance-independent long-range hopping. H_0 describes the Anderson model where a particle hops between neighbor sites of a linear chain in the presence of onsite disorder,

$$H_0 = \sum_{j=1}^{N} \epsilon_j |j\rangle\langle j| + \Omega \sum_{j=1}^{N-1} \left(|j\rangle\langle j+1| + |j+1\rangle\langle j|\right), \tag{7.2}$$

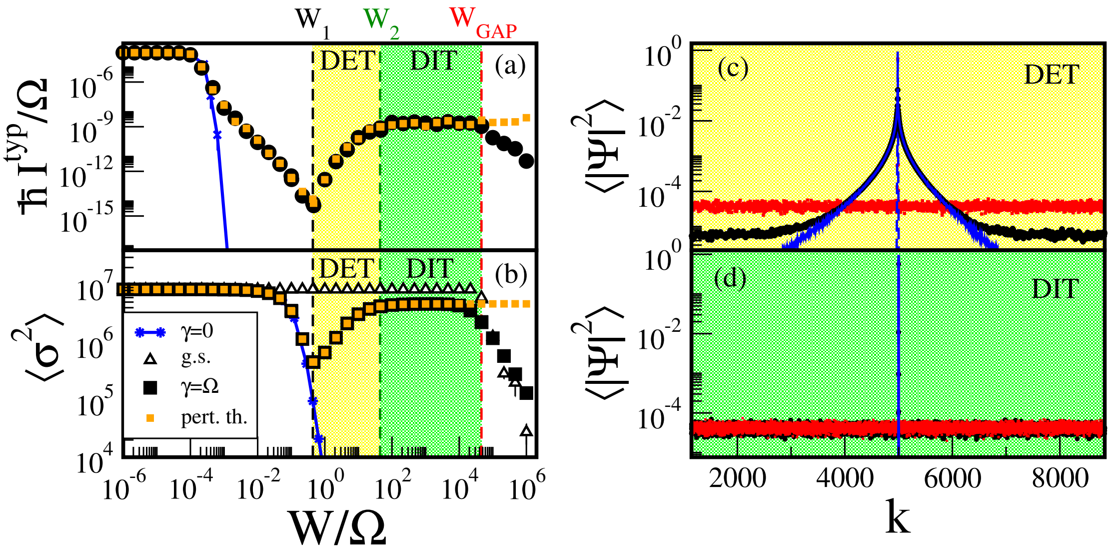

Figure 7.2: (a) Normalized typical current $\hbar I^{\text{typ}}/\Omega$ *vs.* the normalized static disorder W/Ω. (b) Average variance $\langle\sigma^2\rangle$ *vs.* the normalized static disorder W/Ω for the ground state (triangles) and the excited states (all other sets). The blue curves show the case $\gamma = 0$, the orange squares the perturbative approach (details are given in the Appendix). Dashed vertical lines indicate the different critical disorders given by Eqs. (7.3), (7.10) and (7.11). (c,d) Average shape of the eigenfunctions (details concerning the process of averaging are given in Appendix), $\langle|\Psi|^2\rangle$ *vs.* the site basis k. Different disorder regimes are shown: (c) (DET) $W_1 \leq W \leq W_2$, $W/\Omega = 1$ (black) and $W/\Omega = 44.02$ (red); (d) (DIT) $W_2 < W < W_{\text{GAP}}$, $W/\Omega = 10^2$ (black) and $W/\Omega = 10^3$ (red). Here, $N = 10^4$, $\gamma_p = \gamma_d = \gamma = \Omega$ and $N_r = 100$ disorder configurations. In (c,d) symbols are compared with blue curves indicating the case $\gamma = 0$.

where ϵ_i are random energies uniformly distributed in $[-W/2, W/2]$, W is the disorder strength and Ω is the tunneling transition amplitude between nearest neighbor sites.

The eigenstates of the Anderson Model ($\gamma = 0$) are localized exponentially, $\psi_n \sim \exp(-|n - n_0|/\xi)$, where $\xi \approx 105.2\left(\frac{\Omega}{W}\right)^2$ is the localization length in the middle of the energy band. This implies that the transmission always decays exponentially with the disorder strength as $\approx \exp(-N/\xi)$ [231, 232].

In presence of long-range hopping ($\gamma \neq 0$), and in absence of disorder ($W = 0$), the emergence of an energy gap $\Delta = N\gamma/2$ has been found in Refs. [42, 202]. Indeed, the long-range hopping induces the fully symmetric ground state to be gapped from the other excited states. Disorder will destroy the energy gap above the disorder threshold [42] (for details see the Appendix),

$$W_{\text{GAP}} = \frac{\gamma}{2} N \ln N\,. \tag{7.3}$$

In order to understand how transport properties are affected by long-range hopping, we analyze several figures of merit of transport efficiency, focusing on the stationary current widely used in literature [208, 209, 230]. Pumping and draining are introduced at the chain edges, see Fig. 7.1(a) and the dynamics is described by the Lindblad master equation [49]

$$\frac{d\rho}{dt} = -\frac{i}{\hbar}[H,\rho] + \sum_{\eta=p,d} \mathcal{L}_\eta[\rho]\,, \tag{7.4}$$

where $\mathcal{L}_\eta[\rho] = -\{L_\eta^\dagger L_\eta, \rho\} + 2L_\eta \rho L_\eta^\dagger$ are two dissipators inducing pumping on the first site ($L_p = \sqrt{\gamma_p/(2\hbar)}\,|1\rangle\,\langle 0|$) and draining from the last site ($L_d = \sqrt{\gamma_d/(2\hbar)}\,|0\rangle\,\langle N|$), respectively ($|0\rangle$ is the vacuum state). From the steady-state solution of Eq. (7.4) one can find the stationary current

$$I = \frac{\gamma_d}{\hbar}\,\langle N|\,\rho_{SS}\,|N\rangle\ , \tag{7.5}$$

where ρ_{SS} is the steady-state density operator. Since the master equation approach is numerically very expensive, we use a definition of current based on a non-Hermitian Schrödinger equation, computationally less expensive. The results obtained with this approach are identical to the master equation method, as we prove analytically in section 7.6.5 of the Appendix. To define the current, we compute the average time needed to leave the 1D chain if the excitation is initially on the first site $|1\rangle$ and a drain is present on the last site $|N\rangle$. The average transfer time is defined as [233–236]

$$\tau = \frac{\gamma_d}{\hbar}\int_0^\infty dt\, t\,|\Psi_N(t)|^2\,, \tag{7.6}$$

where $\Psi_N(t)$ is the probability amplitude on the drain site at time t, evolved under the effective Hamiltonian H_{eff} [81, 85]

$$(H_{\text{eff}})_{k,l} = (H)_{k,l} - i\,\frac{\gamma_d}{2}\,\delta_{k,N}\delta_{l,N}. \tag{7.7}$$

with H given in Eq. (7.1) and the non-Hermitian term representing the drain. A rate equation can be derived, by assigning a drain frequency $1/\tau$ and a pumping frequency $\gamma_p/\hbar$, connecting the chain population P_e to the vacuum state $|0\rangle$ with population P_0,

$$\begin{aligned} &\frac{dP_0}{dt} = -\frac{\gamma_p}{\hbar}\,P_0 + \frac{1}{\tau}P_e\,,\\ &P_0 + P_e = 1\,. \end{aligned} \tag{7.8}$$

From the steady-state populations $P_e^{SS} = \gamma_p/(\gamma_p + \frac{\hbar}{\tau})$ we obtain the current $I = P_e^{SS}/\tau$ and its typical value,

$$I^{\text{typ}} = e^{\langle \ln I\rangle} \quad \text{with} \quad \langle \ln I\rangle \equiv \left\langle \ln\left(\frac{1}{\tau}\frac{\gamma_p}{\gamma_p + \frac{\hbar}{\tau}}\right)\right\rangle\,, \tag{7.9}$$

where $\langle ...\rangle$ represents the average over disorder configurations.

Another important figure of merit for the transport is the average variance $\langle \sigma^2 \rangle$ of the excited states $|\alpha\rangle$, defined as $\sigma^2 = \frac{1}{N-1} \sum_{\alpha=1}^{N-1} \sigma_\alpha^2$ where $\sigma_\alpha^2 \equiv \langle \alpha | x^2 | \alpha \rangle - \langle \alpha | x | \alpha \rangle^2$. This can be related to the stationary variance obtained from the dynamical spreading of a wave packet initially localized at the center of the chain, see Appendix. Moreover, in the Appendix, we also considered another figure of merit for transport, i.e. the integrated transmission. Transport properties revealed by the three different figures of merit are qualitatively the same.

7.3 Results for long-range systems

In Fig. 7.2(a,b) $\hbar I^{\text{typ}}/\Omega$, see Eq. (7.9), and $\langle \sigma^2 \rangle$ are shown as a function of the normalized disorder strength W/Ω for a chain with $N = 10^4$ sites. For small disorder both quantities decrease with W exponentially, similarly to the Anderson model ($\gamma = 0$, blue curves). Counter-intuitively, by increasing W, the transport efficiency at first increases (DET regime), until it reaches a plateau, where the dependence on the disorder strength is extremely weak for several orders of magnitude of W (DIT regime). The latter persists approximately up to W_{GAP}.

Since the variance $\langle \sigma^2 \rangle$ of the excited eigenstates, Fig. 7.2(b), closely follows the behaviour of the typical current I^{typ}, Fig. 7.2(a), we can try to understand the different transport regimes analyzing the average shape of the eigenfunctions $\langle |\Psi|^2 \rangle$ of the excited states as a function of the site basis k for different disorder strengths W.

Specifically, in presence of long-range hopping [83, 181, 202], in the gapped regime, the excited states have a hybrid nature, with an exponentially localized peak, identical to the Anderson model peak, and extended flat tails, see Fig. 7.2(c,d), where the average shape of the eigenfunctions $\langle |\Psi|^2 \rangle$ in the DET and DIT regimes are shown. Note that, while in the DET regime the tails increase with the disorder strength W, they are independent of it in the DIT regime. Hybrid shapes of the eigenfunctions have been reported in other long-range interacting systems [83, 237].

An analytical expression for the disorder thresholds, separating the different transport regimes, can be found as follows. When the probability of the exponentially localized peak at the chain edges, $\approx \exp(-N/2\xi)$, becomes equal to the average probability in the tails (which scales as $1/N$, see Appendix), we have $\exp\left(-\frac{N}{2\xi}\right) \approx \frac{1}{N}$. Recalling that $\xi \approx 105.2 \left(\frac{\Omega}{W}\right)^2$, we get the disorder threshold W_1,

$$W_1 \approx \sqrt{\frac{210.4 \ln N}{N}}\, \Omega\,. \tag{7.10}$$

For $W > W_1$, the amplitude of the extended tails increases with the disorder strength W, see Fig. 7.2(c), until the eigenfunction tails become independent of W, see Fig. 7.2(d). The disorder threshold W_2 above which this happens can be obtained by imposing that the probability on the closest sites to the peak is equal to the probability in the tails,

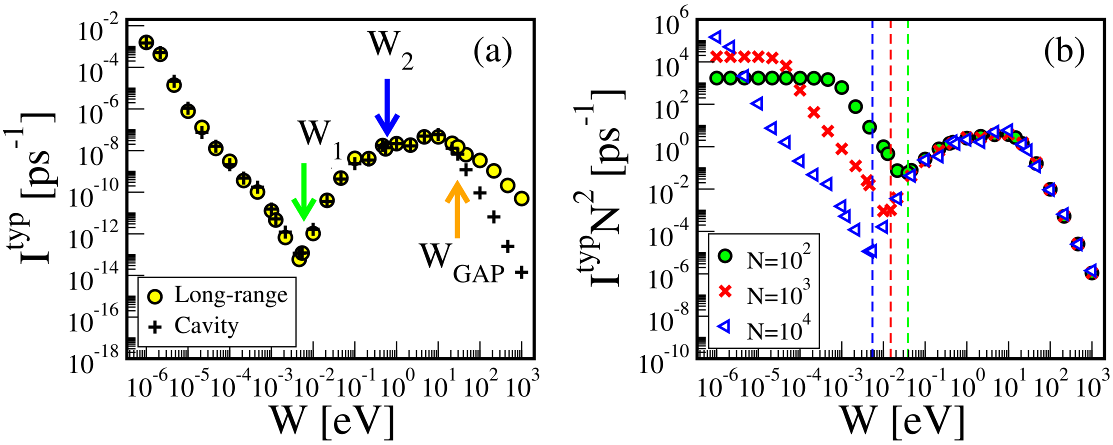

Figure 7.3: (a) Typical current I^{typ}, Eq. (7.9), *vs.* the static disorder W. The results for a linear chain in an optical cavity Eq. (7.12) (crosses) are compared with a long-range hopping model Eq. (7.1) (circles). Parameters for the linear chain in an optical cavity are: $N = 10^4$, $\Omega = 0.0124$ eV, $\hbar\omega_c = 2$ eV, $\mu \approx 36$ D, $g_c = 3.188$ eV, $\gamma_p = \gamma_d = 0.0124$ eV. The long-range hopping model has been obtained using the same Ω value and setting $\gamma = 2g_c/N$ in Eq. (7.1). The number of disorder configurations N_r is such that $N_r \times N = 10^6$. (b) Normalized typical current $I^{\text{typ}}N^2$ *vs.* the static disorder W for a linear chain in an optical cavity for different N values, as indicated in the legend. Vertical dashed lines represent the values of W_1 for different system sizes. Other parameters are the same of panel (a).

$\exp(-1/2\xi) = 1/N$, so that,

$$W_2 \approx \sqrt{210.4 \ln N}\,\Omega\,. \tag{7.11}$$

The validity of the predicted scaling of the different transport regimes with N, γ is discussed here below and also in the Appendix.

One might think that these interesting transport regimes originate from the coupling induced by disorder between the unperturbed excited states and the extended unperturbed ground state. Even if this coupling exists, it is not the main reason for the DET and DIT regimes. Indeed, a semi-analytical perturbative expression for the eigenstates in the gapped regime allows to compute all the relevant observables, see orange dots in Fig. 7.2(a,b), completely neglecting the coupling mediated by disorder between the unperturbed excited states and the extended unperturbed ground state, see details in Appendix. This indicates that the DET and DIT regimes have their origin in the existence of an extended ground state which, by imposing an orthogonality condition on all the excited states, generates their extended tails.

7.4 Applications to molecular chains in optical cavities

Here we show that a chain of emitters in a cavity [208, 209, 230] can be described in terms of an effective long-range hopping model arising from the coupling of the emitters with the cavity mode. This implies that our results are relevant for a vast variety of other systems such as Rydberg atoms, polar molecules and molecular chains [208].

In the following we focus on the case in which the emitters are molecules. This is particularly interesting due to the large coupling (comparable with $k_B T$ with $T = 300\,\mathrm{K}$) between the molecules. Nevertheless the same discussion can be applied to any other kind of emitters. For a molecular chain, at resonance with a cavity mode [208, 230] the Hamiltonian is given by

$$H_{cav} = H_0 + g \sum_{j=1}^{N} \left(|j\rangle \langle c| + |c\rangle \langle j| \right), \tag{7.12}$$

where H_0 is defined in Eq. (7.2) and $|c\rangle$ represents a single excitation in the cavity mode (with no excitation in the chain). The coupling g of the emitters with the resonant optical mode is given by [136]

$$g = \sqrt{\frac{2\pi\mu^2\hbar\omega_c}{V_c}}, \tag{7.13}$$

where μ is the molecular transition dipole, ω_c is the cavity mode frequency and V_c is the cavity mode volume.

Since the coupling to the cavity mode is the same for all molecules, it is possible to show [208, 209] that only the fully symmetric state $|d\rangle$ in the chain is coupled to the cavity mode with a collective coupling strength $g_c = \sqrt{N}g$. This coupling induces two polaritonic states $|p_\pm\rangle = 1/\sqrt{2}\left(|d\rangle \pm |c\rangle\right)$ with an energy splitting of $2g_c$, while the other $N-1$ states with a bandwidth 4Ω, in absence of disorder, are decoupled from the cavity mode. In the strong coupling regime, $g_c \gg \Omega$, one of the polaritonic states will become the ground state of the system and it will be gapped from the excited states by an energy $\approx g_c$. By imposing

$$N\gamma_{\mathrm{eff}}/2 = g_c, \tag{7.14}$$

we determine the effective long-range coupling γ_{eff} which would produce the same energy gap in absence of disorder, see Appendix 7.6.8 for details on the validity of the correspondence between the cavity Hamiltonian (7.12) and the long-range Hamiltonian (7.1).

Since the coupling g is inversely proportional to V_c, see Eq. (7.13), which typically scales like N, in the following we consider a fixed collective coupling $g_c = \sqrt{N}g \approx 3.2$ eV [38, 40], which corresponds to a cavity mode volume $V_c = 10^4\ \mathrm{nm}^3$ [238] for a molecular chain of $N = 10^4$ with $\mu \approx 36$ D [216].

In Fig. 7.3(a) we plot the typical current I^{typ} *vs.* the disorder strength W for a chain of 10^4 molecules in an optical cavity (crosses). Interestingly, this current is reproduced extremely well by the current obtained with the effective long-range coupling Eq. (7.14) (circles) for $W < W_{\text{GAP}}$. For $W > W_{\text{GAP}}$ both polaritonic states mix with all the other states and the differences between the long-range model and the chain in the cavity model emerge. In Fig. 7.3(b) the typical (normalized) current $I^{\text{typ}}N^2$ for the cavity model, Eq. (7.12), is shown for different chain sizes N. Note that $I^{\text{typ}} \propto 1/N^2$ for $W > W_1$, instead of decreasing exponentially with N, as for the localized regime in absence of long-range hopping.

7.5 Conclusions

Controlling the detrimental effects of disorder at the nanoscale is one of the main challenges in achieving efficient energy transport. Here we have shown that long-range hopping can lead to a disorder-enhanced and a disorder-independent transport (DET and DIT) regimes, extending over several orders of magnitude of disorder strength. Our results could be tested in several systems where long-range hopping is present, such as molecular aggregates [85], ion traps [200] and cold atomic clouds [151]. Remarkably, we have also shown that a system of emitters coupled to a cavity mode can be mapped to a long-range hopping system. This makes our results applicable to a vast variety of other physical systems, such as molecular chains in optical cavities, Rydberg atoms and polar molecules [208], see Appendix for realistic parameters. Typically, for molecular chains in optical cavities $\Omega \approx 0.03$ eV, $N \approx 10^5$ and $g_c \approx 1$ eV [208] so that $W_1 \approx 5 \times 10^{-3}$ eV, $W_2 \approx 1.5$ eV and $W_{\text{GAP}} \approx g_c \ln N \approx 11.5$ eV. Since natural disorder typically ranges from $1 - 10\ \Omega$ we can easily reach the DET regime, with currents in the measurable range of tens of nA [216]. In other experimental set-ups, such as ion traps, the spreading of an initially localized excitation in the middle of the chain would provide the best way to access both the DET and DIT regime. Indeed, the stationary variance of the excitation, obtained from the spreading of a localized wave packet, is well described by the average variance of the eigenstates shown in Fig. 7.2(b), see the Appendix for details. In perspective it would be interesting to analyze the effect of thermal noise on transport in long-range systems.

7.6 Appendix

7.6.1 Realistic Parameters for different systems

In the previous sections of this chapters we have shown that long-range hopping can lead to a disorder-enhanced and a disorder-independent transport (DET and DIT) regimes, extending over several orders of magnitude of disorder strength W. We have also shown that a realistic system consisting of a linear chain of emitters in an optical cavity can be mapped to a long-range hopping system. This makes our results applicable to a vast number of physical systems, such as molecular chains, Rydberg atoms, polar molecules and ion traps, to mention a few. Below we give some realistic parameters for the Hamiltionian in Eq. (7.12), with respect to different physical systems. Typically for molecular chains in optical cavities $\Omega \approx 0.03$ eV, $N \approx 10^5$ and $g_c \approx 1$ eV [208] so that $W_1 \approx 5 \times 10^{-3}$ eV, $W_2 \approx 1.5$ eV and $W_{\text{GAP}} \approx g_c \ln N \approx 11.5$ eV. Since natural disorder typically ranges from $1 - 10\ \Omega$ we can easily reach the DET regime. Moreover several other systems consisting of emitters in a cavity could display the same transport properties predicted in this chapter, such as Rydberg atoms [208] for which we have $\Omega \approx 80$ kHz and $\gamma_{\text{eff}} \approx 3$ kHz, polar molecules where $\Omega \approx 50$ Hz and $g \gg \Omega$ or ion traps [200] where $\Omega = 0$ and $\gamma \approx 400$ Hz.

7.6.2 Energy Gap and Long Range Interaction

In the main text of this chapter we have shown that adding long-range hopping to one-dimensional (1D) disordered quantum wires leads to a finite energy gap Δ between the ground state and the excited states which protects the system from disorder [42].

In Fig. 7.4 we plot the energy gap Δ divided by the nearest-neighbor coupling Ω as a function of the coupling strength γ (multiplied by N/Ω) for two values of wire size N and two disorders strengths: $W/\Omega = 100$, Fig. 7.4(a), and $W/\Omega = 1$, Fig. 7.4(b). Here, we compute Δ as [42]

$$\Delta = \max_i \left\{ \min_{j \neq i} \left[\text{dist}\left(E_i, E_j\right) \right] \right\}, \tag{7.15}$$

where $\{E_i\}$ are the eigenvalues of the Hamiltonian

$$H = \sum_{j=1}^{N} \epsilon_j \left| j \right\rangle \left\langle j \right| + \Omega \sum_{j=1}^{N-1} \left(\left| j \right\rangle \left\langle j+1 \right| + \left| j+1 \right\rangle \left\langle j \right| \right) - \frac{\gamma}{2} \sum_{i \neq j} \left| i \right\rangle \left\langle j \right|, \tag{7.16}$$

see Eqs. (7.1)-(7.2), and $\text{dist}\left(E_i, E_j\right) = |E_i - E_j|$.

Note that in Fig. 7.4 we report the average value of Δ over disorder configurations. From Fig. 7.4 we observe that below a critical coupling strength γ_{GAP}, Δ remains constant as a function of $N\gamma$ but decreases for increasing N, while above γ_{GAP}, Δ is an increasing function of $N\gamma$ but it is independent of N. A good approximation for γ_{GAP} can be obtained from the expression for the disorder threshold derived in Ref. [42]

$$W_{\text{GAP}} = \frac{\gamma}{2} N \ln N \tag{7.17}$$

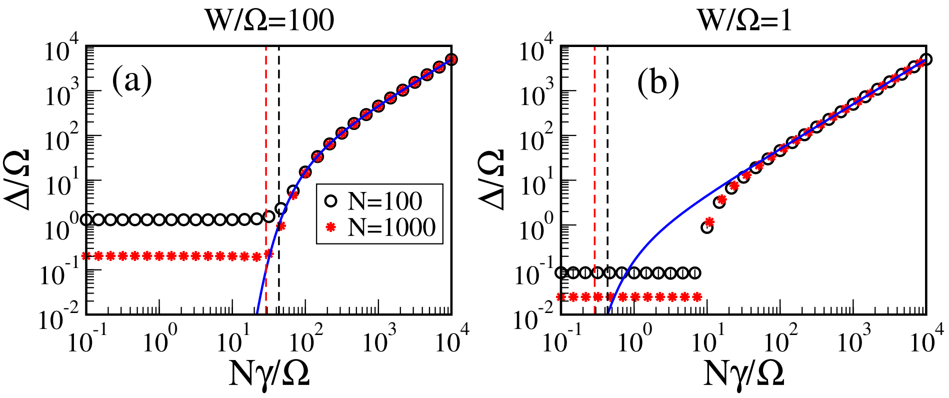

Figure 7.4: Energy gap Δ divided by the nearest-neighbor coupling Ω as a function of $N\gamma/\Omega$ for the disorder strengths (a) $W/\Omega = 100$ and (b) $W/\Omega = 1$. Symbols are given by Eq. (7.15), while the continuous blue curves show the analytical estimate of Eq. (7.19). The dashed vertical lines indicate the critical coupling strength γ_{GAP} from Eq. (7.18). Here, $N = \{100, 1000\}$ and $N_r = 100$ disorder configurations were used.

as

$$\gamma_{\text{GAP}} = \frac{2W}{N \ln N} \,. \tag{7.18}$$

It is relevant to stress that Eq. (7.18) was obtained in Ref. [42] for the Picket-Fence model with all-to-all coupling. The fact that Eq. (7.18) works very well in estimating γ_{GAP} at large disorder strengths W, see the vertical dashed lines in Fig. 7.4(a), allows us to anticipate that the expression

$$\Delta = \frac{W}{e^{2W/N\gamma} - 1} \,, \tag{7.19}$$

also obtained in Ref. [42], may describe well Δ above γ_{GAP} for the 1D Anderson model subject to long-range hopping. Indeed, the good correspondence between Eq. (7.19) (blue-full curve) and the numerically obtained Δ (symbols) is clearly shown in Fig. 7.4(a).

Finally, it is important to add that even if Eq. (7.18) does not provide good predictions for γ_{GAP} for small disorder strengths W/Ω, see Fig. 7.4(b), the analytical expression of Eq. (7.19) still describes well Δ for large $N\gamma$.

7.6.3 Transmission

In the main text of this chapter we analyze two figures of merit to characterize the transport efficiency of 1D disordered quantum wires in presence of long-range hopping: the typical current I^{typ} and the average variance $\langle \sigma^2 \rangle$ of the excited eigenstates. Here we report a third figure of merit: the transmission T, which is widely used in transport studies of low-dimensional disordered quantum systems. We note that according to the experimental set-up either the current as computed in the main text of this chapter

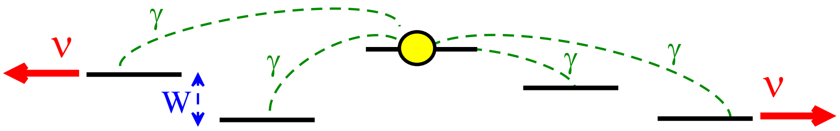

Figure 7.5: Pictorial representation of the scattering setup. The black lines represent the Anderson model spectrum with a random level spacing W while the yellow circle is an excitation which can hop to all the other states with an amplitude γ (green dashed lines). The excitation can then be collected by the leads at the edge sites with an amplitude ν.

or the transmission as discussed here are the relevant figures of merit for transport. Indeed, the integrated transmission T_{int} considered here is relevant in charge transport in presence of a large bias, or when dealing with transmission of an energy broad-band incoming beam.

The transmission through the 1D chain can be studied by turning the setup of Fig. 7.1(a) into a scattering setup. To this end we couple the first and the last sites of the chain (i.e. sites 1 and N) to two different perfect leads with coupling strength ν, so that the components of the *effective* Hamiltonian (i.e. the Hamiltonian of the scattering setup) read [80]

$$(H_{\text{eff}})_{k,l} = (H)_{k,l} - \frac{i}{2}\nu(\delta_{k,1}\delta_{l,1} + \delta_{k,N}\delta_{l,N})\,, \tag{7.20}$$

where H is given in Eq. (7.16). A pictorial representation of the scattering setup is shown in Fig. 7.5, where an excitation which can hop among the chain sites is shown as the yellow circle.

In general, the transmission $T^{a,b}(E)$ from channel a to channel b can be determined by [80]

$$T^{a,b}(E) = |Z^{a,b}(E)|^2\,, \tag{7.21}$$

where

$$Z^{a,b}(E) = \sum_{i,j=1}^{N} A_i^a \left(\frac{1}{E - H_{\text{eff}}}\right)_{i,j} A_j^b \tag{7.22}$$

is the transmission amplitude, H_{eff} is the effective non-Hermitian Hamiltonian in Eq. (7.20) and A_i^a are the decay amplitudes from the discrete internal states i to the external states a. Alternatively, we can also write $T^{a,b}(E)$ by diagonalizing the Hamiltonian H_{eff}. The eigenfunctions of H_{eff}, $|r\rangle$ and $\langle\tilde{r}|$, form a bi-orthogonal complete set,

$$H_{\text{eff}}\,|r\rangle = \mathcal{E}_r\,|r\rangle \ , \qquad \langle\tilde{r}|\,H_{\text{eff}} = \langle\tilde{r}|\,\mathcal{E}_r, \tag{7.23}$$

and its eigenenergies are complex numbers with the form

$$\mathcal{E}_r = E_r - \frac{i}{2}\Gamma_r\,, \tag{7.24}$$

corresponding to resonances centered at the energy E_r with decay widths Γ_r. The decay amplitudes A_i^a are thus transformed according to

$$\mathcal{A}_r^a = \sum_i A_i^a \langle i|r\rangle \,, \quad \tilde{\mathcal{A}}_r^b = \sum_j \langle \tilde{r}|j\rangle \, A_j^b \;\;, \tag{7.25}$$

and the transmission amplitude $Z^{a,b}(E)$ is then given by

$$Z^{a,b}(E) = \sum_{r=1}^{N} \mathcal{A}_r^a \frac{1}{E - \mathcal{E}_r} \tilde{\mathcal{A}}_r^b \,. \tag{7.26}$$

Note that the complex eigenvalues $\mathcal{E}$ of H_{eff} coincide with the poles of the transition amplitude $Z(E)$.

Since the excitation is collected by the leads at the edges of the chain, the amplitudes in Eq. (7.25) are $\mathcal{A}_r^a = \sqrt{\nu}\Psi_r^1$ and $\tilde{\mathcal{A}}_r^b = \sqrt{\nu}\Psi_r^{N*}$, where $\Psi_r^{1,N} = \langle 1, N|r\rangle$ is the amplitude of the eigenfunction $|r\rangle$ of the effective Hamiltonian on sites $1, N$. Moreover, the transmission amplitude $Z^{a,b}(E)$ in Eq. (7.26) becomes

$$Z^{a,b}(E) = \nu \sum_{r=1}^{N} \frac{\Psi_r^1 \Psi_r^{N*}}{E - \mathcal{E}_r} . \tag{7.27}$$

Since the conjugate of the transmission amplitude $Z^{a,b}(E)$ is

$$Z^{a,b}(E)^* = \nu \sum_{k=1}^{N} \frac{\Psi_k^{1*} \Psi_k^{N}}{E - \mathcal{E}_k^*} , \tag{7.28}$$

the transmission $T^{a,b}(E) = |Z^{a,b}(E)|^2 = Z^{a,b}(E) Z^{a,b}(E)^*$ is written as

$$T^{a,b}(E) = \nu^2 \sum_{r=1}^{N} \sum_{k=1}^{N} \frac{\Psi_r^1 \Psi_k^{1*} \Psi_k^N \Psi_r^{N*}}{(E - \mathcal{E}_r)(E - \mathcal{E}_k^*)} \,. \tag{7.29}$$

Now, let us integrate Eq. (7.29) over all the energies, i.e. $T_{\text{int}} = \int_{-\infty}^{\infty} dE \, T^{a,b}(E)$, so we get the expression

$$\begin{aligned} T_{\text{int}} &= \nu^2 \sum_{r=1}^{N} \sum_{k=1}^{N} \Psi_r^1 \Psi_k^{1*} \Psi_k^N \Psi_r^{N*} \int_{-\infty}^{\infty} \frac{dE}{(E - \mathcal{E}_r)(E - \mathcal{E}_k^*)} \\ &= 2\pi\nu^2 \sum_{r=1}^{N} \sum_{k=1}^{N} \frac{\Psi_r^1 \Psi_k^{1*} \Psi_k^N \Psi_r^{N*}}{(\Gamma_r + \Gamma_k)/2 - i(E_k - E_r)} \,. \end{aligned} \tag{7.30}$$

Let us note that Eq. (7.30) is exact and it depends only on the amplitudes of the eigenfunctions at the edges of the chain $\Psi_r^{1,N}$ and the complex eigenvalues $\mathcal{E}_r$ of H_{eff}. The integrated transmission T_{int} represents the overall transmission over a wide spectral energy band and, for instance, is relevant for analyzing the transport under a large applied voltage: the shape of the current-voltage characteristic can sometimes be significantly

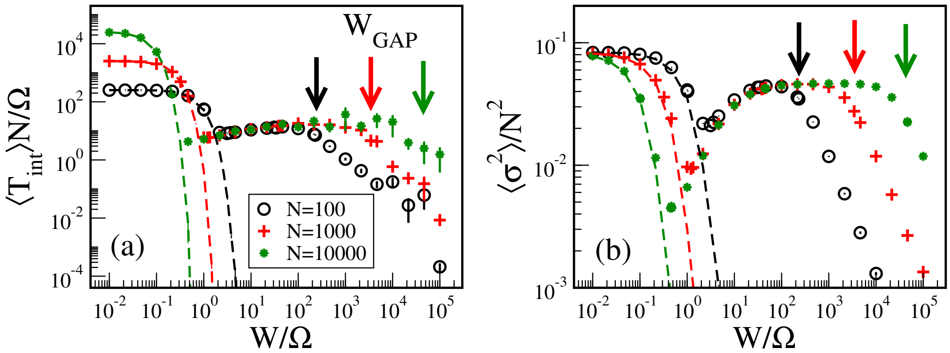

Figure 7.6: (a) Rescaled average integrated transmission $\langle T_{\text{int}}\rangle N/\Omega$ and (b) rescaled average variance $\langle \sigma^2\rangle /N^2$ as a function of the rescaled disorder strength W/Ω for different system sizes N as indicated in the legend. Here, we choose the coupling strength to the leads (a) $\nu = \Omega$ and (b) $\nu = 0$, $\gamma = \Omega$ and the disorder configurations N_r are such that $N_r \times N = 10^5$. Arrows mark the critical disorder W_{GAP} for each system size N according to Eq. (7.17). The dashed (green, red and black) curves show the cases $\gamma = 0$.

different depending on the potential profile or the voltage drop. This is important in determining the maximum current of a transistor [239].

In Fig. 7.6(a) we present the average integrated transmission $\langle T_{\text{int}}\rangle$, multiplied by N/Ω, as a function of the normalized static disorder W/Ω for the coupling strength to the leads $\nu = \Omega$; three wire lengths are reported, i.e. $N = \{100, 1000, 10000\}$. As a reference, we also present the case of the 1D Anderson model without the long-range hopping, i.e. the $\gamma = 0$ case, see the dashed (green, red and black) curves. Interestingly the integrated transmission T_{int} in the DIT regime decays as $1/N$ in contrast to the Anderson model case where it decays exponentially with the system size N. Moreover, by comparing Fig. 7.6(a) with Fig. 7.2, it becomes clear that all the features reported there for the typical current I^{typ} and the average variance $\langle\sigma^2\rangle$ as a function of W are also present in the average integrated transmission $\langle T_{\text{int}}\rangle$. Moreover, in Figs. 7.7(a) and 7.7(c) we plot the curves of $\langle T_{\text{int}}\rangle N/\Omega$ of Fig. 7.6(a) but now as a function of the static disorder W normalized by W_1 and W_2, respectively, see Eqs. (7.10)-(7.11). With this we verify that the estimations for the critical disorders W_1 and W_2 (derived also in the following Section), as given in Eqs. (7.33) and (7.35), respectively, work well for the average integrated transmission $\langle T_{\text{int}}\rangle$.

In addition, for comparison purposes, in Figs. 7.6(b), 7.7(b) and 7.7(d) we present $\langle\sigma^2\rangle /N^2$ for the same parameter values used in Figs. 7.6(a), 7.7(a) and 7.7(c), respectively. $\langle\sigma^2\rangle /N^2$ represents the normalized average variance of the excited eigenstates, defined as

$$\sigma^2 = \frac{1}{N-1}\sum_{\alpha=1}^{N-1}\sigma_\alpha^2 \quad \text{where} \quad \sigma_\alpha^2 \equiv \langle x_\alpha^2\rangle - \langle x_\alpha\rangle^2 \quad \text{and}$$

$$\langle x_\alpha^2\rangle = \sum_i i^2 \mid \langle i|\alpha\rangle \mid^2, \quad \langle x_\alpha\rangle = \sum_i i \mid \langle i|\alpha\rangle \mid^2.$$

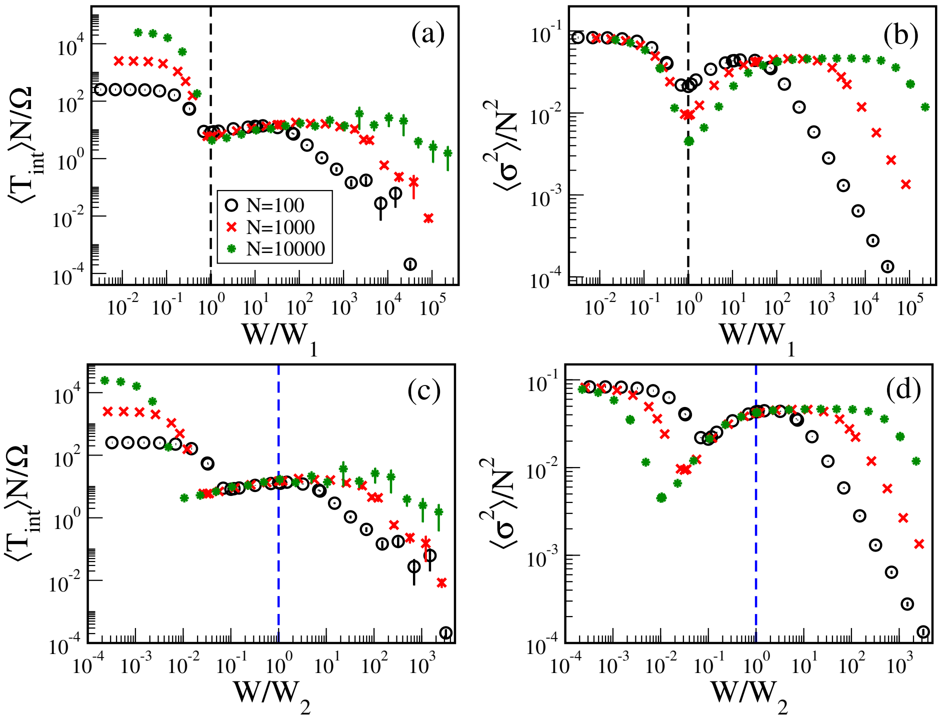

Figure 7.7: (a) Rescaled average integrated transmission $\langle T_{\rm int}\rangle N/\Omega$ and (b) rescaled average variance $\langle\sigma^2\rangle/N^2$ as a function of the normalized static disorder W/W_1. (c) Rescaled average integrated transmission $\langle T_{\rm int}\rangle N/\Omega$ and (d) rescaled average variance $\langle\sigma^2\rangle/N^2$ as a function of the normalized static disorder W/W_2. Vertical dashed lines indicate the critical disorders (a,b) W_1 and (c,d) W_2, which are computed from Eqs. (7.33) and (7.35), respectively. Same parameters of Fig. 7.6 were used.

A good correspondence in the behavior of the curves for the average integrated transmission $\langle T_{\rm int}\rangle$ and the average variance $\langle\sigma^2\rangle$, as a function of W, is clearly observed.

In order to make the two different regimes more explicit, we rescale the disorder strength in the following way: for the DET regime we put on the x-axis the variable

$$W' = (W - W_1)/(W_2 - W_1)$$

so that $W'(W_1) = 0$ and $W'(W_2) = 1$. In this way all data sets with different N in the DET regime have $0 < W' < 1$. As one can see in Fig. 7.8(left panel), in the DET region all the points with different N lie approximately on the same curve. To guide the eye we perform a logarithmic fit, see dashed line in the same panel.

In order to show that the transmission in the DIT regime is approximately constant we perform a similar change of variable, *i.e.*

$$W'' = (W - W_2)/(W_{\rm GAP} - W_2),$$

in such a way that in the DIT regime $0 < W'' < 1$ for all different N. As one can see in Fig. 7.8(right panel), all data sets for different N show that in this regime the transmis-

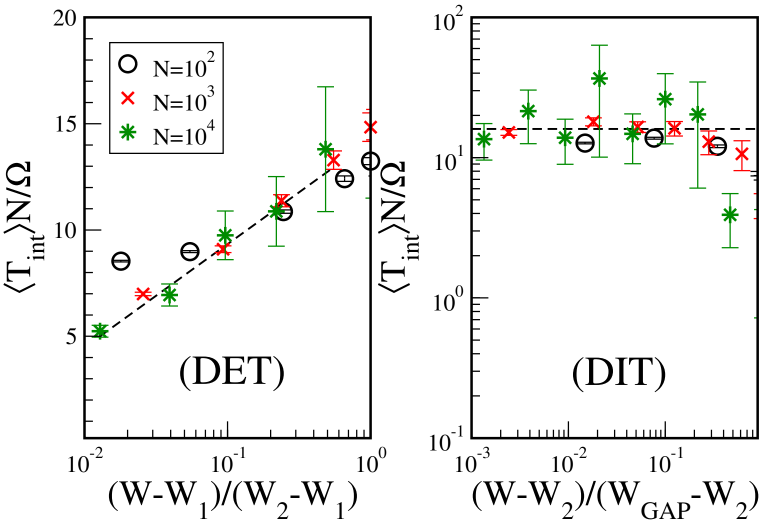

Figure 7.8: Left panel (DET): Rescaled average integrated transmission $\langle T_{\text{int}} \rangle N/\Omega$ *vs.* the rescaled disorder strength $(W - W_1)/(W_2 - W_1)$. The dashed line is a logarithmic fit of all the symbols drawn in order to show the increase of transmission. Right panel (DIT): Rescaled average integrated transmission $\langle T_{\text{int}} \rangle N/\Omega$ *vs.* the rescaled disorder strength $(W - W_2)/(W_{\text{GAP}} - W_2)$. The dashed line is a linear fit of all the symbols drawn in order to show that the transmission is approximately constant. The parameters are the same as in Fig. 7.7. The error bars indicate one standard deviation.

sion is approximately constant. To guide the eye we added a linear fit performed on all the points in this regime (see dashed line).

7.6.4 Shape of Eigenfunctions

Relationship between the shape of eigenfunctions and transport properties

The analysis of the shape of the eigenfunctions is essential to understand the transport properties of the system. Moreover, this analysis will allow us to explain the different transport regimes discussed above and to analytically estimate the different critical disorders discussed in the previous section.

The dependence of the shape of the eigenfunctions on the disorder strength W in our model is much richer than what we have in the Anderson model in absence of long-range hopping. Indeed in the 1D Anderson model, the eigenfunctions are always exponentially localized.

The situation is very different in presence of long-range hopping. For instance, the shape of eigenfunctions in 1D and 3D Anderson models with the addition of all-to-all non-Hermitian couplings have been already analyzed by some of the authors of this manuscript in Ref. [83] and the main results obtained about the shape of eigenfuctions are valid also for our case where the long-range coupling is Hermitian.

Here we analyze the shape of the eigenfunctions in the site basis for different disorder strengths W, fixed γ and N, and no coupling to the leads, i.e. $\nu = 0$. In our numerical experiments, the average shape of the eigenfunctions $\langle|\Psi|^2\rangle$ has been obtained for each disorder configuration as follows:

1. We diagonalize the Hamiltonian given in Eq. (7.1) and reproduced in Eq. (7.16).
2. We consider those eigenfunctions peaked within the 20% of sites around the middle of the chain.
3. We shift the position of the selected eigenfunctions so that all maxima coincide.
4. We determine the average shape of the eigenfunctions $\langle|\Psi|^2\rangle$ by averaging their probability distributions.

In Fig. 7.9 we show the average shape of the eigenfunctions $\langle|\Psi|^2\rangle$ in the site basis k for the coupling strength $\gamma = \Omega$, system size $N = 10^4$ and different disorder strengths W as indicated in the legends. For all disorder strengths W, in each panel, we also show the average shape of the eigenfunctions $\langle|\Psi|^2\rangle$ for the corresponding Anderson model, i.e. with $\gamma = 0$. By analyzing the average shape of the eigenfunctions $\langle|\Psi|^2\rangle$ we can identify the different disorder regimes which are relevant to understand the transport properties of the system, reported in the previous section:

1. ($W < W_1$) For very small disorder strength W, the localization length ξ of the eigenfunctions is larger than the systems size N, so that the eigenfunctions are delocalized. The shape of the eigenfunctions $\langle|\Psi|^2\rangle$ is similar to that of the Anderson model in the absence of long-range coupling, see Fig. 7.9(a). As disorder increases, an exponential peak becomes visible, see Fig. 7.9(b). In this regime the shape of the eigenfunctions $\langle|\Psi|^2\rangle$ is similar to the shape of the eigenfunctions $\langle|\Psi|^2\rangle$ of the 1D Anderson model, up to the threshold strength W_1, as discussed in this chapter. We can define this disorder threshold W_1 taking into consideration that the eigenfuctions of the excited states have a hybrid character as discovered in Ref. [83]. Indeed they present an exponentially localized peak with the same localization length of the 1D Anderson model, and an extended tail which decreases with the system size as $1/N$. Thus, we can estimate the threshold disorder strength for which the eigenfunctions of the Anderson model with long-range hopping will differ from the eigenfuctions of the 1D Anderson model, by finding the disorder strength W for which the probability of the exponentially localized peak at the chain edges becomes comparable to probability in the extended tails. Considering that the extended tails in the gapped regime decrease as $1/N$ and considering that the exponential peak at the chain edges is given by $\exp(-N/2\xi)$, we can determine W_1 by the following equation,

$$\exp\left(-\frac{N}{2\xi}\right) \approx \frac{1}{N} \Rightarrow \quad -\frac{N}{2\xi} \approx -\ln N, \tag{7.31}$$

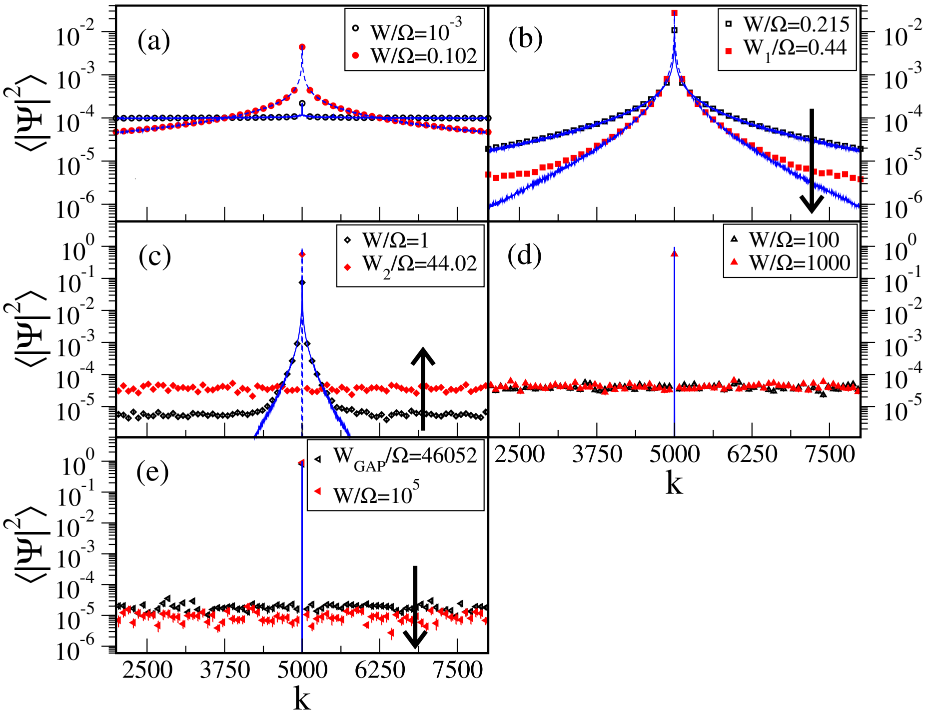

Figure 7.9: Average shape of the eigenfunctions $\langle|\Psi|^2\rangle$ in the site basis k. Different disorder regimes are shown in each panel: (a) $W \leq 0.102\ \Omega$, (b) $0.102\ \Omega < W \leq W_1$, (c) $W_1 < W \leq W_2$, (d) $W_2 < W < W_{\text{GAP}}$ and (e) $W \geq W_{\text{GAP}}$. Here, $N = 10^4$ and $\gamma = \Omega$. The averages are taken over $N_r = 100$ disorder configurations. The continuous lines indicate the corresponding average shape of eigenfunctions $\langle|\Psi|^2\rangle$ for the case $\gamma = 0$. Black arrows indicate increasing W.

where the localization length ξ for $E = 0$ [232] is

$$\xi(E=0) = 105.2\left(\frac{\Omega}{W}\right)^2, \tag{7.32}$$

so that Eq. (7.31) becomes

$$-\frac{N}{210.4}\left(\frac{W_1}{\Omega}\right)^2 \approx -\ln N,$$
$$\Rightarrow W_1 \approx \sqrt{\frac{210.4\ln N}{N}}\,\Omega. \tag{7.33}$$

2. ($W_1 \leq W < W_2$) Above the disorder threshold W_1, the probability of the extended tails increases as the disorder strength W increases, see black arrow in Fig. 7.9(c), and the eigenfunctions change their shape: the probability in the extended tail increases and the peak becomes more localized as the disorder strength W increases. The disorder threshold W_2 can be obtained by imposing the probability

of the closest site to the peak to be equal to the probability in the extended tails. Considering that the tails in the gapped regime decrease as $1/N$, which is independent of the disorder strength W, and that the exponential peak on the closest site is given by $\exp(-1/2\xi)$, we can determine W_2 by the following equation,

$$\exp\left(-\frac{1}{2\xi}\right) \approx \frac{1}{N} \Rightarrow \quad -\frac{1}{2\xi} \approx -\ln N, \tag{7.34}$$

so that Eq. (7.34) becomes

$$-\frac{1}{210.4}\left(\frac{W_2}{\Omega}\right)^2 \approx -\ln N\,,$$
$$\Rightarrow W_2 \approx \sqrt{210.4 \ln N}\,\Omega\,. \tag{7.35}$$

3. ($W_2 \leq W < W_{\rm GAP}$) Above the disorder threshold W_2, the eigenfunctions of the excited states are fully localized and the amplitude of the extended tails is independent of the disorder strength W, see Fig. 7.9(d).

4. ($W \geq W_{\rm GAP}$) Above the critical disorder $W_{\rm GAP}$, the eigenfunctions of the excited states are fully localized on one site with extended tails whose amplitude decreases as the disorder strength W increases, see the vertical black arrow in Fig. 7.9(e).

The analysis of the average shape of the eigenfunctions $\langle|\Psi|^2\rangle$ indicates a strong correlation with the transport properties of the system. Specifically, we observe that the typical current $I^{\rm typ}$, the integrated transmission $T_{\rm int}$ and the variance σ^2 are independent of the disorder strength W in the same disorder range where the extended tails of the average shape of the eigenfunctions $\langle|\Psi|^2\rangle$ are independent, too. Thus, we can claim that the extended tails in the probability distribution of the eigenfunctions support the robustness of transport properties in the gapped regime.

We stress that the analysis of the average shape of the eigenfunctions $\langle|\Psi|^2\rangle$ above also allowed us to determine the disorder thresholds as a function of the model parameters, which define the different transport regimes.

It is relevant to notice that the panorama observed through the three figures of merit we used to characterize the transport efficiency of 1D disordered quantum wires in the presence of long-range hopping (i.e. the typical current $I^{\rm typ}$, the average variance $\langle\sigma^2\rangle$ of the corresponding eigenstates and the integrated transmission $T_{\rm int}$) can be effectively reproduced from the average eigenfunction amplitude of the hybrid states on the extended tails, $\langle|\Psi_{\rm tail}|^2\rangle$. This is shown in Fig. 7.10, where we plot $\langle|\Psi_{\rm tail}|^2\rangle$ as a function of the disorder strength W for hybrid states at the coupling strength $\gamma = \Omega$. $\langle|\Psi_{\rm tail}|^2\rangle$ is computed from a triple average: over the components of the hybrid eigenfunction excluding the exponentially localized peak, over all hybrid eigenfunctions of a disorder wire and over an ensemble of disorder configurations. Indeed, the curve $\langle|\Psi_{\rm tail}|^2\rangle$ *vs.* W of Fig. 7.10 clearly displays all the characteristics of the transport properties, including the disorder-independent regime $W_2 \leq W < W_{\rm GAP}$.

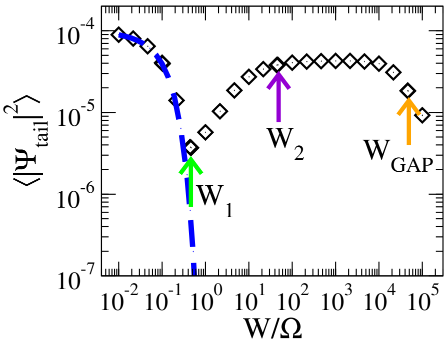

Figure 7.10: Average eigenfunction amplitude on the extended tails of the hybrid states, $\langle|\Psi_{\text{tail}}|^2\rangle$, *vs.* the normalized static disorder W/Ω for the coupling strength $\gamma = \Omega$. Here, $N = 10^4$. The average is performed over $N_r = 10$ disorder configurations. The blue dashed line corresponds to the case $\gamma = 0$. The arrows indicate the different disorders thresholds given by Eqs. (7.17), (7.33) and (7.35).

We also want to remark that the hybrid states plateau has nontrivial statistical properties: the average value of the probability in the plateau goes like $1/N$, while the typical probability value goes like $1/N^2$. By typical probability we mean $\exp\langle\ln|\Psi_{\text{tail}}|^2\rangle$. These two scalings are shown in Fig. 7.21 from the stationary probability distribution obtained by evolving a wave packet initially localized at the center of a linear chain in the DIT regime.

Perturbative approach to the shape of eigenfuctions

Since we demonstrated that the shape of the eigenfunctions allows to understand the transport properties of the system, here we intend to derive a perturbative expression for the shape of the excited eigenfunctions in the gapped regime. For this purpose, we rewrite Eq. (7.16) in its matricial form as follows

$$H = H_0 - \frac{\gamma}{2}Q + \frac{\gamma}{2}I\,, \tag{7.36}$$

where Q is a full matrix with components 1 and I is the identity matrix. The Q matrix can be easily diagonalized. It has only two different eigenvalues. The first eigenvalue, $-\gamma N/2$, corresponding to the lowest energy state, is a fully non degenerated extended state,

$$|d\rangle = \frac{1}{\sqrt{N}}\sum_{j=1}^{N}|j\rangle\,, \tag{7.37}$$

where $|j\rangle$ is the site basis (one excitation on the jth molecule). All the other eigenvalues are zero, corresponding to a $(N-1)$-degenerate subspace spanned by all the states orthogonal to the lowest energy extended state.

Following [240], we can rewrite the Hamiltonian H in Eq. (7.36) in the basis of these eigenstates, using the transformation matrix U, which has as columns the eigenstates of the matrix Q,

$$H = U^T H_0 U - \frac{\gamma}{2} U^T Q U + \frac{\gamma}{2} I = \begin{pmatrix} -\frac{\gamma}{2}(N-1) + \zeta & \vec{h}^T \\ \vec{h} & \tilde{H} \end{pmatrix} . \tag{7.38}$$

Let us note that the component $(1,1)$ of Eq. (7.38) includes the term $\zeta = \sum_n \epsilon_n |\langle n|d\rangle|^2$, where ϵ_n and $|n\rangle$ are, respectively, eigenvalues and eigenvectors of H_0. Here, the matrix elements of the $(N-1) \times (N-1)$ submatrix $\tilde{H}$ on the basis of the excited states of the matrix Q are

$$\begin{aligned} \tilde{H}_{\mu\nu} &= \langle \mu | H_0 - \frac{\gamma}{2} Q + \frac{\gamma}{2} I | \nu \rangle \\ &= \langle \mu | H_0 | \nu \rangle - \langle \mu | \frac{\gamma}{2} Q | \nu \rangle + \frac{\gamma}{2} \delta_{\mu\nu} \, ; \end{aligned}$$

here the second term vanishes since the eigenvalues of the degenerate excited states of Q are 0. If we rewrite the Hamiltonian H_0 in its eigenbasis $|n\rangle$, we get

$$\begin{aligned} \tilde{H}_{\mu\nu} &= \langle \mu | \left(\sum_n \epsilon_n \, |n\rangle \, \langle n| \right) |\nu\rangle + \frac{\gamma}{2} \delta_{\mu\nu} \\ &= \sum_n \epsilon_n \, \langle \mu | n \rangle \, \langle n | \nu \rangle + \frac{\gamma}{2} \delta_{\mu\nu} \, . \end{aligned} \tag{7.39}$$

The components of the vector $\vec{h}$, with dimension $N-1$, in the basis of the eigenstates of the matrix Q are

$$h_\mu = \sum_n \epsilon_n \, \langle d | n \rangle \, \langle n | \mu \rangle \ . \tag{7.40}$$

The $|\mu\rangle$ eigenstates of $\tilde{H}$ are also eigenstates of Q since they belong to the $(N-1)$-degenerate subspace of the Q matrix. Thus, we diagonalize the submatrix $\tilde{H}$ and we call $|\mu\rangle$ its eigenstates with eigenvalues $\tilde{\epsilon}_\mu$, i.e.

$$\tilde{H}_{\mu\nu} = \tilde{\epsilon}_\mu \delta_{\mu\nu}. \tag{7.41}$$

If we multiply Eq. (7.39) by the components $\langle m|\mu'\rangle$, where $|\mu'\rangle$ is an eigenstate of the submatrix $\tilde{H}$ and $|m\rangle$ is an eigenstate of H_0, and we sum over all the states μ', we obtain

$$\begin{aligned}
\sum_{\mu'} \tilde{H}_{\mu'\mu} \langle m|\mu'\rangle &= \sum_{\mu'}\sum_{n} \epsilon_n \langle \mu'|n\rangle \langle n|\mu\rangle \langle m|\mu'\rangle + \frac{\gamma}{2}\sum_{\mu'} \delta_{\mu'\mu} \langle m|\mu'\rangle \\
&= \sum_{n} \epsilon_n \langle n|\mu\rangle \langle m| \left(\sum_{\mu'} |\mu'\rangle \langle \mu'|\right) |n\rangle + \frac{\gamma}{2} \langle m|\mu\rangle \\
&= \sum_{n} \epsilon_n \langle n|\mu\rangle \langle m| \left(I - |d\rangle \langle d|\right) |n\rangle + \frac{\gamma}{2} \langle m|\mu\rangle \\
&= \sum_{n} \epsilon_n \langle n|\mu\rangle \left(\delta_{mn} - \langle m|d\rangle \langle d|n\rangle\right) + \frac{\gamma}{2} \langle m|\mu\rangle \\
&= (\epsilon_m + \frac{\gamma}{2}) \langle m|\mu\rangle - \sum_{n} \epsilon_n \langle d|n\rangle \langle n|\mu\rangle \langle m|d\rangle \\
&= (\epsilon_m + \frac{\gamma}{2}) \langle m|\mu\rangle - h_\mu \langle m|d\rangle \ . \qquad (7.42)
\end{aligned}$$

On the other hand, from Eq. (7.41) we have

$$\sum_{\mu'} \tilde{H}_{\mu'\mu} \langle m|\mu'\rangle = \sum_{\mu'} \tilde{\epsilon}_{\mu'} \delta_{\mu'\mu} \langle m|\mu'\rangle = \tilde{\epsilon}_\mu \langle m|\mu\rangle \ . \qquad (7.43)$$

By comparing Eqs. (7.42) and (7.43), we obtain

$$\tilde{\epsilon}_\mu \langle m|\mu\rangle = (\epsilon_m + \frac{\gamma}{2}) \langle m|\mu\rangle - h_\mu \langle m|d\rangle \ , \qquad (7.44)$$

i.e.,

$$|\mu\rangle = \frac{h_\mu}{H_0 + \gamma/2 - \tilde{\epsilon}_\mu} |d\rangle \ . \qquad (7.45)$$

Equation (7.45) can be rewritten in the Anderson basis as follows

$$|\mu\rangle = h_\mu \sum_n \frac{\langle n|d\rangle}{\epsilon_n + \gamma/2 - \tilde{\epsilon}_\mu} |n\rangle = \frac{h_\mu}{\sqrt{N}} \sum_n \frac{\sum_j \langle n|j\rangle}{\epsilon_n + \gamma/2 - \tilde{\epsilon}_\mu} |n\rangle \ , \qquad (7.46)$$

where $|j\rangle$ is the site basis and the normalization coefficients h_μ are given by

$$h_\mu = \left(\sum_n \frac{\langle d|n\rangle \langle n|d\rangle}{(\epsilon_n + \gamma/2 - \tilde{\epsilon}_\mu)^2} \right)^{-1/2} . \qquad (7.47)$$

In the gapped regime and for sufficiently large disorder $W_2 < W < W_{\mathrm{GAP}}$, where the eigenstates have a hybrid nature, we can assume that the Anderson eigenstates coincide with the site basis, see Fig. 7.9(d). So, Eq. (7.46) with the normalization coefficients h_μ in Eq. (7.47) becomes

$$\begin{aligned}
|\mu\rangle &\approx \left(\frac{1}{N} \sum_i \frac{1}{(\epsilon_i + \gamma/2 - \tilde{\epsilon}_\mu)^2} \right)^{-1/2} \frac{1}{\sqrt{N}} \sum_i \frac{1}{\epsilon_i + \gamma/2 - \tilde{\epsilon}_\mu} |i\rangle \\
&\approx \left(\sum_i \frac{1}{\left(\frac{\epsilon_i - \tilde{\epsilon}_\mu}{W} + \frac{\gamma}{2W}\right)^2} \right)^{-1/2} \sum_i \frac{1}{\frac{\epsilon_i - \tilde{\epsilon}_\mu}{W} + \frac{\gamma}{2W}} |i\rangle \ . \qquad (7.48)
\end{aligned}$$

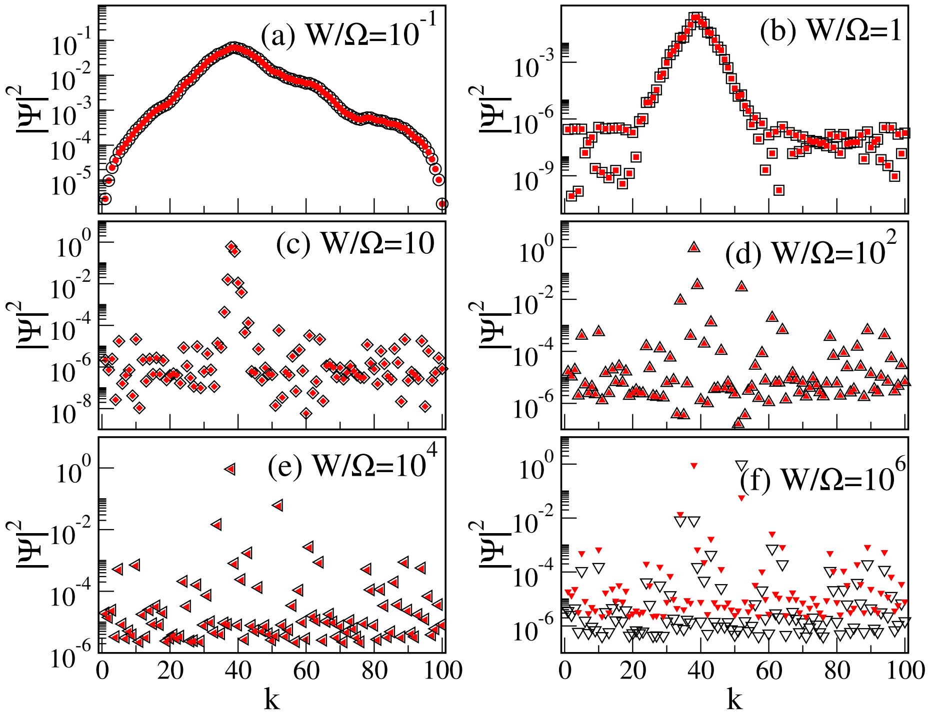

Figure 7.11: Eigenfunction probability $|\Psi|^2$ in the site basis k for the first excited state (of a single disorder configuration) with disorder strengths $W/\Omega = \{10^{-1}, 1, 10, 10^2, 10^4, 10^6\}$. Here, $N = 100$ and $\gamma = 10^3\Omega$. The black symbols represent the exact eigenfunctions of the total Hamiltonian H of Eq. (7.16) and the red symbols are the $|\mu\rangle$ states obtained from Eq. (7.46).

Our perturbative expression allows to explain many features of the average shape of the eigenfunctions $\langle |\Psi|^2 \rangle$ discussed above, mainly the existence of a disorder-independent plateau in the disorder range $W_2 < W < W_{\mathrm{GAP}}$. From Eq. (7.48) we can see that both the normalization coefficients and the weights on the site basis are independent of disorder for $W \gg \gamma$ since both ϵ_i and $\tilde{\epsilon}_\mu$ are proportional to the disorder strength W for large disorder. This is an important result since our perturbative approach is able to explain the independence of the plateau from disorder in the disorder regime $W_2 < W < W_{\mathrm{GAP}}$. That is, since the disorder strength W is uncorrelated from the site basis, the eigenfunction tail becomes a plateau that extends over the entire basis. Moreover, since the term $\frac{(\epsilon_i - \tilde{\epsilon}_\mu)}{W}$ decreases as $1/N$, this also explains the dependence of the probability of the extended tails on the system size for $W \gg \gamma$.

Finally, to validate the perturbative derivation of the $|\mu\rangle$ states above, in Fig. 7.11 we present the eigenfunction probability $|\Psi|^2$, in the site basis k, for the first excited state at several disorder strengths W. In each panel we show the exact eigenfunction of the total Hamiltonian H of Eq. (7.16) (black symbols) and the $|\mu\rangle$ state obtained from Eq. (7.46) (red symbols). In all panels from (a) to (e) we see an excellent correspondence between the exact and the $|\mu\rangle$ state. Note that since $W_{\mathrm{GAP}} \approx 230258$ for the parameter chosen in Fig. 7.11, we cannot expect agreement in panel (f).

Using the perturbative expressions of the eigenstates obtained in Eqs. (7.37) and (7.46) we can compute both the current through Eq. (7.52) and the variance. The results are shown in Fig. 7.2(a,b), see orange squares.

7.6.5 Master Equation *vs.* Schrödinger equation approach to compute the current

In the main text of this chapter we report the transport properties of two models: the 1D Anderson model subject to long-range hopping and a disordered molecular wire placed in an optical cavity. For both systems we report the stationary current as the main figure of merit to characterize transport. However, the standard master equation approach (see Eqs. (7.4)-(7.5)) is numerically very expensive to compute the stationary current through long wires. For this reason, we use a different definition of current that is based on a non-Hermitian Schrödinger Equation (see Eqs. (7.6)-(7.9)) which is computationally less expensive. Here we add some details about the non-Hermitian Schrödinger Equation approach and we analytically prove the identity between the two definitions of the current.

Non-Hermitian Schrödinger equation approach

The non-Hermitian Schrödinger Equation approach described above in the chapter (see Eqs.(7.6)-(7.9)) is based on the calculation of the average escape time from the chain, when the excitation is initialized on the site $|1\rangle$ and in presence of a drain at site $|N\rangle$. Such drain is described by the effective Hamiltonian (see Eq. (7.7))

$$(H_{\mathrm{eff}})_{k,l} = (H)_{k,l} - i\,\frac{\gamma_d}{2}\,\delta_{k,N}\delta_{l,N}, \tag{7.49}$$

where H is the Hamiltonian from Eq. (7.16) and $\delta_{k,N}$ is the Kronecker delta.

The average transfer time τ is defined as (see Eq. (7.6))

$$\tau = \frac{\gamma_d}{\hbar} \int_0^\infty dt\, t\, |\Psi_N(t)|^2, \tag{7.50}$$

with $\Psi_N(t) = \langle N| e^{-iH_{\text{eff}}t/\hbar} |1\rangle$ being the probability amplitude on the drain site of a time-evolved wave function at time t, under the effective Hamiltonian H_{eff} of Eq. (7.49). The integral in Eq. (7.50) can be evaluated analytically by expanding $e^{-iH_{\text{eff}}t/\hbar}$ on the eigenbasis of H_{eff} which, being non-Hermitian, has right and left eigenvectors,

$$H_{\text{eff}} |r_k\rangle = \varepsilon_k |r_k\rangle \qquad \text{and} \qquad \langle \tilde{r}_k| H_{\text{eff}} = \langle \tilde{r}_k| \varepsilon_k \,. \tag{7.51}$$

The average transfer time τ is therefore

$$\tau = \hbar\gamma_d \sum_{k,k'} \frac{\langle N|r_k\rangle \langle \tilde{r}_k|1\rangle \langle N|r_{k'}\rangle^* \langle \tilde{r}_{k'}|1\rangle^*}{-(\varepsilon_k - \varepsilon_{k'}^*)^2} \,, \tag{7.52}$$

it depends only on the eigenvalues and eigenvectors of H_{eff} and it is used in Eqs. (7.8)-(7.9) to compute the steady-state current.

Exact mapping between master equation and Schrödinger equation approaches

Here we consider the master equation, Eq. (7.4), and we prove that the steady-state current, defined in Eq. (7.5), is identical to the Schrödinger equation result, see Eq. (7.9). The master equation, Eq. (7.4), is written explicitly as

$$\begin{aligned}\frac{d\rho}{dt} = &-\frac{i}{\hbar}(H\rho - \rho H) - \frac{\gamma_d}{2\hbar}\left(|N\rangle \langle N| \rho + \rho |N\rangle \langle N|\right) + \frac{\gamma_d}{\hbar}\rho_{NN} |0\rangle \langle 0| \\ &- \frac{\gamma_p}{2\hbar}\left(|0\rangle \langle 0| \rho + \rho |0\rangle \langle 0|\right) + \frac{\gamma_p}{\hbar}\rho_{00} |1\rangle \langle 1| \,,\end{aligned} \tag{7.53}$$

where H is a generic hermitian Hamiltonian acting on the single-excitation subspace, $\gamma_d/\hbar$ is the drain rate from the site $|N\rangle$, $\rho_{NN} = \langle N|\rho|N\rangle$ is the population of the site $|N\rangle$, $|0\rangle$ is the vacuum state, $\gamma_p/\hbar$ is the pumping rate on the site $|1\rangle$ and $\rho_{00} = \langle 0|\rho|0\rangle$ is the population of the vacuum state. First, we note that Eq. (7.53) can be written in terms of the effective Hamiltonian, Eq. (7.49), and it reads

$$\frac{d\rho}{dt} = -\frac{i}{\hbar}\left(H_{\text{eff}}\rho - \rho H_{\text{eff}}^\dagger\right) + \frac{\gamma_d}{\hbar}\rho_{NN} |0\rangle \langle 0| - \frac{\gamma_p}{2\hbar}\left(|0\rangle \langle 0| \rho + \rho |0\rangle \langle 0|\right) + \frac{\gamma_p}{\hbar}\rho_{00} |1\rangle \langle 1| \,. \tag{7.54}$$

We want to compute the steady-state current, which is defined in Eq. (7.5) as

$$I = \frac{\gamma_d}{\hbar} \langle N|\rho^{(ss)}|N\rangle \,, \tag{7.55}$$

where $\rho^{(ss)}$ is the steady-state density matrix, that we obtain by setting $\frac{d\rho}{dt} = 0$ in Eq. (7.54). First, we set the derivative of the vacuum state population to zero, *i.e.*

$$\frac{d}{dt} \langle 0|\rho^{(ss)}|0\rangle = \frac{\gamma_d}{\hbar}\rho_{NN}^{(ss)} - \frac{\gamma_p}{\hbar}\rho_{00}^{(ss)} = 0 \,, \tag{7.56}$$

where we used the fact that H_{eff} acts only on the single-excitation subspace, *i.e.* $H_{\text{eff}} \left|0\right\rangle = 0$. From Eq. (7.56) we have $\gamma_d \rho_{NN}^{(ss)} = \gamma_p \rho_{00}^{(ss)}$, so that the steady-state current, Eq. (7.55) can be expressed as

$$I = \frac{\gamma_d}{\hbar} \rho_{NN}^{(ss)} = \frac{\gamma_p}{\hbar} \rho_{00}^{(ss)} \, . \tag{7.57}$$

Now we proceed to compute $\rho_{00}^{(ss)}$, and we use the fact that the total trace of the density matrix must be unity, *i.e.*

$$\text{Tr}[\rho^{(ss)}] = \rho_{00}^{(ss)} + \sum_j \langle j|\rho^{(ss)}|j\rangle = 1 \, , \tag{7.58}$$

where the states $|j\rangle$ form a generic orthonormal basis on the single-excitation subspace. Now, we recall that the eigenstates of the effective Hamiltonian H_{eff}, see Eq. (7.51), form a biorthogonal basis, *i.e.* $\langle \tilde{r}_k | r_{k'} \rangle = \delta_{k,k'}$. This allows to decompose the identity (on the single-excitation subspace) as

$$\text{Id}_{\text{s.e.s.}} = \sum_k |r_k\rangle \langle \tilde{r}_k| = \sum_k |\tilde{r}_k\rangle \langle r_k| \, . \tag{7.59}$$

Using the above decompositions, we can express the sum over j in Eq. (7.58) as

$$\sum_j \langle j|\rho^{(ss)}|j\rangle = \sum_j \sum_k \sum_{k'} \langle j|r_k\rangle \langle \tilde{r}_k|\rho^{(ss)}|\tilde{r}_{k'}\rangle \langle r_{k'}|j\rangle = \sum_k \sum_{k'} \langle r_{k'}|r_k\rangle \langle \tilde{r}_k|\rho^{(ss)}|\tilde{r}_{k'}\rangle \, . \tag{7.60}$$

Here above we also used the fact that $|j\rangle$ is an orthonormal basis on the single-excitation subspace, so that it is possible to decompose the scalar product $\langle r_k|r_{k'}\rangle = \sum_j \langle r_{k'}|j\rangle \langle j|r_k\rangle$. Note that the eigenstates $|r_k\rangle$ are not orthonormal, so that $\langle r_k|r_{k'}\rangle \neq 0$ for $k \neq k'$. Specifically, we can compute $\langle r_k|r_{k'}\rangle$ as follows. From the non-Hermitian Hamiltonian, see Eq. (7.49), we have the identity

$$H_{\text{eff}} - H_{\text{eff}}^{\dagger} = -i\gamma_d \left|N\right\rangle \left\langle N\right| \, . \tag{7.61}$$

If we take the expectation value of both sides of the above equation between $\langle r_{k'}| \ldots |r_k\rangle$, using Eq. (7.49), we obtain

$$(\varepsilon_k - \varepsilon_{k'}^*) \langle r_{k'}|r_k\rangle = -i\gamma_d \langle r_{k'}|N\rangle \langle N|r_k\rangle \tag{7.62}$$

from which we have

$$\langle r_{k'}|r_k\rangle = \frac{\gamma_d \langle r_{k'}|N\rangle \langle N|r_k\rangle}{i\left(\varepsilon_k - \varepsilon_{k'}^*\right)} \, . \tag{7.63}$$

Now, to evaluate Eq. (7.60), we proceed to compute $\langle \tilde{r}_k|\rho^{(ss)}|\tilde{r}_{k'}\rangle$ by setting $\frac{d\rho}{dt} = 0$. Specifically, from Eq. (7.54), using Eq. (7.49), we obtain

$$\frac{d}{dt} \langle \tilde{r}_k|\rho^{(ss)}|\tilde{r}_{k'}\rangle = -\frac{i}{\hbar} (\varepsilon_k - \varepsilon_{k'}^*) \langle \tilde{r}_k|\rho^{(ss)}|\tilde{r}_{k'}\rangle + \frac{\gamma_p}{\hbar} \rho_{00}^{(ss)} \langle \tilde{r}_k|1\rangle \langle 1|\tilde{r}_{k'}\rangle = 0 \, , \tag{7.64}$$

from which we have

$$\langle \tilde{r}_k | \rho^{(ss)} | \tilde{r}_{k'} \rangle = \gamma_p \rho_{00}^{(ss)} \frac{\langle \tilde{r}_k | 1 \rangle \langle 1 | \tilde{r}_{k'} \rangle}{i \left(\varepsilon_k - \varepsilon_{k'}^* \right)} . \tag{7.65}$$

Now, we substitute Eq. (7.63) and Eq. (7.65) into Eq. (7.60) and obtain

$$\sum_j \langle j | \rho^{(ss)} | j \rangle = \frac{\gamma_p \rho_{00}^{(ss)}}{\hbar} \left[\hbar \gamma_d \sum_{k,k'} \frac{\langle r_{k'} | N \rangle \langle N | r_k \rangle \langle \tilde{r}_k | 1 \rangle \langle 1 | \tilde{r}_{k'} \rangle}{- \left(\varepsilon_k - \varepsilon_{k'}^* \right)^2} \right] . \tag{7.66}$$

Note that the term inside square brackets is equal to the average transfer time τ, see Eq. (7.52), *i.e.*

$$\sum_j \langle j | \rho^{(ss)} | j \rangle = \frac{\gamma_p \tau \rho_{00}^{(ss)}}{\hbar} . \tag{7.67}$$

Therefore, by substituting Eq. (7.67) into Eq. (7.58) we obtain

$$\rho_{00}^{(ss)} + \frac{\gamma_p \tau}{\hbar} \rho_{00}^{(ss)} = 1 , \tag{7.68}$$

from which we obtain the steady-state value of the population of the vacuum state,

$$\rho_{00}^{(ss)} = \frac{1}{1 + \frac{\gamma_p \tau}{\hbar}} . \tag{7.69}$$

Finally, we substitute Eq. (7.69) into Eq. (7.57) and we have

$$I = \frac{\gamma_p}{\gamma_p \tau + \hbar} , \tag{7.70}$$

which is exactly the value of the steady-state current that we obtained with the non-Hermitian Schrödinger equation approach, see Eq. (7.9). Note that in our calculations we did not specify the nature of the hermitian Hamiltonian H, so our results work for a general open quantum system in the single-excitation approximation, with incoherent pumping of excitation on one state of the system (state $|1\rangle$) and incoherent draining of excitation from another state (state $|N\rangle$).

In the following, we compare analytical with numerical results, and we show that the master equation approach gives a steady-state current identical to that obtained via the Schrödinger equation.

In Fig. 7.12 we plot the current multiplied by $\hbar/\Omega$ as a function of the normalized static disorder W/Ω for the long-range Hamiltonian, on a chain of $N = 40$ sites, from both approaches: the master equation approach (black symbols) and the non-Hermitian Schrödinger equation approach (red symbols). We are limited to consider a short chain of $N = 40$ sites because the master equation approach is numerically very expensive. Moreover, we set an unusually large value of the long-range coupling ($\gamma = 10\,\Omega$), to ensure that the disorder threshold W_{GAP} (see Eq. (7.17)) is larger than the disorder threshold W_1 (see Eq. (7.33)) even for such a small system size. Specifically, in the panels of Fig. 7.12 we report: the average $\langle I \rangle$, Fig. 7.12(a); the typical I^{typ},

Fig. 7.12(b); the maximal I_{max}, Fig. 7.12(c) and the minimal I_{min} currents, Fig. 7.12(d); all of them are multiplied by $\hbar/\Omega$. In all cases, we observe a perfect match between the two approaches, thus validating the use of the non-Hermitian Schrödinger equation approach in this chapter. Note that the large error bar for the average current, Fig. 7.12(a), present for $W > 10^5\Omega$ can be explained by an anomalously large value of the current in one of the 100 disorder realizations used to produce the figure, as we verified. Probably, a larger number of realizations would fix this problem, but we are not interested in that since our main results are about the typical current, which is self-averaging and does not present this problem, see Fig. 7.12(b).

Moreover, in Fig. 7.13 we report the normalized average current $\hbar\langle I\rangle/\Omega$ from the master equation approach (black symbols) and the non-Hermitian Schrödinger equation approach (red symbols) as a function of the normalized pumping rate γ_p/Ω (for fixed γ_d), see Fig. 7.13(a), and of the normalized draining rate γ_d/Ω (for fixed γ_p), see

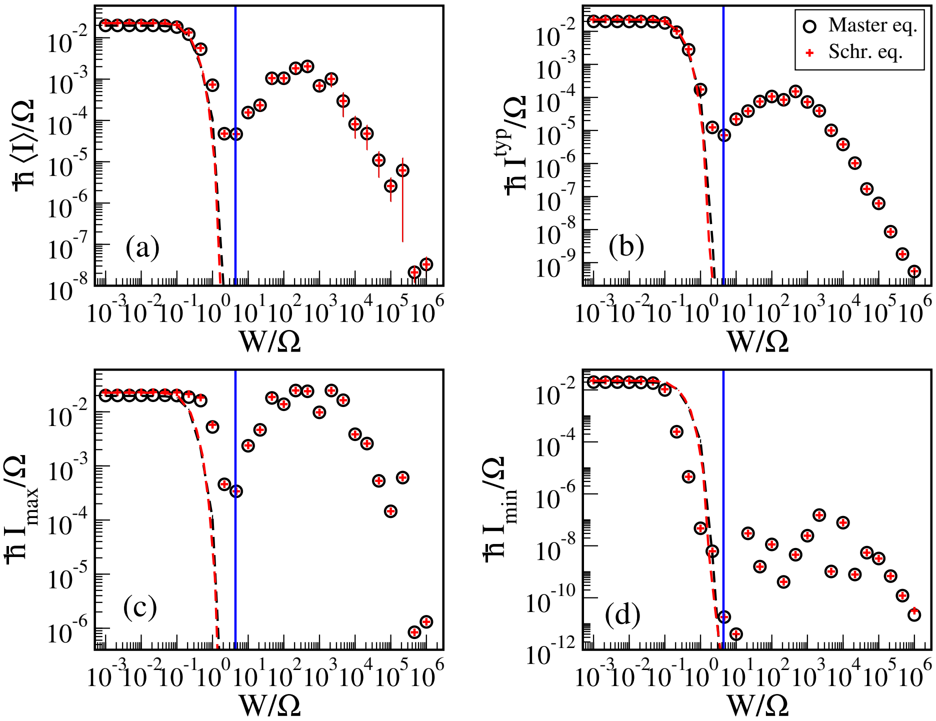

Figure 7.12: (a) Average $\langle I\rangle$, (b) typical $I^{\rm typ}$, (c) maximal I_{max} and (d) minimal I_{min} currents, multiplied by $\hbar/\Omega$, as a function of the normalized static disorder W/Ω for the long-range Hamiltonian, Eq. (7.16). The stationary current is computed with the master equation approach (open circles), see Eqs. (7.4)-(7.5), and with the non-Hermitian Schrödinger equation equation approach (red crosses), see Eqs. (7.6)-(7.9). Here, $N = 40$, $\gamma_d = \gamma_p = \Omega$, $\gamma = 10\,\Omega$. The averages are taken over $N_r = 100$ disorder configurations. The dashed curves indicate the case $\gamma = 0$. Vertical blue lines indicate the critical disorder W_1 given by Eq. (7.33).

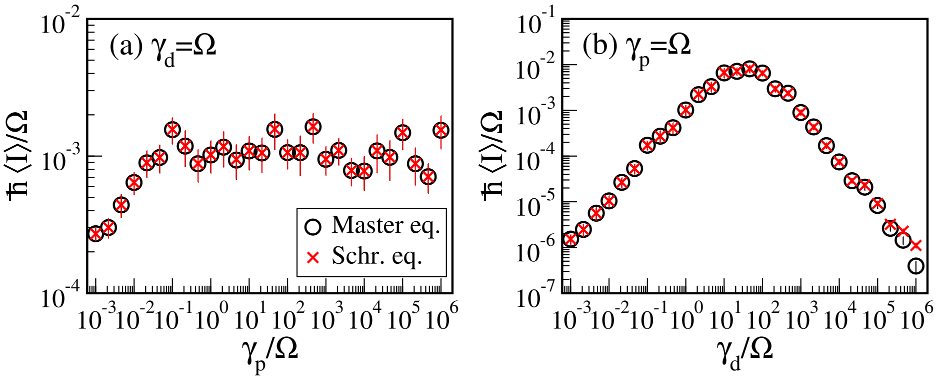

Figure 7.13: (a) Normalized average current $\hbar \langle I \rangle / \Omega$ *vs.* the normalized coupling strength γ_p/Ω for $\gamma_d = \Omega$ and (b) normalized average current $\hbar \langle I \rangle / \Omega$ *vs.* the normalized coupling strength γ_d/Ω for $\gamma_p = \Omega$. The stationary current is computed with the master equation approach (open circles), see Eqs. (7.4)-(7.5), and with the non-Hermitian Schrödinger equation equation approach (red crosses), see Eqs. (7.6)-(7.9). Here, $W = 100\,\Omega$, while the other parameters are the same as in Fig. 7.12.

Fig. 7.13(b), for a fixed value of disorder ($W = 100\Omega$). Similarly to Fig. 7.12, also here we observe a perfect correspondence between the two approaches.

7.6.6 Current and typical current

In Fig. 7.14 the probability distribution functions (PDF) of the stationary current $\hbar I/\Omega$ and of the variable $J = \ln(\hbar I/\Omega)$ are shown for a case in the disorder-independent transport (DIT) regime. As one can see, while the distribution of the current is strongly peaked at the origin and develops a slow-decaying tail, the distribution of J has a bell shape.

Therefore it is important to check which of the two quantities has the self-averaging property, namely, a ratio between the standard deviation I_{rms} and the mean $\langle I \rangle$ decreasing with N for large N values. Results for the variables I and J are shown in Figs. 7.15(a,c). As one can see, while in the first case $I_{rms}/\langle I \rangle$ grows with N, $J_{rms}/|\langle J \rangle|$ decreases with N. For this reason we decided to consider the variable J, and from that the typical current $\hbar I^{\rm typ}/\Omega = \exp(\langle J \rangle)$, in most of our numerical calculations in this chapter.

For completeness in Fig. 7.15(b) we show the average current $\langle I \rangle$ and its standard deviation I_{rms} as a function of the wire size N. Figure 7.15(d) is equivalent to Fig. 7.15(b) but for the variable J. Moreover, in Fig. 7.16 we compare the behavior of the average $\langle I \rangle$, typical $I^{\rm typ}$ and maximal I_{max} currents, in the disordered-independent regime, as a function of the system size N. We observe that all currents reported in Fig. 7.16 are proportional to $1/N^2$, see the dashed line; this size dependence was already reported in Fig. 7.15(b) for the average current $\langle I \rangle$.

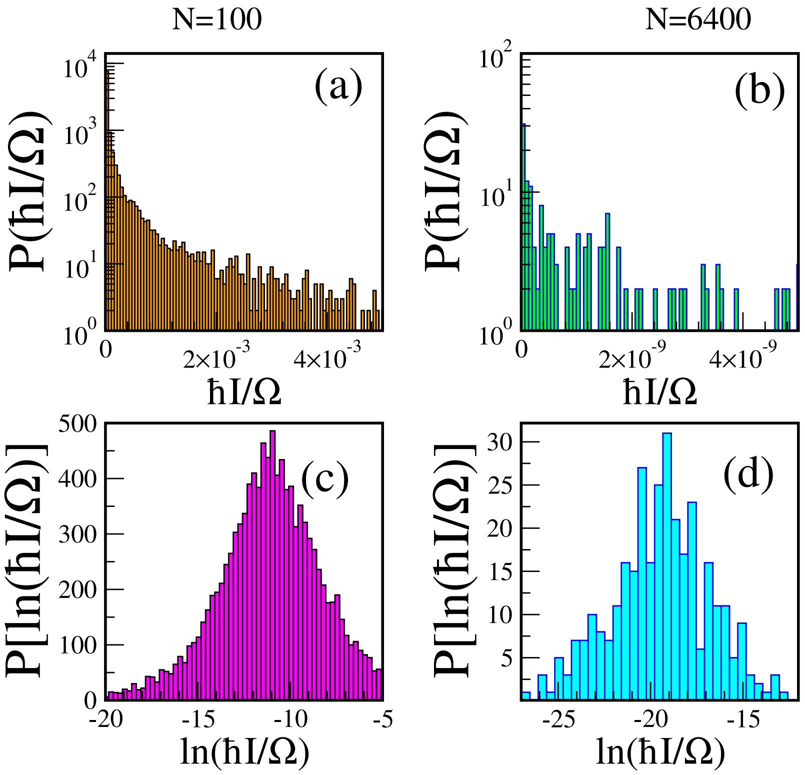

Figure 7.14: Probability distributions of (a,b) the normalized current $\hbar I/\Omega$ and (c,d) the logarithm of the normalized current $\ln(\hbar I/\Omega)$, for two wire sizes (a,c) $N = 100$ and (b,d) $N = 6400$. We considered the 1D Anderson model with long-range hopping, see Eq. (7.16), with $\gamma = \Omega$ and $W = 100\ \Omega$. The number of random disorder configurations is (a,c) $N_r = 10^4$ and (b,d) $N_r = 350$.

7.6.7 Scaling of the transport regimes with the long-range coupling strength

In Fig. 7.17 we present the average $\langle I\rangle$, typical $I^{\rm typ}$, maximal I_{max} and minimal I_{min} currents, multiplied by $\hbar/\Omega$, as a function of the normalized static disorder W/Ω for disordered wires with long-range hopping with different coupling strengths γ, as indicated in panel (b). For comparison purposes in Fig. 7.17(b) we also report the average variance $\langle\sigma^2\rangle$ of the excited eigenstates. As a reference, in panels (a-c) the case of $\gamma = 0$ is also shown, see the orange curves. In all panels the values of W_1 and W_2 are indicated with vertical dashed lines.

From Fig. 7.17 there are some points that deserve to be highlighted: (i) Since we use a fixed wire size, $N = 10^3$, all curves fall one on the top of the other for $W < W_{\rm GAP}$; recall that neither W_1 nor W_2 depend on the coupling strength γ, see Eqs. (7.33) and (7.35), respectively. (ii) Since $W_{\rm GAP} \propto \gamma$, see Eq. (7.17), the larger the value of the coupling strength γ the wider the disorder independent regime $W_2 < W < W_{\rm GAP}$. It is interesting to note that transport properties do not depend on the value of the long range coupling γ in the gapped regime.

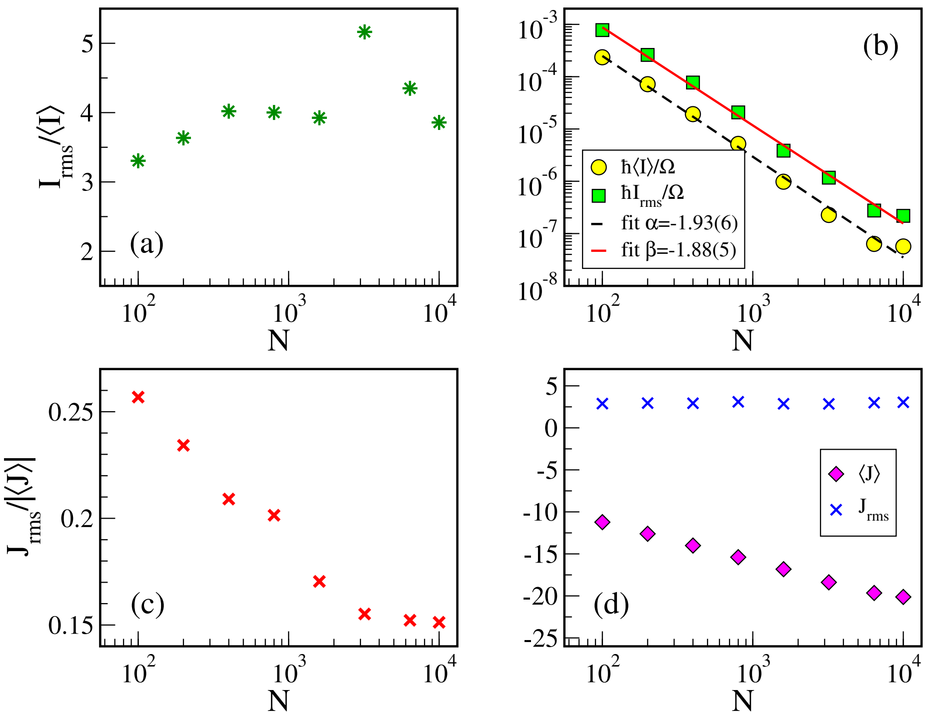

Figure 7.15: (a) The ratio $I_{rms}/\langle I \rangle$, (b) $\langle I \rangle$ and I_{rms} in units of the hopping rate $(\Omega/\hbar)$, (c) the ratio $J_{rms}/|\langle J \rangle|$, and (d) $\langle J \rangle$ and J_{rms} as a function of the wire size N. We considered the 1D Anderson model with long-range hopping, see Eq. (7.16), with $\gamma = \Omega$ and $W = 100\,\Omega$. The full-red and back-dashed lines in panel (b) are power-law fittings to the data with exponents α, β as given in the legend. The number of disorder configurations N_r is such that $N \times N_r = 10^6$.

7.6.8 Mapping between a molecular chain in an optical cavity and a system with long-range hopping

Here we consider a molecular chain in an optical cavity, with an optical mode at resonance with the molecule excitation energy. We show that the common coupling to the cavity mode effectively induces a long-range hopping between the molecules. This mapping, see Fig. 7.3(a), is very accurate even in presence of disorder until $W \approx W_{\text{GAP}}$.

The molecular chain in the cavity is described by the Hamiltonian in Eq. (7.12). First we proceed to prove that in absence of disorder there is an energy gap Δ between the polaritonic ground state and the lowest energy excited state. Indeed, in absence of disorder ($W = 0$), only the fully symmetric state $|d\rangle$, see Eq. (7.37), with energy -2Ω in the molecular chain couples with strength $\sqrt{N}g$ with the cavity mode which is at energy zero (resonant with the molecule excitation energy). Thus, we can compute the polaritonic energies and the energy gap Δ by solving the 2×2 coupling matrix for $|d\rangle$

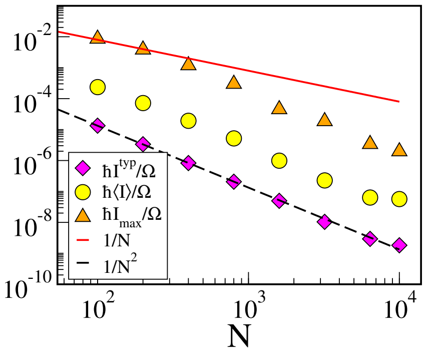

Figure 7.16: Behavior of average $\langle I \rangle$, typical I^{typ} and maximal I_{max} currents (in units of the hopping rate $\Omega/\hbar$) in the disorder-independent regime as a function of the system size N for an all-to-all coupling using the same parameters as Fig. 7.15. The full-red and dashed-black lines are power-laws of N as indicated in the legend.

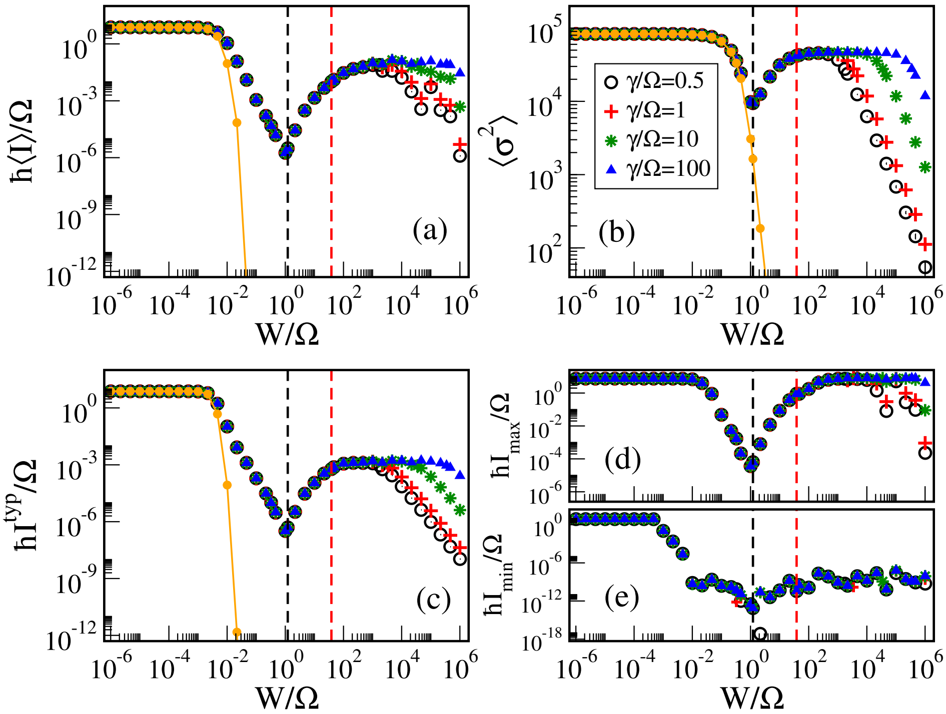

Figure 7.17: (a) Average $\langle I \rangle$, (c) typical I^{typ}, (d) maximal I_{max} and (e) minimal I_{min} currents in units of the hopping rate $\Omega/\hbar$, and (b) average variance $\langle \sigma^2 \rangle$ as a function of the static disorder W for different coupling strengths γ as indicated in the legend. Here, $N = 10^3$ and $\gamma_p = \gamma_d = \Omega$. We used $N_r = 10^3$ disorder configurations. The orange curves show the case $\gamma = 0$ while the vertical dashed lines indicate the critical disorder W_1 (black) and W_2 (red).

and the cavity mode $|c\rangle$,

$$\begin{pmatrix} \langle d|\, H_{cav}\, |d\rangle & \langle d|\, H_{cav}\, |c\rangle \\ \langle c|\, H_{cav}\, |d\rangle & \langle c|\, H_{cav}\, |c\rangle \end{pmatrix} = \begin{pmatrix} -2\Omega & \sqrt{N}g \\ \sqrt{N}g & 0 \end{pmatrix} ,$$

with H_{cav} from Eq. (7.12). Considering that for large N also the first excited state has energy -2Ω, we have

$$\Delta = \sqrt{Ng^2 + \Omega^2} - \Omega \approx \sqrt{N}g \quad \text{for} \quad \sqrt{N}g \gg \Omega\,. \tag{7.71}$$

On the other hand, a molecular chain in presence of long-range hopping of coupling strength γ has an energy gap Δ, in absence of disorder, equal to $N\gamma/2$. By imposing $\gamma_{\text{eff}} = 2g/\sqrt{N}$ we determine the effective long-range coupling which would produce the same energy gap Δ in absence of disorder and for large N. With this choice of γ_{eff}, if we exclude the polaritonic states in the cavity model and the ground state in the long range model, all other eigenstates and eigenvalues between the two models are identical for $W = 0$. This does not prove that they will be equivalent when disorder is added. In order to discuss this point, in the following, we consider the role of disorder using perturbation theory.

By considering the Anderson model,

$$H_0 = \sum_n \epsilon_n \,|n\rangle\,\langle n|$$

(see also Eq. (7.2)) as a perturbation in the regime $\sqrt{N}g \gg (\Omega, W)$ or $\gamma_{\text{eff}} \gg (\Omega, W)$ and following the same approach developed in previous Sections, we can apply a perturbative approach to both the long-range and the cavity model.

Let us start to consider the long-range Hamiltonian. We can write the Hamiltonian H in Eq. (7.1) in the basis which diagonalizes the long-range interaction matrix $V = -\gamma/2 \sum_{i\neq j} |i\rangle\,\langle j|$. This basis is formed by the fully symmetric state $|d\rangle$, with eigenvalue $-\gamma(N-1)/2$, and by the $N-1$ degenerate states $|\mu\rangle$, orthogonal to $|d\rangle$, with eigenvalues $\gamma/2$. In this basis we have

$$H = \begin{pmatrix} -\frac{\gamma}{2}(N-1) + \zeta & \vec{h}^T \\ \vec{h} & \tilde{H} \end{pmatrix} , \tag{7.72}$$

where $\vec{h}$ is the interaction vector between the excited states and the ground state (7.47) of the long-range interaction matrix V with components

$$h_\mu = \sum_n \epsilon_n \langle d|n\rangle\langle n|\mu\rangle\,. \tag{7.73}$$

Moreover,

$$\zeta = \sum_n \epsilon_n |\langle n|d\rangle|^2 \tag{7.74}$$

and $\tilde{H}$ represents the matrix elements of the $N-1$ excited states written in the degenerate basis of the long-range hopping interaction matrix. The matrix elements of $\tilde{H}$ with respect to the $N-1$ degenerate eigenstates of V, $|\mu\rangle, |\nu\rangle$, can be written as

$$\langle\nu|\tilde{H}|\mu\rangle = \sum_n \epsilon_n \langle\nu|n\rangle\langle n|\mu\rangle + \frac{\gamma}{2}\delta_{\nu\mu} \,. \tag{7.75}$$

For the molecular chain in the cavity we can use as a basis the eigenstates of the interaction matrix between the N uncoupled molecules and the cavity mode. In this interaction matrix all the molecules are coupled with strength g with the cavity mode which acts as an additional external site, see Eq. (7.12). This form of the coupling implies that only the state $|d\rangle$ in the molecular chain couples with the cavity mode, forming two polaritonic states $|p_\pm\rangle$ with energies $\pm\sqrt{N}g$. On the other hand all the other $N-1$ degenerate eigenstates $|\mu\rangle$ with energy zero are decoupled from the cavity mode. Note that the $|\mu\rangle$ states defined here are identical to the $|\mu\rangle$ states defined above for the long-range model. Therefore, in the basis $\{|p_\pm\rangle, |\mu\rangle\}$ we can write the Hamiltonian of Eq. (7.12) as:

$$H = \begin{pmatrix} -\sqrt{N}g+\zeta/2 & \zeta/2 & \vec{h}^T/2 \\ \zeta/2 & \sqrt{N}g+\zeta/2 & \vec{h}^T/2 \\ \vec{h}/2 & \vec{h}/2 & \tilde{H} \end{pmatrix} , \tag{7.76}$$

where the matrix elements $\vec{h}$ and $\tilde{H}$ are given above, see Eqs. (7.73,7.74,7.75).

In particular, we note that the zero order matrix $\tilde{H}$ is the same in both cases: the long-range (see Eq. (7.39)) and cavity systems (see Eq. (7.75)). Note also that the $|\mu\rangle$ states are the same for both cases, and they are given by Eq. (7.46). Moreover, also the mixing $\vec{h}$ between the excited states and the ground state/polaritonic states is the same apart from a factor of 2 (compare Eq. (7.72) to Eq. (7.76)). Therefore our mapping is exact if the dynamics starts from the subspace orthogonal to the extended state $|d\rangle$ in absence of disorder, and it is approximate in presence of disorder, where the discrepancies are proportional to the perturbative parameter $W/(\sqrt{N}g)$. Thus, we can expect that by imposing $\gamma_{\text{eff}} = 2g/\sqrt{N}$, the excited states of the long-range model and the non-polaritonic states in the molecular chain in the cavity will be very similar until the disorder threshold $W \approx W_{\text{GAP}}$, above which disorder will strongly mix the subspaces. This hypothesis is verified in Fig. 7.18, where the average shape of the eigenfunctions $\langle|\Psi|^2\rangle$ for both the excited states in the long-range case and the non-polaritonic states for the cavity case are compared and shown to be very similar for all the values of disorder considered in the gapped regime.

7.6.9 Dynamics: wave packet spreading and stationary state

In this Section we analyze the dynamics of a linear chain in presence of long-range hopping and disorder, see Eq. (7.1). We consider a wave packet initially localized on one single site at the center of the chain. We let the initial state evolve in presence of disorder and we compute the variance of the wave packet in time, averaging the probability distribution on the chain sites over the disorder realizations, at each time.

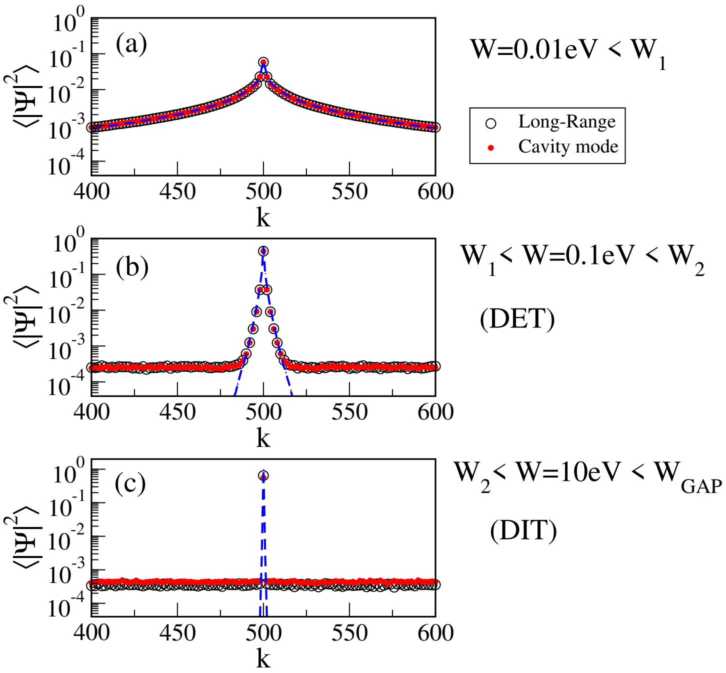

Figure 7.18: Average shape of the eigenfunctions $\langle|\Psi|^2\rangle$ in the site basis k comparing the cavity model (red dots) and the long-range all-to-all coupling γ_{eff} (black circles). In each panel different disorder regimes are shown: (a) $W < W_1$, (b) $W_1 < W < W_2$ and (c) $W_2 < W < W_{\mathrm{GAP}}$. Here, $N = 10^3$, $\Omega = 0.0124$ eV, $\hbar\omega_c = 2$ eV, $\mu \approx 36$ D, $g = 0.1008$ eV, $g_c = 3.188$ eV, $\gamma_{\mathrm{eff}} = 2g/\sqrt{N}$ and the number of disorder configurations $N_r = 10^3$. The blue-dashed lines, shown as a reference, indicate the case $g = 0$.

The variance at different times $\sigma^2(t)$ has been computed as follows,

$$\sigma^2(t) \equiv \overline{\langle\psi(t)|x_\alpha^2|\psi(t)\rangle - \langle\psi(t)|x_\alpha|\psi(t)\rangle^2},$$

where the over-line stands for the disorder average. The results are shown in Fig. 7.19(lower panel). Once the variance reaches a stationary value, we computed the time average of the the stationary variance (red crosses) and we plot it for different disorder strengths W in Fig. 7.19(upper panel), where the average variance of the excited eigenstates is also shown (black circles), see also Fig. 7.2(b). Interestingly the two variances, one obtained by analyzing the eigenstates and the other obtained from the dynamics, are very similar. This shows that the average eigenstate variance analyzed in the main text of this chapter can indeed be considered as a figure of merit for transport.

For some of the red crosses shown in Fig. 7.19(upper panel) we also show the time evolution of the variance $\sigma^2(t)$ in Fig. 7.19(lower panel). At small times, one can observe periodic fluctuations independent of the disorder strength W with frequency $N\gamma/2$ corresponding to the energy gap Δ between the ground state and the excited states. At larger times the variance reaches the stationary value in a ballistic-like way $\sigma^2(t) \propto t^2$

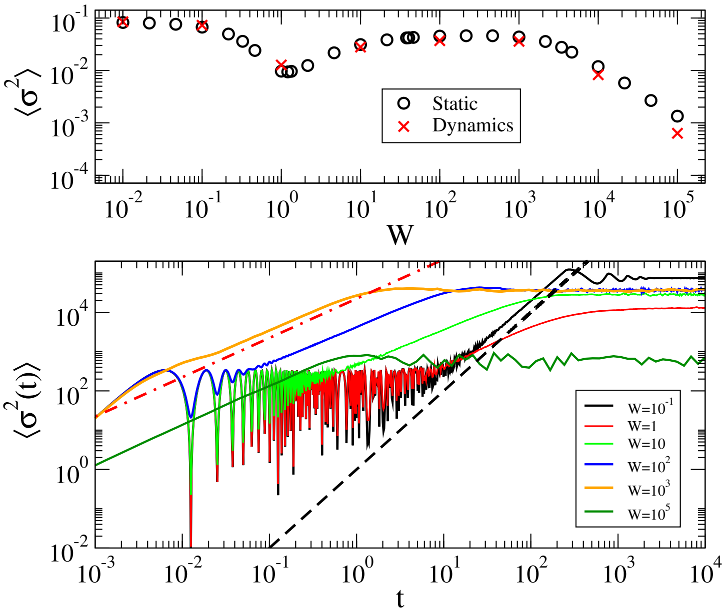

Figure 7.19: Upper Panel: Average eigenstate variance $\langle \sigma^2 \rangle$ *vs.* the disorder strength W of the excited eigenstates (black circles) is compared with the stationary variance (red crosses) obtained by evolving a wave packet initially localized in the middle of the linear chain. The stationary variance has been obtained by averaging over 100 disorder realizations and averaging over time from $500 < t < 10^4$. Lower Panel: Variance obtained by evolving a wave packet initially localized in the middle of the liner chain is shown *vs.* the time t for different disorder strengths W, see legend. At each time the variance has been obtained by averaging over 100 disorder realizations. The ballistic behaviour $\sigma^2 \propto t^2$ is shown as a dashed black line, while the diffusive behaviour $\sigma^2 \propto t$ is shown as a dot-dashed red line. In both panels a linear chain with long-range hopping has been considered, see Eq. (7.16). Parameters are: $N = 1001, \gamma = \Omega, \Omega = 1$ with $W_1 \approx 1.205$, $W_2 \approx 38.126$ and $W_{\mathrm{GAP}} \approx 3457.831$. In both panels, the time is measured in units of the hopping time $\hbar/\Omega$.

for small disorder, see the dashed black line in Fig. 7.19(lower panel), and in a diffusive-like way $\sigma^2(t) \propto t$ for larger disorder, see the dot-dashed red line in Fig. 7.19(lower panel). Note that in the disorder-independent transport regime (DIT) $W_2 < W < W_{\text{GAP}}$, the variance stationary value is independent of the disorder strength W. For even larger disorder, when $W > W_{\text{GAP}}$, the spreading is almost immediately diffusive-like until it saturates.

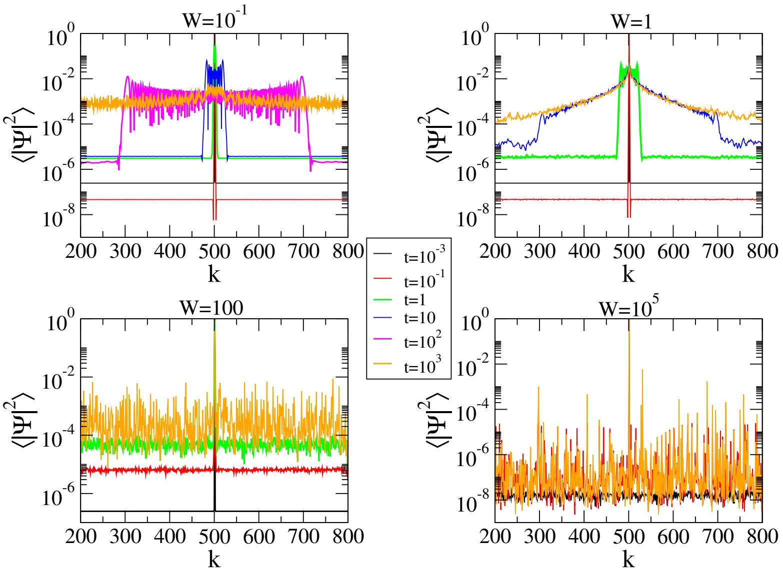

Figure 7.20: Probability distributions are shown at different times t and different disorder strengths W, see legend. The probability distributions have been obtained by evolving an initially localized wave packet at the center of a liner chain. Each probability distribution has been obtained by averaging over 100 disorder realizations. In all panels a linear chain with long-range hopping has been considered, see Eq. (7.1). Parameters are: $N = 1001, \gamma = \Omega, \Omega = 1$. In all panels, the time is measured in units of the hopping time $\hbar/\Omega$.

While the behaviour of $\sigma^2(t)$ suggests a transition from ballistic to diffusive-like spreading as the disorder strength W increases, a closer look at the probability distribution at different times and for different disorders, Fig. 7.20, shows that both the ballistic and diffusive characterization of the wave packet spreading in presence of long-range hopping are not fully correct. Specifically, for large W, the increase of the variance is not due to an increase of the width of the initial wave packet but it is mainly due to the growth of the flat tails of the probability distribution, see lower panels in Fig. 7.20.

Finally, by analyzing the stationary probability distribution obtained from the dynamics we analyzed the tails of the distribution in the disorder-independent transport (DIT) regime. Since in this regime the distribution has only one peak at the center of the chain corresponding to the initial state, in order to analyze the statistical properties of the probability distribution in the tails we averaged the probabilities and their logarithm over all the sites but the central one. As one can see from Fig. 7.21

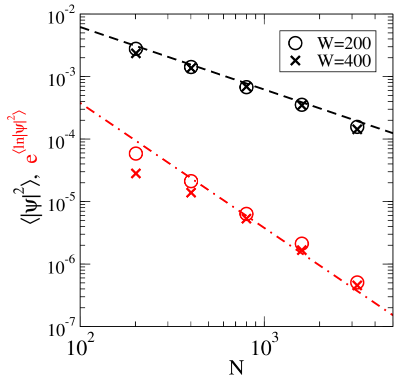

Figure 7.21: Average probability in the tails of the stationary distribution is shown for different number of sites N in a linear chain. The average probability in the tails of the stationary distribution has been obtained by evolving a wave packet initially localized at the center of a linear chain. Here a linear chain with long-range hopping has been considered, see Eq. (7.1). Parameters are: $\gamma = \Omega, \Omega = 1$ and $W = \{200, 400\}$, see legend. Two different methods to obtain the average probability have been considered: the average probability $\langle|\psi|^2\rangle$ (black symbols) and the typical probability $\exp\langle\ln|\psi|^2\rangle$ (red symbols) of the tails of the stationary probability distribution (we averaged over all sites but the central one). An additional average over 100 disorder realizations is considered. The black dashed line shows a linear $(1/N)$ behaviour while the red dot-dashed line shows a quadratic $(1/N^2)$ behaviour.

the average probability in the tails decreases as $\approx 1/N$, while the typical probability $e^{\langle\ln|\psi|^2\rangle} \approx 1/N^2$, showing that the distribution in the tails is very broad and highly non trivial. Moreover, two different values of the disorder strength W (both in the DIT regime) have been considered, showing that the tails are independent of disorder in this regime, as discussed above.

Chapter 8

Conclusions and perspectives

In this thesis different cooperative effects have been studied, with a particular focus on superradiance. The interplay of cooperativity and disorder/noise has been analyzed both for realistic systems and for paradigmatic models of excitation transport, studying also some possible applications. In Chapter 2 a full derivation of a master equation formalism for cooperative light-matter interaction is obtained, that is valid for an aggregate of identical emitters all having different positions and (possibly) different orientations. The obtained formalism is valid both when the aggregate is smaller than λ, the transition wavelength of the emitters, but also for aggregates much larger than λ. At zero temperature, and under the single-excitation approximation, we were able to relate the master equation approach to the well known radiative non-Hermitian Hamiltonian approach. We are therefore able to describe the collective coupling to the electromagnetic field (EMF) both in the weak- and in the strong-coupling regimes, that is both whether the imaginary parts of the complex energies (including the coupling to the EMF) are smaller or larger than the mean level spacing in the single-excitation manifold. Therefore, superradiance can be accurately described. The presented formalism also includes the coupling to a black body at a finite temperature, and it self-consistently describes the absorption and stimulated emission processes induced by the incoming black-body photons interacting with the aggregate. Then, in perspective, it would be interesting to analyze how finite temperature photon baths, or even engineered fields, would affect the interaction between the emitters. Our proposed formalism models sunlight as a black-body at temperature $T \approx 6000$ K, but the problem of modelling sunlight carefully is essential to understand how natural systems harness solar energy. In view of this, there have been several attempts for modelling natural sunlight, for instance as an ensemble of broad-band wavepackets [241] or as a white-noise uncorrelated bath [50, 51]. In particular, the white-noise approach presented in Ref. [50], which is computationally less expensive than our master equation approach for large N, is also equivalent to our approach, for the specific case of a degenerate molecular aggregate under weak excitation. However, the two approaches differ when the site energies are non-degenerate, since the white-noise approach is non-secular, differently from the Lindblad master equation. Nevertheless, even in the case of non-degenerate site energies, if we derive the Lindblad super-operator assuming degenerate sites with an energy equal to the average site energy and applying such Libdblad super-operator *a posteriori* to the non-degenerate Hamiltonian, we obtain dynamical and static coherence between the eigenstates, as we have shown in Chapter 2. These coherences are a non-secular peculiarity of the stochastic white-noise approach and, interestingly, they can be reproduced with such phenomenological Lindblad approach. We leave a systematic justification of this correspondence to a further investigation.

We have used the techniques introduced in Chapter 2 to analyze different realistic systems, whose coupling strength is categorized as weak, strong or ultra-strong, as discussed in section 1.5. As regards weakly-coupled systems, where the collective coupling to the EMF (as measured by the superradiant radiative width $\hbar\Gamma_{SR}$) is smaller than the mean level spacing, in Chapter 3 we have analyzed realistic structures of self-aggregated molecular nanotubes of chlorophyll molecules as found in antenna complexes of Green Sulfur Bacteria. By taking into account position and dipole orientation of chlorophyll molecules which agree with experimental data we have shown that natural structures are able to support macroscopic coherent states even at room temperature. Indeed in natural complexes we have found delocalized thermal excitonic states with a coherence length extending over hundreds of molecules. We have shown show that such thermal coherence length is much larger than that one could expect from the magnitude of the nearest-neighbour coupling and it cannot be explained even by the long-range nature of the interaction between the molecules. Instead, the ability of natural structures to support a large coherence length has been traced back to their specific geometric features. Specifically, our structural analysis of the symmetric arrangement of the molecules in the nanotubes revealed that the spectrum is generated by the superposition of the eigenstates of small sub-units. In each sub-unit, few eigenstates are superradiant, meaning that they have a large dipole strength, and the superposition of the few superradiant eigenstates of each sub-unit generates the lowest-energy part of the spectrum. As we have shown, the coupling between the superradiant states of the sub-units is enhanced by a cooperative super-transfer effect, due to their large dipole strength, and such large couplings determine a large level spacing and, therefore, a lower density of states at low energy. Interestingly, even if the non-hermitian interaction in this system lies in the weak-coupling regime and the hermitian dipole-dipole coupling is short-range, strong cooperative effects like supertransfer can be induced. In perspective, this opens the question on finding a more general way to quantify cooperativity, accounting for both the hermitian and the non-hermitian interactions, and for those cooperative effects that emerge even in absence of long-range interactions. From our results we can predict that symmetry in cylindrical molecular nanotubes is essential (although not enough) to have robust structures, not only to thermal noise, as we have demonstrated here, but also to other sources of noise such as static disorder, as our preliminary results have shown. Nevertheless, the role of static disorder should be analyzed in the future, in a more systematic way. The structural requirement to have robustness to thermal noise is to create a super-transfer coupling between the superradiant eigenstates of cylindrical sub-units able to generate the lower part of the spectrum of the whole structure. In the future it would be important to understand the general structural requirements necessary to induce macroscopic coherent states in generic molecular networks. Moreover, it would be interesting to investigate how the suppressed density of states at low energy affects excitation transport in presence of finite-temperature dephasing. Our results could indicate design principles for efficient nanotubular quantum wires.

In Chapter 4 we considered a different class of natural photosynthetic systems in the weak-coupling regime, *i.e.* those present in Purple Bacteria, and we propose to use them as building blocks for a bio-inspired sunlight-pumped laser. Specifically, we propose a laser medium composed of molecular aggregates, inspired to the design of photosynthetic antenna complexes, which have at their core a molecular dimer composed of two strongly coupled chromophores. The dimer is characterized by a bright state at higher energy and a dark state as its lowest excited state. Even though this so-called H-dimer configuration, which can be easily synthesized in laboratory, seems ideal for achieving population inversion and lasing, we show that natural sunlight is so weak that an unrealistically high level of darkness would be required to reach the lasing threshold. One of the most remarkable aspects of photosynthetic antenna complexes is their ability to efficiently harvest natural sunlight and to transport the collected energy to specific locations with almost unit efficiency. We show that exploiting this property significantly lowers the lasing threshold. Indeed, if pumped by the surrounding photosynthetic complex, the core dimer structure can indeed feature population inversion and reach the lasing threshold under natural sunlight for realistic dimer parameters. Turning the incoherent energy supply provided by the Sun into a coherent laser beam would overcome several of the practical limitations inherent in using sunlight as a source of clean energy. For example, laser beams are highly effective at driving chemical reactions which convert sunlight into chemical energy. Indeed, sunlight-pumped lasers are the basis of one of the most promising renewable energy proposals: the Magnesium Injection Cycle (MAGIC). Further, since bacterial photosynthetic complexes tend to operate in the near-infrared spectral region, our proposal naturally lends itself for realising short-wavelength infrared lasers which would allow their beams to travel nearly losslessly over large distances, thus efficiently distributing the collected sunlight energy.

In Chapter 5 the interplay of superradiance and thermal noise is studied for a novel solid state material, namely perovskite $CsPbBr_3$ quantum-dot superlattices, which can be classified in the strong-coupling regime. Recent observations have revealed superradiant emission from this material at low temperature (6 K), although the estimated degree of cooperativity is surprisingly low. Our results show that superradiance in such material is largely suppressed by thermal noise, even at such low temperature, due to the weak radiative couplings between the quantum dots. Our results also predict that the robustness to noise would improve, therefore enhancing superradiance by up to three orders of magnitude, by lowering the size of the quantum dots, making it possibly observable at higher temperatures. On the other hand, the use of larger quantum dots would make the system more robust to inhomogeneities and static disorder, indicating different possible interesting directions to further investigate. New experiments, aimed at verifying our predictions, are already being developed by the group of Ken Kuno (University of Notre Dame, USA) and by the group of Thilo Stöferle (IBM Zurich, Switzerland[1]). Even if strong superradiance has already been seen in other systems, such as molecular aggregates, achieving controllable cooperative effects in lead halide perovskite quantum dot superlattices would have many advantages, because of the stability of solid state systems, over molecules. Specifically, lead halide perovskite quantum dots are particularly interesting because they possess a very sharp and tunable emission band, whose peak can span the entire visible spectrum just by varying the size of the quantum dots and changing the halide in the compounds. The narrow linewidth reflects that these quantum dots can be easily synthesized with a very low degree of disorder. Moreover, these quantum dots are nearly unique since they have a unity (or near-unity) emission quantum yield, indicating that non-radiative decay processes are nearly absent. Also, their ultrafast radiative lifetime (hundreds of picoseconds) indicates an incredibly strong coupling to the EMF, and their long coherence time reflects slow dephasing processes. All these features make these systems good candidates for efficient photon sensors, and controlling cooperative effects could possibly boost their photon detection efficiency.

In Chapter 6 a comparison between different cooperative effects, single-excitation superradiance and superconductivity, is made with a focus on the spectral signatures in different coupling regimes. Our calculations show that the superradiance transition, governed by the strength of the collective coupling to the EMF, can be seen as a transition to a gapped regime, in clear analogy to superconductivity. The superradiant gap is purely imaginary, as opposed to the superconducting gap, nevertheless we show that both gaps make the system robust to static disorder in the same way. In this context, it would be interesting to further study the comparison between superradiance and superconductivity, focusing on the many-body spectrum. Specifically, in the case of superconductivity a full many-body coherent ground state is formed by the Cooper pairs. On the other hand, in the case of many emitters, excitons are known to undergo Bose-Einstein condensation under some conditions [242, 243]. It would be interesting to study the exciton condensation phenomenon in a superradiant system, comparing its features to the BCS theory of superconductivity, on the line of recent works [244]. Specifically, exciton condensation in the ultra-strong coupling regime seems like a promising direction to pursue.

The analysis in Chapter 6 also proves that the presence of a gap in the spectrum is a general property of long-range interactions, thus opening the question on what is the role of long-range interactions in the transport of excitation through disordered systems. Motivated by that, in Chapter 7 we analyze precisely the effect of long-range interactions in the ultra-strong coupling regime on the transport properties of a disordered system. We analyze a paradigmatic model of a disordered chain with long-range interaction, and we find that the interplay of disorder and long-range interactions produces counter-intuitive transport regimes, where the transport efficiency is enhanced

---

[1] See the video of Stöferle's presentation at the following webpage: `https://youtu.be/ge_C_yRSxMo` (in particular, our work is mentioned at the time 22:25).

by disorder or even independent of it, and we characterize these regimes in detail. Our findings also answer a long-standing problem, highly debated in the literature, about the mutual effects between long-range hopping and disorder. Indeed, even if long-range is typically thought to destroy the disorder-induced localization, thus allowing efficient transport, strong signatures of localization have been found in long-range interacting systems in recent years. Here we demonstrate that since localized states in long-range interacting systems have a hybrid character, with an exponentially localized peak and an extended tail, they can support robust quantum transport. Our results are relevant in several experimental systems where long-range hopping is present, such as cold atomic clouds, molecular aggregates and ion traps. Among other results, but not of minor relevance, we also demonstrate that an ensemble of emitters in a cavity can be mapped into an effective long-range hopping system, thus making our findings applicable to an even larger variety of systems; to quote but a few, molecular chains in optical cavities (on which we explicitly focus in Chapter 7), Rydberg atoms and polar molecules. Realistic parameters for these physical systems are presented in Chapter 7, showing that the regimes we predict are easily reachable in nowadays experiments. Therefore, it could be very interesting to have our predictions checked experimentally. Our detailed description of the different and novel transport regimes, characterized by extremely robust transport, can also inspire novel design principles for quantum devices. Finally, it is worth mentioning that the interesting novel transport regimes obtained in Chapter 7 are obtained in absence of noise and at zero temperature. One could argue that the presence of a large gap could reasonably make the system robust to dephasing, and a finite temperature noise could produce even more interesting results, precisely because of the gap between the ground state and the rest of the spectrum. We just started to pursue an analysis of these issues and we aim to further expand our understanding of the interplay of long-range interactions, static disorder and noise in energy transport. We are considering the effect of dephasing modeled as a white noise, and we aim to analyze the consequences on transport at the steady state and analyzing the diffusive spreading of an excitation initially localized on one site. Diffusion has been extensively studied in a disordered nearest-neighbor chain in presence of noise [245] and in nanotubes [72]. We aim to analyze the effect of long-range hopping on the excitation spread in presence of white noise, also considering finite-temperature environments.

Bibliography

[1] Higgins, K. *et al.* Superabsorption of light via quantum engineering. *Nat. Commun.* **5**, 1–7 (2014).

[2] Hu, X., Ritz, T., Damjanović, A. & Schulten, K. Pigment organization and transfer of electronic excitation in the photosynthetic unit of purple bacteria. *J. Phys. Chem. B* **101**, 3854–3871 (1997).

[3] Strümpfer, J., Şener, M. & Schulten, K. How quantum coherence assists photosynthetic light-harvesting. *J. Phys. Chem. Lett.* **3**, 536–542 (2012).

[4] Hu, X., Damjanović, A., Ritz, T. & Schulten, K. Architecture and mechanism of the light-harvesting apparatus of purple bacteria. *Proc. Natl. Acad. Sci. U.S.A.* **95**, 5935–5941 (1998).

[5] Şener, M. K., Olsen, J. D., Hunter, C. N. & Schulten, K. Atomic-level structural and functional model of a bacterial photosynthetic membrane vesicle. *Proc. Natl. Acad. Sci. U.S.A.* **104**, 15723–15728 (2007).

[6] Bohnet, J. G. *et al.* A steady-state superradiant laser with less than one intracavity photon. *Nature* **484**, 78–81 (2012).

[7] Lloyd, S. & Mohseni, M. Symmetry-enhanced supertransfer of delocalized quantum states. *New J. Phys.* **12**, 075020 (2010).

[8] Council, N. R. *Advancing Land Change Modeling: Opportunities and Research Requirements* (The National Academies Press, Washington, DC, 2014).

[9] Yabe, T. *et al.* High-efficiency and economical solar-energy-pumped laser with fresnel lens and chromium codoped laser medium. *Appl. Phys. Lett.* **90**, 261120 (2007).

[10] Uchida, S. *et al.* Experimental study of solar pumped laser for magnesium-hydrogen energy cycle. In *AIP Conf. Proc.*, vol. 830, 439–446 (American Institute of Physics, 2006).

[11] Graham-Rowe, D. Solar-powered lasers. *Nat. Photonics* **4**, 64 (2010).

[12] Fano, U. A common mechanism of collective phenomena. *Rev. Mod. Phys.* **64**, 313–319 (1992).

[13] Bardeen, J., Cooper, L. N. & Schrieffer, J. R. Theory of superconductivity. *Phys. Rev.* **108**, 1175–1204 (1957).

[14] Bohm, D. & Pines, D. A collective description of electron interactions: Iii. coulomb interactions in a degenerate electron gas. *Phys. Rev.* **92**, 609–625 (1953).

[15] Dicke, R. H. Coherence in spontaneous radiation processes. *Phys. Rev.* **93**, 99–110 (1954).

[16] Schrieffer, J. R. *Theory of superconductivity* (Westview Press, 1964).

[17] Cong, K. *et al.* Dicke superradiance in solids [invited]. *J. Opt. Soc. Am. B* **33**, C80–C101 (2016).

[18] Araújo, M. O., Krešić, I., Kaiser, R. & Guerin, W. Superradiance in a large and dilute cloud of cold atoms in the linear-optics regime. *Phys. Rev. Lett.* **117**, 073002 (2016).

[19] Monshouwer, R., Abrahamsson, M., van Mourik, F. & van Grondelle, R. Superradiance and exciton delocalization in bacterial photosynthetic light-harvesting systems. *J. Phys. Chem. B* **101**, 7241–7248 (1997).

[20] De Boer, S. & Wiersma, D. A. Dephasing-induced damping of superradiant emission in j-aggregates. *Chem. Phys. Lett.* **165**, 45 – 53 (1990).

[21] Fidder, H., Knoester, J. & Wiersma, D. A. Superradiant emission and optical dephasing in j-aggregates. *Chem. Phys. Lett.* **171**, 529 – 536 (1990).

[22] Scheibner, M. *et al.* Superradiance of quantum dots. *Nat. Phys.* **3**, 106–110 (2007).

[23] Brandes, T. Coherent and collective quantum optical effects in mesoscopic systems. *Phys. Rep.* **408**, 315 – 474 (2005).

[24] Bradac, C. *et al.* Room-temperature spontaneous superradiance from single diamond nanocrystals. *Nat. Commun.* **8**, 1–6 (2017).

[25] Celardo, G. L., Giusteri, G. G. & Borgonovi, F. Cooperative robustness to static disorder: Superradiance and localization in a nanoscale ring to model light-harvesting systems found in nature. *Phys. Rev. B* **90**, 075113 (2014).

[26] Celardo, G. L., Poli, P., Lussardi, L. & Borgonovi, F. Cooperative robustness to dephasing: Single-exciton superradiance in a nanoscale ring to model natural light-harvesting systems. *Phys. Rev. B* **90**, 085142 (2014).

[27] Gross, M. & Haroche, S. Superradiance: An essay on the theory of collective spontaneous emission. *Phys. Rep.* **93**, 301 – 396 (1982).

[28] Scully, M. O. & Svidzinsky, A. A. The super of superradiance. *Science* **325**, 1510–1511 (2009).

[29] Guerin, W., Araújo, M. O. & Kaiser, R. Subradiance in a large cloud of cold atoms. *Phys. Rev. Lett.* **116**, 083601 (2016).

[30] Eisele, D. M. *et al.* Utilizing redox-chemistry to elucidate the nature of exciton transitions in supramolecular dye nanotubes. *Nat. Chem.* **4**, 655–662 (2012).

[31] Furumaki, S. *et al.* Absorption linear dichroism measured directly on a single light-harvesting system: The role of disorder in chlorosomes of green photosynthetic bacteria. *J. Am. Chem. Soc.* **133**, 6703–6710 (2011).

[32] Eder, T. *et al.* Switching between h-and j-type electronic coupling in single conjugated polymer aggregates. *Nat. Commun.* **8**, 1–11 (2017).

[33] Kassal, I., Yuen-Zhou, J. & Rahimi-Keshari, S. Does coherence enhance transport in photosynthesis? *J. Phys. Chem. Lett.* **4**, 362–367 (2013).

[34] Baghbanzadeh, S. & Kassal, I. Geometry, supertransfer, and optimality in the light harvesting of purple bacteria. *J. Phys. Chem. Lett.* **7**, 3804–3811 (2016).

[35] Baghbanzadeh, S. & Kassal, I. Distinguishing the roles of energy funnelling and delocalization in photosynthetic light harvesting. *Phys. Chem. Chem. Phys.* **18**, 7459–7467 (2016).

[36] Agranovich, V. M., Litinskaia, M. & Lidzey, D. G. Cavity polaritons in microcavities containing disordered organic semiconductors. *Phys. Rev. B* **67**, 085311 (2003).

[37] Dubin, F. *et al.* Macroscopic coherence of a single exciton state in an organic quantum wire. *Nat. Phys.* **2**, 32–35 (2006).

[38] Gambino, S. *et al.* Exploring light–matter interaction phenomena under ultrastrong coupling regime. *ACS Photonics* **1**, 1042–1048 (2014).

[39] Lidzey, D. G. *et al.* Room temperature polariton emission from strongly coupled organic semiconductor microcavities. *Phys. Rev. Lett.* **82**, 3316–3319 (1999).

[40] Kéna-Cohen, S., Maier, S. A. & Bradley, D. D. Ultrastrongly coupled exciton–polaritons in metal-clad organic semiconductor microcavities. *Adv. Opt. Mater.* **1**, 827–833 (2013).

[41] Giusteri, G. G., Mattiotti, F. & Celardo, G. L. Non-hermitian hamiltonian approach to quantum transport in disordered networks with sinks: Validity and effectiveness. *Phys. Rev. B* **91**, 094301 (2015).

[42] Chávez, N. C., Mattiotti, F., Méndez-Bermúdez, J. A., Borgonovi, F. & Celardo, G. L. Real and imaginary energy gaps: a comparison between single excitation superradiance and superconductivity and robustness to disorder. *Eur. Phys. J. B* **92**, 144 (2019).

[43] Chávez, N. C., Mattiotti, F., Méndez-Bermúdez, J. A., Borgonovi, F. & Celardo, G. L. Disorder-enhanced and disorder-independent transport with long-range hopping: application to molecular chains in optical cavities (2020). `https://arXiv.org/abs/2010.08060`.

[44] Grad, J., Hernandez, G. & Mukamel, S. Radiative decay and energy transfer in molecular aggregates: The role of intermolecular dephasing. *Phys. Rev. A* **37**, 3835–3846 (1988).

[45] Zhang, Y., Celardo, G. L., Borgonovi, F. & Kaplan, L. Optimal dephasing for ballistic energy transfer in disordered linear chains. *Phys. Rev. E* **96**, 052103 (2017).

[46] Giusteri, G. G., Recrosi, F., Schaller, G. & Celardo, G. L. Interplay of different environments in open quantum systems: Breakdown of the additive approximation. *Phys. Rev. E* **96**, 012113 (2017).

[47] Rainò, G. *et al.* Superfluorescence from lead halide perovskite quantum dot superlattices. *Nature* **563**, 671–675 (2018).

[48] Lehmberg, R. H. Radiation from an n-atom system. i. general formalism. *Phys. Rev. A* **2**, 883–888 (1970).

[49] Breuer, H.-P. & Petruccione, F. *The theory of open quantum systems* (Oxford University Press, 2002).

[50] Olšina, J., Dijkstra, A. G., Wang, C. & Cao, J. Can natural sunlight induce coherent exciton dynamics? (2014). `https://arXiv.org/abs/1408.5385`.

[51] Hsieh, C.-Y. & Cao, J. A unified stochastic formulation of dissipative quantum dynamics. i. generalized hierarchical equations. *J. Chem. Phys.* **148**, 014103 (2018).

[52] Engel, G. S. *et al.* Evidence for wavelike energy transfer through quantum coherence in photosynthetic systems. *Nature* **446**, 782–786 (2007).

[53] Panitchayangkoon, G. *et al.* Long-lived quantum coherence in photosynthetic complexes at physiological temperature. *Proc. Natl. Acad. Sci. U.S.A.* **107**, 12766–12770 (2010).

[54] Scholes, G. D. *et al.* Using coherence to enhance function in chemical and biophysical systems. *Nature* **543**, 647–656 (2017).

[55] Huh, J. *et al.* Atomistic study of energy funneling in the light-harvesting complex of green sulfur bacteria. *J. Am. Chem. Soc.* **136**, 2048–2057 (2014).

[56] Sawaya, N. P. D., Huh, J., Fujita, T., Saikin, S. K. & Aspuru-Guzik, A. Fast delocalization leads to robust long-range excitonic transfer in a large quantum chlorosome model. *Nano Lett.* **15**, 1722–1729 (2015).

[57] Fetisova, Z. G., Freiberg, A. M. & Timpmann, K. E. Long-range molecular order as an efficient strategy for light harvesting in photosynthesis. *Nature* **334**, 633–634 (1988).

[58] Fetisova, Z. *et al.* Excitation energy transfer in chlorosomes of green bacteria: theoretical and experimental studies. *Biophys. J.* **71**, 995 – 1010 (1996).

[59] Fetisova, Z., Freiberg, A., Novoderezhkin, V., Taisova, A. & Timpmann, K. Antenna size dependent exciton dynamics in the chlorosomal antenna of the green bacterium chloroflexus aurantiacus. *FEBS Lett.* **383**, 233—236 (1996).

[60] Knoester, J. Modeling the optical properties of excitons in linear and tubular j-aggregates. *Int. J. Photoenergy* **2006**, 061364 (2006).

[61] Didraga, C. & Knoester, J. Excitons in tubular molecular aggregates. *J. Lumin.* **110**, 239 – 245 (2004).

[62] Molina, R. A., Benito-Matías, E., Somoza, A. D., Chen, L. & Zhao, Y. Superradiance at the localization-delocalization crossover in tubular chlorosomes. *Phys. Rev. E* **93**, 022414 (2016).

[63] Chenu, A. *et al.* Light adaptation in phycobilisome antennas: Influence on the rod length and structural arrangement. *J. Phys. Chem. B* **121**, 9196–9202 (2017).

[64] Eisenberg, I. *et al.* Room temperature biological quantum random walk in phycocyanin nanowires. *Phys. Chem. Chem. Phys.* **16**, 11196–11201 (2014).

[65] Eisenberg, I. *et al.* Regulating the energy flow in a cyanobacterial light-harvesting antenna complex. *J. Phys. Chem. B* **121**, 1240–1247 (2017).

[66] Bar Eyal, L. *et al.* Changes in aggregation states of light-harvesting complexes as a mechanism for modulating energy transfer in desert crust cyanobacteria. *Proc. Natl. Acad. Sci. U.S.A.* **114**, 9481–9486 (2017).

[67] Craddock, T. J. A., Friesen, D., Mane, J., Hameroff, S. & Tuszynski, J. A. The feasibility of coherent energy transfer in microtubules. *J. R. Soc. Interface* **11**, 20140677 (2014).

[68] Celardo, G., Angeli, M., Craddock, T. & Kurian, P. On the existence of superradiant excitonic states in microtubules. *New J. Phys.* **21**, 023005 (2019).

[69] Doria, S. *et al.* Photochemical control of exciton superradiance in light-harvesting nanotubes. *ACS Nano* **12**, 4556–4564 (2018).

[70] Eisele, D. M., Knoester, J., Kirstein, S., Rabe, J. P. & Bout, D. A. V. Uniform exciton fluorescence from individual molecular nanotubes immobilized on solid substrates. *Nat. Nanotechnol.* **4**, 658–663 (2009).

[71] Freyria, F. S. *et al.* Near-infrared quantum dot emission enhanced by stabilized self-assembled j-aggregate antennas. *Nano Lett.* **17**, 7665–7674 (2017).

[72] Chuang, C., Lee, C. K., Moix, J. M., Knoester, J. & Cao, J. Quantum diffusion on molecular tubes: Universal scaling of the 1d to 2d transition. *Phys. Rev. Lett.* **116**, 196803 (2016).

[73] Vlaming, S. M., Bloemsma, E. A., Nietiadi, M. L. & Knoester, J. Disorder-induced exciton localization and violation of optical selection rules in supramolecular nanotubes. *J. Chem. Phys.* **134**, 114507 (2011).

[74] Didraga, C. & Knoester, J. Optical spectra and localization of excitons in inhomogeneous helical cylindrical aggregates. *J. Chem. Phys.* **121**, 10687–10698 (2004).

[75] Didraga, C., Klugkist, J. A. & Knoester, J. Optical properties of helical cylindrical molecular aggregates: The homogeneous limit. *J. Phys. Chem. B* **106**, 11474–11486 (2002).

[76] Didraga, C. & Knoester, J. Exchange narrowing in circular and cylindrical molecular aggregates: degenerate versus nondegenerate states. *Chem. Phys.* **275**, 307 – 318 (2002). Photoprocesses in Multichromophoric Molecular Assemblies.

[77] Fidder, H., Knoester, J. & Wiersma, D. A. Optical properties of disordered molecular aggregates: A numerical study. *J. Chem. Phys.* **95**, 7880–7890 (1991).

[78] Moll, J., Daehne, S., Durrant, J. R. & Wiersma, D. A. Optical dynamics of excitons in j aggregates of a carbocyanine dye. *J. Chem. Phys.* **102**, 6362–6370 (1995).

[79] Somoza, A. D., Sun, K.-W., Molina, R. A. & Zhao, Y. Dynamics of coherence, localization and excitation transfer in disordered nanorings. *Phys. Chem. Chem. Phys.* **19**, 25996–26013 (2017).

[80] Celardo, G. L. & Kaplan, L. Superradiance transition in one-dimensional nanostructures: An effective non-hermitian hamiltonian formalism. *Phys. Rev. B* **79**, 155108 (2009).

[81] Zhang, Y., Celardo, G. L., Borgonovi, F. & Kaplan, L. Opening-assisted coherent transport in the semiclassical regime. *Phys. Rev. E* **95**, 022122 (2017).

[82] Giusteri, G. G., Celardo, G. L. & Borgonovi, F. Optimal efficiency of quantum transport in a disordered trimer. *Phys. Rev. E* **93**, 032136 (2016).

[83] Celardo, G., Biella, A., Kaplan, L. & Borgonovi, F. Interplay of superradiance and disorder in the anderson model. *Fortschr. Phys.* **61**, 250–260 (2013).

[84] Scholes, G. D. Designing light-harvesting antenna systems based on superradiant molecular aggregates. *Chem. Phys.* **275**, 373 – 386 (2002).

[85] Celardo, G. L., Borgonovi, F., Merkli, M., Tsifrinovich, V. I. & Berman, G. P. Superradiance transition in photosynthetic light-harvesting complexes. *J. Phys. Chem. C* **116**, 22105–22111 (2012).

[86] Ferrari, D., Celardo, G., Berman, G., Sayre, R. & Borgonovi, F. Quantum biological switch based on superradiance transitions. *J. Phys. Chem. C* **118**, 20–26 (2014).

[87] Clark, K. A., Krueger, E. L. & Vanden Bout, D. A. Direct measurement of energy migration in supramolecular carbocyanine dye nanotubes. *J. Phys. Chem. Lett.* **5**, 2274–2282 (2014).

[88] Eisele, D. M. *et al.* Robust excitons inhabit soft supramolecular nanotubes. *Proc. Natl. Acad. Sci. U.S.A.* **111**, E3367–E3375 (2014).

[89] Yuen-Zhou, J. *et al.* Coherent exciton dynamics in supramolecular light-harvesting nanotubes revealed by ultrafast quantum process tomography. *ACS Nano* **8**, 5527–5534 (2014).

[90] Caram, J. R. *et al.* Room-temperature micron-scale exciton migration in a stabilized emissive molecular aggregate. *Nano Lett.* **16**, 6808–6815 (2016).

[91] Spano, F. C., Kuklinski, J. R. & Mukamel, S. Cooperative radiative dynamics in molecular aggregates. *J. Chem. Phys.* **94**, 7534–7544 (1991).

[92] Ganapathy, S. *et al.* Alternating syn-anti bacteriochlorophylls form concentric helical nanotubes in chlorosomes. *Proc. Natl. Acad. Sci. U.S.A.* **106**, 8525–8530 (2009).

[93] Günther, L. M. *et al.* Structure of light-harvesting aggregates in individual chlorosomes. *J. Phys. Chem. B* **120**, 5367–5376 (2016).

[94] Pšenčík, J., Ma, Y.-Z., Arellano, J. B., Hála, J. & Gillbro, T. Excitation energy transfer dynamics and excited-state structure in chlorosomes of chlorobium phaeobacteroides. *Biophys. J.* **84**, 1161–1179 (2003).

[95] Chew, A. G. M., Frigaard, N.-U. & Bryant, D. A. Bacteriochlorophyllide c c-82 and c-121 methyltransferases are essential for adaptation to low light in chlorobaculum tepidum. *J. Bacteriol.* **189**, 6176–6184 (2007).

[96] Linnanto, J. M. & Korppi-Tommola, J. E. I. Exciton description of chlorosome to baseplate excitation energy transfer in filamentous anoxygenic phototrophs and green sulfur bacteria. *J. Phys. Chem. B* **117**, 11144–11161 (2013).

[97] Hohmann-Marriott, M. F., Blankenship, R. E. & Roberson, R. W. The ultrastructure of chlorobium tepidum chlorosomes revealed by electron microscopy. *Photosynth. Res.* **86**, 145–154 (2005).

[98] Pšenčík, J. *et al.* Lamellar organization of pigments in chlorosomes, the light harvesting complexes of green photosynthetic bacteria. *Biophys. J.* **87**, 1165–1172 (2004).

[99] Oostergetel, G. T., van Amerongen, H. & Boekema, E. J. The chlorosome: a prototype for efficient light harvesting in photosynthesis. *Photosynth. Res.* **104**, 245–255 (2010).

[100] Prokhorenko, V., Steensgaard, D. & Holzwarth, A. Exciton dynamics in the chlorosomal antennae of the green bacteria chloroflexus aurantiacus and chlorobium tepidum. *Biophys. J.* **79**, 2105–2120 (2000).

[101] Prokhorenko, V., Steensgaard, D. & Holzwarth, A. Exciton theory for supramolecular chlorosomal aggregates: 1. aggregate size dependence of the linear spectra. *Biophys. J.* **85**, 3173–3186 (2003).

[102] Akkermans, E., Gero, A. & Kaiser, R. Photon localization and dicke superradiance in atomic gases. *Phys. Rev. Lett.* **101**, 103602 (2008).

[103] Strümpfer, J. & Schulten, K. Light harvesting complex ii b850 excitation dynamics. *J. Chem. Phys.* **131**, 225101 (2009).

[104] Damjanović, A., Kosztin, I., Kleinekathöfer, U. & Schulten, K. Excitons in a photosynthetic light-harvesting system: A combined molecular dynamics, quantum chemistry, and polaron model study. *Phys. Rev. E* **65**, 031919 (2002).

[105] Dostál, J. *et al.* Two-dimensional electronic spectroscopy reveals ultrafast energy diffusion in chlorosomes. *J. Am. Chem. Soc.* **134**, 11611–11617 (2012).

[106] Didraga, C. & Knoester, J. Chiral exciton wave functions in cylindrical j aggregates. *J. Chem. Phys.* **121**, 946–959 (2004).

[107] Saikin, S. K. *et al.* Corrigendum: Chromatic acclimation and population dynamics of green sulfur bacteria grown with spectrally tailored light. *Sci. Rep.* **5**, 9786 (2015).

[108] Linnanto, J. M. & Korppi-Tommola, J. E. Investigation on chlorosomal antenna geometries: tube, lamella and spiral-type self-aggregates. *Photosynth. Res.* **96**, 227 (2008).

[109] Anderson, P. W. Absence of diffusion in certain random lattices. *Phys. Rev.* **109**, 1492–1505 (1958).

[110] Ritz, T., Adem, S. & Schulten, K. A model for photoreceptor-based magnetoreception in birds. *Biophys. J.* **78**, 707–718 (2000).

[111] Rodgers, C. T. & Hore, P. J. Chemical magnetoreception in birds: the radical pair mechanism. *Proc. Natl. Acad. Sci. U.S.A.* **106**, 353–360 (2009).

[112] Gauger, E. M., Rieper, E., Morton, J. J., Benjamin, S. C. & Vedral, V. Sustained quantum coherence and entanglement in the avian compass. *Phys. Rev. Lett.* **106**, 040503 (2011).

[113] Hiscock, H. G. *et al.* The quantum needle of the avian magnetic compass. *Proc. Natl. Acad. Sci. U.S.A.* **113**, 4634–4639 (2016).

[114] Beatty, J. T. *et al.* An obligately photosynthetic bacterial anaerobe from a deep-sea hydrothermal vent. *Proc. Natl. Acad. Sci. U.S.A.* **102**, 9306–9310 (2005).

[115] Reusswig, P. D. *et al.* A path to practical solar pumped lasers via radiative energy transfer. *Sci. Rep.* **5**, 14758 (2015).

[116] Spano, F. C. & Mukamel, S. Superradiance in molecular aggregates. *J. Chem. Phys.* **91**, 683–700 (1989).

[117] Gullì, M. *et al.* Macroscopic coherence as an emergent property in molecular nanotubes. *New J. Phys.* **21**, 013019 (2019).

[118] Patlolla, P. R., Mahapatra, A. D., Mallajosyula, S. S. & Datta, B. Template-free h-dimer and h-aggregate formation by dimeric carbocyanine dyes. *New J. Chem.* **42**, 6727–6734 (2018).

[119] Caselli, M., Latterini, L. & Ponterini, G. Consequences of h-dimerization on the photophysics and photochemistry of oxacarbocyanines. *Phys. Chem. Chem. Phys.* **6**, 3857–3863 (2004).

[120] Gavrilenko, V. & Noginov, M. Ab initio study of optical properties of rhodamine 6g molecular dimers. *J. Chem. Phys.* **124**, 044301 (2006).

[121] Hestand, N. J. & Spano, F. C. Expanded theory of h-and j-molecular aggregates: the effects of vibronic coupling and intermolecular charge transfer. *Chem. Rev.* **118**, 7069–7163 (2018).

[122] Scully, M. O. Quantum photocell: Using quantum coherence to reduce radiative recombination and increase efficiency. *Phys. Rev. Lett.* **104**, 207701 (2010).

[123] Dorfman, K. E., Voronine, D. V., Mukamel, S. & Scully, M. O. Photosynthetic reaction center as a quantum heat engine. *Proc. Natl. Acad. Sci. U.S.A.* **110**, 2746–2751 (2013).

[124] Scully, M. O., Chapin, K. R., Dorfman, K. E., Kim, M. B. & Svidzinsky, A. Quantum heat engine power can be increased by noise-induced coherence. *Proc. Natl. Acad. Sci. U.S.A.* **108**, 15097–15100 (2011).

[125] Creatore, C., Parker, M. A., Emmott, S. & Chin, A. W. Efficient biologically inspired photocell enhanced by delocalized quantum states. *Phys. Rev. Lett.* **111**, 253601 (2013).

[126] Fruchtman, A., Gómez-Bombarelli, R., Lovett, B. W. & Gauger, E. M. Photocell optimization using dark state protection. *Phys. Rev. Lett.* **117**, 203603 (2016).

[127] Zhang, Y., Oh, S., Alharbi, F. H., Engel, G. S. & Kais, S. Delocalized quantum states enhance photocell efficiency. *Phys. Chem. Chem. Phys.* **17**, 5743–5750 (2015).

[128] Brown, W. M. & Gauger, E. M. Light harvesting with guide-slide superabsorbing condensed-matter nanostructures. *J. Phys. Chem. Lett.* **10**, 4323–4329 (2019).

[129] Gierschner, J., Varghese, S. & Park, S. Y. Organic single crystal lasers: A materials view. *Adv. Opt. Mater.* **4**, 348–364 (2016).

[130] Özçelik, S., Özçelik, I. & Akins, D. L. Superradiant lasing from j-aggregated molecules adsorbed onto colloidal silver. *Appl. Phys. Lett.* **73**, 1949–1951 (1998).

[131] Hindman, J. C., Kugel, R., Wasielewski, M. R. & Katz, J. J. Coherent stimulated light emission (lasing) in covalently linked chlorophyll dimers. *Proc. Natl. Acad. Sci. U.S.A.* **75**, 2076–2079 (1978).

[132] Shatokhin, V. N., Walschaers, M., Schlawin, F. & Buchleitner, A. Coherence turned on by incoherent light. *New J. Phys.* **20**, 113040 (2018).

[133] Pavlopoulos, T. G. Scaling of dye lasers with improved laser dyes. *Prog. Quantum. Electron.* **26**, 193–224 (2002).

[134] Würfel, P. & Würfel, U. *Physics of solar cells: from basic principles to advanced concepts* (John Wiley & Sons, 2016).

[135] Deshmukh, A. P. *et al.* Design principles for two-dimensional molecular aggregates using kasha's model: Tunable photophysics in near and short-wave infrared. *J. Phys. Chem. C* **123**, 18702–18710 (2019).

[136] Scully, M. O. & Zubairy, M. S. *Quantum Optics* (Cambridge University Press, 1997).

[137] Zhu, S., Scully, M., Fearn, H. & Narducci, L. Lasing without inversion. *Z. Phys. D* **22**, 483–493 (1992).

[138] Hu, X. & Schulten, K. Model for the light-harvesting complex i (b875) of rhodobacter sphaeroides. *Biophys. J.* **75**, 683–694 (1998).

[139] Hu, X., Ritz, T., Damjanović, A., Autenrieth, F. & Schulten, K. Photosynthetic apparatus of purple bacteria. *Q. Rev. Biophys.* **35**, 1–62 (2002).

[140] Yao, J., Yang, X., Yin, X., Bartal, G. & Zhang, X. Three-dimensional nanometer-scale optical cavities of indefinite medium. *Proc. Natl. Acad. Sci. U.S.A.* **108**, 11327–11331 (2011).

[141] Ma, R.-M. & Oulton, R. F. Applications of nanolasers. *Nat. Nanotechnol.* **14**, 12–22 (2019).

[142] Amarnath, K., Bennett, D. I., Schneider, A. R. & Fleming, G. R. Multiscale model of light harvesting by photosystem ii in plants. *Proc. Natl. Acad. Sci. U.S.A.* **113**, 1156–1161 (2016).

[143] Madjet, M. E., Abdurahman, A. & Renger, T. Intermolecular coulomb couplings from ab initio electrostatic potentials: Application to optical transitions of strongly coupled pigments in photosynthetic antennae and reaction centers. *J. Phys. Chem. B* **110**, 17268–17281 (2006).

[144] Ritz, T., Park, S. & Schulten, K. Kinetics of excitation migration and trapping in the photosynthetic unit of purple bacteria. *J. Phys. Chem. B* **105**, 8259–8267 (2001).

[145] Fujita, T., Brookes, J. C., Saikin, S. K. & Aspuru-Guzik, A. Memory-assisted exciton diffusion in the chlorosome light-harvesting antenna of green sulfur bacteria. *J. Phys. Chem. Lett.* **3**, 2357–2361 (2012).

[146] Bonifacio, R. & Lugiato, L. A. Cooperative radiation processes in two-level systems: Superfluorescence. *Phys. Rev. A* **11**, 1507–1521 (1975).

[147] Murray, C. B., Kagan, C. R. & Bawendi, M. G. Synthesis and characterization of monodisperse nanocrystals and close-packed nanocrystal assemblies. *Annu. Rev. Mater. Sci.* **30**, 545–610 (2000).

[148] Shevchenko, E. V., Talapin, D. V., Kotov, N. A., O'Brien, S. & Murray, C. B. Structural diversity in binary nanoparticle superlattices. *Nature* **439**, 55–59 (2006).

[149] Becker, M. A. *et al.* Bright triplet excitons in caesium lead halide perovskites. *Nature* **553**, 189–193 (2018).

[150] Bellando, L., Gero, A., Akkermans, E. & Kaiser, R. Cooperative effects and disorder: A scaling analysis of the spectrum of the effective atomic hamiltonian. *Phys. Rev. A* **90**, 063822 (2014).

[151] Guerin, W., Rouabah, M. & Kaiser, R. Light interacting with atomic ensembles: collective, cooperative and mesoscopic effects. *J. Mod. Opt.* **64**, 895–907 (2017).

[152] Bettles, R. *Cooperative interactions in lattices of atomic dipoles* (Springer, 2017).

[153] Brennan, M. C. *et al.* Superlattices are greener on the other side: How light transforms self-assembled mixed halide perovskite nanocrystals. *ACS Energy Lett.* **5**, 1465–1473 (2020).

[154] Vovk, I. A. *et al.* Excitonic phenomena in perovskite quantum-dot supercrystals. *Phys. Chem. Chem. Phys.* **20**, 25023–25030 (2018).

[155] Spano, F. C., Kuklinski, J. R. & Mukamel, S. Temperature-dependent superradiant decay of excitons in small aggregates. *Phys. Rev. Lett.* **65**, 211–214 (1990).

[156] Meier, T., Zhao, Y., Chernyak, V. & Mukamel, S. Polarons, localization, and excitonic coherence in superradiance of biological antenna complexes. *J. Chem. Phys.* **107**, 3876–3893 (1997).

[157] Brennan, M. C. *et al.* Origin of the size-dependent stokes shift in cspbbr3 perovskite nanocrystals. *J. Am. Chem. Soc.* **139**, 12201–12208 (2017).

[158] Frantsuzov, P., Kuno, M., Janko, B. & Marcus, R. A. Universal emission intermittency in quantum dots, nanorods and nanowires. *Nat. Phys.* **4**, 519–522 (2008).

[159] Frantsuzov, P. A., Volkán-Kacsó, S. & Jankó, B. Model of fluorescence intermittency of single colloidal semiconductor quantum dots using multiple recombination centers. *Phys. Rev. Lett.* **103**, 207402 (2009).

[160] Frantsuzov, P. A., Volkán-Kacsó, S. & Jankó, B. Universality of the fluorescence intermittency in nanoscale systems: Experiment and theory. *Nano Lett.* **13**, 402–408 (2013).

[161] Baranov, D., Toso, S., Imran, M. & Manna, L. Investigation into the photoluminescence red shift in cesium lead bromide nanocrystal superlattices. *J. Phys. Chem. Lett.* **10**, 655–660 (2019).

[162] van der Burgt, J. S. *et al.* Cuboidal supraparticles self-assembled from cubic cspbbr3 perovskite nanocrystals. *J. Phys. Chem. C* **122**, 15706–15712 (2018).

[163] Nagaoka, Y. *et al.* Nanocube superlattices of cesium lead bromide perovskites and pressure-induced phase transformations at atomic and mesoscale levels. *Adv. Mater.* **29**, 1606666 (2017).

[164] Tong, Y. *et al.* Spontaneous self-assembly of perovskite nanocrystals into electronically coupled supercrystals: Toward filling the green gap. *Adv. Mater.* **30**, 1801117 (2018).

[165] Imran, M. *et al.* Shape-pure, nearly monodispersed cspbbr3 nanocubes prepared using secondary aliphatic amines. *Nano Lett.* **18**, 7822–7831 (2018).

[166] Kovalenko, M. V. & Bodnarchuk, M. I. Lead halide perovskite nanocrystals: From discovery to self-assembly and applications. *CHIMIA International Journal for Chemistry* **71**, 461–470 (2017).

[167] Wang, K.-H., Yang, J.-N., Ni, Q.-K., Yao, H.-B. & Yu, S.-H. Metal halide perovskite supercrystals: Gold–bromide complex triggered assembly of cspbbr3 nanocubes. *Langmuir* **34**, 595–602 (2018).

[168] Brennan, M. C. *et al.* Universal size-dependent stokes shifts in lead halide perovskite nanocrystals. *J. Phys. Chem. Lett.* **11**, 4937–4944 (2020).

[169] Kayanuma, Y. Quantum-size effects of interacting electrons and holes in semiconductor microcrystals with spherical shape. *Phys. Rev. B* **38**, 9797–9805 (1988).

[170] Ashcroft, N. W. & Mermin, N. D. *Solid state physics* (Holt, Rinehart and Winston, 1976).

[171] Brus, L. E. Electron–electron and electron-hole interactions in small semiconductor crystallites: The size dependence of the lowest excited electronic state. *J. Chem. Phys.* **80**, 4403–4409 (1984).

[172] Meiser, D. & Holland, M. J. Steady-state superradiance with alkaline-earth-metal atoms. *Phys. Rev. A* **81**, 033847 (2010).

[173] Zhu, B. *et al.* Synchronization of interacting quantum dipoles. *New J. Phys.* **17**, 083063 (2015).

[174] Sakurai, J. J. *Modern quantum mechanics, revised edition* (Addison-Wesley Publishing Company, 1995).

[175] Anderson, P. W. More is different. *Science* **177**, 393–396 (1972).

[176] Dagotto, E. Complexity in strongly correlated electronic systems. *Science* **309**, 257–262 (2005).

[177] van Loo, A. F. *et al.* Photon-mediated interactions between distant artificial atoms. *Science* **342**, 1494–1496 (2013).

[178] Santos, L. F., Borgonovi, F. & Celardo, G. L. Cooperative shielding in many-body systems with long-range interaction. *Phys. Rev. Lett.* **116**, 250402 (2016).

[179] Laurent, T. *et al.* Superradiant emission from a collective excitation in a semiconductor. *Phys. Rev. Lett.* **115**, 187402 (2015).

[180] Pustovit, V. N. & Shahbazyan, T. V. Cooperative emission of light by an ensemble of dipoles near a metal nanoparticle: The plasmonic dicke effect. *Phys. Rev. Lett.* **102**, 077401 (2009).

[181] Biella, A., Borgonovi, F., Kaiser, R. & Celardo, G. L. Subradiant hybrid states in the open 3d anderson-dicke model. *EPL* **103**, 57009 (2013).

[182] Arecchi, F., Bonifacio, R. & Scully, M. *Coherence in Spectroscopy and Modern Physics* (Springer, 1977).

[183] DiRienzo, A. *et al.* Superconductivity and quantum optics. In *Coherence in Spectroscopy and Modern Physics*, 231–259 (Springer, 1978).

[184] Jung, C., Müller, M. & Rotter, I. Phase transitions in open quantum systems. *Phys. Rev. E* **60**, 114–131 (1999).

[185] Sokolov, V. & Zelevinsky, V. On a statistical theory of overlapping resonances. *Phys. Lett. B* **202**, 10 – 14 (1988).

[186] Rotter, I. A continuum shell model for the open quantum mechanical nuclear system. *Rep. Prog. Phys.* **54**, 635–682 (1991).

[187] von Delft, J. Superconductivity in ultrasmall metallic grains. *Ann. Phys.* **10**, 219–276 (2001).

[188] Faribault, A., Calabrese, P. & Caux, J.-S. Exact mesoscopic correlation functions of the richardson pairing model. *Phys. Rev. B* **77**, 064503 (2008).

[189] Smith, R. A. & Ambegaokar, V. Effect of level statistics on superconductivity in ultrasmall metallic grains. *Phys. Rev. Lett.* **77**, 4962–4965 (1996).

[190] Schechter, M., von Delft, J., Imry, Y. & Levinson, Y. Two pairing parameters in superconducting grains. *Phys. Rev. B* **67**, 064506 (2003).

[191] Yuzbashyan, E. A., Baytin, A. A. & Altshuler, B. L. Finite-size corrections for the pairing hamiltonian. *Phys. Rev. B* **71**, 094505 (2005).

[192] Owusu, H. K., Wagh, K. & Yuzbashyan, E. A. The link between integrability, level crossings and exact solution in quantum models. *J. Phys. A: Math. Theor.* **42**, 035206 (2008).

[193] Yuzbashyan, E. A. & Shastry, B. S. Quantum integrability in systems with finite number of levels. *J. Stat. Phys.* **150**, 704–721 (2013).

[194] Cooper, L. N. Bound electron pairs in a degenerate fermi gas. *Phys. Rev.* **104**, 1189–1190 (1956).

[195] Celardo, G. L., Izrailev, F. M., Zelevinsky, V. G. & Berman, G. P. Open system of interacting fermions: Statistical properties of cross sections and fluctuations. *Phys. Rev. E* **76**, 031119 (2007).

[196] Celardo, G. L., Auerbach, N., Izrailev, F. M. & Zelevinsky, V. G. Distribution of resonance widths and dynamics of continuum coupling. *Phys. Rev. Lett.* **106**, 042501 (2011).

[197] Sorathia, S., Izrailev, F. M., Celardo, G. L., Zelevinsky, V. G. & Berman, G. P. Internal chaos in an open quantum system: From ericson to conductance fluctuations. *EPL* **88**, 27003 (2009).

[198] Celardo, G., Izrailev, F., Zelevinsky, V. & Berman, G. Transition from isolated to overlapping resonances in the open system of interacting fermions. *Phys. Lett. B* **659**, 170 – 175 (2008).

[199] Biella, A., Borgonovi, F., Kaiser, R. & Celardo, G. L. Subradiant hybrid states in the open 3d anderson-dicke model. *EPL* **103**, 57009 (2013).

[200] Jurcevic, P. *et al.* Quasiparticle engineering and entanglement propagation in a quantum many-body system. *Nature* **511**, 202–205 (2014).

[201] Richerme, P. *et al.* Non-local propagation of correlations in quantum systems with long-range interactions. *Nature* **511**, 198–201 (2014).

[202] Celardo, G. L., Kaiser, R. & Borgonovi, F. Shielding and localization in the presence of long-range hopping. *Phys. Rev. B* **94**, 144206 (2016).

[203] De Gennes, P.-G. *Superconductivity of metals and alloys* (Addison-Wesley Publishing Company, 1966).

[204] Álvarez, G. A., Danieli, E. P., Levstein, P. R. & Pastawski, H. M. Environmentally induced quantum dynamical phase transition in the spin swapping operation. *J. Chem. Phys.* **124**, 194507 (2006).

[205] Pastawski, H. M. Revisiting the fermi golden rule: Quantum dynamical phase transition as a paradigm shift. *Physica B* **398**, 278 – 286 (2007).

[206] Dente, A. D., Bustos-Marún, R. A. & Pastawski, H. M. Dynamical regimes of a quantum swap gate beyond the fermi golden rule. *Phys. Rev. A* **78**, 062116 (2008).

[207] Ruderman, A., Dente, A. D., Santos, E. & Pastawski, H. M. Molecular dissociation in the presence of catalysts: interpreting bond breaking as a quantum dynamical phase transition. *J. Phys.: Condens. Matter* **27**, 315501 (2015).

[208] Schachenmayer, J., Genes, C., Tignone, E. & Pupillo, G. Cavity-enhanced transport of excitons. *Phys. Rev. Lett.* **114**, 196403 (2015).

[209] Feist, J. & Garcia-Vidal, F. J. Extraordinary exciton conductance induced by strong coupling. *Phys. Rev. Lett.* **114**, 196402 (2015).

[210] Coles, D. M. *et al.* Polariton-mediated energy transfer between organic dyes in a strongly coupled optical microcavity. *Nat. Mater.* **13**, 712–719 (2014).

[211] Zhong, X. *et al.* Energy transfer between spatially separated entangled molecules. *Angew. Chem. Int. Ed.* **56**, 9034–9038 (2017).

[212] Lerario, G. *et al.* High-speed flow of interacting organic polaritons. *Light Sci. Appl.* **6**, e16212–e16212 (2017).

[213] Reitz, M., Mineo, F. & Genes, C. Energy transfer and correlations in cavity-embedded donor-acceptor configurations. *Sci. Rep.* **8**, 9050 (2018).

[214] Du, M. *et al.* Theory for polariton-assisted remote energy transfer. *Chem. Sci.* **9**, 6659–6669 (2018).

[215] Schäfer, C., Ruggenthaler, M., Appel, H. & Rubio, A. Modification of excitation and charge transfer in cavity quantum-electrodynamical chemistry. *Pro. Natl. Acad. Sci. U.S.A.* **116**, 4883–4892 (2019).

[216] Orgiu, E. *et al.* Conductivity in organic semiconductors hybridized with the vacuum field. *Nat. Mater.* **14**, 1123–1129 (2015).

[217] Hagenmüller, D., Schachenmayer, J., Schütz, S., Genes, C. & Pupillo, G. Cavity-enhanced transport of charge. *Phys. Rev. Lett.* **119**, 223601 (2017).

[218] Hagenmüller, D., Schütz, S., Schachenmayer, J., Genes, C. & Pupillo, G. Cavity-assisted mesoscopic transport of fermions: Coherent and dissipative dynamics. *Phys. Rev. B* **97**, 205303 (2018).

[219] Abrahams, E. *50 Years of Anderson Localization* (World Scientific, Singapore, 2010).

[220] Storch, D.-M., Van den Worm, M. & Kastner, M. Interplay of soundcone and supersonic propagation in lattice models with power law interactions. *New J. Phys.* **17**, 063021 (2015).

[221] Deng, X., Kravtsov, V., Shlyapnikov, G. & Santos, L. Duality in power-law localization in disordered one-dimensional systems. *Phys. Rev. Lett.* **120**, 110602 (2018).

[222] Nosov, P. A., Khaymovich, I. M. & Kravtsov, V. Correlation-induced localization. *Phys. Rev. B* **99**, 104203 (2019).

[223] Nosov, P. A. & Khaymovich, I. M. Robustness of delocalization to the inclusion of soft constraints in long-range random models. *Phys. Rev. B* **99**, 224208 (2019).

[224] de Moura, F., Malyshev, A., Lyra, M., Malyshev, V. & Domínguez-Adame, F. Localization properties of a one-dimensional tight-binding model with nonrandom long-range intersite interactions. *Phys. Rev. B* **71**, 174203 (2005).

[225] Liu, F. *et al.* Confined quasiparticle dynamics in long-range interacting quantum spin chains. *Phys. Rev. Lett.* **122**, 150601 (2019).

[226] Lerose, A., Žunkovič, B., Silva, A. & Gambassi, A. Quasilocalized excitations induced by long-range interactions in translationally invariant quantum spin chains. *Phys. Rev. B* **99**, 121112 (2019).

[227] Mori, T. Prethermalization in the transverse-field ising chain with long-range interactions. *J. Phys. A* **52**, 054001 (2019).

[228] Levitov, L. S. Absence of localization of vibrational modes due to dipole-dipole interaction. *EPL* **9**, 83–86 (1989).

[229] Evers, F. & Mirlin, A. D. Anderson transitions. *Rev. Mod. Phys.* **80**, 1355–1417 (2008).

[230] Botzung, T. *et al.* Dark state semilocalization of quantum emitters in a cavity. *Phys. Rev. B* **102**, 144202 (2020).

[231] Thouless, D. J. *Ill-Condensed Matter* (edited by R. Balian, R. Maynard, and G. Toulouse, North-Holland, Amsterdam, 1979).

[232] Izrailev, F. M., Ruffo, S. & Tessieri, L. Classical representation of the one-dimensional anderson model. *J. Phys. A* **31**, 5263–5270 (1998).

[233] Kropf, C. M. *et al.* Towards high-temperature coherence-enhanced transport in heterostructures of a few atomic layers. *Phys. Rev. B* **100**, 035126 (2019).

[234] Kropf, C. M., Celardo, G. L., Giannetti, C. & Borgonovi, F. Electric-field assisted optimal quantum transport of photo-excitations in polar heterostructures. *Physica E Low Dimens. Syst. Nanostruct.* **120**, 114023 (2020).

[235] Mohseni, M., Rebentrost, P., Lloyd, S. & Aspuru-Guzik, A. Environment-assisted quantum walks in photosynthetic energy transfer. *J. Chem. Phys.* **129**, 174106 (2008).

[236] Rebentrost, P., Mohseni, M., Kassal, I., Lloyd, S. & Aspuru-Guzik, A. Environment-assisted quantum transport. *New J. Phys.* **11**, 033003 (2009).

[237] Botzung, T. *et al.* Algebraic localization from power-law couplings in disordered quantum wires. *Phys. Rev. B* **100**, 155136 (2019).

[238] Vahala, K. J. Optical microcavities. *Nature* **424**, 839–846 (2003).

[239] Datta, S. *Quantum Transport: Atom to Transistor* (Cambridge University Press, 2005).

[240] Sokolov, V. V., Rotter, I., Savin, D. V. & Müller, M. Interfering doorway states and giant resonances. i. resonance spectrum and multipole strengths. *Phys. Rev. C* **56**, 1031–1043 (1997).

[241] Chenu, A., Brańczyk, A. M., Scholes, G. D. & Sipe, J. E. Thermal light cannot be represented as a statistical mixture of single pulses. *Phys. Rev. Lett.* **114**, 213601 (2015).

[242] Szymanska, M. H. Bose condensation and lasing in optical microstructures - part 1 (2002). Ph.D. dissertation, `https://arXiv.org/abs/cond-mat/0204294`.

[243] Szymanska, M. H. Bose condensation and lasing in optical microstructures - part 2 (2002). Ph.D. dissertation, `https://arXiv.org/abs/cond-mat/0204307`.

[244] Mazza, G. & Georges, A. Superradiant quantum materials. *Phys. Rev. Lett.* **122**, 017401 (2019).

[245] Moix, J. M., Khasin, M. & Cao, J. Coherent quantum transport in disordered systems: I. the influence of dephasing on the transport properties and absorption spectra on one-dimensional systems. *New J. Phys.* **15**, 085010 (2013).